Advancing Applications of Synthetic Aperture Radar for Cryopshere Studies in Alpine Regions

Author(s):
Li, Shiyi

Publication date:
2025

Permanent link:
https://doi.org/https://doi.org/10.3929/ethz-c-000785960

DISS. ETH NO. 31265

ADVANCING APPLICATIONS OF SYNTHETIC APERTURE RADAR FOR CRYOPSHERE STUDIES IN ALPINE REGIONS

A thesis submitted to attain the degree of

Doctor of Sciences
(Dr. sc. ETH Zurich)

presented by

SHIYI LI

born on July 22, 1992

accepted on the recommendation of

Prof. Dr. Irena Hajnsek
Prof. Dr. Andreas Kääb
Prof. Dr. Emmanuel Trouvé
Prof. Dr. Matthias Braun

2025

Shiyi Li: *Advancing Applications of Synthetic Aperture Radar for Cryopshere Studies in Alpine Regions,* © 2025

DOI: 10.3929/ethz-a-

To mom and dad,
for your unconditional love and support.

致我的父母，
感谢你们无条件的爱和支持。

ABSTRACT

The cryosphere is a crucial component of Earth's climate system, influencing global climate patterns, sea-level rise, and freshwater availability. Within this system, the alpine cryosphere is especially important due to its sensitivity to climatic changes and their substantial impact on regional hydrology, ecosystems, and natural hazard dynamics. The accurate monitoring and assessment of alpine cryosphere presents significant challenges, primarily due to the complexity of the terrain and the variability of the environmental conditions.

This dissertation aims to address these challenges by advancing synthetic aperture radar (SAR) methodologies to enhance the understandings about cryosphere processes. Particularly, the application of SAR in three essential cryosphere research areas were investigated, including glacier dynamics monitoring, snowmelt mapping, and glacier mass balance assessments. The studies were conducted in various alpine regions, including the Swiss Alps and the Karakoram, utilizing high-resolution SAR data from multiple satellite missions.

The first study developed a novel cross-correlation stacking method to improve offset tracking for measuring glacier surface displacements. By leveraging temporal redundancy in SAR image series, the method significantly reduced noise interference and improved the accuracy and coverage of displacement estimations. The method was successfully applied and validated on the Aletsch Glacier in the Swiss Alps, demonstrating broad applicability and enhanced performance across different SAR sensors.

The second study proposed an integrated framework combining SAR data with topographic information to accurately map seasonal snow melting in mountainous regions. The adaptive integration of SAR-based wet snow detection and terrain corrections significantly improved mapping accuracy compared to conventional methods. Applied in the Karakoram region, this approach provided valuable insights into snowmelt dynamics, aiding water resource management and climate adaptation strategies.

The third study developed a comprehensive framework leveraging digital elevation models (DEMs) derived from the high-resolution TanDEM-X SAR data to assess the elevation and mass changes of glaciers in the Karakoram region. The proposed framework effectively integrated InSAR DEM generation, elevation change mapping and mass balance estimation, providing a

scalable and robust approach for glacier mass balance assessments. The study revealed the updated mass balance of glaciers in Karakoram and detailed the spatial distribution of glacier elevation changes, contributing to a better understanding of glacier dynamics in this region.

Collectively, these studies demonstrated the substantial potential of advanced SAR techniques to address challenges in alpine cryosphere research, offering scalable and accurate tools essential for climate resilience, sustainable water management, and environmental monitoring.

ZUSAMMENFASSUNG

Die Kryosphäre ist eine entscheidende Komponente des Klimasystems der Erde, da sie globale Klimaerscheinungen, den Meeresspiegelanstieg und die Verfügbarkeit von Süßwasser wesentlich beeinflusst. Wegen ihrer Sensibilität gegenüber klimatischen Veränderungen sowie aufgrund ihrer signifikanten Zusammenhänge mit Ökosystemen, dem regionalen Wasserkreislauf und diversen Naturgefahren spielt die alpine Kryosphäre innerhalb dieses Systems eine besonders wichtige Rolle. Ihre präzise Überwachung und Einschätzung birgt erhebliche Herausforderungen, vor allem aufgrund der Komplexität des Geländes und der Variabilität der Umweltbedingungen.

Gegenstand dieser Dissertation ist die Weiterentwicklung von Synthetic-Aperture-Radar- (SAR-)Methoden mit dem Ziel, Prozesse in der Kryosphäre besser zu verstehen und die genannten Herausforderungen zu bewältigen. Insbesondere wurde die Anwendung von SAR in drei wesentlichen Forschungsbereichen der Kryosphäre untersucht: Überwachung der Gletscherdynamik, Kartierung der Schneeschmelze und Bewertung der Gletschermassenbilanz. Die Studien wurden in verschiedenen alpinen Regionen durchgeführt, darunter die Alpen und der Karakorum, unter Verwendung hochauflösender SAR-Daten aus mehreren Satellitenmissionen.

Die erste Studie entwickelte eine neuartige Cross-Correlation-Stacking-Methode, um das Offset-Tracking zur Messung von Gletscheroberflächenbewegungen zu verbessern. Durch die Nutzung der zeitlichen Redundanz in SAR-Bildserien konnte diese Methode die Signalqualität sowie die Genauigkeit und Abdeckung der Verschiebungsschätzungen erheblich verbessern. Die Methode wurde erfolgreich auf den Aletschgletscher in den Schweizer Alpen angewendet und validiert, wobei sie eine breite Anwendbarkeit und verbesserte Leistung über verschiedene SAR-Sensoren hinweg demonstrierte.

Die zweite Studie schlug ein System vor, SAR-Daten mit topografischen Informationen zu kombinieren, um die saisonale Schneeschmelze in Bergregionen genau zu kartieren. Die adaptive Integration von SAR-basierter Nassschneeerkennung und Geländekorrektur verbesserte die Kartierungsgenauigkeit im Vergleich zu herkömmlichen Methoden signifikant. Diese Methode wurde im Karakorum angewendet und lieferte wertvolle Erkenntnisse über die Dynamik der Schneeschmelze, die hilfreich für die Wasserressourcenbewirtschaftung und Klimaanpassung sind.

Die dritte Studie entwickelte ein umfassendes System, das digitale Höhenmodelle (DEMs) aus den hochauflösenden TanDEM-X-SAR-Daten nutzt, um die Höhen- und Massenänderungen von Gletschern im Karakorum zu bewerten. Das vorgeschlagene System vereinte effektiv die Erstellung von DEMs, die Kartierung von Höhenänderungen sowie die Schätzung der Massenbilanz und bietet einen skalierbaren und robusten Ansatz zur Bewertung der Gletschermassenbilanz. Die Studie enthüllte die aktualisierte Massenbilanz der Gletscher im Karakorum und beschrieb detailliert die räumliche Verteilung der Gletscherhöhenänderungen, was zu einem besseren Verständnis der Gletscherdynamik in dieser Region beitrug.

Insgesamt haben diese Studien das erhebliche Potenzial von SAR-Methoden zur Bewältigung von Herausforderungen in der alpinen Kryosphärenforschung demonstriert und skalierbare sowie präzise Werkzeuge bereitgestellt, die für Klimaresilienz, nachhaltiges Wassermanagement und Umweltüberwachung unerlässlich sind.

ACKNOWLEDGEMENTS

It was a tough journey to finally finish this dissertation after six years of work. Luckily, it was not a lonely journey. Along the way, I received help, guidance, encouragement, and support from many people. I would like to take this opportunity to express my gratitude to all of them.

First and foremost, I would like to express my profound gratitude to my supervisor, Prof. Dr. Irena Hajnsek, for her continuous support and guidance throughout my PhD journey. She has been patient, understanding, and encouraging, always willing to help and provide constructive feedback. I am deeply grateful for her trust in me and the freedom she gave me to explore my own ideas.

I would like to extend my sincere thanks to Dr. Silvan Leinss, who has been my mentor and collaborator during my doctoral studies, as well as a great friend. I am grateful for his guidance, inspiration, and motivation. His support has always been reliable and invaluable, and his help could always be counted on.

During my time at ETH, I have been fortunate to work with many talented, inspiring, and supportive colleagues. I would like to thank Othmar, Roberto, Philipp, Lanqing, and Marcel, who welcomed me on my first day in the group and generously shared their knowledge and experience with me. After I was no longer a "newcomer," I had the pleasure of welcoming new members, including Magnus, Kathrin, Esther, Jiayin, Yanyan, Didi, and Marion. I am grateful for the cheerful atmosphere you created in the group and the enjoyable coffee breaks and lunch times. I would also like to express my special gratitude to Ani, who has always been so considerate and warm-hearted. I am thankful not only for her help in my work but also for caring about my life as a friend.

To the "new" friends I made in the last year after moving to the new office — Yaxing, Edoardo, Flavio, Shuntian and many other colleagues at IfU — thank you for the fun times at the ping-pong table and around the coffee corner. These moments brought me much joy during the stressful period of finalizing my dissertation.

A special person in my life is Lu, who has been my partner in life and accompanied me throughout this journey. There were ups and downs in life and study, but she has always been there for me, having faith in me

and supporting me unconditionally. I am deeply grateful for her love and understanding.

Finally, my deepest gratitude goes to my parents, who have always been my strongest supporters. They gave me the freedom to pursue my dreams and have always provided me with full understanding and encouragement. Throughout my life, they have worked so hard to provide me with the best education and environment to grow. I am endlessly grateful for their love and support.

To all of you who love me and who I love, thank you for being part of my life.

CONTENTS

1

INTRODUCTION

1.1 Advancing Observations of the Cryosphere with Synthetic Aperture Radar

The cryosphere refers to all frozen water components of the Earth system, including glaciers, snow cover, ice sheets, permafrost, and frozen water bodies in oceans, lakes, and rivers [1–4]. It is a crucial component of the Earth's climatic, ecological, and economic systems, influencing every living being on the planet directly and indirectly. While the cryosphere is concentrated in polar and high-latitude regions, it also extends to high-altitude regions such as High Mountain Asia (HMA), the Alps, and the Andes. In these alpine regions, cryosphere components, such as glaciers and seasonal snow cover, are particularly important due to their essential role in modulating regional climates and regulating water resources (Fig. 1.1).

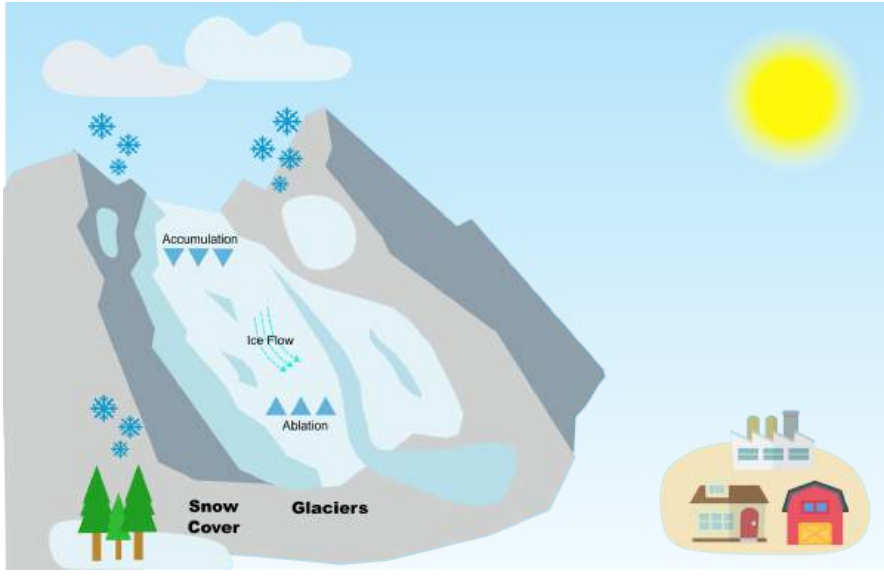

FIGURE 1.1: The cryosphere in alpine environments.[1]

1 Credit: National Snow and Ice Center, https://nsidc.org/learn/what-cryosphere

The cryosphere plays an important role in regulating the Earth's energy balance through affecting the surface albedo with the reflective white surfaces of snow and ice [5]. Additionally, the cold environments of the cryosphere provide unique habitats for diverse species, supporting biodiversity and ecosystem functioning [6, 7]. Changes in the cryosphere, such as glacier and ice sheet melting, directly contribute to sea-level rise, posing significant threats to coastal communities and ecosystems [8]. Furthermore, the melting of glaciers and snow directly regulates the hydrological cycle, affecting freshwater availability and distribution [9, 10]. Rapid cryosphere changes can destabilize local environments, increasing hazards such as glacial lake outburst floods (GLOFs), avalanches, and ice shelf collapses, posing severe risks to nearby communities [11–15].

Under the pressure of climate change, the cryosphere is becoming increasingly vulnerable, undergoing strong changes in recent decades [16–18]. For example, global glaciers have experienced accelerated melting and retreat, with a mass loss rate of 267 ± 16 Gt/yr between 2000 and 2019 [19]. Snow cover in mountain regions has also declined since the mid-20th century, characterized by shorter durations and reduced snow depth [16, 20, 21]. Similarly, Arctic sea ice extent, concentration, and thickness have decreased significantly in recent decades [22, 23].

The increasing vulnerability of the cryosphere highlights the urgent need for comprehensive observations and assessments of cryosphere environments and processes. Remote sensing techniques, particularly Synthetic Aperture Radar (SAR), have emerged as effective tools for observing the cryosphere across large spatial scales and over extended time periods.

SAR is an active microwave imaging technique that offers unique advantages for studying cryosphere environments. Compared to passive imaging sensors, SAR transmits radar pulses and measures their reflections, enabling active imaging regardless of illumination conditions. Operating in the microwave spectrum, it penetrates clouds, fog, and precipitation, ensuring reliable observations in all weather. By synthesizing a large antenna aperture via the motion of the sensor platform (hence the name), SAR achieves high-resolution imaging without being constrained by the physical size of the antenna, allowing the observation of large spatial areas with fine details [24–27]. Additionally, SAR preserves phase information in its radar signals, enabling the measurement of surface elevation and displacements using the interferometric SAR (InSAR) technique [28]. All these unique capabilities make SAR an indispensable tool for cryosphere research, providing

high-resolution, all-weather imaging and precise measurements to monitor dynamic processes in polar and glacial environments [29–33].

Despite these advantages, it remains challenging to apply SAR technology to cryosphere studies in high-altitude alpine regions. In these regions, the backscattering signal, dielectric responses and InSAR measurement accuracy are strongly affected by the complex topography, high surface roughness, and varying properties of snow and ice. These factors can strongly distort the backscattering signals and complicate the interpretation of results [34–37].

To address these challenges and advance the application of SAR in alpine cryosphere studies, this dissertation developed innovative methods to process and analyze SAR data in alpine regions. These methods were applied to various cryosphere processes in the Alps and the Karakoram region of High Mountain Asia, demonstrating their robust performance in representative alpine environments. The SAR datasets obtained through the proposed methods provided valuable insights into the cryosphere processes and dynamics occurring within these regions.

Specifically, this dissertation investigated three main application areas of SAR in alpine cryosphere studies.

The first application focused on measuring glacier ice flow velocities in the Alps to facilitate robust mapping of glacier dynamics in complex alpine topography. This work addressed the need for accurate, high-resolution glacier velocity maps capable of robustly increasing spatial coverage across alpine glaciers.

The second application involved large-scale seasonal snow cover mapping in the Karakoram region using SAR data. This research aimed to develop a robust and efficient method for seasonal snow mapping in high-altitude mountain regions, thereby providing detailed datasets for analyzing snowmelt dynamics and supporting water resource management.

The third application targeted at the development of a comprehensive framework for generating high-quality Digital Elevation Models (DEMs) through advanced InSAR processing and analysis. This framework enabled accurate estimation of glacier elevation and mass changes in the complex topography of the Karakoram. This work was motivated by the need to produce highly accurate glacier elevation change maps, thus improving the understanding of spatial patterns and distribution of glacier mass balance within the region.

1.2 Principles of Synthetic Aperture Radar

Since the early development of operational SAR systems in the 1970s, SAR technology has advanced significantly, leading to the emergence of various SAR missions and systems [38]. In this section, an overview of the principles of SAR is provided, including the imaging mechanism, SAR image properties, and SAR interferometry.

1.2.1 Imaging mechanism of SAR

A typical SAR system consists of a transmitter, a receiver, and signal processing units. Radar pulses at a specific frequency f are transmitted from the transmitter toward the target area, and the backscattered signals reflected from the target surface are received by the receiver. These signals are then processed to generate an image.

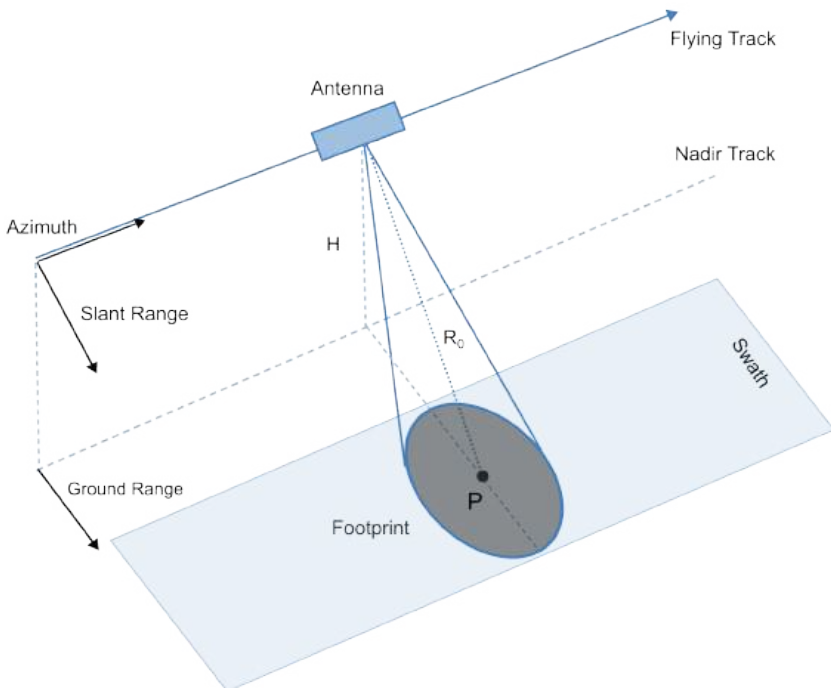

FIGURE 1.2: Imaging geometry of a typical SAR system.

The SAR imaging geometry is characterized by a side-looking configuration (Fig. 1.2). In this configuration, the sensor is oriented perpendicular to the flight direction of the platform, and the antenna beam scans the target area

line by line as the platform moves forward. The flying direction along the track is the *azimuth* direction, while the direction perpendicular to the azimuth is the *slant range* (also often referred as *range*) direction. The projection of the slant range onto the ground is called the *ground range*. The radar's measurements are made along its *line-of-sight* (LOS), which represents the direct path between the sensor and the target. The angle between the LOS and the vertical direction is called the *incidence angle* (θ), which varies with the distance from the sensor and the topography of the target area.

Due to the side-looking geometry, several geometric distortions often occur in SAR images, especially in mountainous areas with complex topography. These distortions include *layover*, *foreshortening* and *shadowing* [39, 40].

Layover occurs when different target points are mapped into the same range cell (i.e. a pixel) in SAR images. This often happens on steep slopes where the top of the slope is imaged before the bottom. Layover region typically shows strong backscattering (i.e. bright pixels) in a SAR intensity image. The foreshortening effect is caused by small local terrain slope angles. When the local terrain slop angle is smaller than the local incidence angle, the slopes appears shortened in the SAR image, indicating a worse range resolution for these area. Similar to layover, foreshortening also leads to strong backscattering in an image. Shadowing regions are those areas that are not illuminated by the radar signal, such as the back side of a steep slope. Both layover and foreshortening also contribute to shadowing. Shadowing regions typically appear dark in an image as no backscattered signal is received.

1.2.2 SAR image properties

In SAR images, each pixel represents the backscattered radar pulses from the target surface. These backscattered signals are recorded as complex numbers, preserving both the amplitude and phase information of the radar wave. Such imagery is referred to as Single-Look Complex (SLC) images, which can be mathematically expressed as:

$$S(x,y) = A(x,y)e^{j\phi(x,y)} \tag{1.1}$$

where $A(x,y)$ and $\phi(x,y)$ denote the amplitude and phase of the backscattered signal, respectively, and (x,y) are the pixel coordinates in the image. The amplitude represents the strength of the radar signal, while the phase provides information about the distance between the radar and the target surface.

In order to visualize and interpret SAR images, the SLC images are often converted to an intensity image by taking the square of the amplitude, i.e.,

$I(x,y) = A^2(x,y)$. In the intensity image, the strength of the backscatter signal can be directly visualized from the brightness of the pixel. However, unlike images generated by optical sensors, the imaging process of SAR is fundamentally a coherent scattering process. This introduces a unique phenomenon in the image called "speckle," which appears as a noise-like pattern. It is important to note that speckles are noise-like but not noise. In fact, they are real radar measurements resulting from the constructive and destructive interference of scattered signals [41]. While speckle can obscure fine details in the image, it also carries valuable information about the scattering properties of the surface [42].

Before analyzing intensity images, it is essential to apply calibration to ensure accurate interpretation of radar signals. Radiometric calibration is performed to normalize the backscattering intensity by accounting for the local illuminated area, resulting in the backscattering coefficient σ^0 [28, 43–45]. This process corrects for variations in radar signal strength caused by imaging geometry and ensures that the measured intensity represents the actual scattering properties of the surface. For most applications in alpine regions, it is necessary to further correct the backscattering coefficient σ^0 for terrain effects, yielding the terrain-corrected backscattering coefficient γ^0 [46]. Both σ^0 and γ^0 are expressed in decibels (dB) and provide a quantitative basis for analyzing radar signals.

The backscattering strength is influenced by several key parameters, including object geometries and surface roughness, incidence angles, radar wavelength, dielectric properties of the target material, and polarization of the radar wave. These parameters determine how radar waves interact with the surface and provide insights into the physical and geometric properties of the target.

Object geometries and surface roughness are essential parameters that determine the backscattering intensity by altering the scattering behavior of radar waves. Curved or rough surfaces scatter radar energy in multiple directions, typically resulting in higher backscattering coefficients compared to smooth surfaces. In contrast, flat or smooth surfaces, such as calm water bodies, reflect most of the incident radar energy away from the sensor, leading to very low backscatter. This property is particularly useful for applications like detecting glacier crevasses or mapping iceberg boundaries, where the contrast between rough and smooth surfaces is critical [41, 47].

The incidence angle also has strong impact on how radar waves interact with the surface. On ground surfaces with sparse or no vegetation layers, the backscatter generally decreases as the incidence angle increases. Such

decrease in backscatter is less pronounced for vegetated or rough ground surfaces. When applying backscattering intensity for applications such as wetland classification, the backscattering intensity is often normalized by the local incidence angle to produce an incidence-independent backscatter coefficient. In these cases, a linear or a cosine model is often employed to simulate the empirical backscatter based on incidence angles [48, 49].

The wavelength of the radar wave is another key factor that affects backscatter. Longer wavelengths, such as L-band and P-band, penetrate deeper into the ground surface, making them suitable for studying subsurface structures like forest biomass, soil moisture, and snow pack structures. In contrast, shorter wavelengths, such as X-band and C-band, have limited penetration depth but are more sensitive to surface features. Consequently, short-wavelength sensors are preferred for applications that focus on surface properties, such as monitoring elevation changes or mapping snow cover extent. The choice of wavelength depends on the specific application and the type of information required [41].

The dielectric constant of the target material also influences backscatter by determining how much of the radar energy is absorbed and reflected. Materials with higher dielectric constants, such as wet snow or moist soil, tend to absorb more energy and exhibit weaker backscatter compared to materials with lower dielectric constants, like dry snow or dry soil. This sensitivity to moisture content enables SAR systems to detect changes in surface moisture or snowmelt conditions, which are crucial for hydrological studies and climate monitoring [25, 50].

Polarization, which refers to the orientation of the electric field of the transmitted and received radar wave, further affects the interaction between radar waves and surface features [28]. Common polarimetric configurations include horizontal-horizontal (HH), vertical-vertical (VV), and cross-polarized (HV and VH). Each polarization interacts with the surface in distinct ways, resulting in various backscattering mechanisms such as surface scattering, volume scattering, and double-bounce scattering. By analyzing and decomposing polarimetric information, it is possible to extract complementary insights into these scattering mechanisms, enabling detailed characterization of surface properties. Therefore, polarimetric SAR systems, which simultaneously acquire multiple polarization channels, are particularly valuable for applications such as land cover classification and vegetation structure analysis [51].

1.2.3 SAR interferometry

SAR interferometry is a unique and powerful technique that leverages the phase information of SAR images to measure surface elevation and displacements. Depends on the acquisition geometry of SAR sensors used for interferometry, the InSAR technique can be classified into the *single-pass* and the *repeat-pass* InSAR. The single-pass InSAR employs two or more SAR sensors to acquire images of the same target area simultaneously, providing accurate measurement of surface elevations. The repeat-pass InSAR, on the other hand, uses a single (or multiple) SAR sensor to acquire images of the same area at different times. This technique is primarily used to measure surface displacements, such as subsidence and ground deformation [52–55]. The following discussion exclusively focuses on single-pass InSAR.

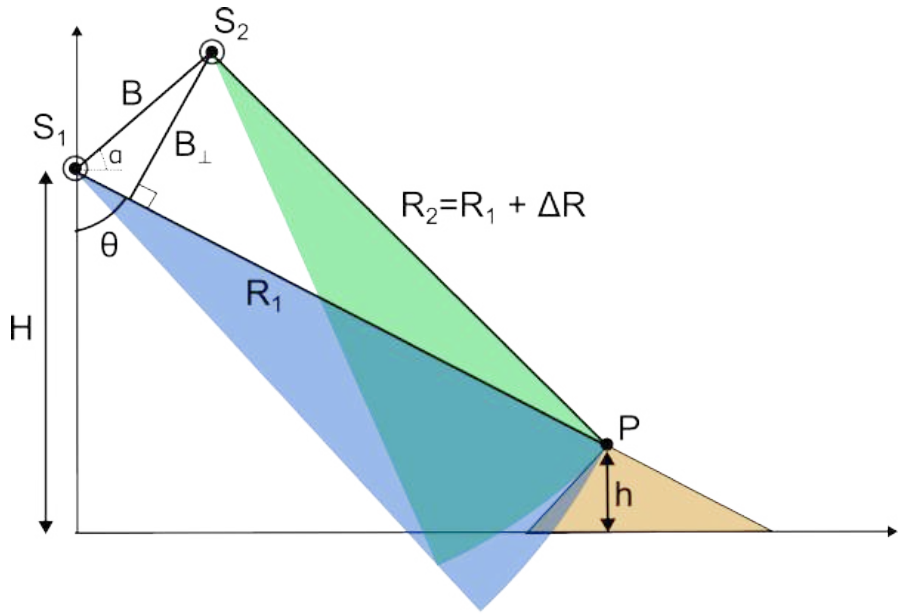

FIGURE 1.3: Acquisition geometry of single-pass InSAR.

The acquisition geometry of single-pass InSAR with two SAR sensors is shown in Fig. 1.3. The two SAR sensors, S_1 and S_2, fly over the same target P with a fixed baseline distance B. The different positions of the two sensors lead to a difference of ΔR between the range distances R_1 and R_2 from the two sensors to the target point. The elevation h of the target point can be calculated using the simple trigonometric relationship:

$$h = H - R_1 \cos\theta \tag{1.2}$$

where H is the height of the sensor above the ground, and θ is the incidence angle of the primary sensor S_1. To solve for the incidence angle θ, the law-of-cosine can be applied to the triangle formed by the two sensors and the target point. Assuming both ΔR and baseline B are small compared to the range distance R_1 [56], the following approximation can be made:

$$\Delta R \approx B \sin(\theta - \alpha) \tag{1.3}$$

where α is the horizontal angle of the baseline vector. Note that $B \sin(\theta - \alpha)$ is equivalent to the parallel baseline $B_{\parallel}$ in the acquisition geometry.

The range distance difference ΔR can be accurately measured using interferometry. Let $S_1(x, y)$ and $S_2(x, y)$ be the two SLC images acquired by the two sensors, the interferogram is generated by taking the complex conjugate of the two SLC images:

$$S_1(x, y) \cdot S_2^*(x, y) = |S_1(x, y)||S_2(x, y)|e^{j(\phi_1(x,y) - \phi_2(x,y))} \tag{1.4}$$

where the phase of the two SLC images are

$$\begin{aligned} \phi_1(x, y) &= -\frac{4\pi}{\lambda} R_1 + \phi_{1,\text{scatter}}(x, y) \\ \phi_2(x, y) &= -\frac{4\pi}{\lambda} R_2 + \phi_{2,\text{scatter}}(x, y) \end{aligned} \tag{1.5}$$

For single-pass acquisitions, the phase of the scatterers in the two images, $\phi_{1,\text{scatter}}$ and $\phi_{2,\text{scatter}}$, are assumed to be the same and thus are canceled out in the interferogram. The resulted phase in the interferogram is then proportional to ΔR:

$$\phi(x, y) = \phi_1(x, y) - \phi_2(x, y) = -\frac{4\pi}{\lambda}(R_1 - R_2) = -\frac{4\pi}{\lambda}\Delta R \tag{1.6}$$

A relationship between the interferogram phase and the change in elevation can be further established as [57]:

$$\frac{\partial \phi}{\partial h} = -\frac{4\pi}{\lambda} \frac{B \cos(\theta - \alpha)}{R_1 \sin\theta} = -\frac{4\pi}{\lambda} \frac{B_{\perp}}{R_1 \sin\theta} \tag{1.7}$$

where $B_{\perp}$ is the perpendicular baseline. This expression describes the sensitivity of the interferometric phase to elevation height. Considering a phase fringe of a cycle of 2π, the height of ambiguity (HoA) can then be defined as:

$$h_a = -\frac{\lambda R_1 \sin\theta}{2B_{\perp}} \tag{1.8}$$

The HoA is a crucial parameter for InSAR applications, as it describes the maximum range of height that corresponds to one full phase cycle of 2π. A smaller HoA indicates a higher sensitivity to height differences. Although it is benefiting to reduce HoA for high-precision measurements, it is also important to consider the trade-off between the HoA and the radar geometry. A smaller HoA is often associated with a larger baseline, which can lead to increased decorrelation and reduced coherence in the interferogram [58].

Another important parameter in InSAR is the *interferometric coherence*, which quantifies the correlation between two SLC images used to generate the interferogram. The coherence is defined using the normalized intensity of the interferogram, expressed as:

$$\gamma = \frac{|\langle S_1(x,y) S_2^*(x,y) \rangle|}{\sqrt{\langle |S_1(x,y)|^2 \rangle \langle |S_2(x,y)|^2 \rangle}} \tag{1.9}$$

where $\langle \cdot \rangle$ denotes the expectation operator. The coherence value ranges from 0 to 1, with 1 indicating perfect correlation and 0 indicating no correlation. The coherence is influenced by several factors, including the temporal decorrelation caused by changes in the target surface between acquisitions, the spatial decorrelation due to the spatial variability of the target surface, and the noise in the radar signal [53].

1.3 SAR Applications in Cryosphere Studies

The advancements of SAR in the recent decades have enabled the application of SAR in diverse fields. The following sections provide an overview of SAR applications in cryosphere research, focusing on three main areas: glacier velocity monitoring, snow cover mapping, as well as glacier elevation and mass change estimation.

1.3.1 Monitoring alpine glacier velocity with SAR

Glacier velocity is a key parameter for understanding glacier dynamics, mass balance and the responses of glaciers to climate change [59]. Within a glacier, the velocity field reflects the movement of ice under the process of internal deformation and basal sliding. Closely monitoring changes in glacier velocity provides valuable insights into the processes related to various glacier properties, such as ice thickness, basal conditions, surface topography changes and surge dynamics [60, 61]. Additionally, the measurement of glacier velocity are critical inputs to glacier models, enabling the prediction of future glacier behavior and its impacts on sea-level rise and hydrology [62,

63]. Furthermore, glacier dynamics in alpine regions are closely linked to the stability of surrounding slopes and the potential for glacier-related hazards, such as ice avalanches and GLOFs. Monitoring glacier velocity can help assess risks associated with these hazards and inform risk management strategies [13, 14, 64].

Due to the remote location and large area of glaciers, traditional in-situ measurements of glacier velocity are often limited in spatial coverage and temporal resolution. In contrast, remote sensing techniques, especially SAR techniques, have emerged as powerful tools for monitoring glacier velocity over large areas and extended time periods [65–68].

Monitoring glacier velocity based on SAR imagery is typically achieved through two main approaches, including the differential interferometry SAR (DInSAR) technique and offset tracking methods. Both approaches have their advantages and limitations, and the choice of method depends on the specific application and the characteristics of the target glacier.

DInSAR measures glacier velocity based on the phase difference within an interferogram formed by two SAR images, typically using the repeat-pass InSAR technique with two or more SAR images acquired from the same track but at different times [57, 58]. DInSAR measurement can reach very high precision of about a few millimeters for displacement measurements along the LOS direction, and can be extended to 3-D velocity vectors when combining with offset tracking [30, 68]. However, the application of DInSAR on glaciers is often limited by the decorrelation of the interferogram, primarily caused by the fast velocity with respect to the acquisition frequency and the temporal change of glacier surface conditions (e.g. the melting conditions, precipitation, and changes of surface roughness). As a result, DInSAR is primarily effective in polar regions with stable surface conditions [30, 69–71] or areas covered by short temporal baseline acquisitions [72].

Offset tracking, in contrast, relies on the intensity information of SAR images and stable features on the glacier (e.g. crevasses and ice ridges) to track the displacement over time. Although it is of lower precision comparing to DInSAR, this approach is more robust against temporal decorrelation, making it suitable for monitoring velocities of glaciers with rapid surface changes, such as those in alpine regions [65, 66]. Offset tracking is versatile and can be applied to both optical and SAR images. In SAR applications, it can utilize different input modalities such as complex values, coherent speckles or intensity, leading to variations like *coherence tracking*, *speckle tracking* and *intensity tracking* [73]. The flexibility and resilience to surface changes make offset tracking a valuable tool for monitoring glacier velocity in alpine regions.

The following part of this section exclusively focus on SAR offset tracking, with an overview of the principles of offset tracking and its applications in alpine glacier velocity monitoring.

1.3.1.1 Offset tracking with SAR

The principle of offset tracking is to identify the offset that can maximize the similarity between a primary image and a secondary image, thereby determining the movement of objects or features from one image patch to another. To evaluate the similarity, the Normalized-Cross-Correlation (NCC) is often used, which is defined as:

$$\mathrm{NCC}(x,y) = \frac{\sum_{i,j}(I_1(i,j)-\bar{I_1})(I_2(i+x,j+y)-\bar{I_2})}{\sqrt{\sum_{i,j}(I_1(i,j)-\bar{I_1})^2}\sqrt{\sum_{i,j}(I_2(i+x,j+y)-\bar{I_2})^2}} \tag{1.10}$$

where I_1 and I_2 are the two image patches, $\bar{I_1}$ and $\bar{I_2}$ are the mean values of the two patches, and (x,y) is the offset between the two patches. The offset vector from the center of the patch to the location of the maximum NCC value is considered as the offset for the best matching, which can be converted into a velocity vector by dividing the offset by the time interval between the two images.

To successfully retrieve the offset vector, the maximum NCC value should be significantly larger than the noise level in the NCC field, thereby allowing the high-confident determination of the offset vector. To evaluate the confidence of the offset vector, the signal-to-noise ratio (SNR) of the NCC field can be defined as below:

$$\mathrm{SNR} = \log_{10}\left(c_p^2/\overline{c_f^2}\right) \tag{1.11}$$

where c_p is the normalized cross-correlation (i.e. the maximum value of the NCC) of the two images and $\overline{c_f^2}$ denotes the mean value of the ambient NCC field [74].

In practice, offset tracking is typically implemented in a windowed manner, where a small window is moved across the image to calculate the NCC for each pixel. The choice of window size is crucial for the success of offset tracking. A small window size can improve the spatial resolution of the derived velocity field over the image, but it also reduces the information content and available features inside the window, leading to a lower signal-to-noise ratio (SNR) in the NCC field and unreliable velocity vectors. In contrast, a larger window size can increase the SNR but may also lead to a loss of spatial resolution and details in the velocity field. This is especially important

when applying the method to alpine glaciers, where the size of glacier is often small and limiting the size of the window.

1.3.1.2 Development and applications of offset tracking

Since the early 2000s, offset tracking based on SAR imagery has been widely adopted to monitor glacier velocities. The early applications primarily used offset tracking to complement DInSAR methods in cases where temporal decorrelation limited the generation of coherent interferograms. These studies focused predominantly on polar regions, where extensive ice sheets and stable surface conditions were expected to facilitate reliable measurements [75–77].

Building on this foundation, intensity tracking and coherence tracking using SAR imagery were developed and tested by Strozzi *et al.* [36] to monitor a tidewater glacier in Svalbard. This work demonstrated the effectiveness of offset tracking for glaciers with strong dynamics. Subsequently, Lange, Luckman & Murray [74] further advanced the method by applying offset tracking to ERS-2 SAR data on an outlet glacier in Greenland. They proposed the use of a high-pass filter to focus the cross-correlation on smaller features, thereby improving the coverage and robustness of velocity estimates. Similarly, Quincey *et al.* [78] also used the ERS SAR data and applied offset tracking to measure the velocity of the Baltoro Glacier in the Karakoram mountains. The results underscored the robust performance of the method in challenging mountain terrains. These innovations marked crucial steps in refining the technique for broader use across diverse glacier types and environmental conditions.

In parallel with advancements in SAR offset tracking, significant progress was also made for optical images. Various algorithms for image matching were proposed using optical imagery, such as the NCC algorithm [65], the phase correlation algorithm [79], and the orientation correlation algorithm [80]. Additionally, Debella-Gilo & Kääb [81] demonstrated an interpolation method that successfully enhanced the precision of offset tracking to a sub-pixel level. A comprehensive evaluation revealed that most image matching algorithms achieved reliable velocity measurement at sub-pixel precision, with phase correlation and cross-correlation on orientation images being the most robust [82]. Furthermore, improvements were also proposed to adaptively adjust the similarity matching window size, thereby making offset tracking more robust and automatic. These attempts include the locally adaptive template size optimization method [83] and the multiple-image-multiple-chip algorithm [81]. These advancements in optical offset tracking not only expanded its applications but also influenced SAR offset track-

ing methodologies, as both techniques benefited from similar algorithmic principles and workflows.

Until the early 2010s, SAR applications for glacier velocity monitoring were primarily focused on polar regions and limited to short temporal periods due to data availability constraints. The emergence of new SAR missions later expanded the study area to a wider range of alpine glaciers. For instance, the X-band TerraSAR-X [84] data has been applied to glaciers in the Himalayas, the Alps, Central Asia, and Svalbard [85–89]; the L-band ALOS/PALSAR [90] was used together with DEMs to investigate mountain glacier motion in Central Tian Shan and Mt. Muztagh Ata [91, 92]; and the X-band COSMO-SkyMed [93] was adopted to study glacier dynamics in Argentina [94, 95]. Collectively, these missions enhanced the ability to monitor glacier dynamics in diverse and challenging environments.

Another remarkable shift occurred after 2015 with the launch of the Sentinel-1 SAR mission [96]. The Sentinel-1 mission introduced free and openly accessible SAR data with high resolution and short revisit times. This transformative leap has greatly contributed to the expansion of studied areas to include more glaciers in the low latitude regions, such as the High-Mountain-Asia (HMA) area and the Andes Mountains [97–99]. It also facilitated the generation of large scale ice velocity maps over Greenland and globally [100, 101].

The growing Sentinel-1 data archive has provided new opportunities for glacier velocity tracking but also demanded new methods to effectively exploit the data of large spatial coverage and extended temporal period. In response to these demands, this dissertation aims to develop a novel method that leverages SAR image time-series to improve the spatial coverage of robust velocity estimates for alpine glaciers. By leveraging the dense temporal sampling and consistent data quality offered by modern SAR systems, this work seeks to advance glacier monitoring methodologies and address limitations in traditional approaches.

1.3.2 Mapping snow cover in alpine regions with SAR

As a fundamental component of the cryosphere, snow has substantial impacts on the global climate system, water cycles and ecosystems. This significance has led it to be identified as one of the Essential Climate Variables [102]. Snow cover significantly influences the surface energy balance by reflecting a considerable portion of solar radiation, playing a crucial role in regulating global and regional temperatures and climate patterns. Regarding the regional water cycle, snowmelt directly contributes to streamflow and groundwater recharge,

thereby supporting water supply for local communities and ecosystems. The seasonality and variability of snow cover also regulate ecosystem processes, such as vegetation growth, animal migration, and habitat availability. Due to these significant impacts, mapping snow cover is essential for understanding climate interactions, managing water resources, and assessing ecosystem health [103, 104].

To effectively map snow cover, remote sensing techniques have been widely adopted. Optical remote sensing has traditionally been the primary method for snow cover mapping, leveraging the spectral reflectance properties of snow in different bands. However, limited by cloud cover and illumination conditions, the application of optical remote sensing is often restricted in alpine regions, where weather conditions are frequently unstable. As a valuable alternative, SAR systems have shown great potential due to their advantages of all-weather capability and high spatial resolution.

The principle behind snow cover mapping using SAR is based on the interaction between radar waves and the snowpack. Within the snowpack, dielectric properties are predominantly determined by the liquid water content (LWC) and snowpack density [105, 106]. Dry snow, characterized by lower LWC and a higher proportion of ice particles and air voids, typically exhibits a lower dielectric constant compared to wet snow. This leads to less energy absorption and consequently higher backscattering. As the snowpack becomes wet, the dielectric constant significantly increases due to higher LWC, resulting in altered radar backscattering behavior. Even a small increase in LWC can induce substantial changes in dielectric properties and backscattering strength. By analyzing these changes in backscattering properties, the snowpack can be mapped and classified into different snow types, such as dry and wet snow.

Early attempts to use SAR for snow cover mapping primarily focused on analyzing the varying responses of SAR backscattering to different snow types. Rott [34] first analyzed differences in backscattering over mountain regions across various surface types, including wet snow, glaciers, and other land covers. Their results suggested that incidence angle and wavelength considerably influence backscattering coefficients. The relationship between backscattering mechanisms and snowpack properties was further investigated by Shi & Dozier [107], demonstrating the effective use of C-band SAR to distinguish between snow and glaciers. The potential of early SAR systems, such as ERS-1 and RADARSAT, for wet snow mapping was also demonstrated [50, 108].

With the launch of the Sentinel-1 mission, mapping snow cover over large areas has become more feasible. The freely available data and short revisit time of Sentinel-1 have enabled the generation of large-scale snow cover maps, essential for monitoring snow cover dynamics and understanding their impacts on climate and hydrology. For instance, Nagler *et al.* [109] systematically evaluated the potential of Sentinel-1 for snow cover mapping and proposed an effective algorithm based on radar backscattering coefficients. This algorithm has been widely adopted in subsequent studies and has shown promising performance across many regions.

In Nagler's method, a series of Sentinel-1 SAR images are used to calculate the backscattering ratio as follows:

$$R_i = \gamma_i^0 / \gamma_{i,ref}^0 \tag{1.12}$$

where γ_i^0 and $\gamma_{i,ref}^0$ are the terrain-corrected backscattering coefficient of the image i and the reference image, respectively. The reference image is typically selected from a series of SAR images acquired under dry snow or snow free conditions. Considering the different response of backscattering to the local incidence angle (θ) under different polarization channels (i.e., VV and VH), a composite ratio is further proposed to combine the backscattering ratios of different polarizations. The composite ratio is defined as:

$$R_c = W R_{vv} + (1 - W) R_{vh} \tag{1.13}$$

where R_{vv} and R_{vv} are the ration for the VV and VH polarization channels, W is the weighting factor defined based on the local incidence angle (θ) as the following:

$$W = \begin{cases} 0 & (\theta < \theta_1) \\ 0.5(1 + \frac{\theta - \theta_1}{\theta_2 - \theta_1}) & (\theta_1 \leq \theta \leq \theta_2) \\ 0.5 & (\theta > \theta_2) \end{cases} \tag{1.14}$$

with $\theta_1 = 20^\circ$ and $\theta_2 = 45^\circ$. The resulting ratio is then used to classify snowpack conditions using a threshold value of -2 dB as suggested in the original work.

Although Nagler's method has been successfully applied to many regions, the fixed threshold value of -2 dB is not always effective, especially in mountainous areas where complex terrain and surface conditions introduce substantial uncertainty into backscattering measurements. To address these challenges, soft thresholds have been proposed to enhance the robustness of

snow cover classification [110–112]. These flexible thresholds accommodate varying conditions, making them more suitable for the complexities of alpine regions. Additionally, selecting an appropriate reference image is crucial for accurately calculating the backscattering ratio. Different approaches have been proposed to address this issue. For instance, Koskinen, Pulliainen & Hallikainen [113] suggested selecting a stable winter scene as the reference image, assuming consistent dry snow conditions. Alternatively, Luojus *et al.* [114] recommended averaging multiple SAR images acquired under dry snow conditions to minimize temporal variations and noise. Another approach by Pettinato *et al.* [115] employed linear interpolation between SAR acquisitions at the start and end of the snowmelt season to generate a dynamic reference image, aiming to better capture seasonal variability. These methods highlight the importance of careful reference image selection in improving the reliability of SAR-based snow cover mapping. Furthermore, auxiliary data such as DEMs, land cover maps, and meteorological models have been utilized to further enhance snow cover mapping accuracy [116, 117]. These approaches have shown promising results in improving accuracy and robustness in alpine regions.

Despite considerable advancements in SAR snow cover mapping, alpine regions still pose significant challenges due to complex terrain and rapidly changing snow conditions. One representative example is the Karakoram region, where pronounced topographic effects often cause significant distortions in SAR signals, hindering accurate and robust snow cover mapping. Additionally, the vast spatial extent of this region complicates the development of universally effective algorithms.

Given these challenges, this dissertation aims to develop a robust method utilizing Sentinel-1 SAR image series and topographic features derived from high-resolution DEMs to improve snow cover mapping accuracy and reliability in the Karakoram region.

1.3.3 Measure glacier elevation change and mass balance with SAR

Measuring the elevation change of glacier surfaces is crucial for quantifying glacier mass balance and understanding glacier dynamics. Glacier mass balance refers to the total mass gain or loss of a glacier over a specific period, typically expressed as the difference between accumulation (mass gain) and ablation (mass loss) [60]. Monitoring glacier mass balance is essential for understanding how glaciers respond to climate change, as variations in temperature and precipitation directly influence accumulation and ablation processes. On a global scale, glacier mass balance is a significant contributor

to sea-level rise, accounting for approximately 27 ± 22 mm of global mean sea-level rise [8, 118]. On regional scales, glacier mass balance plays a critical role in local hydrology and ecosystems by supplying meltwater to water resources [119].

Traditional methods for measuring glacier mass balance, such as *in-situ* point-wise measurements on glacier surfaces, are often constrained by limited accessibility and high uncertainty when extrapolating to larger scales [118]. Since the advent of modern spaceborne remote sensing sensors in the 1990s, remote sensing imagery has become the primary approach for regional and global glacier mass balance studies [120].

1.3.3.1 InSAR DEMs for glacier mass balance measurements

One widely used method for measuring glacier mass balance with remote sensing data is DEM differencing, also known as the *geodetic method* [120]. This technique involves generating two DEMs from data acquired at different times and calculating the elevation change between them. The elevation change (dh) and the time interval (dt) are used to derive the elevation change rate (dh/dt), which can be converted into mass balance by applying an assumption about the ice density [121].

The two primary data sources for DEM generation are optical stereo imagery and SAR interferometric image pairs. Compared to optical stereo imagery, SAR imagery offers several advantages, including the imaging capabilities under all-weather conditions, as well as higher vertical accuracy and spatial resolution (e.g., about 6 m for TanDEM-X DEM compared to about 100 m for ASTER stereo optical DEM [33]), thereby making SAR a powerful tool for glacier mass balance measurement.

The first near-global InSAR DEM was generated during the Shuttle Radar Topography Mission (SRTM) in 2000 by employing a C-band system [122]. Later, the TanDEM-X mission was launched in 2010, with the goal of producing a high-resolution global DEM [123]. TanDEM-X utilizes two X-band SAR satellites flying in close formation to acquire interferometric data, enabling the creation of high-resolution DEMs with a vertical accuracy of 3.49 m overall and 0.88 m in areas excluding vegetation and snow/ice coverage [124].

The SRTM and TanDEM-X DEMs have been extensively utilized in numerous studies to derive glacier mass balance [120, 125]. In these studies, the two DEM products have served dual purposes: either as reference DEMs to facilitate data processing tasks (e.g. orthorectification and geocoding), or as primary datasets for DEM differencing. In the latter case, it is important to note that the global TanDEM-X DEM product is post-processed using a

mosaic of acquisitions taken at different times. This temporal inconsistency makes the global TanDEM-X DEM unsuitable for deriving accurate elevation change rates over glaciers. To address this limitation, individual TanDEM-X acquisitions are preferred for generating DEMs that preserve accurate timestamps, allowing for more reliable elevation change measurements.

The application of InSAR-derived DEMs for DEM differencing has been successfully demonstrated across various alpine regions, offering valuable insights into glacier dynamics. For example, Malz *et al.* [126] investigated elevation and mass changes in glaciers within the Southern Patagonia Icefield using TanDEM-X and SRTM DEMs. Similarly, [127] assessed glacier mass balance in the Puruogangri Ice Field located in the inner Tibetan Plateau. Paul & Haeberli [128] utilized SRTM DEM and measured elevation changes in glaciers across the Swiss Alps. Moreover, an inter-comparison experiment conducted by Piermattei *et al.* [129] analyzed geodetic mass balance estimates derived from TanDEM-X, SRTM, and ASTER stereo-optical DEMs. This study emphasized the importance of establishing best practices within the research community to enhance understanding of physical processes in cryosphere studies.

1.3.3.2 Challenges of alpine terrain for InSAR DEM generation

Despite numerous successful applications, generating and analyzing InSAR DEMs in mountainous regions remains challenging due to specific limitations, such as difficulties in phase unwrapping and errors arising from radar signal penetration.

The first major challenge is phase unwrapping errors caused by rugged alpine terrain and intricate water bodies. Phase unwrapping is a critical step in InSAR processing that reconstructs the absolute phase from its wrapped form. In steep and complex topography, abrupt elevation changes can create discontinuities in phase data, leading to errors in the final DEM. These errors primarily affect DEMs in two ways. First, they result in large data voids, particularly in regions with steep slopes or intricate terrain where radar signals fail to adequately capture the surface. Such voids reduce the spatial coverage and completeness of the DEM, making it difficult to achieve a continuous representation of the topography. Second, geometric distortions, such as layover effects, introduce phase unwrapping errors by misrepresenting the true topography. For example, a mountain peak may appear incorrectly connected to its base, leading to erroneous phase unwrapping results. These distortions complicate the phase unwrapping process, often producing unreliable or inaccurate DEMs in rugged alpine regions.

Another challenge involves the signal penetration of radar waves, which introduces significant uncertainties in DEM differencing. This is particularly noticeably when combining datasets from different wavelengths (e.g., C-band SRTM and X-band TanDEM-X) or modalities (e.g., optical and SAR) [130]. Radar signals penetrate snow and ice to varying degrees depending on their wavelength and surface conditions, causing discrepancies in elevation measurements. For instance, X-band signals used in TanDEM-X generally penetrate less deeply into snow and ice compared to the longer-wavelength C-band signals used in SRTM, potentially introducing systematic biases when comparing the two datasets. Similarly, combining SAR-derived DEMs with optical DEMs (e.g., from ASTER or SPOT) for geodetic elevation change measurements can also lead to discrepancies due to differences in signal penetration and sensitivity to surface conditions. These discrepancies can result in significant errors in elevation change estimates, particularly in regions with complex surface conditions, such as snow-covered or debris-covered glaciers.

To address these challenges, this dissertation proposes a novel three-module framework for glacier mass balance assessment in the Karakoram region. The framework comprises three key components: the first module generates DEMs with the InSAR technique using individual TanDEM-X acquisitions to preserve accurate timestamps; the second module processes elevation change maps, ensuring consistency and minimizing errors; and the third module performs mass balance analysis with rigorous uncertainty propagation. By leveraging long-term TanDEM-X acquisitions from the 2010s to the 2020s, this work provides updated and highly detailed measurements of glacier mass balances in the Karakoram, with unprecedented high resolution and accuracy.

1.4 Research Objectives and Questions

The importance and increasing vulnerability of the cryosphere highlighted the urgent need for closely monitoring and measuring its components. This is particularly pronounced in alpine regions where high-altitude mountain environments face heightened vulnerability and maintain direct connections to local communities through water resources, tourism, and hazard management.

This dissertation aims to advance the application of SAR, a powerful Earth observation technique, to alpine cryosphere studies. The research comprises three self-contained contributions that address the challenges of applying

SAR in the alpine cryosphere environments. Each contribution develops innovative methodologies to use SAR for observing and measuring different cryosphere components, accompanied by comprehensive data analysis that enhances our understanding of specific cryosphere processes.

The following section outlines the specific research objectives and questions addressed in each of these three contributions.

1.4.1 Cross-correlation stacking for robust offset tracking using SAR image time-series

This study presents an innovative approach to enhance offset tracking for glacier velocity monitoring using SAR data. Traditional NCC-based offset tracking methods typically rely on a single pair of images to compute the NCC field and measure the offset vector. While effective in some contexts, these methods encounter significant challenges in mountainous regions, where complex terrain and environmental variability limit their reliability. Additionally, alpine glaciers are often smaller in size compared to those in polar regions, further constraining the size of the NCC window that can be applied. These limitations highlight the need for a more robust and high-resolution offset mapping method tailored to such conditions.

To address these challenges, this research aims to develop an innovative method for robust alpine glacier velocity mapping by leveraging the extensive archive of SAR time series data. Building on the temporal redundancy of SAR image series, a novel cross-correlation stacking technique is introduced. By averaging multiple consecutive NCC results, this method suppresses noise and enhances offset tracking accuracy. The approach enables reliable measurements with smaller image templates while maintaining broader spatial coverage, overcoming the constraints posed by traditional methods.

The investigation is guided by three key research questions:

1. How does cross-correlation stacking improve the robustness of displacement estimation compared to single-pair NCC methods?

2. Can smaller image templates achieve comparable spatial coverage to larger templates when combined with stacking?

3. How does the method generalize across SAR sensors with different resolutions and acquisition characteristics?

1.4.2 Mapping seasonal snow melting in Karakoram using SAR and topographic data

Seasonal snowmelt monitoring in the Karakoram region plays a vital role in managing regional water resources, assessing natural hazards, and understanding the interactions between climate and hydrology. While existing SAR-based snowmelt mapping techniques have proven effective in many regions, their application in the Karakoram is limited by the area's complex terrain and rapidly changing surface conditions. These challenges make it difficult to achieve reliable and accurate results using conventional methods.

To address these limitations and enable the generation of large-scale snowmelt datasets, this study proposes a robust framework that integrates SAR imagery with topographic data. By leveraging this integration, the framework aims to improve the accuracy of wet snow mapping in mountainous environments where traditional methods often struggle. The research focuses on developing solutions to overcome terrain-induced errors and enhance the reliability of snowmelt monitoring in this challenging region.

The study is structured around three key research questions:

1. How can SAR and topographic data be effectively integrated to mitigate terrain-induced errors in wet snow classification?

2. Does the proposed method outperform conventional SAR or optical-based approaches in mapping accuracy?

3. What temporal and spatial insights into snowmelt patterns can be derived from the application of the method across major basins in Karakoram?

1.4.3 Geodetic glacier mass balance in the Karakoram (2011–2019) from TanDEM-X: An InSAR DEM differencing framework

Measuring glacier elevation and mass changes is essential for understanding glacier dynamics, assessing their response to climate change, and evaluating their contributions to sea-level rise and regional water resources. In recent decades, the Karakoram region has exhibited anomalous glacier behavior, with slight thickening trends that contrast sharply with the widespread mass loss observed globally. This unique phenomenon, often referred to as the "Karakoram anomaly," highlights the need for detailed investigations to unravel the underlying dynamics of glacier mass change in this region.

To address this, the study focuses on quantifying glacier elevation changes (dh/dt) and mass balance in the Karakoram from 2011 to 2019, utilizing nearly

a decade of TanDEM-X InSAR data. A robust and scalable framework was developed to tackle the challenges posed by the region's complex terrain, enabling high-resolution assessments of glacier dynamics with a strong emphasis on uncertainty quantification. This approach not only enhances the accuracy of glacier mass balance measurements but also provides a deeper understanding of the processes driving glacier behavior in heterogeneous mountainous regions.

The study seeks to address the following three key research questions:

1. What are the spatial patterns and magnitude of elevation changes (dh/dt) and glacier mass balance in the Karakoram region during 2011–2019?
2. How do surge-type and non-surge glaciers differ in their elevation change and mass balance behaviors?
3. Can a comprehensive framework combining advanced DEM generation, elevation change mapping, and uncertainty analysis improve glacier mass balance assessments in complex terrains?

1.5 Thesis Structure

This dissertation is structured into five chapters. Chapters 2, 3, and 4 present the three primary studies that constitute the foundation of this research. Each chapter corresponds to a study that has either been published or submitted for publication in peer-reviewed journals. Chapter 5 concludes the dissertation by summarizing the key findings and proposing directions for future research.

References

1. Rignot, E., Jacobs, S., Mouginot, J. & Scheuchl, B. Ice-Shelf Melting Around Antarctica. *Science* **341**, 266 (2013).
2. Obu, J., Westermann, S., Bartsch, A., Berdnikov, N., Christiansen, H. H., Dashtseren, A., Delaloye, R., Elberling, B., Etzelmüller, B., Kholodov, A., Khomutov, A., Kääb, A., Leibman, M. O., Lewkowicz, A. G., Panda, S. K., Romanovsky, V., Way, R. G., Westergaard-Nielsen, A., Wu, T., Yamkhin, J. & Zou, D. Northern Hemisphere Permafrost Map Based on TTOP Modelling for 2000–2016 at 1 km2 Scale. *Earth-Science Reviews* **193**, 299 (2019).
3. Parkinson, C. L. Global Sea Ice Coverage from Satellite Data: Annual Cycle and 35-Yr Trends. *Journal of Climate* **27**, 9377 (2014).

4. Barry, R. G. & Gan, T. Y. *The Global Cryosphere: Past, Present and Future* 2nd ed (Cambridge university press, Cambridge New York, 2021).

5. Flanner, M. G., Shell, K. M., Barlage, M., Perovich, D. K. & Tschudi, M. A. Radiative Forcing and Albedo Feedback from the Northern Hemisphere Cryosphere between 1979 and 2008. *Nature Geoscience* **4**, 151 (2011).

6. Vincent, W. F., Callaghan, T. V., Dahl-Jensen, D., Johansson, M., Kovacs, K. M., Michel, C., Prowse, T., Reist, J. D. & Sharp, M. Ecological Implications of Changes in the Arctic Cryosphere. *AMBIO* **40**, 87 (2011).

7. Fountain, A. G., Campbell, J. L., Schuur, E. A. G., Stammerjohn, S. E., Williams, M. W. & Ducklow, H. W. The Disappearing Cryosphere: Impacts and Ecosystem Responses to Rapid Cryosphere Loss. *BioScience* **62**, 405 (2012).

8. Zemp, M., Huss, M., Thibert, E., Eckert, N., McNabb, R., Huber, J., Barandun, M., Machguth, H., Nussbaumer, S. U., Gärtner-Roer, I., Thomson, L., Paul, F., Maussion, F., Kutuzov, S. & Cogley, J. G. Global Glacier Mass Changes and Their Contributions to Sea-Level Rise from 1961 to 2016. *Nature* **568**, 382 (2019).

9. Jonas, T., Marty, C. & Magnusson, J. Estimating the Snow Water Equivalent from Snow Depth Measurements in the Swiss Alps. *Journal of Hydrology* **378**, 161 (2009).

10. Beniston, M., Farinotti, D., Stoffel, M., Andreassen, L. M., Coppola, E., Eckert, N., Fantini, A., Giacona, F., Hauck, C., Huss, M., Huwald, H., Lehning, M., López-Moreno, J.-I., Magnusson, J., Marty, C., Morán-Tejéda, E., Morin, S., Naaim, M., Provenzale, A., Rabatel, A., Six, D., Stötter, J., Strasser, U., Terzago, S. & Vincent, C. The European Mountain Cryosphere: A Review of Its Current State, Trends, and Future Challenges. *The Cryosphere* **12**, 759 (2018).

11. Brown, M. E., Racoviteanu, A. E., Tarboton, D. G., Gupta, A. S., Nigro, J., Policelli, F., Habib, S., Tokay, M., Shrestha, M. S., Bajracharya, S., Hummel, P., Gray, M., Duda, P., Zaitchik, B., Mahat, V., Artan, G. & Tokar, S. An Integrated Modeling System for Estimating Glacier and Snow Melt Driven Streamflow from Remote Sensing and Earth System Data Products in the Himalayas. *Journal of Hydrology* **519**, 1859 (2014).

12. Hogg, A. E. & Gudmundsson, G. H. Impacts of the Larsen-C Ice Shelf Calving Event. *Nature Climate Change* **7**, 540 (2017).

13. Round, V., Leinss, S., Huss, M., Haemmig, C. & Hajnsek, I. Surge Dynamics and Lake Outbursts of Kyagar Glacier, Karakoram. *The Cryosphere* **11**, 723 (2017).

14. Kääb, A., Leinss, S., Gilbert, A., Bühler, Y., Gascoin, S., Evans, S. G., Bartelt, P., Berthier, E., Brun, F., Chao, W.-A., Farinotti, D., Gimbert, F., Guo, W., Huggel, C., Kargel, J. S., Leonard, G. J., Tian, L., Treichler, D. & Yao, T. Massive Collapse of Two Glaciers in Western Tibet in 2016 after Surge-like Instability. *Nature Geoscience* **11**, 114 (2018).

15. Ding, Y., Mu, C., Wu, T., Hu, G., Zou, D., Wang, D., Li, W. & Wu, X. Increasing Cryospheric Hazards in a Warming Climate. *Earth-Science Reviews* **213**, 103500 (2021).

16. Intergovernmental Panel On Climate Change (Ipcc). *The Ocean and Cryosphere in a Changing Climate: Special Report of the Intergovernmental Panel on Climate Change* 1st ed. (Cambridge University Press, 2022).

17. Slaymaker, O. & Kelly, R. E. J. *The Cryosphere and Global Environmental Change* 261 pp. (Blackwell Pub, Malden, MA, 2007).

18. Derksen, C., Smith, S. L., Sharp, M., Brown, L., Howell, S., Copland, L., Mueller, D. R., Gauthier, Y., Fletcher, C. G., Tivy, A., Bernier, M., Bourgeois, J., Brown, R., Burn, C. R., Duguay, C., Kushner, P., Langlois, A., Lewkowicz, A. G., Royer, A. & Walker, A. Variability and Change in the Canadian Cryosphere. *Climatic Change* **115**, 59 (2012).

19. Hugonnet, R., McNabb, R., Berthier, E., Menounos, B., Nuth, C., Girod, L., Farinotti, D., Huss, M., Dussaillant, I., Brun, F. & Kääb, A. Accelerated Global Glacier Mass Loss in the Early Twenty-First Century. *Nature* **592**, 726 (7856 2021).

20. Callaghan, T. V., Johansson, M., Brown, R. D., Groisman, P. Y., Labba, N., Radionov, V., Barry, R. G., Bulygina, O. N., Essery, R. L. H., Frolov, D. M., Golubev, V. N., Grenfell, T. C., Petrushina, M. N., Razuvaev, V. N., Robinson, D. A., Romanov, P., Shindell, D., Shmakin, A. B., Sokratov, S. A., Warren, S. & Yang, D. The Changing Face of Arctic Snow Cover: A Synthesis of Observed and Projected Changes. *AMBIO* **40**, 17 (2011).

21. Tang, Q., Zhang, X. & Francis, J. A. Extreme Summer Weather in Northern Mid-Latitudes Linked to a Vanishing Cryosphere. *Nature Climate Change* **4**, 45 (2014).

22. Stroeve, J., Holland, M. M., Meier, W., Scambos, T. & Serreze, M. Arctic Sea Ice Decline: Faster than Forecast. *Geophysical Research Letters* **34** (2007).

23. Vihma, T. Effects of Arctic Sea Ice Decline on Weather and Climate: A Review. *Surveys in Geophysics* **35**, 1175 (2014).

24. Winsvold, S. H., Kääb, A., Nuth, C., Andreassen, L. M., van Pelt, W. J. J. & Schellenberger, T. Using SAR Satellite Data Time Series for Regional Glacier Mapping. *The Cryosphere* **12**, 867 (2018).

25. Pichierri, M. & Rabus, B. *Applications of SAR Remote Sensing in the Arctic: A Review* in *2018 18th International Symposium on Antenna Technology and Applied Electromagnetics (ANTEM)* 2018 18th International Symposium on Antenna Technology and Applied Electromagnetics (ANTEM) (2018), 1.

26. Taylor, L. S., Quincey, D. J., Smith, M. W., Baumhoer, C. A., McMillan, M. & Mansell, D. T. Remote Sensing of the Mountain Cryosphere: Current Capabilities and Future Opportunities for Research. *Progress in Physical Geography* **45**, 931 (2021).

27. Mahmud, M. S., Nandan, V., Singha, S., Howell, S. E. L., Geldsetzer, T., Yackel, J. & Montpetit, B. C- and L-band SAR Signatures of Arctic Sea Ice during Freeze-Up. *Remote Sensing of Environment* **279**, 113129 (2022).

28. Moreira, A., Prats-Iraola, P., Younis, M., Krieger, G., Hajnsek, I. & Papathanassiou, K. P. A Tutorial on Synthetic Aperture Radar. *IEEE Geoscience and Remote Sensing Magazine* **1**, 6 (2013).

29. Leinss, S., Wiesmann, A., Lemmetyinen, J. & Hajnsek, I. Snow Water Equivalent of Dry Snow Measured by Differential Interferometry. *IEEE Journal of Selected Topics in Applied Earth Observations and Remote Sensing* **8**, 3773 (2015).

30. Mouginot, J., Rignot, E. & Scheuchl, B. Continent-Wide, Interferometric SAR Phase, Mapping of Antarctic Ice Velocity. *Geophysical Research Letters* **46**, 9710 (2019).

31. Bernhard, P., Zwieback, S., Leinss, S. & Hajnsek, I. Mapping Retrogressive Thaw Slumps Using Single-Pass TanDEM-X Observations. *IEEE Journal of Selected Topics in Applied Earth Observations and Remote Sensing* **13**, 3263 (2020).

32. Tsokas, A., Rysz, M., Pardalos, P. M. & Dipple, K. SAR Data Applications in Earth Observation: An Overview. *Expert Systems with Applications* **205**, 117342 (2022).

33. Berthier, E., Floriciou, D., Gardner, A. S., Gourmelen, N., Jakob, L., Paul, F., Treichler, D., Wouters, B., Belart, J. M. C., Dehecq, A., Dussaillant, I., Hugonnet, R., Kääb, A., Krieger, L., Pálsson, F. & Zemp, M. Measuring Glacier Mass Changes from Space—a Review. *Reports on Progress in Physics* **86**, 036801 (2023).

34. Rott, H. The Analysis of Backscattering Properties from SAR Data of Mountain Regions. *IEEE Journal of Oceanic Engineering* **9**, 347 (1984).

35. Gelautz, M., Frick, H., Raggam, J., Burgstaller, J. & Leberl, F. SAR Image Simulation and Analysis of Alpine Terrain. *ISPRS Journal of Photogrammetry and Remote Sensing* **53**, 17 (1998).

36. Strozzi, T., Luckman, A., Murray, T., Wegmuller, U. & Werner, C. L. Glacier Motion Estimation Using SAR Offset-Tracking Procedures. *IEEE Transactions on Geoscience and Remote Sensing* **40**, 2384 (2002).

37. Colesanti, C. & Wasowski, J. Investigating Landslides with Space-Borne Synthetic Aperture Radar (SAR) Interferometry. *Engineering Geology* **88**, 173 (2006).

38. Franceschetti, G. & Lanari, R. *Synthetic Aperture Radar Processing* First edition (CRC Press, Boca Raton, FL, 2018).

39. Kropatsch, W. & Strobl, D. The Generation of SAR Layover and Shadow Maps from Digital Elevation Models. *IEEE Transactions on Geoscience and Remote Sensing* **28**, 98 (1990).

40. Chen, X., Sun, Q. & Hu, J. Generation of Complete SAR Geometric Distortion Maps Based on DEM and Neighbor Gradient Algorithm. *Applied Sciences* **8**, 2206 (11 2018).

41. Massonnet, D. & Souyris, J.-C. *Imaging with Synthetic Aperture Radar* oth ed. (EPFL Press, 2008).

42. Argenti, F., Lapini, A., Bianchi, T. & Alparone, L. A Tutorial on Speckle Reduction in Synthetic Aperture Radar Images. *IEEE Geoscience and Remote Sensing Magazine* **1**, 6 (2013).

43. Freeman, A. SAR Calibration: An Overview. *IEEE Transactions on Geoscience and Remote Sensing* **30**, 1107 (1992).

44. Small, D., Holecz, F., Meier, E., Nüesch, D. & Barmettler, A. Geometric and Radiometric Calibration of RADARSAT Images. *Proc. of Geomatics in the Era of RADARSAT, Ottawa, Canada* (1997).

45. Atwood, D. K., Small, D. & Gens, R. Improving PolSAR Land Cover Classification With Radiometric Correction of the Coherency Matrix. *IEEE Journal of Selected Topics in Applied Earth Observations and Remote Sensing* **5**, 848 (2012).

46. Frey, O., Santoro, M., Werner, C. L. & Wegmuller, U. DEM-Based SAR Pixel-Area Estimation for Enhanced Geocoding Refinement and Radiometric Normalization. *IEEE Geoscience and Remote Sensing Letters* **10**, 48 (2013).

47. Ulaby, F. T., Moore, R. K. & Fung, A. K. in. *Remote Sensing* 3 (Addison-Wesley, Reading, Mass, 1982).

48. Pathe, C., Wagner, W., Sabel, D., Doubkova, M. & Basara, J. B. Using ENVISAT ASAR Global Mode Data for Surface Soil Moisture Retrieval Over Oklahoma, USA. *IEEE Transactions on Geoscience and Remote Sensing* **47**, 468 (2009).

49. O'Grady, D., Leblanc, M. & Gillieson, D. Relationship of Local Incidence Angle with Satellite Radar Backscatter for Different Surface Conditions. *International Journal of Applied Earth Observation and Geoinformation* **24**, 42 (2013).

50. Baghdadi, N., Gauthier, Y., Bernier, M. & Fortin, J.-P. Potential and Limitations of RADARSAT SAR Data for Wet Snow Monitoring. *IEEE Transactions on Geoscience and Remote Sensing* **38**, 316 (2000).

51. *Polarimetric Synthetic Aperture Radar: Principles and Application* (eds Hajnsek, I. & Desnos, Y.-L.) (Springer International Publishing, Cham, 2021).

52. Wright, T. J., Parsons, B. E., Jackson, J. A., Haynes, M., Fielding, E. J., England, P. C. & Clarke, P. J. Source Parameters of the 1 October 1995 Dinar (Turkey) Earthquake from SAR Interferometry and Seismic Bodywave Modelling. *Earth and Planetary Science Letters* **172**, 23 (1999).

53. Fornaro, G. & Pascazio, V. in *Academic Press Library in Signal Processing* (eds Sidiropoulos, N. D., Gini, F., Chellappa, R. & Theodoridis, S.) 1043 (Elsevier, 2014).

54. Dai, K., Li, Z., Tomás, R., Liu, G., Yu, B., Wang, X., Cheng, H., Chen, J. & Stockamp, J. Monitoring Activity at the Daguangbao Mega-Landslide (China) Using Sentinel-1 TOPS Time Series Interferometry. *Remote Sensing of Environment* **186**, 501 (2016).

55. Novellino, A., Pennington, C., Leeming, K., Taylor, S., Alvarez, I. G., McAllister, E., Arnhardt, C. & Winson, A. Mapping Landslides from Space: A Review. *Landslides* **21**, 1041 (2024).

56. Zebker, H. A. & Goldstein, R. M. Topographic Mapping from Interferometric Synthetic Aperture Radar Observations. *Journal of Geophysical Research: Solid Earth* **91**, 4993 (1986).

57. Rosen, P., Hensley, S., Joughin, I., Li, F., Madsen, S., Rodriguez, E. & Goldstein, R. Synthetic Aperture Radar Interferometry. *Proceedings of the IEEE* **88**, 333 (2000).

58. *InSAR Principles: Guidelines for SAR Interferometry Processing and Interpretation* (eds Fletcher, K., European Space Agency & European Space Research and Technology Centre) *ESA TM* **19**. 1 p. (ESA Publications, ESTEC, Noordwijk, the Netherlands, 2007).

59. Paul, F., Bolch, T., Kääb, A., Nagler, T., Nuth, C., Scharrer, K., Shepherd, A., Strozzi, T., Ticconi, F., Bhambri, R., Berthier, E., Bevan, S., Gourmelen, N., Heid, T., Jeong, S., Kunz, M., Lauknes, T. R., Luckman, A., Merryman Boncori, J. P., Moholdt, G., Muir, A., Neelmeijer, J., Rankl, M., VanLooy, J. & Van Niel, T. The Glaciers Climate Change Initiative: Methods for Creating Glacier Area, Elevation Change and Velocity Products. *Remote Sensing of Environment* **162**, 408 (2015).

60. Paterson, W. S. B. & Paterson, W. S. B. *The Physics of Glaciers* 3rd ed (Pergamon, Oxford, OX, England Tarrytown, N.Y., U.S.A, 1994).

61. Dehecq, A., Altena, B., Gardner, A. S., Trouvé, E. & Leinss, S. in *Surface Displacement Measurement from Remote Sensing Images* 339 (John Wiley & Sons, Ltd, 2022).

62. Millan, R., Mouginot, J., Rabatel, A. & Morlighem, M. Ice Velocity and Thickness of the World's Glaciers. *Nature Geoscience* **15**, 124 (2022).

63. Copland, L., Pope, S., Bishop, M. P., John F. Shroder, J., Clendon, P., Bush, A., Kamp, U., Seong, Y. B. & Owen, L. A. Glacier Velocities across the Central Karakoram. *Annals of Glaciology* **50**, 41 (2009).

64. Bhambri, R., Hewitt, K., Kawishwar, P., Kumar, A., Verma, A., Snehmani, Tiwari, S. & Misra, A. Ice-Dams, Outburst Floods, and Movement Heterogeneity of Glaciers, Karakoram. *Global and Planetary Change* **180**, 100 (2019).

65. Berthier, E., Vadon, H., Baratoux, D., Arnaud, Y., Vincent, C., Feigl, K., Rémy, F. & Legrésy, B. Surface Motion of Mountain Glaciers Derived from Satellite Optical Imagery. *Remote Sensing of Environment* **95**, 14 (2005).

66. Dehecq, A., Gourmelen, N. & Trouve, E. Deriving Large-Scale Glacier Velocities from a Complete Satellite Archive: Application to the Pamir–Karakoram–Himalaya. *Remote Sensing of Environment* **162**, 55 (2015).

67. Dirscherl, M., Dietz, A. J., Dech, S. & Kuenzer, C. Remote Sensing of Ice Motion in Antarctica – A Review. *Remote Sensing of Environment* **237**, 111595 (2020).

68. Feng, X., Chen, Z., Li, G., Ju, Q., Yang, Z. & Cheng, X. Improving the Capability of D-InSAR Combined with Offset-Tracking for Monitoring Glacier Velocity. *Remote Sensing of Environment* **285**, 113394 (2023).

69. Joughin, I., Kwok, R. & Fahnestock, M. Estimation of Ice-Sheet Motion Using Satellite Radar Interferometry: Method and Error Analysis with Application to Humboldt Glacier, Greenland. *Journal of Glaciology* **42**, 564 (1996).

70. Joughin, I., Smith, B. E., Howat, I. M., Scambos, T. & Moon, T. Greenland Flow Variability from Ice-Sheet-Wide Velocity Mapping. *Journal of Glaciology* **56**, 415 (2010).

71. Rignot, E., Mouginot, J. & Scheuchl, B. Ice Flow of the Antarctic Ice Sheet. *Science* **333**, 1427 (2011).

72. Trouve, E., Vasile, G., Gay, M., Bombrun, L., Grussenmeyer, P., Landes, T., Nicolas, J.-M., Bolon, P., Petillot, I., Julea, A., Valet, L., Chanussot, J. & Koehl, M. Combining Airborne Photographs and Spaceborne SAR Data to Monitor Temperate Glaciers: Potentials and Limits. *IEEE Transactions on Geoscience and Remote Sensing* **45**, 905 (2007).

73. Leinss, S., Li, S., Yan, Y. & Altena, B. in *Surface Displacement Measurement from Remote Sensing Images* 59 (John Wiley & Sons, Ltd, 2022).

74. Lange, R. d., Luckman, A. & Murray, T. Improvement of Satellite Radar Feature Tracking for Ice Velocity Derivation by Spatial Frequency Filtering. *IEEE Transactions on Geoscience and Remote Sensing* **45**. 2309 (2007).

75. Gray, A., Mattar, K., Vachon, P., Bindschadler, R., Jezek, K., Forster, R. & Crawford, J. *InSAR Results from the RADARSAT Antarctic Mapping Mission Data: Estimation of Glacier Motion Using a Simple Registration Procedure* in *IGARSS '98. Sensing and Managing the Environment. 1998 IEEE International Geoscience and Remote Sensing. Symposium Proceedings. (Cat. No.98CH36174)* IGARSS '98. Sensing and Managing the Environment. 1998 IEEE International Geoscience and Remote Sensing. Symposium Proceedings. (Cat. No.98CH36174) (IEEE, Seattle, WA, USA, 1998), 1638.

76. Michel, R. & Rignot, E. Flow of Glaciar Moreno, Argentina, from Repeat-Pass Shuttle Imaging Radar Images: Comparison of the Phase Correlation Method with Radar Interferometry. *Journal of Glaciology* **45**, 93 (1999).

77. Gray, A., Short, N., Mattar, K. & Jezek, K. Velocities and Flux of the Filchner Ice Shelf and Its Tributaries Determined from Speckle Tracking Interferometry. *Canadian Journal of Remote Sensing* **27**, 193 (2001).

78. Quincey, D., Copland, L., Mayer, C., Bishop, M., Luckman, A. & Belò, M. Ice Velocity and Climate Variations for Baltoro Glacier, Pakistan. *Journal of Glaciology* **55**, 1061 (2009).

79. Leprince, S., Barbot, S., Ayoub, F. & Avouac, J.-P. Automatic and Precise Orthorectification, Coregistration, and Subpixel Correlation of Satellite Images, Application to Ground Deformation Measurements. *IEEE Transactions on Geoscience and Remote Sensing* **45**, 1529 (2007).

80. Haug, T., Kääb, A. & Skvarca, P. Monitoring Ice Shelf Velocities from Repeat MODIS and Landsat Data – a Method Study on the Larsen C Ice Shelf, Antarctic Peninsula, and 10 Other Ice Shelves around Antarctica. *The Cryosphere* **4**, 161 (2010).

81. Debella-Gilo, M. & Kääb, A. Sub-pixel precision image matching for measuring surface displacements on mass movements using normalized cross-correlation. *Remote Sensing of Environment* **115**, 130 (2011).

82. Heid, T. & Kääb, A. Evaluation of Existing Image Matching Methods for Deriving Glacier Surface Displacements Globally from Optical Satellite Imagery. *Remote Sensing of Environment* **118**, 339 (2012).

83. Debella-Gilo, M. & Kääb, A. Locally adaptive template sizes for matching repeat images of Earth surface mass movements. *ISPRS journal of photogrammetry and remote sensing* **69**, 10 (2012).

84. Werninghaus, R. & Buckreuss, S. The TerraSAR-X Mission and System Design. *IEEE Transactions on Geoscience and Remote Sensing* **48**, 606 (2010).

85. Kumar, V., Venkataraman, G., Høgda, K. A. & Larsen, Y. Estimation and Validation of Glacier Surface Motion in the Northwestern Himalayas Using High-Resolution SAR Intensity Tracking. *International Journal of Remote Sensing* **34**, 5518 (2013).

86. Schubert, A., Faes, A., Kääb, A. & Meier, E. Glacier surface velocity estimation using repeat TerraSAR-X images: Wavelet- vs. correlation-based image matching. *ISPRS Journal of Photogrammetry and Remote Sensing* **82**. 49 (2013).

87. Ponton, F., Trouvé, E., Gay, M., Walpersdorf, A., Fallourd, R., Nicolas, J.-M., Vernier, F. & Mugnier, J.-L. Observation of the Argentière Glacier Flow Variability from 2009 to 2011 by TerraSAR-X and GPS Displacement Measurements. *IEEE Journal of Selected Topics in Applied Earth Observations and Remote Sensing* **7**, 3274 (2014).

88. Neelmeijer, J., Motagh, M. & Wetzel, H.-U. Estimating Spatial and Temporal Variability in Surface Kinematics of the Inylchek Glacier, Central Asia, Using TerraSAR–X Data. *Remote Sensing* **6**, 9239 (10 2014).

89. Schellenberger, T., Dunse, T., Kääb, A., Kohler, J. & Reijmer, C. H. Surface Speed and Frontal Ablation of Kronebreen and Kongsbreen, NW Svalbard, from SAR Offset Tracking. *The Cryosphere* **9**, 2339 (2015).

90. Rosenqvist, A., Shimada, M., Ito, N. & Watanabe, M. ALOS PALSAR: A Pathfinder Mission for Global-Scale Monitoring of the Environment. *IEEE Transactions on Geoscience and Remote Sensing* **45**, 3307 (2007).

91. Yan, S., Guo, H., Liu, G. & Ruan, Z. Mountain Glacier Displacement Estimation Using a DEM-assisted Offset Tracking Method with ALOS/PALSAR Data. *Remote Sensing Letters* **4**, 494 (2013).

92. Li, J., Li, Z.-w., Ding, X.-l., Wang, Q.-j., Zhu, J.-j. & Wang, C.-c. Investigating Mountain Glacier Motion with the Method of SAR Intensity-Tracking: Removal of Topographic Effects and Analysis of the Dynamic Patterns. *Earth-Science Reviews* **138**, 179 (2014).

93. F.Covello, Battazza, F., Coletta, A., Lopinto, E., Fiorentino, C., Pietranera, L., Valentini, G. & Zoffoli, S. COSMO-SkyMed an Existing Opportunity for Observing the Earth. *Journal of Geodynamics. WEGENER 2008 - Proceedings of the 14th General Assembly of Wegener* **49**, 171 (2010).

94. Ciappa, A., Pietranera, L. & Battazza, F. Perito Moreno Glacier (Argentina) Flow Estimation by COSMO SkyMed Sequence of High-Resolution SAR-X Imagery. *Remote Sensing of Environment* **114**, 2088 (2010).

95. Riveros, N., Euillades, L., Euillades, P., Moreiras, S. & Balbarani, S. Offset Tracking Procedure Applied to High Resolution SAR Data on Viedma Glacier, Patagonian Andes, Argentina. *Advances in Geosciences* **35**, 7 (2013).

96. Bourbigot, M., Johnsen, H., Piantanida, R., Hajduch, G., Poullaouec, J. & Hajduch, G. *Sentinel-1 Product Definition* tech. rep. (ESA, 2016).

97. Yan, S., Liu, G., Wang, Y. & Ruan, Z. Accurate Determination of Glacier Surface Velocity Fields with a DEM-Assisted Pixel-Tracking Technique from SAR Imagery. *Remote Sensing* **7**, 10898 (2015).

98. Kos, A., Amann, F., Strozzi, T., Osten, J., Wellmann, F., Jalali, M. & Dufresne, A. The Surface Velocity Response of a Tropical Glacier to Intra and Inter Annual Forcing, Cordillera Blanca, Peru. *Remote Sensing* **13**, 2694 (2021).

99. Jiang, Z., Wu, K., Liu, S., Wang, X., Zhang, Y., Tahir, A. A. & Long, S. Surging Dynamics of South Rimo Glacier, Eastern Karakoram. *Environmental Research Letters* **16**, 114044 (2021).

100. Nagler, T., Rott, H., Hetzenecker, M., Wuite, J. & Potin, P. The Sentinel-1 Mission: New Opportunities for Ice Sheet Observations. *Remote Sensing* **7**, 9371 (2015).

101. Friedl, P., Seehaus, T. & Braun, M. Global Time Series and Temporal Mosaics of Glacier Surface Velocities Derived from Sentinel-1 Data. *Earth System Science Data* **13**, 4653 (2021).

102. GCOS, W. M. O. *Systematic Observation Requirements for Satellite-Based Data Products for Climate—2011 Update* (Geneva, Switzerland, 2011).

103. DeWalle, D. R. & Rango, A. *Principles of Snow Hydrology* 1st ed. (Cambridge University Press, 2008).

104. Dietz, A. J., Kuenzer, C. & Dech, S. Global SnowPack: A New Set of Snow Cover Parameters for Studying Status and Dynamics of the Planetary Snow Cover Extent. *Remote Sensing Letters* **6**, 844 (2015).

105. Tiuri, M., Sihvola, A., Nyfors, E. & Hallikaiken, M. The Complex Dielectric Constant of Snow at Microwave Frequencies. *IEEE Journal of Oceanic Engineering* **9**, 377 (1984).

106. Snehmani, Singh, M. K., Gupta, R., Bhardwaj, A. & Joshi, P. K. Remote Sensing of Mountain Snow Using Active Microwave Sensors: A Review. *Geocarto International* **30**, 1 (2015).

107. Shi, J. & Dozier, J. Measurements of Snow- and Glacier-Covered Areas with Single-Polarization SAR. *Annals of Glaciology* **17**, 72 (1993).

108. Baghdadi, N., Gauthier, Y. & Bernier, M. Capability of multitemporal ERS-1 SAR data for wet-snow mapping. *Remote Sensing of Environment* **60**, 174 (1997).

109. Nagler, T., Rott, H., Ripper, E., Bippus, G. & Hetzenecker, M. Advancements for Snowmelt Monitoring by Means of Sentinel-1 SAR. *Remote Sensing* **8**, 348 (2016).

110. Malnes, E. & Guneriussen, T. *Mapping of snow covered area with Radarsat in Norway* in. **1** (2002), 683.

111. Longepe, N., Allain, S., Ferro-Famil, L., Pottier, E. & Durand, Y. Snowpack Characterization in Mountainous Regions Using C-Band SAR Data and a Meteorological Model. *IEEE Transactions on Geoscience and Remote Sensing* **47**, 406 (2009).

112. Rondeau-Genesse, G., Trudel, M. & Leconte, R. Monitoring snow wetness in an Alpine Basin using combined C-band SAR and MODIS data. *Remote Sensing of Environment* **183**, 304 (2016).

113. Koskinen, J., Pulliainen, J. & Hallikainen, M. The use of ers-1 sar data in snow melt monitoring. *IEEE Transactions on Geoscience and Remote Sensing* **35**, 601 (1997).

114. Luojus, K., Pulliainen, J., Metsamaki, S. & Hallikainen, M. Accuracy assessment of SAR data-based snow-covered area estimation method. *IEEE Transactions on Geoscience and Remote Sensing* **44**. 277 (2006).

115. Pettinato, S., Santi, E., Paloscia, S., Aiazzi, B., Baronti, S. & Garzelli, A. Snow cover area identification by using a change detection method applied to COSMO-SkyMed images. *Journal of Applied Remote Sensing* **8**. 084684 (2014).

116. Liu, C., Li, Z., Zhang, P. & Wu, Z. Seasonal snow cover classification based on SAR imagery and topographic data. *Remote Sensing Letters* **13**, 269 (2022).

117. Tsai, Y.-L. S., Dietz, A., Oppelt, N. & Kuenzer, C. Wet and Dry Snow Detection Using Sentinel-1 SAR Data for Mountainous Areas with a Machine Learning Technique. *Remote Sensing* **11**. 895 (2019).

118. Meier, M. F. Contribution of Small Glaciers to Global Sea Level. *Science* **226**, 1418 (1984).

119. Huss, M. & Hock, R. Global-Scale Hydrological Response to Future Glacier Mass Loss. *Nature Climate Change* **8**, 135 (2018).

120. Bamber, J. L. & Rivera, A. A Review of Remote Sensing Methods for Glacier Mass Balance Determination. *Global and Planetary Change* **59**, 138 (2007).

121. Huss, M. Density assumptions for converting geodetic glacier volume change to mass change. *The Cryosphere* **7**, 877 (2013).

122. Rodríguez, E., Morris, C. S. & Belz, J. E. A Global Assessment of the SRTM Performance. *Photogrammetric Engineering & Remote Sensing* **72**, 249 (2006).

123. Krieger, G., Zink, M., Bachmann, M., Bräutigam, B., Schulze, D., Martone, M., Rizzoli, P., Steinbrecher, U., Walter Antony, J., De Zan, F., Hajnsek, I., Papathanassiou, K., Kugler, F., Rodriguez Cassola, M., Younis, M., Baumgartner, S., López-Dekker, P., Prats, P. & Moreira, A. TanDEM-X: A Radar Interferometer with Two Formation-Flying Satellites. *Acta Astronautica* **89**, 83 (2013).

124. Rizzoli, P., Martone, M., Gonzalez, C., Wecklich, C., Borla Tridon, D., Bräutigam, B., Bachmann, M., Schulze, D., Fritz, T., Huber, M., Wessel, B., Krieger, G., Zink, M. & Moreira, A. Generation and Performance Assessment of the Global TanDEM-X Digital Elevation Model. *ISPRS Journal of Photogrammetry and Remote Sensing* **132**, 119 (2017).

125. Marzeion, B., Champollion, N., Haeberli, W., Langley, K., Leclercq, P. & Paul, F. in *Integrative Study of the Mean Sea Level and Its Components* (eds Cazenave, A., Champollion, N., Paul, F. & Benveniste, J.) 107 (Springer International Publishing, Cham, 2017).

126. Malz, P., Meier, W., Casassa, G., Jaña, R., Skvarca, P. & Braun, M. H. Elevation and Mass Changes of the Southern Patagonia Icefield Derived from TanDEM-X and SRTM Data. *Remote Sensing* **10**, 188 (2 2018).

127. Liu, L., Jiang, L., Jiang, H., Wang, H., Ma, N. & Xu, H. Accelerated Glacier Mass Loss (2011–2016) over the Puruogangri Ice Field in the Inner Tibetan Plateau Revealed by Bistatic InSAR Measurements. *Remote Sensing of Environment* **231**, 111241 (2019).

128. Paul, F. & Haeberli, W. Spatial Variability of Glacier Elevation Changes in the Swiss Alps Obtained from Two Digital Elevation Models. *Geophysical Research Letters* **35**, 2008GL034718 (2008).

129. Piermattei, L., Zemp, M., Sommer, C., Brun, F., Braun, M. H., Andreassen, L. M., Belart, J. M. C., Berthier, E., Bhattacharya, A., Boehm Vock, L., Bolch, T., Dehecq, A., Dussaillant, I., Falaschi, D., Florentine, C., Floricioiu, D., Ginzler, C., Guillet, G., Hugonnet, R., Huss, M., Kääb, A., King, O., Klug, C., Knuth, F., Krieger, L., La Frenierre, J., McNabb, R., McNeil, C., Prinz, R., Sass, L., Seehaus, T., Shean, D., Treichler, D., Wendt, A. & Yang, R. Observing Glacier Elevation Changes from Spaceborne Optical and Radar Sensors – an Inter-Comparison Experiment Using ASTER and TanDEM-X Data. *The Cryosphere* **18**, 3195 (2024).

130. Dehecq, A., Millan, R., Berthier, E., Gourmelen, N., Trouvé, E. & Vionnet, V. Elevation Changes Inferred From TanDEM-X Data Over the Mont-Blanc Area: Impact of the X-Band Interferometric Bias. *IEEE Journal of Selected Topics in Applied Earth Observations and Remote Sensing* **9**, 3870 (2016).

2

CROSS-CORRELATION STACKING FOR ROBUST OFFSET TRACKING USING SAR IMAGE TIME-SERIES

Shiyi Li[1], Silvan Leinss[1], and Irena Hajnsek[1,2]

1 Institute of Environmental Engineering, ETH Zurich, Switzerland

2 Microwaves and Radar Institute, German Aerospace Center DLR, Germany

Article published in *IEEE Journal of Selected Topics in Applied Earth Observations and Remote Sensing*
Citation: Li, S., Leinss, S. & Hajnsek, I. Cross-Correlation Stacking for Robust Offset Tracking Using SAR Image Time-Series. *IEEE Journal of Selected Topics in Applied Earth Observations and Remote Sensing* **14**, 4765 (2021)

Key findings:

- Introduced cross-correlation stacking to enhance offset tracking robustness and precision.
- Achieved high spatial coverage with small templates using the proposed method.
- Demonstrated method's adaptability across SAR sensors and robust performance on the alpine glacier.

Author's contributions:

- Developed and implemented the presented methodology.
- Processed and analyzed the data over the study area.
- Interpreted the results and wrote the manuscript.

Co-author's contributions:

- S. Leinss contributed to methodology development, data evaluation, and revision of the manuscript.
- I. Hajnsek contributed to the study design, result discussion, and revision of the manuscript.

Abstract

Offset tracking is widely applied for measuring ground surface displacements from remote sensing data. Displacements are determined by the offset where two image templates match best. The match can be evaluated with normalized cross-correlation (NCC), in which the height and location of the NCC peak represent the matching quality and the corresponding offset. Attaining robust offset estimations requires an unambiguous tracking of the peak in the NCC noise floor. To improve offset estimations, we propose a cross-correlation stacking method that can significantly suppress the noise floor of NCC. Instead of deriving offsets from each pair-wise NCC, we stack a series of consecutive pair-wise NCCs and determine the offset after averaging the NCC stack. Thereby, tracking benefits from the redundant information in multiple NCCs and is more robust to noise. We assessed the method by measuring the flow velocity of the Great Aletsch Glacier in Switzerland using image time series collected by the synthetic aperture radar (SAR) satellites TanDEM-X and Sentinel-1A. Using relatively small templates of 48×48 *pixels combined with a stack of seven pair-wise NCCs of TanDEM-X images, we obtain velocity fields whose spatial coverage are almost equivalent to the coverage of velocity fields obtained with templates of* 96×96 *pixels applied on a single image pair. Similar improvements in spatial coverage are observed for Sentinel-1A. The results demonstrate that the stacking method can greatly enhance both the spatial resolution and the coverage of the obtained velocity fields.*

Keywords

Offset tracking, glacier velocity, cross-correlation, stacking, synthetic aperture radar (SAR)

2.1 Introduction

Measuring ground surface displacement using either optical or synthetic aperture radar (SAR) images is of interests to many environment-related studies, and two mostly used methods for this purpose are offset tracking and differential interferometric SAR (D-InSAR). The focus of this study is offset tracking, which has been successfully applied to many studies such as detecting landslides [1–3], estimating co-seismic slips [4, 5], and measuring glacier surface velocities [6–15].

Offset tracking is a template matching method which can be robustly applied to either optical or SAR images [6, 16]. It is often referred as feature tracking when applied to optical images [17]. For SAR images, it is also called

coherence tracking when using SAR single-look complex images, or intensity tracking when only using real-valued intensity images [6]. The concept of offset tracking is to estimate displacement offsets through measuring the similarity between two images taken over the same area and at different times. In practice, image pairs are firstly partitioned into templates, and then the agreement between two templates are calculated based on certain similarity measures, such as least square difference [18], maximum likelihood [19], and normalized cross-correlation (NCC) [16, 20]. The templates are shifted against each other until the best agreement is found, for which the shift defines the estimated offset.

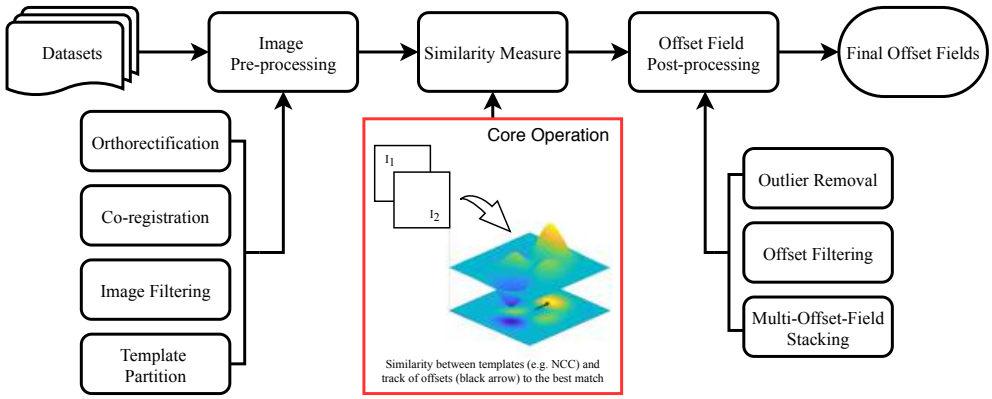

FIGURE 2.1: Common procedure for offset tracking. The core operation of offset tracking is highlighted with the red box.

So far, plenty of efforts have been made in order to improve offset tracking. The first family of improvement are mainly focused on the image pre-processing steps. For instance, Leprince *et al.* [17] proposed a software named COSI-CORR to achieve automatic and precise orthorectification, co-registration, and subpixel correlation for optical images; Lange, Luckman & Murray [21] suggested applying spatial high-pass filters to SAR imagery before cross-correlation to focus the offset tracking on small surface features; Debella-Gilo & Kääb [22] developed a technique to locally optimize template sizes for image partition.

Techniques for the post-processing of offset fields have also been proposed in previous studies, which mainly exploit redundant offset measurements to attain robust offset fields (e.g. smoothing, detecting outliers, median filters). Ahn & Howat [23] proposed a multiple-image multiple-chip (MIMC) algorithm, in which multiple NCCs are generated with template pairs under different configurations (i.e. template sizes, convolution filters, etc.), and a

population of offset vectors are obtained from every individual pair-wise NCC so that a final offset vector can be voted from the population. Similarly, Stumpf, Malet & Delacourt [3] proposed a multiple pairwise image correlation (MPIC) technique, which generates multiple offsets for each pixel location using pair-wise NCC and then summarizes the stack of offsets using developed indicators.

The previous attempts have greatly pushed forward the performance of offset tracking for displacement measurement. These works, focusing either on pre-processing of images or on post-processing of offset fields, derive all information from a pair-wise NCC and use the apparent peak of the NCC field to estimate offsets [16]. Unfortunately, for a pair-wise NCC with low signal-to-noise ratio (SNR), the apparent peak could be found at a false location when the NCC is dominated by noise. Even though redundant offsets estimated from multiple pair-wise NCCs can be used to reduce false detection (e.g. Stumpf, Malet & Delacourt [3]), directly separating the time-invariant NCC component from noise has almost never been explored for SAR offset tracking.

In this work, we propose a method to improve the performance of SAR incoherent offset tracking by firstly creating a stack of pair-wise NCCs from an image time-series and then averaging the NCC stack for offset estimation. Thereby, we make the NCC more robust for tracking by exploiting the entire information of the NCC to reduce the noise floor and to enhance the SNR. The concept has been adopted for Particle Image Velocimetry (PIV) [24, 25], for medical image tracking [26, 27], and recently for ice fall tracking with optical imagery [28]. In these works, different terms were used for the concept, including mean cross-correlation, ensemble tracking, ensemble correlation or ensemble matching. We prefer to refer to the method as "cross-correlation stacking" (or specifically "NCC stacking"), because these words can best represent the core operation of the method and correspond to a widely used terminology for SAR image time-series analysis [29–32]. So far, NCC stacking has not been adopted for SAR images, where we expect significant improvement by reduction of speckle noise.

In this paper, we described the NCC stacking method for SAR imagery, and assessed its effectiveness by measuring the flow velocities of the Great Aletsch Glacier in Switzerland using SAR image series collected by the satellites TanDEM-X [33] and Sentinel-1 [34].

2.2 Methodology

2.2.1 NCC stacking

2.2.1.1 NCC decomposition

Classical offset tracking algorithms commonly use NCC to evaluate the similarity between a pair of image templates with a workflow similar to Fig. 2.1. The NCC can be calculated in either the spatial domain or the frequency domain. In the frequency domain the NCC between the two templates I_1 and I_2, extracted from two SAR intensity images taken over the same area and at different times, can be conveniently calculated as

$$\hat{\gamma} = \frac{\hat{I}_1^* \cdot \hat{I}_2}{\sqrt{E\{|\hat{I}_1|^2\} \cdot E\{|\hat{I}_2|^2\}}} \tag{2.1}$$

with $\hat{I}_i = \mathcal{F}(I_i)$ the Fourier transform of the template I_i, * the complex conjugation, and $E\{|\hat{I}_1|^2\}$ and $E\{|\hat{I}_2|^2\}$ the total energy of the two templates. The obtained spectrum $\hat{\gamma}$ is transformed back to obtain the NCC in the spatial domain

$$\gamma = \mathcal{F}^{-1}(\hat{\gamma})$$

where the offset is estimated by tracking the location of the peak in γ.

Robust tracking relies on unambiguous identification of the NCC peak, which requires the template pair to contain abundant trackable features, such as rigidly shifted geometric structures. On the other hand, noise that hampers the successful offset estimation is added to the NCC field by temporally uncorrelated contents, such as incoherent speckle, non-rigidly translated features (e.g. collapsing crevasses, distorted landscape), and temporally changing surface properties (e.g. snow cover, water content or vegetation change).

From the perspective of offset tracking, an image template, and also its Fourier transform, can be considered as being composed of signal $\hat{s}$ and noise $\hat{n}$:

$$\hat{I} = \hat{s} + \hat{n}.$$

The signal $\hat{s}$ corresponds to the correlated content (i.e. $\hat{s}_1 = \hat{s}_2$) that generates the signal of the NCC, whereas the noise $\hat{n}$ represents the uncorrelated content. Then, we can re-write Eq. (2.1) as

$$\hat{\gamma} = \frac{\hat{s}_1^*\hat{s}_2 + \hat{s}_1^*\hat{n}_2 + \hat{n}_1^*\hat{s}_2 + \hat{n}_1^*\hat{n}_2}{\sqrt{E\{|\hat{I}_1|^2\} \cdot E\{|\hat{I}_2|^2\}}}, \tag{2.2}$$

which decomposes $\hat{\gamma}$ into four elementary cross-correlations, including a shifted auto-correlation, $\hat{s}_1^* \hat{s}_2$, and three cross-correlations between signals and noise ($\hat{s}_1^* \hat{n}_2$, $\hat{n}_1^* \hat{s}_2$ and $\hat{n}_1^* \hat{n}_2$). Since the noise in one template is independent from either the noise or the signal in the other template, we can consider the latter three components as noise contributing to $\hat{\gamma}$. Therefore, in order to attain reliable offset estimations, the Fourier transform of $\hat{s}_1^* \hat{s}_2$ must present a dominant peak in γ that greatly surpasses the superposition of all noise components. The dominance of this peak can be characterized by the signal-to-noise ratio (SNR) of the NCC, defined as

$$\mathrm{SNR} = 10 \log_{10} \left(\frac{c_p^2}{\overline{c_f^2}} \right) \tag{2.3}$$

with c_p the NCC peak height and $\overline{c_f^2}$ the average of the squared ambient NCC field γ. To ensure reliable tracking, the SNR should be sufficiently high. Otherwise the tracking delivers false results because the peak that represents the true offset can not reveal itself from the noise floor (*i.e.* the SNR is too low).

2.2.1.2 NCC stacking using image time-series

To make offset tracking more robust against noise, we can create a stack of pair-wise NCCs using image time-series and then average the NCC stack to suppress the noise floor. An overview of our general workflow is presented in Fig. 2.2.

Suppose a short time-series of N co-registered image is collected with a repeat interval of t. With integer multiples a of the repeat interval t, we can calculate a stack of $N - a$ pair-wise NCCs from Eq. (2.1) using all template pairs with a time interval of $T = at$. In this stack, each pair-wise NCC captures a snapshot of the displacement represented by the template pair. Assuming constant surface velocities during acquisition of the time-series, we can expect that all pair-wise NCCs record identical offsets. Hence, it can be presumed that the peaks generated by $\hat{s}_1^* \hat{s}_2$ in all pair-wise NCCs γ are located at more or less the same position, whereas the ambient noise field, generated by $\hat{s}_1^* \hat{n}_2 + \hat{n}_1^* \hat{s}_2 + \hat{n}_1^* \hat{n}_2$, averages out in the stack.

This principle can be easily extended to multiple image time-series, such as image series acquired in multiple different years, in different spectral or polarimetric channels, or even from different imaging sensors. For that, suppose M image time-series are collected and each time-series i consists of N_i ($i = 1...M$) images, we can then create a total stack that consists of

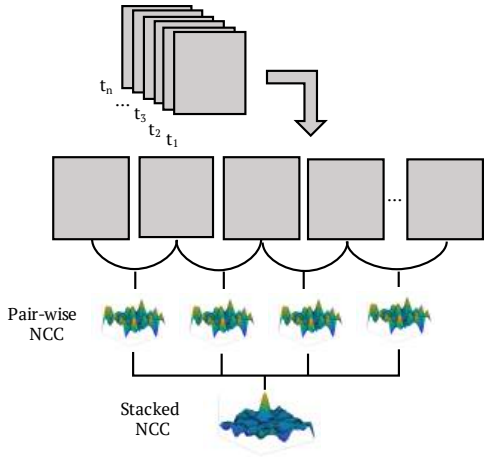

FIGURE 2.2: A conceptual workflow of the NCC stacking method. With the acquired image time-series, an NCC stack is obtained by calculating pair-wise NCCs consecutively, and then the stack is averaged to track the peak. The shown stacking workflow can be directly inserted into the core operation in Fig. 2.1(red box) to replace the pair-wise NCC.

M sub-stacks of pair-wise NCCs, each of which consists of $N_i - a$ pair-wise NCCs. Assuming identical surface velocities for all individual time-series, we can average the total stack of pair-wise NCCs in spatial domain to get the averaged NCC in which the offset is tracked:

$$\overline{\gamma} = \frac{\sum_{i=1}^{M} \sum_{j=1}^{N_i - a} \gamma_{i,j}}{\sum_{i=1}^{M} (N_i - a)} \tag{2.4}$$

Particularly, seasonal velocity variations, or the so-called "phase-averaged velocity fields" [25], can be resolved with Equation (2.4) when sub-stacks for each phase of a year (e.g. months) are averaged over multiple years. Equation (2.4) also permits to track step-like displacement (e.g. co-seismic slips) using a stack of correlation pairs in which each pair is composed of pre- and post-event images.

2.2.2 Offset tracking with sub-pixel precision

In practice, precise tracking requires sub-pixel precision, which is achieved by firstly fitting the NCC peak with a continuous function (e.g. polynomial or Gaussian function), and then finding the location of the maximum of the

fitted function [35]. In this work, we used a Gaussian function $g(x, y)$ in the form of Eq. (2.5) to fit the NCC peak.

$$g(x, y) = Ae^{(-P(x-x_0)^2+Q(x-x_0)(y-y_0)+R(y-y_0)^2)} + b \tag{2.5}$$

where

$$P = \frac{\cos^2\theta}{2\sigma_x^2} + \frac{\sin^2\theta}{2\sigma_y^2}$$
$$Q = \frac{-\sin 2\theta}{2\sigma_x^2} + \frac{\sin 2\theta}{2\sigma_y^2}$$
$$R = \frac{\sin^2\theta}{2\sigma_x^2} + \frac{\cos^2\theta}{2\sigma_y^2}$$

The Gaussian function $g(x, y)$ is parameterized by its center location (x_0, y_0), standard deviation (σ_x, σ_y), the maximum value A, the rotation parameter θ and the vertical shift b. In order to fit the Gaussian function, we firstly extracted a window Ω of a few pixels size (see Sect. 2.3.2) centered at the NCC peak, and then up-sampled the extracted window by a factor of ten using bilinear B-Spline interpolation. Within the up-sampled window Ω', we solve a non-linear least-squares (LS) problem to minimize the cost function

$$F = \frac{1}{2} \sum_{(x,y)\in\Omega'} (\mathrm{NCC}(x, y) - g(x, y))^2 \tag{2.6}$$

with x, y coordinates of the up-sampled window Ω'. To ensure convergence, the window size for extraction and initial value of parameters must be carefully selected. In this work, we used the following values for initialization:

- (x_0, y_0): the center location of the up-sampled window;
- (σ_x, σ_y): $1/4$ of the width and height of the up-sampled window respectively;
- A: the NCC peak height;
- θ: zero;
- b: mean value of the ambient field.

For successful fits, the peak position $\vec{p}_{\mathrm{fit}} = (x_{\mathrm{o,fit}}, y_{\mathrm{o,fit}})$ is used. If minimization fails, the initial values $\vec{p} = (x_0, y_0)$ are kept. Once the peak location is determined, the offset vector $\vec{D} = (D_x, D_y)$ can be estimated by measuring

the shift from the NCC center $\vec{c} = (x_c, y_c)$ to the peak with $\vec{D} = \vec{p} - \vec{c}$, and the obtained offset vector field can be converted to a velocity field by

$$\vec{v} = \frac{\vec{D}}{T}. \tag{2.7}$$

2.2.3 Evaluating the obtained velocity field

To quantify the performance gain between the stacked and the pair-wise NCC, we calculated the following three parameters from the obtained velocity fields. As these parameters vary strongly for different image pairs, we evaluated for each stack size all possible combinations of correlation pairs and obtained mean, minimum, and maximum values for the spatial coverage and the velocity residuals.

2.2.3.1 Spatial coverage

In offset tracking applications, the obtained velocity field is often post-processed by removing outliers and unreliable estimations. In this work, we used two thresholds for this purpose, one is based on the maximum velocity magnitude and the other is based on the minimum acceptable SNR (values are defined in Sect. 2.3.2). Thresholding the velocity field leads to voids in the velocity maps, and this allows us to evaluate the robustness of different methods by measuring the spatial coverage R_{cov} of the velocity map as

$$R_{\text{cov}} = \frac{A_{\text{map}}}{A_{\text{total}}} \tag{2.8}$$

with A_{map} the area of the map excluding voids and A_{total} the total area of the study region (black glacier outline in Fig. 2.3).

2.2.3.2 Velocity residuals

The accuracy of offset tracking can be evaluated by examining velocity residuals over static ground, assuming that velocities of such region should be equal to zero. For that, we define the residual ratio within selected static regions as

$$R_{\text{res}} = \frac{A_{\text{residual}}}{A_{\text{static}}} \tag{2.9}$$

with A_{residual} the area covered by residual velocities within the static ground and A_{static} the total area of the static ground (red dashed rectangles in Fig. 2.3). Particularly, we define residual velocity as the velocity vector whose corresponding offsets larger than one pixel in either $x-$ or $y-$ directions.

2.2.3.3 SNR gain

Reliable tracking can be characterized by the SNR value. To evaluate the improvement of confidence level on the obtained velocity field, we can calculate the SNR gain by

$$\mathrm{SNR}_{\mathrm{gain}} = \mathrm{SNR}_{\mathrm{stack}} - \mathrm{SNR}_{\mathrm{pair}}. \tag{2.10}$$

With the SNR gain, it is possible to examine the change of SNR at every template location in the image scene. Specifically, $\mathrm{SNR}_{\mathrm{gain}} > 0$ indicates increased confidence level, whereas $\mathrm{SNR}_{\mathrm{gain}} < 0$ indicates decreased confidence level.

2.3 Study Site and Data

2.3.1 Study site

To evaluate NCC stacking, we derive the surface velocity of the Great Aletsch Glacier located in central Switzerland. The glacier represents one of the largest alpine glacier systems in the European Alps (Fig. 2.3). The Great Aletsch glacier consists of three main tributaries, including the Aletschfirn, the Jungfraufirn, and the Ewigschneefaeld, and these tributaries merge at Konkordiaplatz and flow into the main stream of the Great Aletsch Glacier.

The Great Aletsch glacier has been used as a test site for many studies to explore methods for glacier surface velocity estimations. For instance, Prats *et al.* [37] used airborne interferometric repeat pass SAR data in L- and P-band to measure the surface velocity field around Konkordiaplatz; Erten [38] proposed a method based on polarimetric similarity measure for velocity tracking and tested it here; Schubert *et al.* [39] compared a wavelet-based and correlation-based image matching methods for glacier velocity retrieval using repeat TerraSAR-X stripmap and spotlight images acquired in August 2009 and obtained velocity estimates over the strongly crevassed area (ice fall, tongue) of Aletsch Glacier.

An almost complete velocity map has been generated by Leinss & Bernhard [40] based on pair-wise cross-correlation using a time series of about 130 TanDEM-X acquisitions. They also provided the in-situ GPS velocity measurement at 22 locations on the glacier (red dots in Fig. 2.3). In our study, we used these GPS measurement to validate our velocity results. For that we calculated the root-mean-square error (RMSE) as

$$\mathrm{RMSE} = \sqrt{\frac{1}{n}\sum_{i=1}^{n}(v_i^{\mathrm{track}} - v_i^{\mathrm{meas}})^2} \tag{2.11}$$

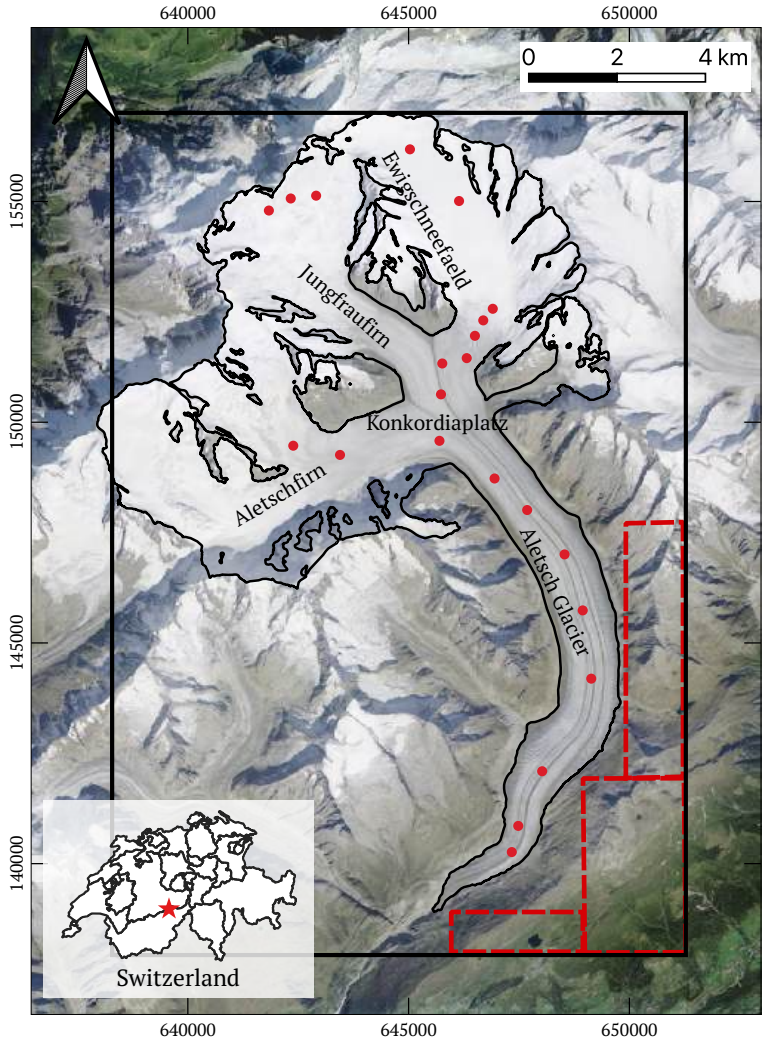

FIGURE 2.3: Overview of the Great Aletsch Glacier. The glacier outline is delineated in black according to Paul *et al.* [36]. The area within the black glacier outline was used to calculate the spatial coverage of successful velocity estimates. Locations of in-situ velocity measurements by GPS are marked with red dots. Glacier-free regions used for residual velocity evaluation are indicated by red dashed rectangles. The processed area of the SAR images is shown by the black rectangle. The approximate location of the Great Aletsch Glacier within Switzerland is indicated by the star in the inset. The base image is taken from SWISSIMAGE 25, 2017© 2019 swisstopo (JD100042).

with v_i^{track} one component (x, y) of the tracked velocity, v_i^{meas} the corresponding measured velocity and n the total number of velocity points that is kept after thresholding.

2.3.2 SAR data, pre-processing and thresholding

To test the proposed stacking method, we processed two distinct SAR datasets. The first dataset was collected by TanDEM-X, which is a high-resolution interferometric X-band SAR mission launched at June 21, 2010 [33]. Our dataset is a subset of the dataset used in [40] and consists of eight dual-pol stripmap (SM) images acquired between 2017-01-10 and 2017-03-28 with equal repeat interval of 11 days (Table 2.1). All acquisitions were made from orbit 154 (descending) at an incident angle of 32°, resulting in a ground range resolution of 6.6 × 2.2 m (az x rg) [41]. The second dataset is collected from Sentinel-1A, which is a C-band SAR mission launched by ESA (European Space Agency) in April, 2014 [34]. This dataset includes two image series acquired from the same orbit (66, descending). One consists of eight images acquired between 2017-01-03 and 2017-03-28, and the other consists of seven images acquired between 2018-01-22 and 2018-03-23 (Table 2.1). All images were acquired in Interferometric Wide Swath (IW2) mode with dual-polarization (VV and VH) and at identical incident angle of 41°, resulting in a resolution of 22 × 4.7 m (az x rg) [42]. Acquisitions were made with equal repeat interval of 12 days within each time series.

	TanDEM-X	Sentinel-1A	
Acquisition Dates	2017-01-10	2017-01-03	2018-01-10
	2017-01-21	2017-01-15	2018-01-22
	2017-02-01	2017-02-08	2018-02-03
	2017-02-12	2017-02-20	2018-02-15
	2017-02-23	2017-02-27	2018-02-27
	2017-03-06	2017-03-04	2018-03-11
	2017-03-17	2017-03-16	2018-03-23
	2017-03-28	2017-03-28	

Table 2.1: Acquisition for this study

For each sensor, the images were co-registered to a common reference scene followed by orthorectification using the SwissAlti3D elevation model obtained from the Federal Office of Topography (swisstopo). As all data were acquired in two polarizations, we averaged the intensity of the two polarizations to reduce SAR speckle. For Sentinel-1A we weighted the VH polarization by the ratio of mean intensities, $\langle VV \rangle / \langle VH \rangle$; for TanDEM-X we did not apply any weighting because the VV and HH polarization have very similar backscatter intensities. We did not apply oversampling of the amplitude before intensity calculation [43] as both dataset are already oversampled compared to their native radar pixel spacing. No multi-looking was applied to neither of the datasets, though the two interpolation steps of coregistration and orthorectification can be considered as multilooking to some grade. After the pre-processing, the pixel spacing of TanDEM-X imagery is 2 m $\times$ 2 m, and that of Sentinel-1A is 5 m $\times$ 5 m. All images were converted to log-scale before cross-correlation. Examples of SAR images from the two datasets are presented in Fig. 2.4. The figure illustrates how different image resolution impacts visible surface feature details [Fig. 2.4(c)-(d)].

Before cross-correlation, we applied high-pass filters to both datasets to better focus on small scale features [21]. The high-pass filter is implemented using a Gaussian kernel whose size is 51 $\times$ 51 pixels and standard deviation is 17 $\times$ 17 pixels. To study the influence of template sizes on the behavior of the stacked NCC, we used a large template size of 96 $\times$ 96 pixels and a small template size of 48 $\times$ 48 pixels for image partition. For tracking the NCC peak with sub-pixel accuracy, extraction windows of 11 $\times$ 11 pixels and 7 $\times$ 7 pixels were used for TanDEM-X and Sentinel-1A images respectively. The chosen window sizes ensured that the curve fitting procedure successfully converged at 99% of the templates for the two datasets.

For TanDEM-X data, image pairs were grouped with time interval of 11 days ($a = 1$) to calculate pair-wise NCCs, and thus we obtained in total seven pair-wise NCCs from the acquisitions listed in Table. 2.1. For Sentinel-1A, due to its larger pixel sizes compared to TanDEM-X, the time interval used to form image pairs was set to be 24 days ($a = 2$) to accommodate larger offsets. Therefore, we obtained in total 11 pair-wise NCCs for Sentinel-1A imagery, including six from the time-series of 2017 and five from the time-series of 2018.

For both datasets, considering the maximum velocity measured in previous studies [37, 38, 40], the threshold of maximum velocity magnitude was set to $v_{\max} = 1 \text{ m} \cdot \text{d}^{-1}$. Higher velocities were considered as outliers and were removed. Threshold on minimum SNR for unreliable estimation removal

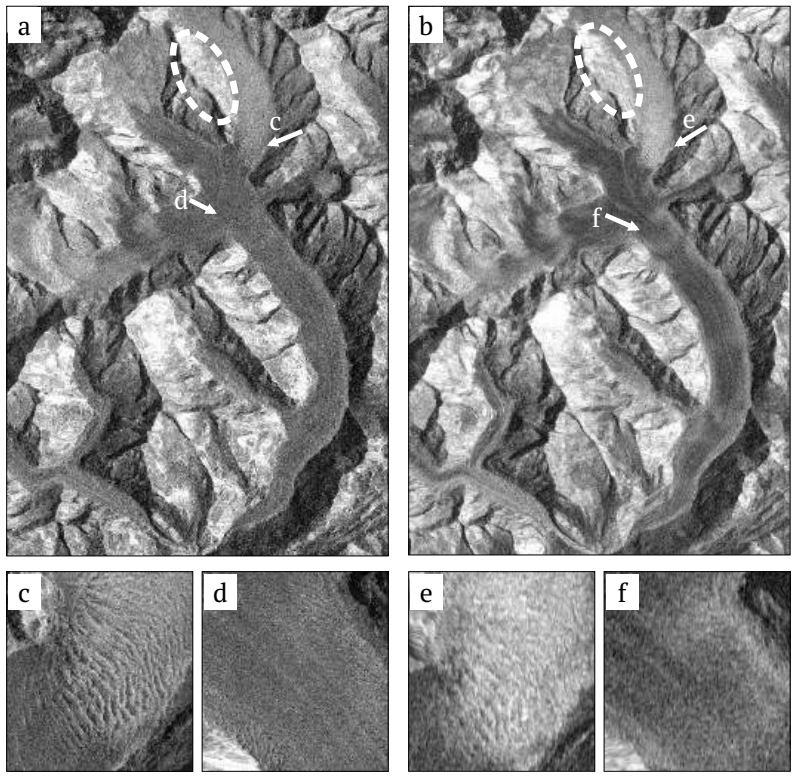

FIGURE 2.4: Example orthorectified SAR images taken from (a) TanDEM-X and (b) Sentinel-1A. No smoothing filter was applied for speckle removal to preserve the spatial resolution. The zoom-in figures (c)-(f) show the effect of different resolution. Very bright mountain slopes are affected by layover (e.g. the east-facing slope of Ewigschneefaeld as indicated by the dashed oval).

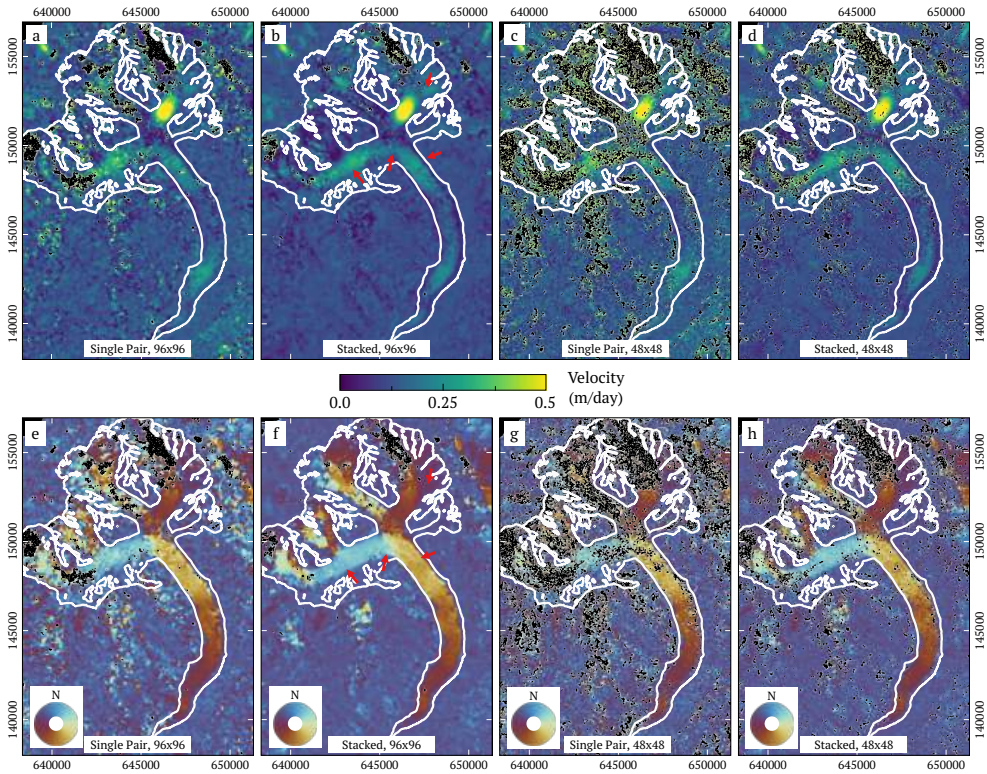

FIGURE 2.5: Magnitude (top) and direction maps (bottom) of velocity fields produced using TanDEM-X SAR images. The left four figures, (a)(e) and (b)(f), are generated with large template (96×96 pixels), the right four figures, (c)(d) and (g)(h), with small templates (48×48 pixels). (a)(c) and (e)(g) are produced with a single pair-wise NCC for which the *best* coverage among all pair-wise results was obtained (2017-01-21 vs. 2017-02-01); (b)(d) and (f)(h) are generated by stacking seven pair-wise NCCs calculated from acquisitions between 2017-01-10 and 2017-03-28 (Table 2.1). Black voids represent removed outlier and results with an SNR below 10 dB. The glacier outline is delineated in white. Axes are labeled with Swiss Coordinates (CH1903/LV03) of unit meters.

was set as $SNR_{min} = 10$ dB. These thresholds were not optimized for glacier velocity filtering, as the major focus of this work is to compare the performance of different algorithms rather than obtain optimum velocity fields for glacier dynamic studies. The threshold to identify residual velocities in the glacier-free regions (Fig. 2.3) was set to be 0.2 $m \cdot d^{-1}$, corresponding to an offset of about one pixel, for both datasets.

2.4 Results

2.4.1 Velocity fields: pair-wise vs. stacked cross-correlation

Velocity fields obtained from TanDEM-X imagery are presented in Fig. 2.5 for pair-wise and stacked NCCs with large (96×96 pixels, 2 m pixel spacing) and small (48×48 pixels) templates. Black voids in the figure are caused by removing outlier and unreliable estimates. The two velocity fields of pairwise NCC [Fig. 2.5(a, c)] are produced with images acquired at 2017-01-21 and 2017-02-01. This image pair represent the *best* coverage of reliable estimates (92% and 74% respectively) among the seven other velocity fields generated with pair-wise NCC. The averaged velocity maps of all seven pair-wise velocity fields (Fig. 2.12 in the appendix) show less noise in the glacier free area, but the coverage over the glacier is greatly reduced than the selected ones. Either picking the best one or averaging all velocity maps are user-defined post-processing steps, and thus it is difficult to determine which one represents the fairest comparison between NCC stacking and pair-wise NCC velocity estimation. We consider our choice of picking the best pair-wise map for comparison to be of disadvantage for NCC stacking which, nevertheless, shows a better spatial coverage.

In Fig. 2.5(a)-(d), velocity magnitude fluctuations along the glacier central line are consistent in all results, with the highest velocities at the ice fall between Ewigschneefaeld and Konkordiaplatz. The orientation of velocities [Fig. 2.5(e)-(h)] is a good indicator to verify the consistency of velocity fields and our results show generally consistent orientation patterns that conform with glacier geometries.

The velocity fields generated by NCC stacking [Fig. 2.5(b, d)] show much less noise than results generated by the single pair-wise NCC [Fig. 2.5(a, c)] for both template sizes. Focusing on areas indicated by red arrows in Fig. 2.5(b, f) and comparing them to Fig. 2.5(a, e), the stacked NCCs produce much smoother fields for both velocity magnitude and orientation than a pair-wise NCC. For small templates and pair-wise NCC [Fig. 2.5(c, g)], areas

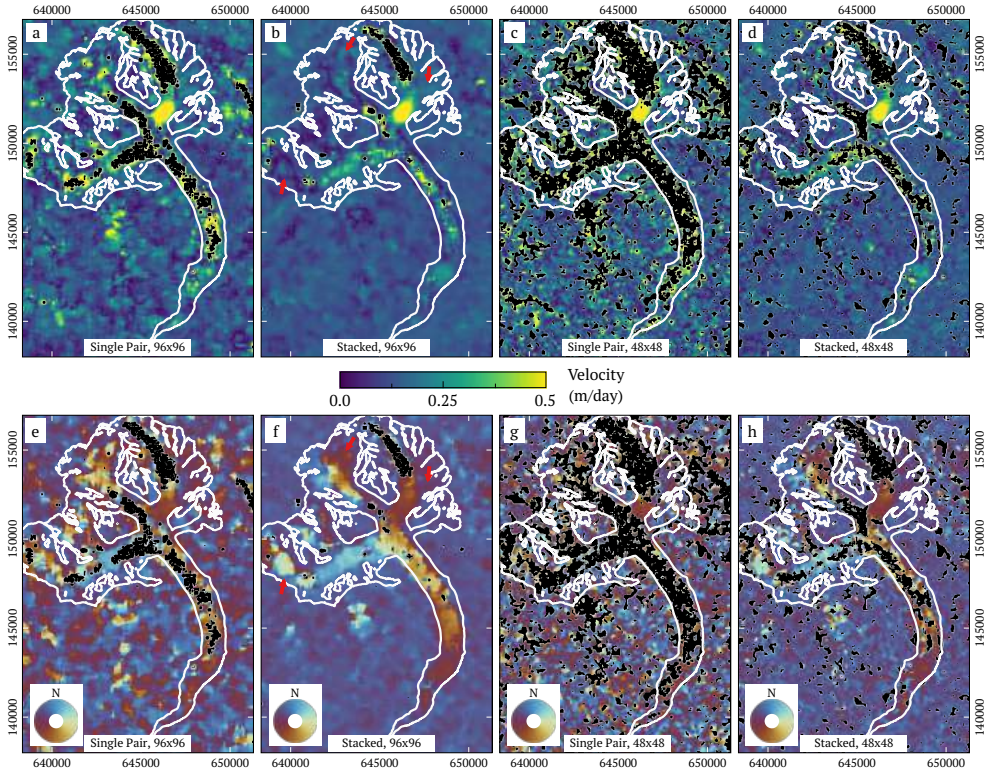

FIGURE 2.6: Magnitude (a-d) and direction map (e-f) of velocity fields produced using Sentinel-1A images. Panels are arranged the same way as Fig. 2.5. The results of pair-wise NCC [(a, e) and (c, g)] are produced using the image pair from which the *best* spatial coverage of 11 NCC pairs was obtained (2017-01-15 and 2017-02-08). Results of stacked NCC [(b, f) and (d, h)] are produced by stacking 11 pair-wise NCC calculated from winter acquisitions between 2017-01-03 and 2018-03-23 (Table 2.1). Black voids in velocity fields are caused by removing outlier and unreliable estimates. The glacier outline is delineated in white.

of arrows are mostly covered by widely spreading voids, suggesting that it is difficult to obtain accountable velocity measurements over these areas.

Velocity fields obtained from Sentinel-1A imagery are shown in Fig. 2.6 for large and small templates (96×96 and 48×48 pixels at 5 m pixel spacing). Results of pair-wise NCCs shown in Fig. 2.6(a, c) and (e, g) are produced from the image pair 2017-01-15 and 2017-02-08, which represent again the *best* coverage (86% and 53% respectively) among the 11 results of pair-wise NCCs. The average of the 11 pair-wise velocity maps (Fig. 2.12 in the appendix) shows a comparable coverage for large templates (96 px) and a slightly better coverage for small templates (48 px). However, the additionally covered area shows many velocity artifacts. Hence, the single pair-wise NCC with the best coverage was chosen for further study. Compared to Fig. 2.5, the Sentinel-1A results show much lower spatial resolution and also less spatial coverage. Nevertheless, results obtained by NCC stacking show reduced noise compared to pair-wise NCCs, and velocity fields at specific locations [red arrows in Fig. 2.6(b, f)] are smoother for stacked NCCs than for pair-wise NCCs.

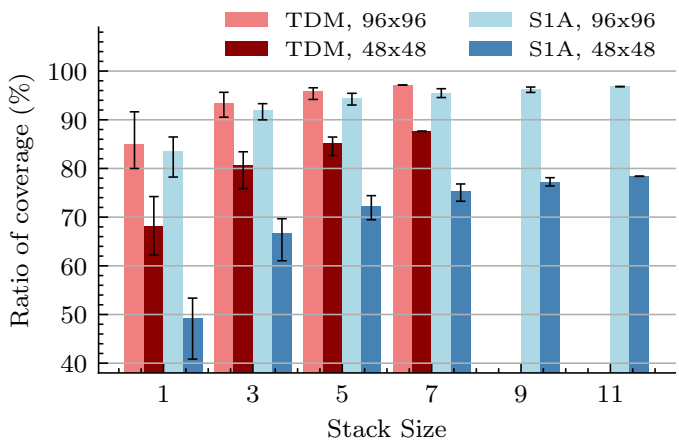

FIGURE 2.7: Change of spatial coverage when using different stack sizes (i.e. number of pair-wise NCC in the stack). A single pair-wise NCC corresponds to a stack size of one. In each group, all possible combinations of pair-wise NCC for stacking are evaluated. The bar height indicates the mean value of the group, and the black error bars indicate the maximum and minimum value in each group.

2.4.2 Spatial coverage of velocity fields

For the high elevations in the accumulation area of all glacier tributaries, velocity estimation from TanDEM-X failed using pair-wise NCCs [Fig. 2.5(a)]. In contrast, the uncovered region shrink to only the upper part of Ewigschneefaeld when applying NCC stacking [Fig. 2.5(b)]. When decreasing template sizes, the spatial coverage decreases for pair-wise and stacked NCC [Fig. 2.5(c, d)], but the pair-wise NCC shows a more serious decline of spatial coverage than the stacked NCC. Remarkably, the velocity map of stacked NCCs with small templates [Fig. 2.5(d, h)] reaches a level of coverage that is almost as good as the coverage of pair-wise NCCs and big templates [Fig. 2.5(a, e)]. Noteworthy, the small templates doubled the spatial resolution compared to the big ones.

For Sentinel-1A, when applying pair-wise NCCs and large templates [Fig. 2.6(a)], velocities can only be properly estimated in areas showing large crevasses including the ice fall, the glacier tongue, as well as the upper part of the Aletschfirn and the Jungfraufirn. However, with NCC stacking [Fig. 2.6(b)], the whole body of the Great Aletsch Glacier, except for the upper part of Ewigschneefaeld, is successfully tracked. For pair-wise NCCs and small templates [Fig. 2.6(c)], the successfully tracked area is further reduced comparing to Fig. 2.6(a). Only the ice fall can still be tracked due to well visible crevasses [Fig. 2.4(c)]. With stacked NCC the area of reliable estimates is significantly increased at the glacier tongue, the top of the Aletschfirn, and the Jungfraufirn [Fig. 2.6(d)].

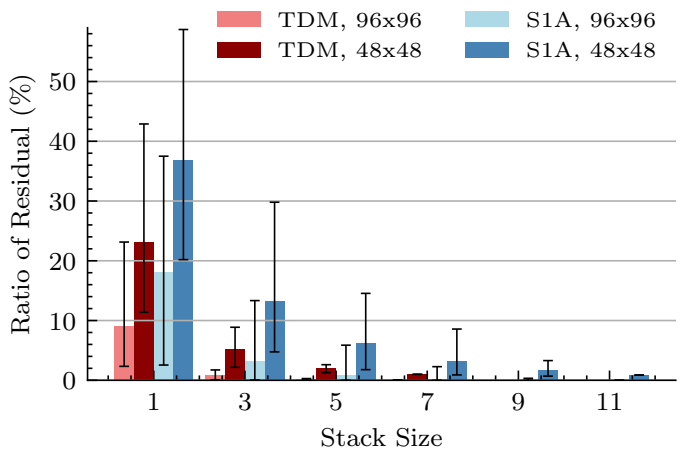

FIGURE 2.8: Same as Fig. 2.7 but for the change of residual ratios with difference stack sizes.

Fig. 2.7 shows the systematic analysis of the influence of the stack size on the spatial coverage of reliable velocity estimates. In general, the coverage ratio increases when increasing stack sizes for both template sizes and for both datasets. For pair-wise NCC applied on TanDEM-X data (light and dark red bars in Fig. 2.7), the average coverage ratio is 85% for templates of 96×96 pixels and 68% for templates of 48×48 pixels. They are increased to 97% and 88% with a stack size of seven. For Sentinel-1A (light and dark blue bars in Fig. 2.7), the average coverage ratio is increased from 83% to 96% for templates of 96×96 pixels, and from 49% to 77% for templates of 48×48 pixels.

For both datasets, the biggest relative coverage improvement are observed when employing stack size of three. At this point, the best coverage ratio of TanDEM-X results increased by 4% to 96% for large templates and by 11% to 83% for small templates. With Sentinel-1A imagery, the best coverage ratio increased by 7% to 93% for large templates, and by 17% to 70% for small templates. Further increasing the stack size keeps improving the coverage ratio but it gradually saturates at a certain level. For large templates, almost fully coverage for both datasets is obtained, whereas for small templates the coverage seems to saturate at about 89% for TanDEM-X and 79% for Sentinel-1A. This implies that for the given dataset the stacking NCC has mostly exploited the information content in the image series that contributes to the successful tracking. In the remaining uncovered areas, mostly located in the snow covered accumulation zone, no trackable features seem to be present. Higher coverage could be expected for image pairs where a certain level of coherence is maintained so that also speckle pattern can be tracked in the feature-free snow-covered areas.

Fig. 2.5 and 2.6 show that the coverage of successful velocity estimates using NCC stacking and small templates was very similar to the coverage of the single NCC pair estimates where, however, doubled template size was used. This is confirmed by the statistics shown in Fig. 2.7. Specifically, the difference of coverage ratio between NCC stacking with small templates and single pair-wise NCC with large templates is only 4% (88% versus 92%) for the TanDEM-X results and 9% (77% versus 86%) for the Sentinel-1A results.

2.4.3 Residual velocities of velocity fields

In the glacier free areas of Fig. 2.5 and Fig. 2.6, the pair-wise NCC results show stronger noise and more residuals than the results of NCC stacking. The systematic analysis of these velocity residuals in Fig. 2.8 shows that

the residual ratio, Eq. 2.9, decreases with the increase of stack size for both datasets and both template sizes.

Similar to the spatial coverage ratio, the biggest relative decrease of residual ratio is observed when stacking three pair-wise NCCs. For TanDEM-X and at stack size of three, the average residual ratio (red in Fig. 2.8) decreased from 9% to less than 1% with large templates and from 23% to 5% with small templates. With Sentinel-1A, it decreased from 18% to 3% with large templates, and from 37% to 13% with small templates (blue in Fig. 2.8). For large templates, the minimum residual ratios already reduce to almost zero with stack size of three for both TanDEM-X and Sentinel-1A. Very big ranges between the maximum and minimum residual ratios are observed for pair-wise NCCs. However, with NCC stacking, the ranges quickly narrow to much smaller extents for both datasets.

2.4.4 SNR gain

Fig. 2.9 illustrates the SNR gain of stacked NCC compared to the pair-wise NCC with the best coverage ratio for both datasets. For most areas, the SNR increases regardless of template sizes and sensor. For TanDEM-X data and both template sizes, large areas of strong SNR gain (in red) are found at the Aletschfirn and the Jungfraufirn. In these areas velocity fields are noisy and contain many gaps for the pair-wise results shown in Fig. 2.5 and 2.6 whereas the stacking results show increased spatial coverage and much smoother velocity orientations. Areas showing an SNR decrease (in blue) seem to be located in areas where the velocity maps do not show much improvement either because the area is well traceable already with a single pair or because the area is not traceable, neither with pair-wise nor with stacked NCC. For the well traceable areas (e.g. center of the Aletsch Glacier), the SNR dramatically decreases, because the pair-wise NCC with best coverage already represents the highest SNR in the NCC stack, and thus averaging the stack brings the SNR down.

To gain insight into the reason of SNR change, we chose two representative templates with an SNR increase and decrease, selected from the red and blue area within the white boxes in Fig. 2.9(a)(d). For these templates, the pair-wise and stacked NCC fields are presented in Fig. 2.10. In the upper row of the figure, the SNR decrease for both TanDEM-X and Sentinel-1A can be attributed to the drop of the averaged NCC peak, which is caused by the variation of peak strength within the NCC stack. Moreover, for Sentinel-1A, the bright diagonal pattern in the stacked NCC indicates that the major energy of pair-wise NCC are evenly distributed along the diagonal, and image

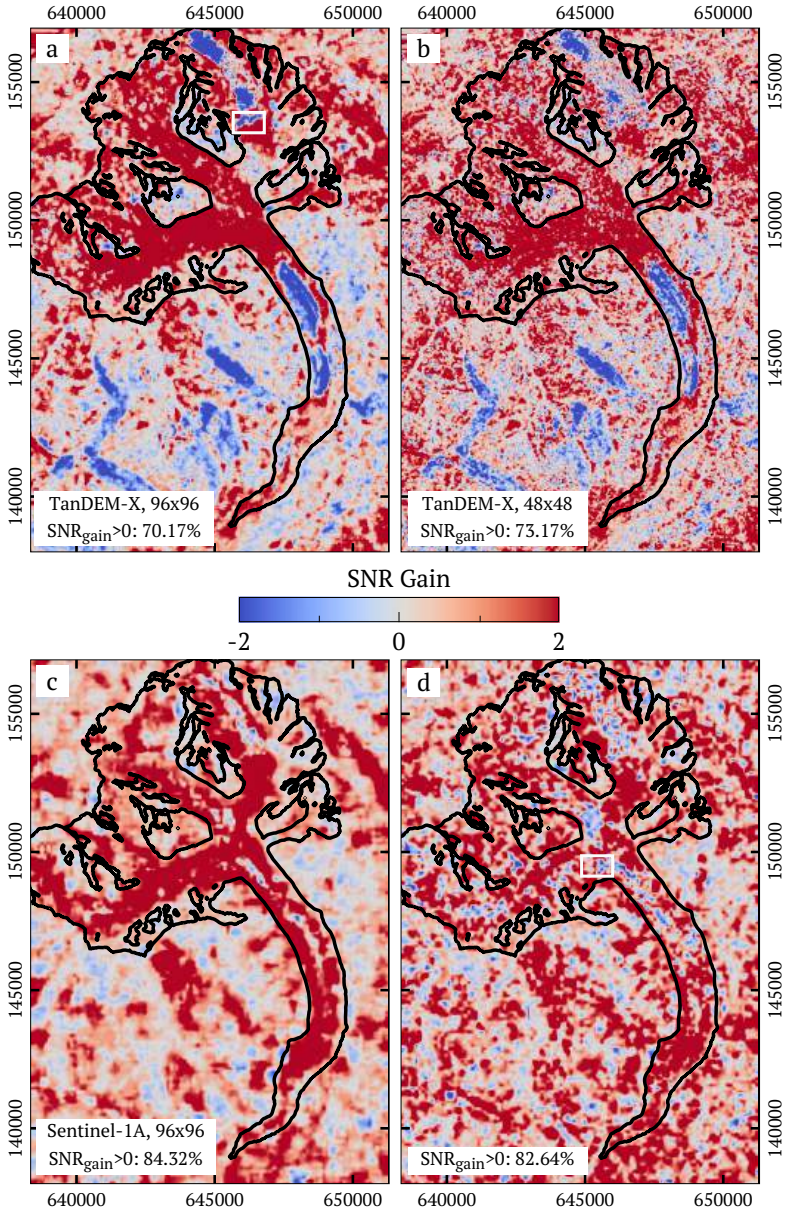

FIGURE 2.9: SNR gain of stacked compared to pair-wise NCC. (a) TanDEM-X with 96×96 templates; (b) TanDEM-X with 48×48 templates; (c) Sentinel-1A with 96×96 templates; and (d) Sentinel-1A with 48×48 templates.

features within templates very likely have periodic patterns. Although not shown, but comprehensible from lower row of Fig. 2.10, the SNR reduction in very difficult areas can also be caused by an apparent peak picked from the noise, which can show a larger SNR in pair-wise NCC compared to the SNR of the true peak identified in the stacked NCC. In this sense, the SNR improvement in the lower row of Fig. 2.10 for both TanDEM-X and Sentinel-1A shows the successful suppression of ambient noise with stacking.

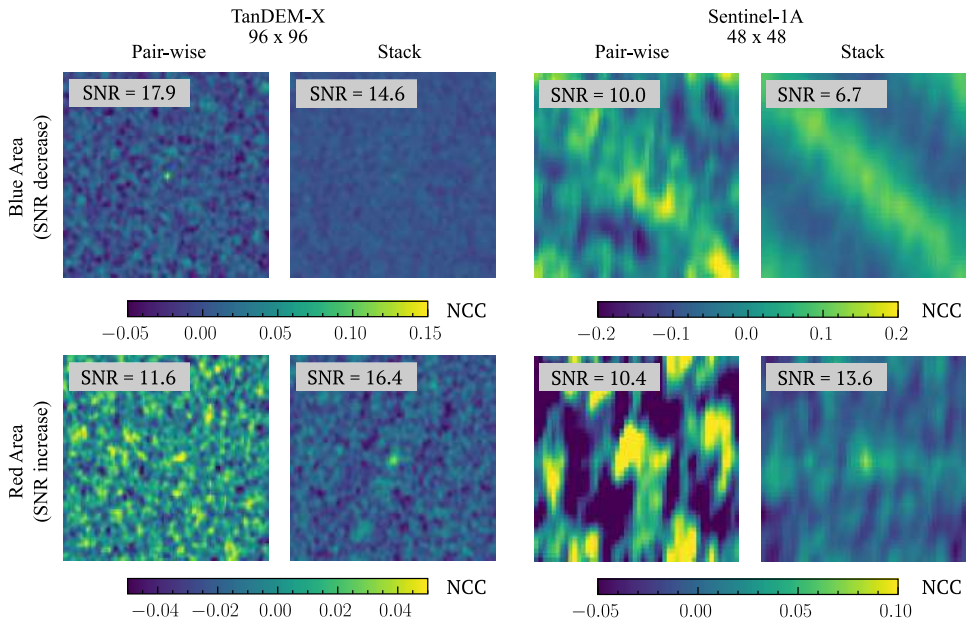

FIGURE 2.10: Example NCC fields extracted from blue and red areas within the black box of Fig. 2.9 (a)(d). The pair-wise NCC shown here represent the highest SNR in all pair-wise NCCs.

2.4.5 Validation against in-situ measurements

Velocities obtained by the different methods are validated by comparing velocity magnitudes and components along the easting (v_x) and northing (v_y) with the in-situ measurement. Results are presented in Fig. 2.11. Positive v_x indicates east pointing velocity vector, and positive v_y indicates south pointing velocity vector. For both TanDEM-X and Sentinel-1A, the RMSE value for stacked NCCs are in general smaller than that for pair-wise NCCs.

For TanDEM-X, most velocities estimated are somewhat smaller than the GPS data, in both $x-$ (easting) and $y-$ (northing) directions, shown by the right-wards biased point cloud in Fig. 2.11(a)-(d). Velocities estimated with

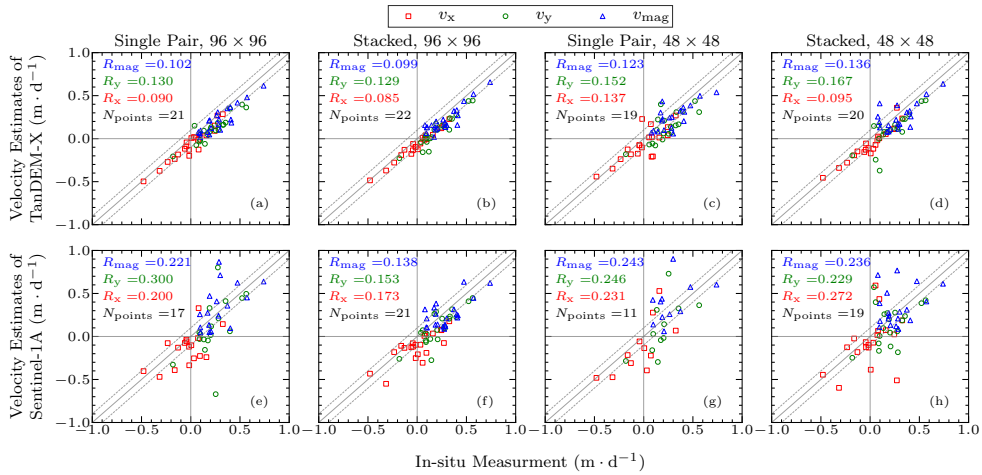

FIGURE 2.11: Validation of estimated velocities with respect to in-situ measurements for TanDEM-X (upper row) and for Sentinel-1A (lower row). The four columns shows result of a single pair-wise NCC and large templates (96 × 96 pixels) (a, e), stacked NCC and large templates (b, f), a single pair-wise NCC and small templates (48 × 48 pixels) (c, g), as well as stacked NCC and small templates (d, h). The diagonal solid grey line indicates a 1:1 match, and the two dashed grey lines indicate a mismatch of $\pm 0.1 \text{m} \cdot \text{d}^{-1}$. RMSE values for velocity magnitude and components are reported in each panel with corresponding color. Due to the incomplete velocity coverage, not all of the 22 measurement points are used for validation. The number of points (N_{points}) used for RMSE calculation are reported in associated panels.

Sentinel-1A imagery have higher uncertainty than that with TanDEM-X as shown by the more randomly distributed point cloud. However, more than half of the points are biased to the right side of the 1:1 line, showing that results of Sentinel-1A are also somewhat smaller than the in-situ measurement.

For both sensors, points of high velocity magnitude v_{mag} show less scatter from the 1:1 line than points of small velocity magnitude, indicating that fast moving surfaces are estimated with higher confidence. For TanDEM-X, RMSE values in northing (R_y) are in general higher than that in easting (R_x). In contrast, although R_y for Sentinel-1A are also higher than R_x with pair-wise NCCs, they turn to be smaller than R_x with stacked NCCs. The RMSE of Sentinel-1 results are in general higher than the RMSE of TanDEM-X results. This is also illustrated by the increased outliers contained in Fig. 2.11(e)–(h) comparing to Fig. 2.11(a)–(d). This is partly determined by the different image

resolution of the two sensors. Moreover, as the stacked NCC greatly extended the coverage of the velocity map (see Fig. 2.6), the number of points being used for validation are increased for the stacking results [Fig. 2.11(f, h)]. As show in Table 2.2, the added points are estimated with larger uncertainties comparing to the points that are kept in both methods. Hence the outliers in Sentinel-1 results are increased.

	Points added to the result of stacking	Points kept in both results
96×96 pixels	$R_{mag} = 0.196$ $R_y = 0.078$ $R_x = 0.278$	$R_{mag} = 0.120$ $R_y = 0.166$ $R_x = 0.138$
48×48 pixels	$R_{mag} = 0.312$ $R_y = 0.310$ $R_x = 0.350$	$R_{mag} = 0.159$ $R_y = 0.144$ $R_x = 0.196$

TABLE 2.2: RMSE values for different group of validation points in the results of Sentinel-1A

2.5 Discussion

2.5.1 Spatial Coverage

The spatial coverage of reliable offset estimates is a crucial parameter for the obtained offset field. As seen from the comparison between results of large and small templates in Fig. 2.5 and Fig. 2.6, it is clear that using large templates can effectively increase reliable estimates. This is because large templates can accommodate more image features than small ones, and thus can enhance the auto-correlation peak height and the SNR of the NCC. For offset tracking using SAR images, larger templates are required, compared to optical images, to compensate for the noise introduced by temporally uncorrelated (incoherent) SAR speckles.

However, using large templates inevitably depreciates the spatial resolution of the obtained offset field, and thus is not of advantage for studying small-scaled problems (e.g. small glaciers or landslides). In addition, large templates are also not suitable for studying non-homogeneous velocity fields such as

shear zones, where strong velocity gradient can cause non-uniform shifts of image contents within one template and thus can lead to dispersed peaks in the NCC.

When large templates are not applicable, our results suggest that NCC stacking can provide a powerful solution for robust tracking at high spatial resolution. As shown in Fig. 2.7, the spatial coverage of NCC stacking with templates of 48×48 pixels is almost equivalent to that of pair-wise NCC with templates of 96×96 pixels for both sensors. This suggests that NCC stacking permits to use smaller templates to get velocity fields of equivalent coverage as using big templates for pair-wise NCC.

2.5.2 Estimation accuracy

In this study, we firstly evaluated the accuracy of velocity estimation using residuals over static ground. Comparing to the validation against the in-situ measurement, this is an indirect method of evaluating the estimation accuracy, as it is difficult to precisely quantify to what degree the accuracy over glacier-free area actually represents that over glacier covered regions. However, many studies have used this method due to the lack of in-situ measurement [13]. In Fig. 2.8, the decrease of the residual ratio with increasing stack size shows that NCC stacking effectively reduced the uncertainty of velocity estimation. In addition, when using pair-wise NCC, the range between the maximum and minimum residual ratios is quite big, suggesting that different imaging conditions have a strong influence on the estimation accuracy. With stacking, the ranges quickly narrow down, showing that temporally stacking pair-wise NCCs can average out the change of image conditions and thus make it more accurate for velocity estimation than just a single pair-wise NCC.

Using the in-situ measurement, we also directly quantified the error of estimation at selected locations on the glacier. In general, estimated velocities show quite small RMSE values with respect to the in-situ measurement, but the satellite-based velocities are, in average, slightly below the in-situ data. Velocity time series indicate that the seasonal velocity increase starts around early May [40]. Considering that in-situ velocities were measured between 2019-04-30 and 2019-05-06, it is reasonable that the in-situ measurement appear slightly higher than the winter velocities obtained by offset tracking.

The confidence level of offset tracking depends on surface structures but also on the sensor resolution. We observed a higher confidence for fast moving regions where strong and well visible features are induced by fast glacier flow (e.g. big crevasses). Differences of confidence levels also occur between velocity components along the northing and easting, which is likely caused by

the different resolution along the azimuth (mostly along the northing) and the slant-range (mostly along the easting) direction of the used SAR images. At the Great Aletsch Glacier, the image scene is rotated by about 10° in average between northing-easting and azimuth-range due to orthorectification. The resolution (az × rg) is about 6.6 m × 2.2 m for TanDEM-X [41] and about 22 m × 4.7 m for Sentinel-1A [42]. Therefore, RMSE along the northing R_y is in general higher than RMSE along the easting R_x. Despite the lower resolution along the northing, we obtain comparable uncertainties for v_x and v_y.

2.5.3 Stack size

The results show that NCC stacking is able to sufficiently improve the tracking performance by increasing both spatial coverage and tracking accuracy. Although the performance keeps improving with the increased stack sizes, we found the biggest relative improvement of the performance for a stack size of three. This indicates that the most prominent relative performance gain is not necessarily achieved using many pair-wise NCCs for stacking. Therefore, when the size of NCC stack is limited by the amount of available data (i.e. too little images available), stacking over a limited number of pair-wise NCC can still provide considerable performance enhancement. A small NCC stack is also of advantage when high temporal resolution is desired. For instance, when studying temporal velocity variations (e.g. glacier surge, seasonality, or fast landslides), large stacks would either average out transient velocities or, in worst case, could lead to strong blurring of the NCC peak such that it cannot be tracked anymore. Using relatively small NCC stack can better compromise the need of improving spatial coverage without sacrificing too much temporal resolution.

For example, studying the seasonal fluctuations of a glacier's flow velocity requires high temporal resolution. With the increasingly available SAR images of short revisit time, it is possible to collect many images within a few months during which the seasonal velocity variations are limited. Hence, we can compose an image series within one season to make velocity variations between seasons traceable. Another example is to apply the stacking method to fast-flowing glaciers. Fast-flowing glaciers often behave complex dynamics with strong acceleration and deceleration NCC, and thus the NCC peaks are shifted in the NCC series. In this case, we can adjust the stacking size such that the velocity fluctuation within one stack is minimized.

2.5.4 TanDEM-X versus Sentinel-1A

The comparison of Fig. 2.5 and Fig. 2.6 shows that velocity fields obtained from TanDEM-X imagery have better spatial coverage than that of Sentinel-1A, for the same template size. We think that the coverage difference could originate from the different resolutions of the sensors. High resolution means that the image template could contain more distinguishable features than templates of the same pixel size but generated from low resolution data. A similar effect has been observed for optical imagery where low resolution sensors often underestimate the velocities observed by high resolution sensors [44]. For example, the two meter resolution of TanDEM-X can better resolve features like crevasses which are often only a few meters large. For Sentinel-1, it is more likely that multiple crevasses are contained in one resolution cell and thus add up to speckle patterns by interference of the radiation scattered at different locations of the crevasse. The transformation of features to speckle degrades the correlation process.

The high resolution of TanDEM-X obviously improved the accuracy of offset estimation. In Fig. 2.11, RMSE values for Sentinel-1A are in general twice as large as for TanDEM-X, which is comparable to the difference of resolutions of the two sensors. Moreover, different pixel sizes also affect the choice of time intervals between image pairs. In the experiment, due to the large pixel sizes, time intervals between Sentinel-1A image pairs were set to be $T = 24$ days, which are about twice as long as the repeating time of TanDEM-X. Taking long time interval ensures that image features shift far enough for detection. If the time interval were not sufficiently large, image features would not move out of one resolution cell for low resolution sensors such as Sentinel-1. In this case, the NCC would not be able to track the displacement. However, larger time intervals also increases temporal decorrelation between the image pair [40], and thus degrades the SNR of the NCC.

Although TanDEM-X has the advantage of having high resolution, the data coverage of TanDEM-X is not as applaudable as Sentinel-1. Sentinel-1 has very good global coverage and constant re-visiting time of 12 days (six days for Sentinel-1A/B together), making it especially preferred for time-series collection. We found that the Great Aletsch Glacier is almost at the limit for Sentinel-1A offset tracking with pair-wise NCC, but the stacked NCC shows promising results. The NCC stacking method could show further improvement when combining very short sequences of Sentinel-1A/B, e.g. average 6-day SAR image pairs of Sentinel-1A/B before calculating cross-correlation over significantly larger time intervals.

2.6 Conclusion

In this work, we presented a cross-correlation stacking method to improve offset tracking. Instead of estimating displacement offsets from a single pair-wise NCC, we firstly calculate a stack of multiple pair-wise NCCs from image time-series, and then average the NCC stack before tracking the NCC peak. With the assumption that the surface object moves with constant velocity during the image series acquisition, we can effectively suppress the noise floor and meanwhile maintain the NCC peak height.

The proposed stacking method is assessed by measuring the flow velocity of the Great Aletsch Glacier using both TanDEM-X and Sentinel-1A images. The result shows that the SNR of the NCC are greatly improved by stacking, leading to extended coverage of velocity field and more precise velocity estimates. Remarkably, the coverage of NCC stacking with small templates is equivalent to the coverage of pair-wise NCC with big templates. This makes NCC stacking the preferred method when the template size is limited by a study area with small glaciers. Assessing the performance improvement with respect to different stack sizes shows that prominent performance gain does not necessarily rely on a large number of pair-wise NCCs in the stack, which suggests that the stacking method can also be applied to small NCC stacks when only short image time-series is available or high temporal resolution is required.

In this work, we evaluated NCC stacking with equally spaced time-series data of a single sensor. However, as long as the spatial offset can be assumed to be the same for all NCC pairs, various data sources can by used as input, e.g. different spectral or polarization channels, data from different sensors (e.g. SAR and optical), data from the same period of the year or different image combinations of before and after seismic events. Resampling of the cross-correlation function before stacking could even allow for NCC stacking over image series with unequal time intervals. With the increasingly growing archives of remote sensing data, cross-correlation stacking provides a promising method to benefit from the acquired time series for robust offset tracking.

Appendix

Using the pair-wise NCC, we obtained series of velocity maps for the collected TanDEM-X and Sentinel-1A images. After applying the same thresholds with $v_{\max} = 1\ \mathrm{m} \cdot \mathrm{d}^{-1}$ and $\mathrm{SNR}_{\min} = 10$ dB, the velocity map series are averaged to produce the averaged velocity maps (Fig. 2.12). The spatial coverage ratio

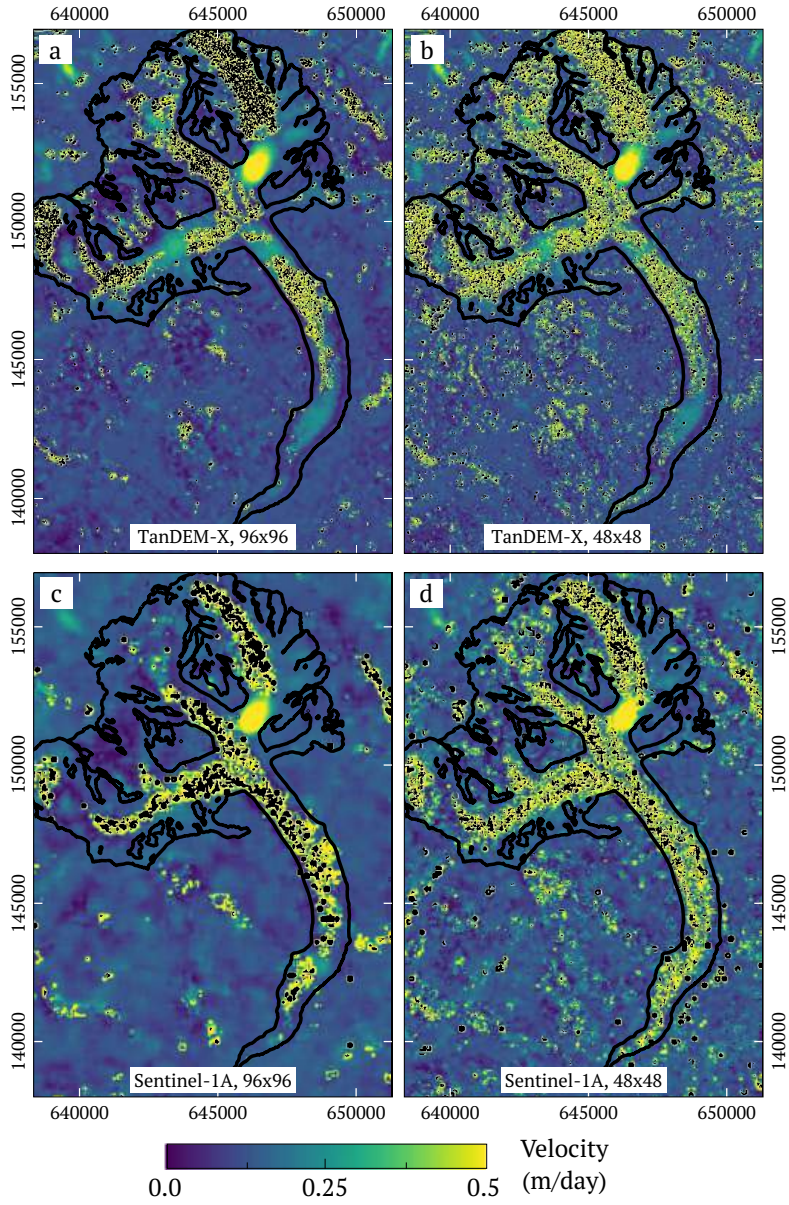

FIGURE 2.12: Averaged velocity magnitude maps produced using TanDEM-X [(a)(b)] and Sentinel-1A images [(c)(d)] with large (96×96 pixels) and small (48×48 pixels). Acquisitions are listed in Table 2.1). Black voids represent removed outlier and results with an SNR below 10 dB. The spatial coverage ratio of each panel are listed in Table 2.3. The glacier outline is delineated in black. Axes are labeled with Swiss Coordinates (CH1903/LV03) of unit meters.

of the averaged velocity maps are presented in Table 2.3. For TanDEM-X results, the coverage ratio of the averaged velocity maps [Fig. 2.12 (a)(b)] are lower than the best coverage as presented in Fig. 2.5. For Sentinel-1A, although the coverage ratio of the averaged velocity maps [Fig. 2.12 (c)(d)] are somewhat higher than the selected map with the most spatial coverage (Fig. 2.6), the additionally covered area in the averaged velocity maps reveals very noisy velocity data.

Template Size	96×96 pixels	48×48 pixels
TanDEM-X	88.77%	89.91%
Sentinel-1A	89.7%	91.8%

TABLE 2.3: Spatial coverage of the averaged velocity maps

Acknowledgment

The authors would like to thank the two anonymous reviewers for their valuable comments on this paper. The authors would like to thank A. Kääb for his valuable suggestion on including Sentinel-1A data in this work and O. Frey for fruitful discussion of the method and interpretation of the results. The TanDEM-X data used in this study was provided by the German Space Agency DLR via proposal XTI_GLAC6780.

References

1. Singleton, A., Li, Z., Hoey, T. & Muller, J.-P. Evaluating sub-pixel offset techniques as an alternative to D-InSAR for monitoring episodic landslide movements in vegetated terrain. *Remote Sensing of Environment* **147**, 133 (2014).
2. Shi, X., Zhang, L., Balz, T. & Liao, M. Landslide deformation monitoring using point-like target offset tracking with multi-mode high-resolution TerraSAR-X data. *ISPRS Journal of Photogrammetry and Remote Sensing* **105**, 128 (2015).
3. Stumpf, A., Malet, J.-P. & Delacourt, C. Correlation of satellite image time-series for the detection and monitoring of slow-moving landslides. *Remote Sensing of Environment* **189**, 40 (2017).

4. Fielding, E. J., Lundgren, P. R., Taymaz, T., Yolsal-Çevikbilen, S. & Owen, S. E. Fault-slip source models for the 2011 M 7.1 Van earthquake in Turkey from SAR interferometry, pixel offset tracking, GPS, and seismic waveform analysis. *Seismological Research Letters* **84**, 579 (2013).

5. Himematsu, Y. & Furuya, M. Fault source model for the 2016 Kumamoto earthquake sequence based on ALOS-2/PALSAR-2 pixel-offset data: evidence for dynamic slip partitioning. *Earth, Planets and Space* **68**, 169 (2016).

6. Strozzi, T., Luckman, A., Murray, T., Wegmuller, U. & Werner, C. L. Glacier motion estimation using SAR offset-tracking procedures. *IEEE Transactions on Geoscience and Remote Sensing* **40**, 2384 (2002).

7. Joughin, I. Ice-sheet velocity mapping: a combined interferometric and speckle-tracking approach. *Annals of Glaciology* **34**, 195 (2002).

8. Luckman, A., Quincey, D. & Bevan, S. The potential of satellite radar interferometry and feature tracking for monitoring flow rates of Himalayan glaciers. *Remote sensing of Environment* **111**, 172 (2007).

9. Scherler, D., Leprince, S. & Strecker, M. R. Glacier-surface velocities in alpine terrain from optical satellite imagery—Accuracy improvement and quality assessment. *Remote Sensing of Environment* **112**, 3806 (2008).

10. Dehecq, A., Gourmelen, N. & Trouvé, E. Deriving large-scale glacier velocities from a complete satellite archive: Application to the Pamir–Karakoram–Himalaya. *Remote Sensing of Environment* **162**, 55 (2015).

11. Schellenberger, T., Dunse, T., Kääb, A., Kohler, J. & Reijmer, C. Surface speed and frontal ablation of Kronebreen and Kongsbreen, NW Svalbard, from SAR offset tracking. *The Cryosphere* **9**, 2339 (2015).

12. Paul, F., Bolch, T., Kääb, A., Nagler, T., Nuth, C., Scharrer, K., Shepherd, A., Strozzi, T., Ticconi, F., Bhambri, R., *et al.* The glaciers climate change initiative: Methods for creating glacier area, elevation change and velocity products. *Remote Sensing of Environment* **162**, 408 (2015).

13. Round, V., Leinss, S., Huss, M., Haemmig, C. & Hajnsek, I. Surge dynamics and lake outbursts of Kyagar Glacier, Karakoram. *The Cryosphere* **11**, 723 (2017).

14. Li, T., Liu, Y., Li, T., Hui, F., Chen, Z. & Cheng, X. Antarctic surface ice velocity retrieval from MODIS-based mosaic of Antarctica (MOA). *Remote Sensing* **10**, 1045 (2018).

15. Merryman Boncori, J. P., Langer Andersen, M., Dall, J., Kusk, A., Kamstra, M., Bech Andersen, S., Bechor, N., Bevan, S., Bignami, C., Gourmelen, N., *et al.* Intercomparison and validation of SAR-based ice velocity measurement techniques within the Greenland Ice Sheet CCI Project. *Remote Sensing* **10**, 929 (2018).

16. Heid, T. & Kääb, A. Evaluation of existing image matching methods for deriving glacier surface displacements globally from optical satellite imagery. *Remote Sensing of Environment* **118**, 339 (2012).

17. Leprince, S., Barbot, S., Ayoub, F. & Avouac, J.-P. Automatic and precise orthorectification, coregistration, and subpixel correlation of satellite images, application to ground deformation measurements. *IEEE Transactions on Geoscience and Remote Sensing* **45**, 1529 (2007).

18. Debella-Gilo, M. & Kääb, A. Measurement of surface displacement and deformation of mass movements using least squares matching of repeat high resolution satellite and aerial images. *Remote sensing* **4**, 43 (2012).

19. Erten, E., Reigber, A., Hellwich, O. & Prats, P. Glacier velocity monitoring by maximum likelihood texture tracking. *IEEE Transactions on Geoscience and Remote Sensing* **47**, 394 (2009).

20. Scambos, T. A., Dutkiewicz, M. J., Wilson, J. C. & Bindschadler, R. A. Application of image cross-correlation to the measurement of glacier velocity using satellite image data. *Remote sensing of environment* **42**, 177 (1992).

21. Lange, R. d., Luckman, A. & Murray, T. Improvement of Satellite Radar Feature Tracking for Ice Velocity Derivation by Spatial Frequency Filtering. *IEEE Transactions on Geoscience and Remote Sensing* **45**. 2309 (2007).

22. Debella-Gilo, M. & Kääb, A. Locally adaptive template sizes for matching repeat images of Earth surface mass movements. *ISPRS journal of photogrammetry and remote sensing* **69**, 10 (2012).

23. Ahn, Y. & Howat, I. M. Efficient automated glacier surface velocity measurement from repeat images using multi-image/multichip and null exclusion feature tracking. *IEEE Transactions on Geoscience and Remote Sensing* **49**, 2838 (2011).

24. Keane, R. D. & Adrian, R. J. Theory of cross-correlation analysis of PIV images. *Applied scientific research* **49**, 191 (1992).

25. Meinhart, C. D., Wereley, S. T. & Santiago, J. G. A PIV algorithm for estimating time-averaged velocity fields. *J. Fluids Eng.* **122**, 285 (2000).

26. Bohs, L., Geiman, B. J., Nightingale, K., Choi, C., Friemel, B. & Trahey, G. *Ensemble tracking: a new method for 2D vector velocity measurement* in *1995 IEEE Ultrasonics Symposium. Proceedings. An International Symposium* **2** (1995), 1485.

27. Bohs, L. N., Geiman, B. J., Anderson, M. E., Breit, S. M. & Trahey, G. E. Ensemble tracking for 2D vector velocity measurement: experimental and initial clinical results. *IEEE transactions on ultrasonics, ferroelectrics, and frequency control* **45**, 912 (1998).

28. Altena, B. & Kääb, A. Ensemble matching of repeat satellite images applied to measure fast-changing ice flow, verified with mountain climber trajectories on Khumbu icefall, Mount Everest. *Journal of Glaciology*, 1 (2020).

29. Yague-Martinez, N., De Zan, F. & Prats-Iraola, P. Coregistration of interferometric stacks of Sentinel-1 TOPS data. *IEEE Geoscience and Remote Sensing Letters* **14**, 1002 (2017).

30. Ansari, H., De Zan, F. & Bamler, R. Sequential Estimator: Toward Efficient InSAR Time Series Analysis. *IEEE Transactions on Geoscience and Remote Sensing* **55**, 5637 (2017).

31. De Zan, F. Coherent shift estimation for stacks of SAR images. *IEEE Geoscience and Remote Sensing Letters* **8**, 1095 (2011).

32. De Zan, F. & Lopez-Dekker, P. SAR Image Stacking for the Exploitation of Long-Term Coherent Targets. *IEEE Geoscience and Remote Sensing Letters* **8**, 502 (2011).

33. Krieger, G., Moreira, A., Fiedler, H., Hajnsek, I., Werner, M., Younis, M. & Zink, M. TanDEM-X: A satellite formation for high-resolution SAR interferometry. *IEEE Transactions on Geoscience and Remote Sensing* **45**, 3317 (2007).

34. Torres, R., Snoeij, P., Geudtner, D., Bibby, D., Davidson, M., Attema, E., Potin, P., Rommen, B., Floury, N., Brown, M., *et al.* GMES Sentinel-1 mission. *Remote Sensing of Environment* **120**, 9 (2012).

35. Debella-Gilo, M. & Kääb, A. Sub-pixel precision image matching for measuring surface displacements on mass movements using normalized cross-correlation. *Remote Sensing of Environment* **115**, 130 (2011).

36. Paul, F. (, Azzoni, R. S., Fugazza, D., Le Bris, R., Nemec, J., Paul, F., Rabatel, A., Ramusovic, M., Rastner, P., Schaub, Y. & Schwaizer (nee Bippus), G. (*GLIMS Glacier Database. Boulder, CO.* 2019.

37. Prats, P., Scheiber, R., Reigber, A., Andres, C. & Horn, R. Estimation of the Surface Velocity Field of the Aletsch Glacier Using Multibaseline Airborne SAR Interferometry. *IEEE Transactions on Geoscience and Remote Sensing* **47**, 419 (2009).

38. Erten, E. Glacier Velocity Estimation by Means of a Polarimetric Similarity Measure. *IEEE Transactions on Geoscience and Remote Sensing* **51**, 3319 (2013).

39. Schubert, A., Faes, A., Kääb, A. & Meier, E. Glacier surface velocity estimation using repeat TerraSAR-X images: Wavelet- vs. correlation-based image matching. *ISPRS Journal of Photogrammetry and Remote Sensing* **82**. 49 (2013).

40. Leinss, S. & Bernhard, P. TanDEM-X: Deriving Height and Velocity Dynamics of Great Aletsch Glacier. *IEEE Journal of Selected Topics of Remote Sensing*. (2021).

41. Fritz, T., Eineder, M., Bräutigam, M., Schättler, B., Balzer, W., Buckreuß, S. & R., W. *TerraSAR-X - Ground Segment - Basic Product Specification Document, TX-GS-DD-3302, Issue 1.9* tech. rep. (DLR, 2013).

42. Bourbigot, M., Johnsen, H., Piantanida, R., Hajduch, G., Poullaouec, J. & Hajduch, G. *Sentinel-1 Product Definition* tech. rep. (ESA, 2016).

43. Werner, C., Wegmuller, U., Strozzi, T. & Wiesmann, A. *Precision estimation of local offsets between pairs of SAR SLCs and detected SAR images* in *International Geoscience and Remote Sensing Symposium* **7** (2005), 4803.

44. Millan, R., Mouginot, J., Rabatel, A., Jeong, S., Cusicanqui, D., Derkacheva, A. & Chekki, M. Mapping surface flow velocity of glaciers at regional scale using a multiple sensors approach. *Remote Sensing* **11**, 2498 (2019).

3

MAPPING SEASONAL SNOW MELTING IN KARAKORAM USING SAR AND TOPOGRAPHIC DATA

Shiyi Li[1], Lanqing Huang[2], Philipp Bernhard[3], and Irena Hajnsek[1,4]

1 Institute of Environmental Engineering, ETH Zurich, Switzerland

2 Center for Polar Observation and Modeling, University College London, London, United Kingdom

3 GAMMA Remote Sensing AG, Switzerland

4 Microwaves and Radar Institute, German Aerospace Center DLR, Germany

Article published in *The Cryosphere*
Citation: Li, S. *et al.* Mapping seasonal snow melting in Karakoram using SAR and topographic data. *The Cryosphere* **19**, 1621 (2025)

Key findings:

- Developed a novel SAR-topography framework for accurate wet snow mapping.
- Improved wet snow classification validated against Sentinel-2 snow cover maps.
- Generated large-scale snowmelt maps revealing temporal-spatial dynamics in Karakoram.

Author's contributions:

- Developed and implemented the presented methodology.
- Processed and analyzed the data over the study area.
- Interpreted the results and wrote the manuscript.

Co-author's contributions:

- All co-authors collectively contributed to the method development, result discussion, and revision of the manuscript.

Abstract

Mapping seasonal snow melting is crucial for assessing its impacts on water resources, natural hazards, and regional climate in Karakoram. However, complex terrain in the high-mountain region poses great challenges to remote-sensing-based wet snow mapping methods. In this study, we developed a novel framework that incorporates synthetic aperture radar (SAR) and topographic data for robust and accurate mapping of wet snow over Karakoram. Our method adopts the Gaussian mixture model (GMM) to adaptively determine a wet snow index (WSI), and a computed topographic snow index (TSI) considering the impact of terrain on wet snow distribution to improve the accuracy of mapping. We validated the mapping results against Sentinel-2 snow cover maps, which demonstrated significantly improved accuracy using the proposed method. Applied across three major water basins in Karakoram, our method generated large-scale wet snow maps and provided valuable insights into the temporal dynamics of regional snow melting extent and duration. This study offers a practical and robust method for snow melting monitoring over challenging terrains. It can contribute to a significant step forward in better managing water resources under climate change in vulnerable regions.

3.1 Introduction

Monitoring seasonal snow melting is of global importance within cryosphere studies, given the profound and far-reaching impacts of snow on climate, hydrology, and ecosystems. Snow cover plays a crucial role in modulating the Earth's energy balance by altering surface albedo, thereby exerting cooling effects on the terrestrial surface and influencing climate patterns at local and regional scales. Notably, in high-altitude areas, the accumulation of snow serves as a primary water source for downstream flows and governs the runoff dynamics in many mountainous basins [1].

The Karakoram region, characterized by its elevated topography and unique climatic conditions, is of exceptional significance in snow cover monitoring. Situated at the center of the Hindukush–Karakoram–Himalaya (HKH) mountain system, the Karakoram is renowned for hosting some of the world's highest peaks and harboring the largest alpine glacier system outside the polar regions [2]. Across its expansive landscape, snow and ice reserves are substantial, encompassing an area exceeding 20,000 km^2, with seasonal snow covering nearly 90% of this expanse [3–5].

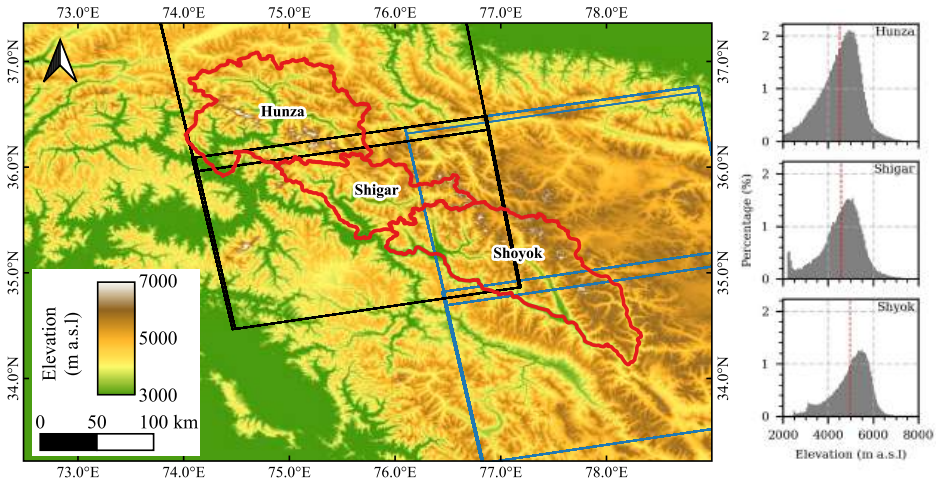

FIGURE 3.1: Geolocation of the Karakoram region overlaid on the COP-30 DEM. The study region includes three major water basins: Hunza, Shigar, and Shyok, which are delineated in red. Elevation histograms of the tree basins are shown in the right panel. Median elevations of basins are indicated with vertical red lines in histograms. Footprints of S1 images used in the study are shown with black and blue boxes (black: relative orbit 27; blue: relative orbit 129).

In the expansive and challenging terrain of the Karakoram region, ground-based observation methods struggle to effectively cover the vast and rugged terrain, and hence remote sensing techniques have become the primary approach for snow cover mapping. While spaceborne optical and multi-spectral sensors like MODIS, Landsat-7/8, and Sentinel-2 (S2) have been employed in numerous studies, their reliability is often compromised by cloud cover and illumination conditions [4, 6–10]. To overcome this limitation, synthetic aAperture radar (SAR) presents a valuable alternative for monitoring snow regardless of weather and daylight conditions.

The foundation of snow classification in SAR imagery was established based on the unique backscattering responses generated from the distinctive interactions of snow with SAR signals. For dry snow, radar signals can penetrate through the snowpack down to a specific depth depending on the signal wavelength and thus generate a strong backscattering signal at the snow-ground boundary [11, 12]. As the snowpack undergoes melting, its liquid water content increases in the wet snow pack and causes high dielectric losses, resulting in significant reductions in backscattering intensities [11, 13]. Based on the change in backscattering intensities, early wet snow detection methods were developed using the ratio of SAR backscattering coefficients [11, 14]. The ratio was derived from SAR images acquired during the snow melting season and reference images obtained under snow-free or dry snow conditions. An empirical threshold of -2 dB on C-band Sentinel-1 (S1) ratio images was proposed to classify snow, distinguishing wet from dry snow, and has proven to be effective [13].

Subsequent refinements were proposed to enhance the algorithm for robust application on various ground surface types. For example, sigmoid functions were introduced as a soft threshold to replace -2 dB, and it was shown to be effective in resolving the uncertainties arising from mixed pixels of wet snow and other constituents [15–17]. Various strategies for selecting bias-free reference images were devised, such as choosing a specific reference scene during winter [18], averaging multiple images over a defined period [19], or employing linear interpolation between images at the beginning and end of the melting period [20]. In practice, auxiliary data were usually combined to improve the accuracy of snow detection, such as digital elevation models (DEMs), land category maps, meteorological model, and snow cover maps derived from optical multi-spectral sensors [13, 14, 21–23]. Recent developments in machine learning also brought opportunities to further improve SAR snow mapping. Supervised classification algorithms, such as support vector machine and random forest, were applied to different SAR products

and have shown promising results [23, 24]. Deep learning algorithms were also exploited and have exhibited great potential in achieving more robust and accurate wet snow classification [25].

Despite the efforts to improve the method for robust SAR-based snow mapping, challenges remain in mountainous regions such as Karakoram, where complex topography may strongly distort SAR signals and thus lead to considerable uncertainties when applying a single-valued threshold for snow classification [3, 26–28]. Furthermore, large-scale application of wet snow mapping in Karakoram requires a method to be adaptively responsive to basin-specific variations, posing practical challenges to efficient method development [17]. ML techniques may offer versatile solutions, but their application in this region is limited by the availability of training data [23, 25].

To address these challenges, this study proposes a novel framework that integrates SAR and topographic data for versatile and robust wet snow mapping covering three major water basins of Karakoram. In the first step, we employed an unsupervised learning algorithm, namely the Gaussian mixture model (GMM), to adaptively determine the wet snow index (WSI). Secondly, a topographic snow index (TSI) was calculated to account for the influence of topography on snow distribution. We applied the proposed method to a time series of SAR imagery acquired by Sentinel-1 (S1) between 2017-2021 and generated regional-wide wet snow maps of high spatial and temporal resolution. The validation using S2 images showed considerable improvements compared to conventional threshold-based methods. Crucial snow dynamic variables including the wet snow extent (WSE) and snow melting duration (SMD) were derived from the snow maps, demonstrating the significance of closely monitoring wet snow in watershed management.

The paper is organized as follows. Section 2 introduces the study site and data. Section 3 explains the proposed method in detail. Section 4 presents the result of the study, including the validation and the snow dynamic variables. Section 5 discusses the method and its implications for snow mapping. Section 6 concludes the study and provides an outlook for the future development.

3.2 Study area and data

3.2.1 Study area

The Karakoram region, spanning extensively across parts of Pakistan, India, and China, is bordered by some of the highest mountain systems on Earth, including the Himalayas, the Pamir Mountains, and the Hindu Kush moun-

	Relative orbit	Orbit direction	Revisit interval	Start date	End date	Number of acquisitions
Hunza	27	Ascending	12 days	2017-02-05	2021-12-29	148
Shigar	27	Ascending	12 days	2017-02-05	2021-12-29	148
Shyok	129	Ascending	12 days	2017-03-20	2021-12-24	146

TABLE 3.1: Information on Sentinel-1 (S1) images used for the generation of wet snow maps. The ascending pass crossed over the study region in the late afternoon (around 18:00 local time).

tain ranges (Fig. 3.1). The study area encompasses the majority of Karakoram, covering an expansive geographical domain of approximately 450,000 km^2. This region extends from approximately 35°N to 38°N latitude and 76°E to 78°E longitude, characterized by a wide range of altitudes from around 2,000 m a.s.l (above sea level) in the valleys to well over 8,000 m a.s.l at the highest summits. The extreme topographic variation gives rise to rugged terrain, including steep valleys and towering mountain peaks.

Karakoram is situated upstream of both the Upper Indus Basin (UIB) and the Tarim River Basin. It covers three significant watersheds: Hunza, Shigar, and Shyok, as shown in Fig. 3.1. These basins serve as the upstream sources of the UIB and contributes 65-85% of annual flows to the Indus River with the melting water from snow and glaciers, sustaining the livelihoods of millions of residents residing within these basins [6, 29, 30]. The hydrological importance of Karakoram emphasizes the important role of mapping snow melting in the region.

3.2.2 Data

3.2.2.1 Sentinel-1 SAR imagery

The SAR imagery used in our research was acquired by the spaceborne C-band S1 SAR sensor. The S1 SAR satellite provides high geolocation accuracy and a short orbit repeat cycle of 12 days, facilitating precise and frequent monitoring of snow melting [13].

In this study, we use single-look-complex (SLC) data from S1 acquired in interferometric wide (IW) swath mode. These data cover scenes with a swath width of 250 km at a spatial resolution of $\sim 5 \times 20$ m in the range and azimuth direction. Both VV and VH dual-polarization data were employed for the following analysis. The details of the S1 images utilized in this study, including orbit numbers and acquisition dates, are provided in Table 3.1.

3.2.2.2 Copernicus digital elevation model

Digital elevation models (DEM) provide essential topographic information crucial for both SAR image pre-processing and snow distribution mapping, particularly in the rugged landscapes of mountainous regions. In this study, we employed the Copernicus Global 1-arcsec (COP-30) DEM, recently released by the European Space Agency (ESA) in 2020, to facilitate the SAR image processing and snow mapping. The COP-30 DEM product was derived from the TanDEM-X SAR data acquired between 2010 and 2015, providing global coverage at a resolution of 30 meters and a vertical root mean square error as low as 1.68 m [31, 32].

The COP-30 DEM data covering the study regions were downloaded through the Copernicus Space Component Data Access PANDA Catalogue [33], as shown in the base map in Fig. 3.1. The DEM products are referenced in geographic coordinates using the World Geodetic System 1984 (WGS84). The vertical heights are referenced to the EGM2008 geoid model.

3.2.2.3 Sentinel-2 Level-2A imagery

To validate the snow maps generated using the proposed method, we also derived snow cover maps on selected dates using multi-spectral S2 images. The S2 sensor operates in a sun-synchronous orbit with a revisit time of 5 days [34]. Equipped with 13 spectral bands ranging from visible and near-infrared to shortwave infrared, S2 images offer valuable spectral information for land cover characterization and have been widely used in snow cover mapping. In this study, we used the S2 Level-2A (L2A) products to generate snow cover maps for validation purposes. The L2A product is orthorectified bottom-of-atmosphere surface reflectance data, that are derived through the atmospheric correction of the Level-1C products using the Sen2Cor method [35]. Practically useful supplementary data are also included in the L2A product, including cloud and snow confidence maps and a scene classification map that identifies elements like clouds, cloud shadows, and snow. The spatial resolution of images under different spectral bands varies from 10 to 60 meters.

We selected S2 L2A images taken during the summer months with minimal cloud cover as potential candidates. From these, only images that could be matched with an S1 SAR image within a window of ± 3 days were used to generate reference snow maps with the Let-it-snow (LIS) algorithm (Section 3.3.5; [36]). The LIS algorithm employed RGB spectral bands B2 (blue), B3 (green), and B4 (red), as well as infrared bands B8 (NIR) and B11 (SWIR), for snow-cloud-ice classification. We accessed the S2 data through the Copernicus Open Access Hub.

3.3 Methodology

This section describes the proposed method for integrating SAR and topographic data to map melting wet snow. The key steps of the method are summarized in Fig. 3.2.

The raw S1 SLC data were first pre-processed to generate backscatter images. Same-orbit SLC time series were co-registered to a common reference scene to accurately align the geolocation of pixels. Then we multi-looked each SLC with a window size of 12×1 (rg $\times$ az) to obtain backscattering intensity images with squared pixel spacing of approximately 14×14 m. The intensity images were further converted to γ^0 images with terrain-based radiometric correction [37]. All pre-processing steps were conducted using the GAMMA software [38].

3.3.1 SAR backscattering ratio

With the pre-processed γ^0 images, we derived the composite backscatter ratio (R_c) following the method proposed by [13]. The R_c metric combines the backscatter ratios from both the VV and VH channels to comprehensively assess surface condition changes associated with snow melting. This approach incorporates a weighting factor W, which is determined by the local incidence angle (LIA, θ), to account for variations in backscatter due to differing incidence angles. This adjustment enables more robust snowmelt detection across varying terrain geometries.

To compute R_c, we first calculated the SAR backscatter ratio R_i for each polarization $i \in \mathrm{vv}, \mathrm{vh}$ using the following equation:

$$R_i = \gamma_i^0 / \gamma_{i,ref}^0 \tag{3.1}$$

where $\gamma_{i,ref}^0$ represents a reference image constructed using the average of multiyear winter images. Note that this differs from other alpine regions, such as the Alps, where summer months are often used as the reference due

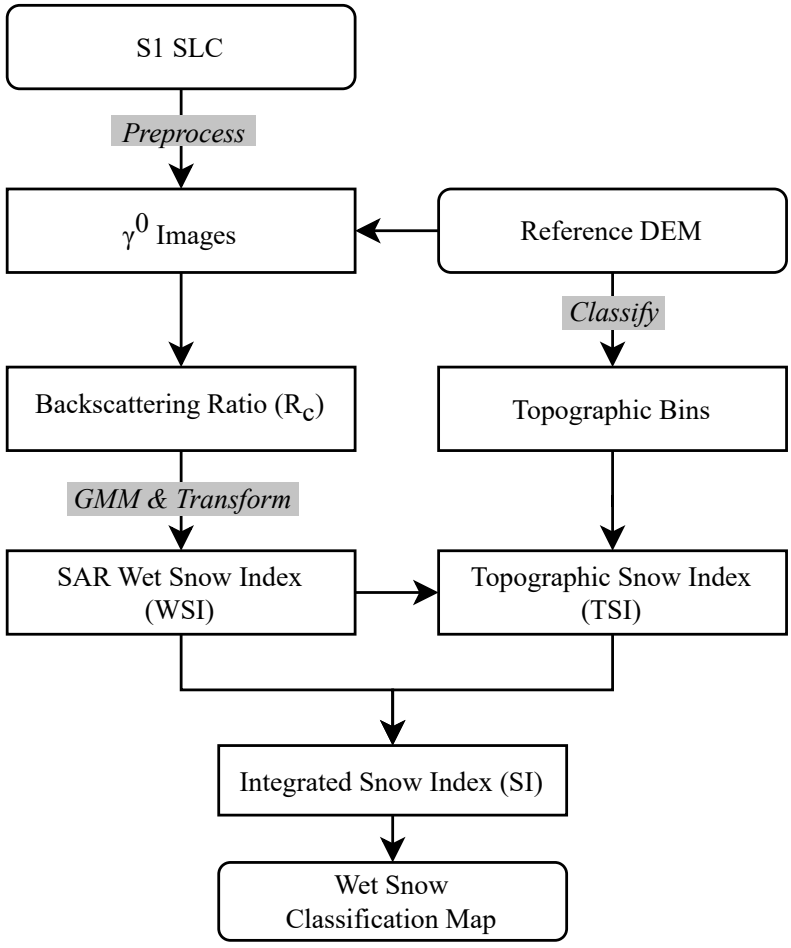

FIGURE 3.2: The developed method for mapping snow melting. Critical processing steps are shown in the gray box. The COP-30 DEM was used as the reference DEM. GMM stands for the Gaussian mixture model.

to snow-free conditions. In Karakoram, due to the all-year-long snow cover at the higher elevations, we used winter images as a reference to leverage the dry snow conditions in winter for highlighting the contrast in backscattering intensity between summer wet snow (lower intensity due to water absorption) and winter dry snow

With R_i for each polarization, the composite ratio R_c was calculated as a weighted sum of R_{vv} and R_{vh}

$$R_c = WR_{vv} + (1 - W)R_{vh} \tag{3.2}$$

where the weighting factor W is defined based on the LIA as:

$$W = \begin{cases} 0 & (\theta < \theta_1) \\ 0.5(1 + \frac{\theta - \theta_1}{\theta_2 - \theta_1}) & (\theta_1 \leq \theta \leq \theta_2) \\ 0.5 & (\theta > \theta_2) \end{cases} \tag{3.3}$$

with $\theta_1 = 20^\circ$ and $\theta_2 = 45^\circ$.

3.3.2 Wet snow index

While R_c alone effectively indicates surface condition changes, it can be sensitive to local variations and does not inherently incorporate adaptive boundaries for wet snow classification. Therefore, instead of directly applying a threshold to R_c for wet snow classification, we propose using a GMM to convert R_c into a Wet snow index (WSI) to have a probabilistic measure that better captures the varying conditions of wet snow across different terrains. By leveraging the density distribution of R_c values, the WSI enables a dynamic scaling of the classification based on the underlying distribution of R_c values.

The GMM is an unsupervised probabilistic model for clustering and density estimation. We configured the GMM to identify two clusters corresponding to the wet snow pixels and the no-snow (or dry snow) pixels as

$$P(R_c) = \sum_{i=1}^{2} \pi_i \cdot N(R_c | \mu_i, \sigma_i), \tag{3.4}$$

where $P(\cdot)$ the probability density function (PDF) of R_c, π_i the i-th Gaussian component's mixing coefficient for wet snow ($i = 1$) and no-snow (or dry snow) ($i = 2$) clusters, and $N(R_c | \mu_i, \sigma_i)$ the Gaussian distribution with mean μ_i and standard deviation σ_i. We used the full covariance structure in the GMM, i.e. each component has its own general covariance matrix, after testing different types of covariance structures.

To train the GMM and determine its parameters (π_i, μ_i, and σ_i), we randomly sampled 10^6 unlabeled pixels from the summer R_c images of each basin and employed the expectation-maximization (EM) algorithm to fit the model for each basin with the sampled pixels [39]. During the training, the maximum number of EM iterations were set to 100, and the convergence threshold was set to 10^{-3}. With the estimated GMM parameters, the WSI can be determined using a modified logistic function:

$$\mathrm{WSI} = \frac{L}{1 + e^{k(x - x_0)}} \tag{3.5}$$

with

$$\begin{cases} k = \dfrac{|\mu_1 - \mu_2|}{\sigma_1 + \sigma_2} \\ x_0 = \dfrac{\mu_1 + \mu_2}{2} \end{cases}$$

where k is the slope factor, x_0 the logistic curve's midpoint and L the carrying capacity representing the supremum of the function. Here the carry capacity L was set to 10 to amplify the differences between pixels of different R_c values.

In the WSI logistic function, the slope factor k is determined by the separation between the two clusters, providing a flexible and adaptive control over the sensitivity of WSI to the difference between snow conditions. In the case when the two clusters are perfectly distinct from each other (i.e. $|\mu_1 - \mu_2| \gg \sigma_1 + \sigma_2$), the WSI is transformed into a step function and thus effectively acts as a single-value hard threshold at x_0. Therefore, Nagler's method can be taken as a special case under this assumption with $x_0 = -2$ dB. Contrarily, the mixed clusters (i.e. $|\mu_1 - \mu_2| \ll \sigma_1 + \sigma_2$) would lead to progressively flattened WSI and soft segmentation boundaries. A similar form of logistic function was proposed by Rondeau-Genesse, Trudel & Leconte [17], which was determined with empirical parameters and used as soft thresholds to replace the hard threshold of -2 dB on R_c. In our approach, the GMM allows for an adaptive choice of the parameter k based on the distribution density of R_c, thereby enabling flexible and robust applications at large scale.

3.3.3 Topographic snow index

Given the strong impact of terrain properties on snow distribution, we introduce the TSI as a component of the proposed method to account for the terrain influence on snow presence.

Terrain properties, including the elevation, slope, and aspect, collectively influence the spatial and temporal distribution of snow. Compared to lower

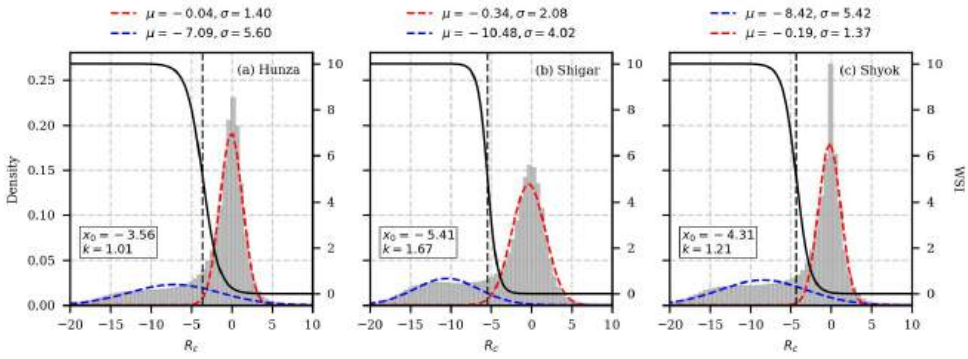

FIGURE 3.3: Parameters of the GMM and WSI used for (a) Hunza, (b) Shigar and (c) Shyok. The gray shaded histogram shows the density of R_c of the sampled points. Dashed red and blue curve represent the PDF (scaled on the left y axis) of the two clusters in the GMM. Solid black lines (scaled on the right y axis) show the WSI. The vertical dashed black line marks the center of WSI curves (where $R_c = x_0$). The mean (μ) and standard deviation (σ) of the GMM are reported above the panel.

altitudes, regions of higher elevation experience lower temperatures and are conducive to more snow accumulation. The steepness of slopes and the orientation of aspects, on the other hand, impact the snow distribution through the solar illumination and wind exposure. To take these factors into account, we calculated the TSI in two steps. First, we derived the discrete topographic bin maps using the COP-30 DEM by partitioning the terrain with its elevation, slope and aspect. The partition was based on slope below or above 20°, elevation in every 100m, and aspect in every 15°. The topographic bin map can effectively capture the localized terrain attributes that influence the occurrence of snow. The median WSI value within each topographic bin was then calculated to obtain the TSI, so that the regional propensity of wet snow occurrence under the specific topographic conditions could be quantified.

An example TSI distribution for Hunza at different elevation, slope, and aspect are presented in Fig. 3.4. In this example, TSI values show different patterns across seasons and topographic conditions. In spring, strong TSI signals are found around 4000 m.a.s.l for east-facing slopes (aspect $0 \sim 190°$) over flat terrain (slope $\theta < 20°$), while no obvious TSI signal is observed for steep terrain (slope $\theta > 20°$). This can be explained by the limited snowmelt during the spring season of Karakoram. In summer, strong TSI signals are ob-

served above ∼5000 m.a.s.l. for all slope and aspect conditions, indicating the presence of wet snow. However, steep slopes showed an unevenly distributed TSI across slope aspects, which can be attributed to the shadowing effect of the surrounding terrain. In autumn, TSI signals generally decrease due to the absence of wet snow, and the snow line retreats to higher elevations. This example indicates that the dynamic influence of topography on snowmelt can be effectively captured by the designed TSI signal.

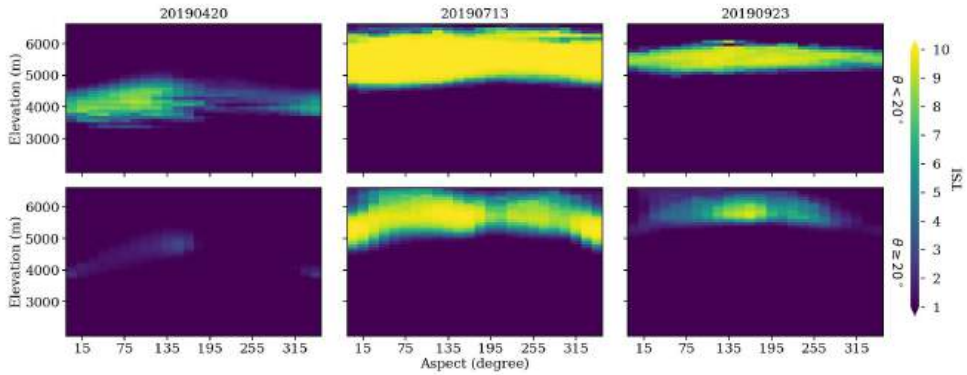

FIGURE 3.4: TSI values at different elevation (y axis), aspect (x axis) and slope classes (top row: flat slope with $\theta < 20°$, bottom row: step slope with $\theta < 20°$) for Hunza basin. Three observation dates in spring (left column), summer (middle column) and late autumn (right column) are displayed. Aspects of 0, 90, 180 and 270 degrees align with the north, east, south,and west direction, respectively.

3.3.4 Integrated snow index

As illustrated in Fig. 3.2, the final step generated an integrated snow index (SI) map through pixel-wise multiplication of WSI and TSI. This multiplication scales the WSI by incorporating terrain characteristics, thereby linking the observed SAR backscattering ratio directly to terrain properties.

In order to classify the integrated SI into binary snow maps, it is crucial to apply an adaptive threshold that accounts for the variation in topographic features across different basins. The variation in SAR backscatter response within a basin is inherently handled by the GMM when deriving the WSI. In contrast, the TSI is time-varying and basin-specific, requiring an optimal coefficient to condition the SI for classification. This coefficient should moderate the influence of TSI in the SI formulation and compensate for the concentration of TSI values within a limited range so that the impact

of TSI can be normalized to align with the traditional -2 dB reference. To determine this coefficient, we performed a sensitivity analysis, evaluating F1 score, precision, and recall across different values using the S2 validation snow map. The results (Fig. 3.12) demonstrate that Hunza and Shyok exhibit similar responses, with optimal coefficients close to 3.5, while Shigar reaches its optimum at approximately 2.5. However, to avoid overfitting to specific basins or validation dates, we selected 3.5 as an overall coefficient to balance classification performance across all basins. This coefficient also reflects a moderate threshold applied to the TSI to determine the overall SI threshold for each basin.

The threshold was then calculated using the following equation:

$$\text{SI Threshold} = 3.5 \times \text{WSI}|_{R_c=-2} \tag{3.6}$$

where $\text{WSI}|_{R_c=-2}$ represents the WSI at a backscatter ratio of $R_c = -2 \ \ dB$ for each basin. This value is basin-specific, allowing the threshold to adapt based on each basin's distinct characteristics. Together, these conditions form an integrated, basin-adaptive thresholding mechanism, combining SAR backscatter and topographic information into a single index to determine the SI threshold.

Note that while the SI threshold is basin-specific, it is time-independent. The WSI is derived from a GMM trained on samples collected from multiple summer scenes over several years, ensuring that it represents an aggregated measure for each basin and is not tied to individual scenes or seasons. This design ensures robustness to seasonal variations in liquid water content and enables consistent application across different validation dates.

3.3.5 Sentinel-2 snow cover maps

The proposed method was validated using S2 snow cover maps generated following the LIS algorithm proposed by [36]. Before running the LIS algorithm, the input S2 multi-spectral bands were resampled to a pixel size of 20m $\times$ 20m to match the resolution of different bands. The COP-30 DEM was also resampled to the same pixel size as the S2 images.

The LIS algorithm started by generating provisional snow masks by applying thresholds on the normalized difference snow index (NDSI) and the red band reflectance (ρ_{red}) with the condition:

$$(NDSI > n_i) \ \ AND \ \ (\rho_{\text{red}} > r_i) \tag{3.7}$$

where $n_i = 0.4$ and $r_i = 0.2$ [36]. This step was designed to identify snow-covered areas while excluding non-snow surfaces such as vegetation and

bare ground. However, this approach could sometimes exclude snow-covered pixels due to errors in cloud masking. To correct the errors, a refinement step was introduced to reassign dark cloud pixels that were initially misclassified. Following Gascoin et al. (2019), dark clouds were identified by applying a threshold of 0.3 on the bilinearly downsampled red band, which reduced the resolution of the red band from 20m to 240m by a factor of 12. This process helped to exclude cloud shadows and high-altitude cirrus clouds from the snow classification. Afterwards, the provisional snow masks were further refined using the basin snow line calculated from the COP-30 DEM. We calculated the total snow cover fraction (SCF) within every 100m elevation band using the provisional snow mask, and defined the snow line using the lowest elevation band where the SCF exceeded 30%. For pixels identified as dark clouds above the determined snowline, the conditions used in Equation (3.7) were reapplied with adjusted thresholds to account for the unique conditions at high altitudes. Specifically, the relaxed thresholds of $n_i = 0.15$ and $r_i = 0.04$ were used to classify snow pixels, and dark cloud pixels with $\rho_{\text{red}} > 0.1$ were reassigned as cloud, while other pixels were categorized as "no snow." These adjusted thresholds help to differentiate snow from dark clouds in challenging high-altitude environments, ensuring a more accurate classification. Following the adjustment of the snow mask, we extended the LIS algorithm by further applying a threshold on the NIR band with $\rho_{\text{NIR}} > 0.4$ to classify glacier ice and water bodies from snow [40].

3.4 Results

3.4.1 Validation of snow classification maps

The validation of snow classification results was carried out for three basins on specifically suited summer dates (Table 3.2). These dates were chosen based on conditions of minimal cloud cover and the shortest possible intervals between acquisitions of S1 and S2 images. As S2 snow cover maps classify snow (both dry and wet) rather than only wet snow, we have chosen only the summer dates as listed in Table 3.2 to ensure that the S2 snow cover maps were mostly covered by wet snow. For Hunza and Shyok, two S2 images with an acquisition interval of 2 days were combined to achieve a complete coverage of the basin, whereas same-day acquisitions of S1 and S2 were found for Shigar in 2019.

In the three basins, adaptive SI thresholds were used to generate the snow classification maps. The threshold values for each basin are also reported in Table 3.2. These thresholds provided basin-adaptive and time-independent

	S1 date	S2 dates	SI threshold
Hunza	2020-07-31	2020-07-29 2020-07-31	14.62
Shigar	2019-08-06	2019-08-06	5.44
Shyok	2019-07-08	2019-07-07 2019-07-09	12.33

TABLE 3.2: Sentinel-1 (S1) and Sentinel-2 (S2) data as well as SI thresholds used for the validation. Different acquisition dates and adaptive SI thresholds were used for basins.

classification boundaries to distinguish wet snow and dry snow or snow-free pixels.

Figure 3.5 shows maps of R_c and SI, as well as the SI snow map and the S2 snow map over the three basins. Compared to the R_c map, the SI map shows much clearer boundary that separates wet snow pixels from no-snow or dry snow pixels. Over glacier surfaces and valley regions (shown with the zoomed-in insets), R_c falls in the value range of -4 to 0 dB, making it sensitive to the choice of threshold values. The R_c map over these regions presents noisy patterns, likely due to the complex scattering mechanisms on glacier surfaces. Over glacier surface, especially in the ablation zone, radar backscatter responses are highly variable due to refreezing, supraglacial features (e.g., crevasses, sun cups, debris cover) and the presence of wet debris or bare ice [41]. These features contribute to significant spatial variability in backscatter within a single pixel, making it challenging to distinguish dry snow, wet snow, and ice with R_c alone. Additionally, glacier movement between winter and summer scenes introduces further variability, compounding the uncertainty in detection.

In Fig. 3.5(b), it is observed that the variation of SI values is within different ranges across the three basins. This is due to the different density distributions of R_c, WSI, TSI and SI in the three basins as shown in Fig. 3.7, underscoring the necessity of applying dynamically adaptive thresholds for each basin to generate classification results.

The snow maps in Fig. 3.5(c) and (d) offer a visual comparison between the snow maps produced by the proposed method and the S2 LIS algorithm.

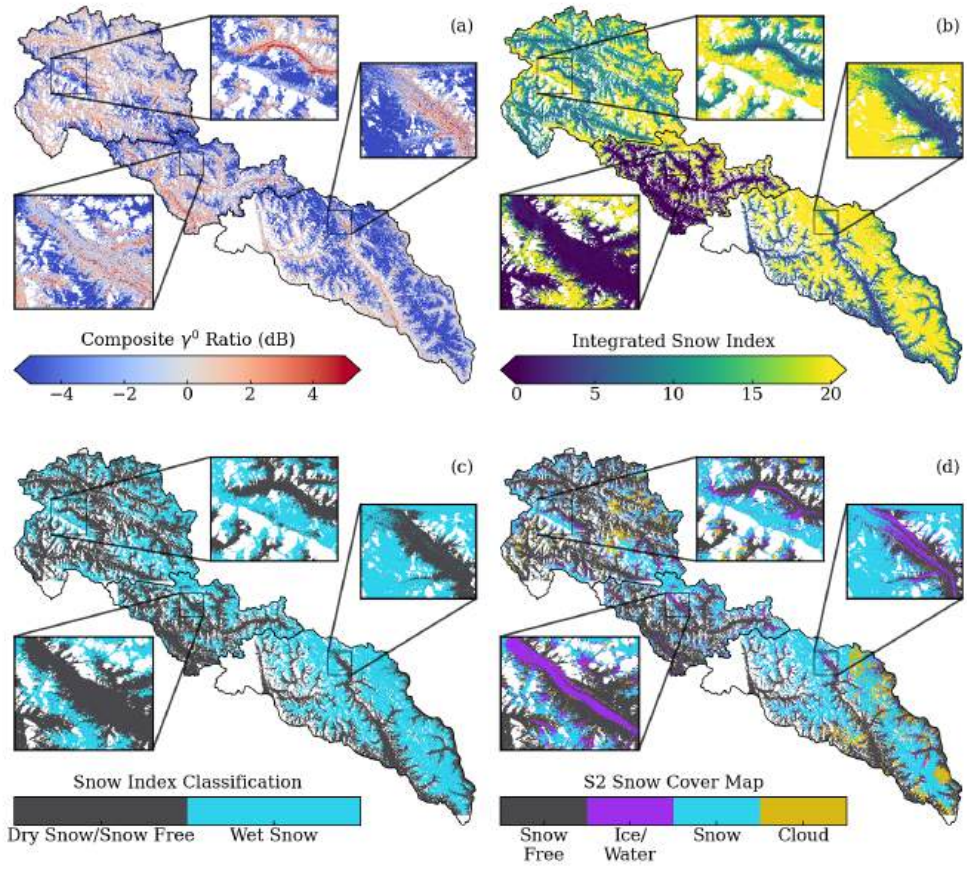

FIGURE 3.5: (a) R_c, (b) integrated SI, (c) SI classification map, and (d) S2 snow cover map (as a reference) for all three basins (Hunza, Shigar, and Shyok). The S2 snow map was generated using the Let-it-snow (LIT) algorithm, as described in Section 3.3.5. Zoomed insets provide a closer view of selected locations in each basin, highlighting performance differences on glacier surfaces.

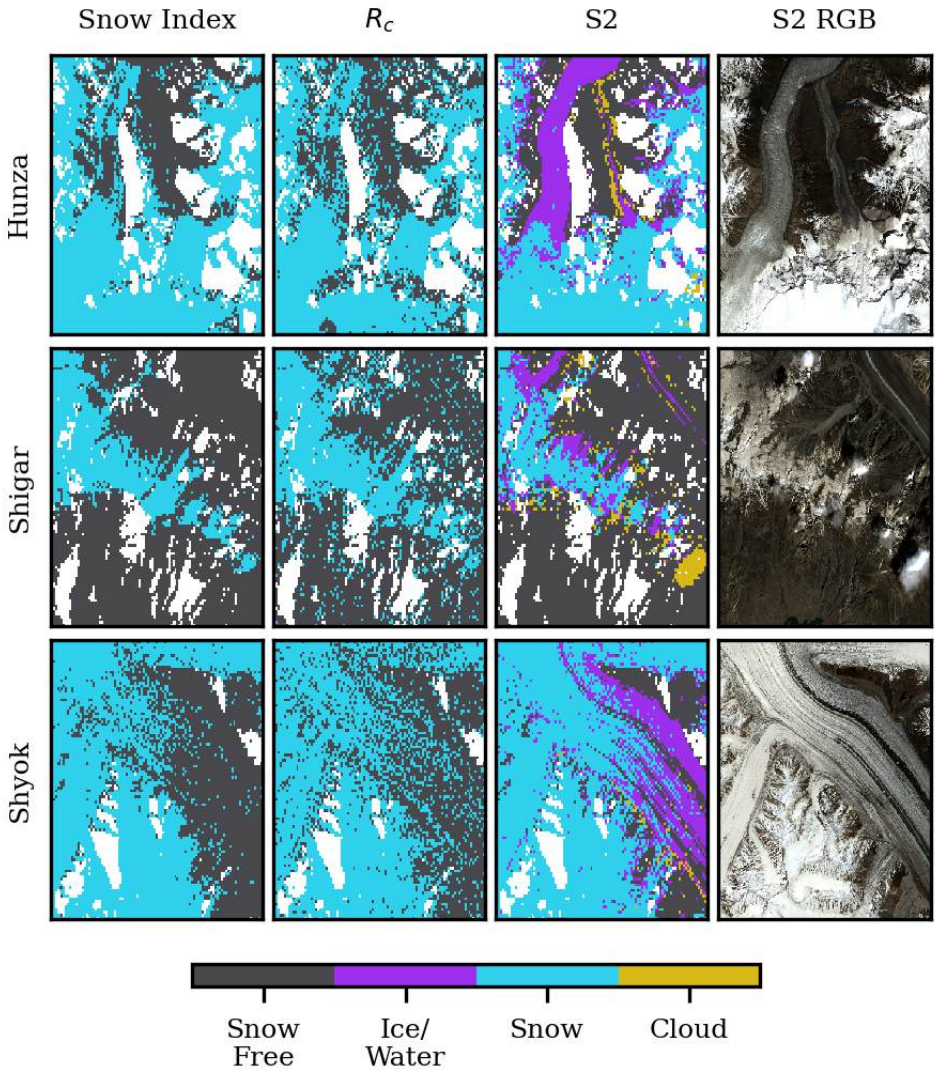

FIGURE 3.6: Detailed comparison between the snow classification map obtained using SI (left column), R_c (middle column) and the S2 snow cover map (right column, reference) for Hunza (top row), Shigar (middle row), and Shyok (bottom row) basins. Class labels are indicated in the color bar. Note that the selected regions were located in the mid-elevation range of the area, and hence the snow class in both S1 and S2 results both refers to wet snow.

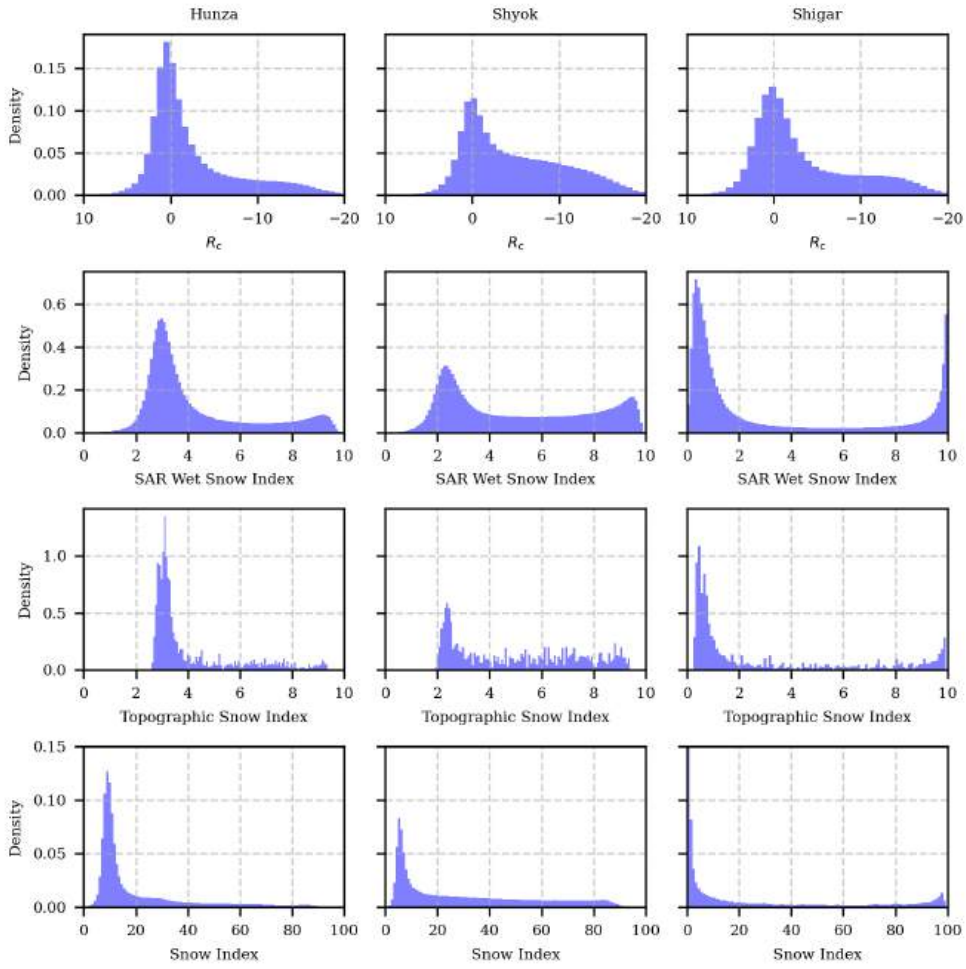

FIGURE 3.7: Density distribution of R_c, WSI, TSI and SI in three basins (left: Hunza, middle: Shyok, right: Shigar). The x-axis of R_c is inverted as negative R_c corresponds to higher probability of wet snow.

A detailed comparison is further illustrated in Fig. 3.6. Overall, the two methods show good agreement, demonstrating the effectiveness of the proposed approach. Notably, the SI-based classification exhibits reduced false positives and cleaner snow-free classifications in valleys and over glacier surfaces, as evident in the detailed comparison. This improvement is primarily attributed to the incorporation of topographic information through TSI, which smooths SI values within each topographic bin. However, a consistent mismatch in the ice/water category can be observed between the SAR (both the SI and ratio methods) and S2 results, particularly over glacier surfaces. This discrepancy arises from the differing detection principles of the two approaches: the S2 results classify glacier ice using thresholds on the NIR band, while the SAR-based methods do not explicitly resolve glacier ice. On the observed date, glacier ice in the ablation zone may have partially melted, reducing the SAR backscatter ratio and leading to its misclassification as wet snow in the SAR results. As discussed earlier, glacier surfaces present unique challenges for SAR-based methods due to their complex scattering mechanisms. While the inclusion of TSI improves the robustness of our method by integrating topographic controls, it does not explicitly account for the heterogeneity of glacier surfaces. Consequently, glacier-specific conditions, such as localized melting or scattering from mixed ice-snow surfaces, may lead to underestimation or misclassification.

We further quantified the comparison using a confusion matrix and the F1 score, as listed in Table 3.3. In the confusion matrix, S2 snow-free (S2-SF) and S2 snow (S2-S) pixels are used as negative and positive labels, respectively, while S1 snow classification maps designate no-snow or dry snow (S1-N/D) and wet snow (S1-WS) pixels as their counterparts. To minimize errors caused by the presence of dry snow at high altitudes, areas above 5500 m a.s.l. were excluded from the calculation. This elevation threshold, representing 11.08% of pixels in Hunza, 12.95% in Shigar, and 30.43% in Shyok (19.60% in total), was chosen because such areas are consistently classified as non-melting zones due to persistently low air temperatures that inhibit snowmelt. Across all three basins, the proposed method shows an improvement in classification performance. In Hunza and Shyok, both true negative and true positive rates increased, while in Shigar, the true negative rate improved by 0.11, though the true positive rate decreased slightly by 0.04. Despite this, the overall F1 scores improved for all three basins, highlighting the method's enhanced precision and recall.

We also evaluated the accuracy of the classification map using the elevation profile of snow distributions. As illustrated in Fig. 3.8, the profile

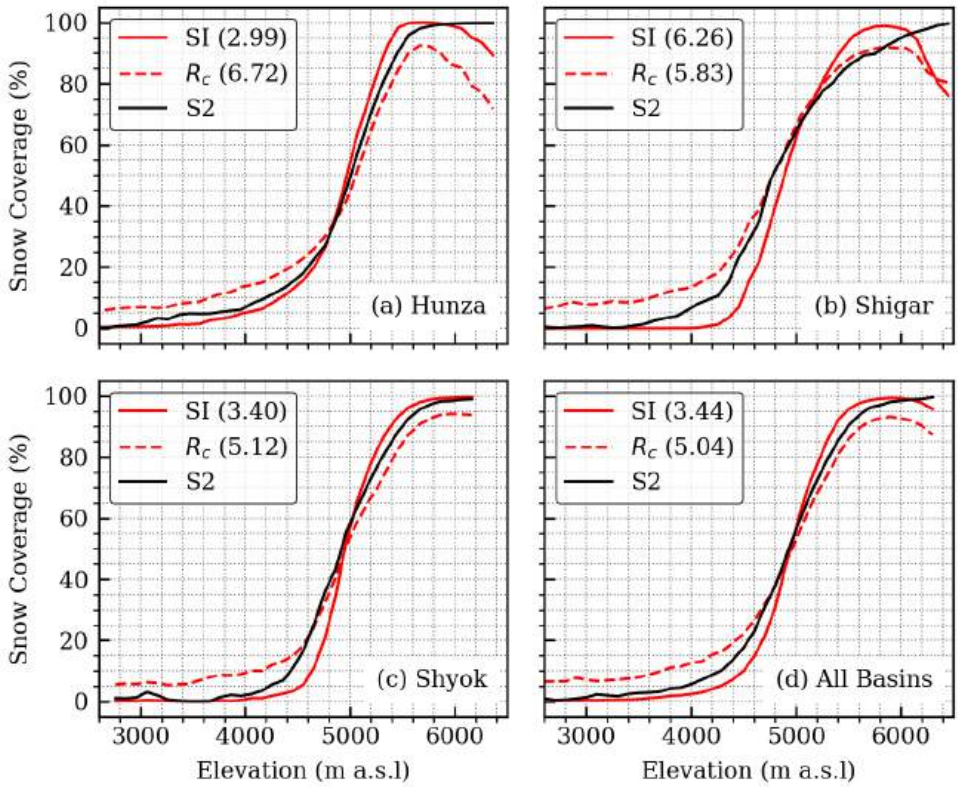

FIGURE 3.8: Snow coverage profile along elevation bands. Elevation bands were binned every 100m, and the snow coverage within a band was calculated based on the aggregated snow pixel percentage within every band. Numbers reported in legends measured the mean absolute error (MAE) between the profile curve of SAR wet snow classification and the S2 snow cover map.

Basin		Confusion Matrix		F1 Score
		S2-SF (N)	S2-S (P)	
Hunza	S1-N/D (N)	**0.93** | 0.88	**0.07** | 0.12	**0.86** | 0.78
	S1-WS (P)	**0.13** | 0.21	**0.87** | 0.79	
Shigar	S1-N/D (N)	**0.94** | 0.83	**0.06** | 0.17	**0.84** | 0.79
	S1-WS (P)	**0.22** | 0.18	**0.78** | 0.82	
Shyok	S1-N/D (N)	**0.90** | 0.87	**0.10** | 0.13	**0.93** | 0.89
	S1-WS (P)	**0.08** | 0.13	**0.92** | 0.87	
All Basins	S1-N/D (N)	**0.92** | 0.86	**0.08** | 0.14	**0.89** | 0.84
	S1-WS (P)	**0.12** | 0.16	**0.88** | 0.84	

TABLE 3.3: Confusion matrix and F_1 score between S1 snow classification maps and S2 snow cover maps. Snow-free (S2-NS) and snow (S2-S) pixels in S2 snow cover maps correspond to the negative (N) and positive (P) labels, respectively. The associated labels in S1 snow classification maps are no-snow or dry snow (S1-N/D) pixels and wet snow (S1-WS) pixels. Results of the proposed method are highlighted in bold, whereas the R_c threshold based results are reported in normal font.

of snow coverage was analyzed along 100m elevation bands. Below 4500m a.s.l, snow coverage was overestimated by approximately 7% when using the R_c thresholds, leading to a misrepresentation of the actual snow line, especially over the challenging conditions on glacier surfaces and valleys (Fig. 3.5). In contrast, the SI method provided a snow classification closer to the S2 profiles in the low-elevation regions. Between 4500m and 5500m a.s.l, the SI curve exhibited a noticeably steeper slope than the S2 curve, with an underestimation of snow coverage between 4000m and 5000m and an overestimation from 5000m to 5500m. This pattern suggests that the SI uncertainties in mixed snow conditions within transition zones might have led to a nonlinear exaggeration of the TSI response to snow cover. A more precisely calibrated TSI model could further align snow coverage profiles between the SI method and S2 results. Above 5500m a.s.l, where expansive dry snow cover predominates, both R_c and SI maps showed a greater reduction in wet snow coverage compared to S2, highlighting the differing sensitivities of SAR signals to dry snow conditions in these methods compared to S2's multi-spectral data.

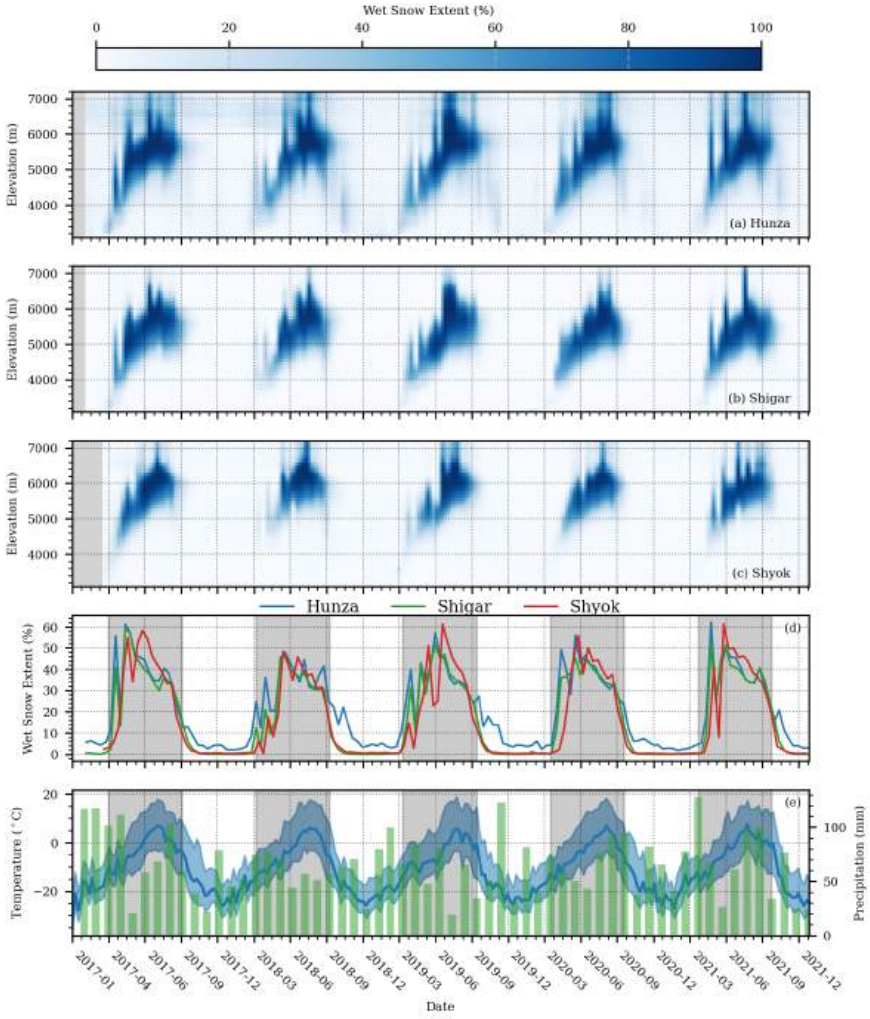

FIGURE 3.9: Temporal and elevation dependence of WSE in (a) Hunza, (b) Shigar and (c) Shyok, as well as (d) the total WSE of the three basins within the studied period, and (e) temperature and precipitation record obtained from the ERA5 dataset. In panel s(a)∼(c), the WSE is represented by the color scale. In panel (d), blue line indicates the weekly average temperature of the three basins, and the shaded blue indicates the range between the weekly maximum and minimum temperature. Monthly averaged precipitation is shown with the green bar. The shaded gray zone shows the summer of the year. The WSE was calculated as the ratio of wet snow-covered area to the total area within each respective elevation band.

3.4.2 Temporal dynamics of snow melting

In this section, we further applied the proposed method to the collected S1 image time series between 2017-2021 to generate wet snow maps across all three basins. The generated wet snow maps were resampled from the original SAR image resolution of 14×14m to 30×30m before the analysis to speed up the processing. The temporal interval of the time series was 12 days, the same as the acquisition interval of S1 images. We analyze two key properties of snow cover dynamics derived from the time series data: the wet snow extent (WSE) and the snow melting duration (SMD). It is worth noting that these properties represent just a subset of the potential insights that can be derived from this dataset.

3.4.2.1 Wet snow extent

The temporal patterns and elevation dependencies of WSE across the Hunza, Shigar, and Shyok basins are depicted in Fig. 3.9 (a)∼(c). WSE was calculated as the percentage of wet snow pixels within each 100-meter elevation band, offering a granular view of snowmelt progression. Over the 5-year period analyzed, a consistent interannual pattern was observed in all three basins. Melting is typically initiated by the end of March to early April and is concluded by late September to early October. As temperatures rose from spring (i.e., April to May) into summer, the melting front (e.g. the upper and lower elevation boundary of the melting area) ascended along the altitude gradient. Specifically, the lower elevation boundary of wet snow extended upwards as snow at lower altitudes fully melted, while the upper boundary extended to higher altitudes as higher temperatures resulted in melting at greater elevations. In the peak melting months (i.e., July and August), the upper boundary of melting snow reached its maximum altitude before descending, whereas the lower boundary extended to its highest extent and stabilized until the end of the melt season.

Fig. 3.9 d∼e illustrate the interactions between total WSE, temperature, and precipitation within the region using data from the ERA5 reanalysis dataset [42]. The temperature data, averaged weekly, include mean, maximum, and minimum temperatures of air at 2m above the surface of land across the Karakoram region, providing insights into the thermal conditions influencing snow melting. The precipitation data are the accumulated liquid and frozen water falling to the Earth's surface. They were compiled and averaged monthly to complement the temperature analysis by revealing precipitation trends and their impact on snowpack. While the three basins demonstrated similar interannual variability, annual discrepancies were pronounced within the time

series. For instance, the peak WSE in 2018, around 40%, was notably lower than the approximately 50% observed in other years. This reduction in WSE is related to diminished winter precipitation during the 2017-2018 season, as indicated by the precipitation data. The onset of snow melting aligned well with the period when maximum temperatures rise above freezing, suggesting that peak temperatures were a more sensitive indicator for the onset of snow melting than mean temperatures. These complex interannual fluctuations underscore the snowpack's responsiveness to immediate weather conditions, such as temperature spikes and precipitation events.

3.4.2.2 Snow melting duration

The SMD reflects the temporal persistence of wet snow cover within a given year, allowing for consistent comparisons across years with varying numbers of observation days. To compute the SMD for each year, we first determined the ratio of days with wet snow cover (M) to the total number of observed days (N) for each pixel. Since the number of observation days (N) varied each year and was typically less than 365, we re-scaled this ratio to a 365-day basis using the formula $(M/N) \times 365$ to standardize the annual average of wet snow cover days and enable consistent comparisons between years.

Fig. 3.10 presents the annual average SMD across the study region from 2017 to 2021. The average SMD displays a pronounced terrain dependency: valley areas at lower altitudes typically exhibit an SMD of fewer than 60 days, while higher altitudes, such as glacier accumulation zones, generally experience SMD exceeding 120 days. In certain high-altitude regions, the wet snow cover can persist for more than 180 days annually.

To assess the temporal and spatial dynamics of SMD, we evaluated the annual fraction of SMD for each basin, as depicted in Fig. 3.11. SMD was categorized into four ranges: 0-60 days (blue), 60-120 days (orange), 120-180 days (green), and 180-240 days (red). In Hunza, the area with a SMD of less than 60 days saw a decline from 2017 to 2019, followed by an increase from 2020 to 2021. This change was inversely related to the 60-120 days category, which expanded from 2017 to 2019 before contracting. The fraction of WSD exceeding 120 days initially decreased from 2017 to 2019 and then increased as the 60-120 days category diminished. A pronounced peak within the 180-240 days range occurred in 2017. The Shigar basin exhibited more pronounced annual oscillations in SMD. The area with an SMD below 60 days fluctuated around an average of 0.5, while the 60-180 days category mirrored the pattern in Hunza, increasing from 2017 to 2019 before a subsequent decline. The SMD range of 120-180 days remained relatively stable at about

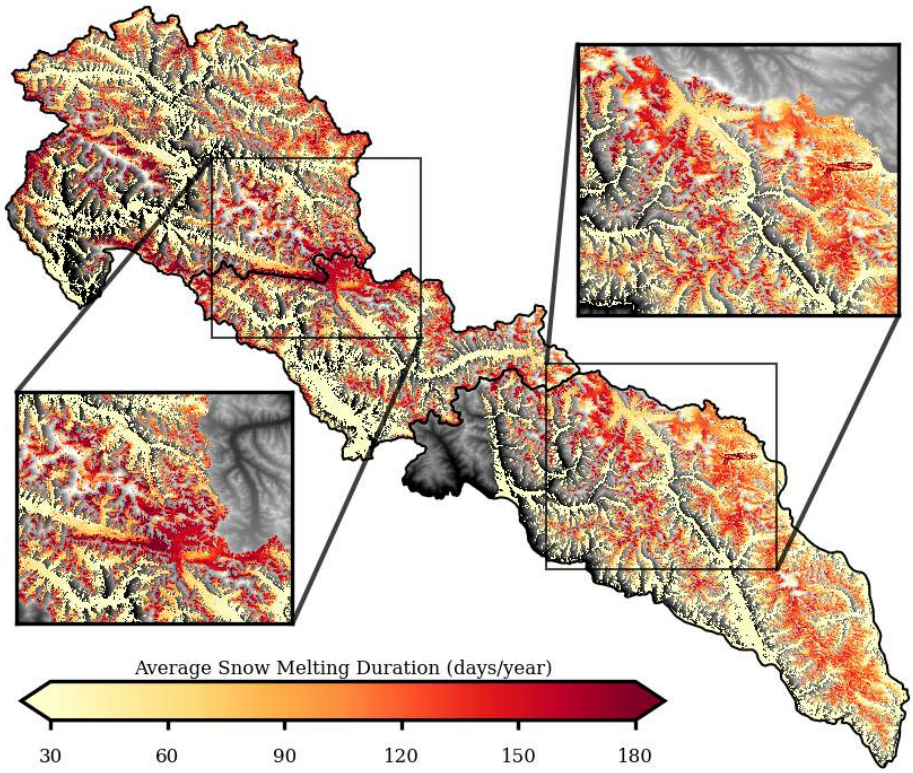

FIGURE 3.10: Annual average SMD of the study region, calculated based on the 5-year observation.

0.2, with periods exceeding 180 days noted only in 2017 and 2020. The Shyok basin experienced the most substantial temporal variation in SMD. The 0-60 days category showed strong variance around the 0.5 level. The 60-120 days category peaked in 2019, representing a larger fraction (∼0.5) compared to those in Hunza (∼0.3) and Shigar (∼0.35). The 180-240 days range was present exclusively in 2017.

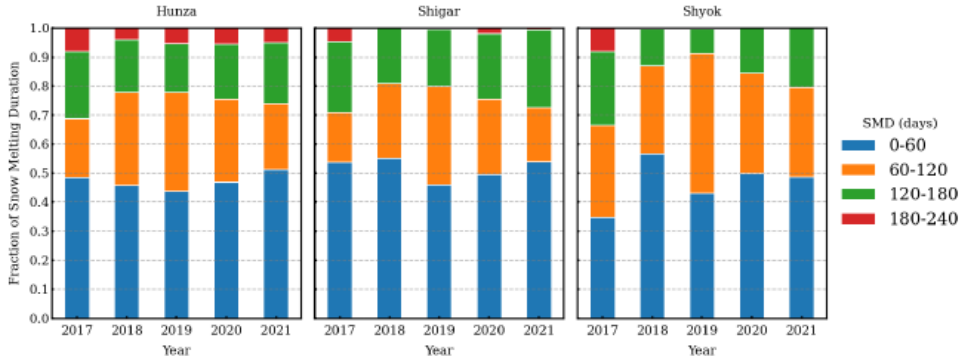

FIGURE 3.11: Fraction of snow melting duration in the three basins between 2017-2021. SMD was segmented into four categories as represented by different colors.

3.5 Discussion

3.5.1 Classification performance

Compared to the conventional methods where only a single-value threshold are used on the R_c map, the proposed method has effectively improved the mapping accuracy in the validation. This is primarily attributed to the transformation of R_c into WSI and the incorporation of TSI.

The GMM enabled a data-driven approach that allowed adaptively transforming the R_c into WSI based on the local SAR signal responses. As shown in Fig. 3.3, the WSI function for each basin was characterized by distinct center (x_0) and slope (k) parameters determined from the GMM, indicating that varied local responses of SAR backscattering were raised by the diverse nature of wet snow distribution in different basins. This provides the flexibility required for large-scale application and thus offered an approach for robust wet snow mapping in complex and diverse landscapes.

Furthermore, the proposed method enriched the terrain analysis in snow mapping by incorporating multiple topographical factors (i.e., elevation, slope,

and aspect) beyond the traditional use of snow line elevation. The add-on information from slope and aspect enables accurate capture of snow spatial distribution over the complex terrain, which is particularly important in the Karakoram region. As exemplified in Fig. 3.4 for the Hunza basin, the TSI values vary with elevation, aspect, and slope across different times of the year. At the onset of snowmelt, flat and east-facing slopes at altitudes between 3500m a.s.l and 5000m a.s.l exhibited higher TSI values than the other regions, suggesting snow in such areas was more susceptible to melting, likely due to solar exposure. As the season progressed into summer, altitude increasingly dictated the snowmelt on flat terrains, while on steeper slopes, aspect also played a significant role. Approaching late autumn, the snow line stabilized at similar altitudes across the two slope classes, yet variations were observed across the aspect with higher TSI values on south-facing slopes (approximate aspect of $75^\circ - 255^\circ$), indicating conditions more conducive to melting. This level of detail in our analysis demonstrated the potential of our method to provide a more comprehensive understanding of wet snow dynamics than analysis using only snow line elevations.

While the proposed method demonstrates strong performance across the three basins in Karakoram, several limitations should be acknowledged. First, the choice of the SI threshold relies on the coefficient determined through sensitivity analysis for the selected study areas. While this approach balances classification performance across the basins, it is not fully dynamic and may require adaptation for larger, more topographically diverse regions, such as global-scale applications. Future work could explore supervised learning models, such as random forests or neural networks, to capture more complex, nonlinear relationships between SAR backscatter, topography, and snow conditions, enabling dynamic threshold adaptation.

Second, glacier surfaces present unique challenges for SAR-based snow classification. As shown in the results, glacier-specific scattering mechanisms, including contributions from wet debris, bare ice, and supraglacial features, introduce variability in radar backscatter that is not explicitly modeled in the current method. This limitation may lead to underestimation of wet snow on glacier surfaces and highlights the need for further refinement of the method to better handle glacier-specific conditions, potentially by incorporating land surface type information.

Finally, the use of TSI introduces potential bias in regions where topographic conditions deviate significantly from the assumptions underlying its calculation. As shown in Fig. 3.7, the long-tailed distribution of TSI values reflects the cumulative statistical nature of TSI, which relies on using a sin-

gle median value to represent each topographic bin. This approach may be inadequate in bins with strong terrain variations, especially when the TSI distribution of pixels within a bin is highly skewed. In such cases, using the median can lead to systematic overestimation or underestimation — overestimating in left-skewed distributions and underestimating in right-skewed ones — ultimately affecting precision and recall in the classification results (see Sect. S2 of the Supplement for detailed visualizations). For instance, low TSI values in ablation zones may lead to underestimation of wet snow, as noted in the comparison with S2 results. While the inclusion of TSI improves overall robustness by integrating terrain characteristics, future studies should evaluate strategies to mitigate these biases, especially in regions with complex topography or unique land surface characteristics.

It is also important to note that while we followed Nagler's method [13] to generate the R_c image, we did not apply the same post-processing steps, such as median filtering and land cover masking. These smoothing and filtering steps may influence accuracy, and future work could incorporate them to further evaluate their impact and potentially improve snow mapping performance.

3.5.2 Implications of wet snow maps

Large-scale wet snow maps, especially the ones with high spatial and temporal resolution, have significant implications for hydrological studies, water resource management, and climate impact assessments [43]. Snow data obtained from remote sensing and field site stations have proven to be fundamental for the development, calibration, and validation of snowpack, hydrology, and runoff prediction models [44–48].

Using the wet snow maps generated from the proposed method, our study has extracted and analyzed two critical snow variables, i.e., WSE and SMD, which are crucial for understanding regional snow melting dynamics. The analysis of WSE uncovered detailed patterns of snowmelt changes over time and across elevations, which can provide valuable observations for calibrating snowpack models or forecasting runoff events [48]. The interpretation of SMD highlighted the yearly differences in snow melting duration across the basins, with Hunza exhibiting relative stability and Shyok demonstrating the most variability. A long-term SMD observation record will provide key insights into the changes of the regional climate pattern.

3.6 Conclusions

In this study, we proposed a novel approach for mapping wet snow in complex mountainous regions, such as Karakoram, by effectively combining S1 SAR data with topographic information. We first adopted the GMM to adaptively transform the SAR backscattering ratio R_c into the WSI as a robust representation of wet snow under complex surface conditions. Then, we introduced the TSI to capture the likelihood of snow presence influenced by topographic conditions. Validation with S2 snow cover maps demonstrated a notable improvement in the accuracy of wet snow classification.

With the collected time series of S1 images over the three major water basins in Karakoram, we produced large-scale wet snow maps using the proposed method. The wet snow maps have enabled detailed analysis of crucial snow variables including the WSE and SMD. Analysis of the two variables revealed the dynamic pattern of the temporal-spatial distribution of wet snow in Karakoram, suggesting that the comprehensive dataset produced with this study can offer further enhancement for hydrological model calibrations and validation, thereby ensuring informed water resource management and climate modeling.

Future work involves integrating the approach with in situ observations and hydrological models to further improve the accuracy and utility of water resource planning tools. Continuing to advance this research would provide results that are greatly beneficial for fostering climate resilience and sustainability in Karakoram.

Appendix: Sensitivity analysis on SI threshold

We applied a sensitivity analysis to TSI coefficients to find the optimal SI threshold finding. A series of TSI coefficients were tested using validation images to examine how the TSI coefficient in the SI threshold affected the classification results. Three metrics, including the F1 score, precision and recall, were evaluated and used as the selection criteria. The result (Fig. 3.12) showed that the optimal coefficients for Hunza and Shyok were close to 3.5, while a lower coefficient of around 2.5 was found to be optimal for Shigar.

References

1. Barnett, T. P., Adam, J. C. & Lettenmaier, D. P. Potential impacts of a warming climate on water availability in snow-dominated regions. *Nature* **438**. 303 (2005).

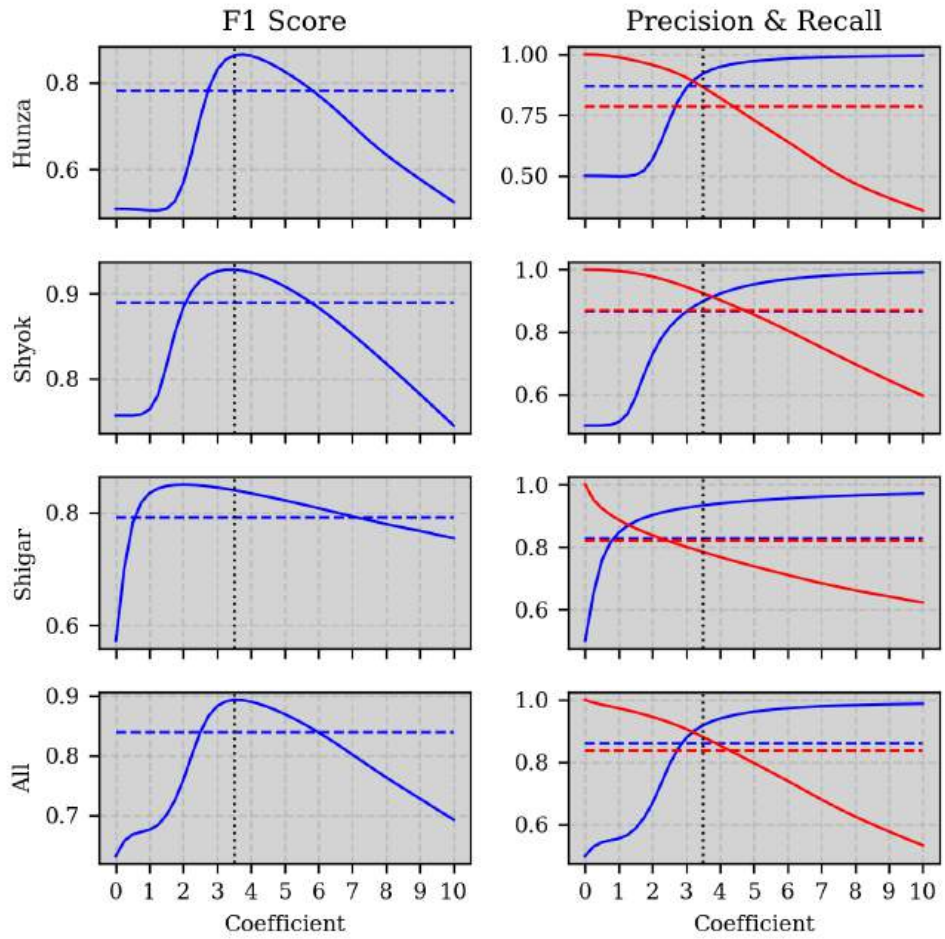

FIGURE 3.12: Sensitivity analysis of the choice of TSI coefficients for SI thresholds. The left panel shows the F1 score, and the right panel is for precision (blue) and recall (red). Dashed lines are results using $R_c = -2\ dB$ as the threshold. The dotted vertical line indicates where the coefficient is 3.5.

2. Nie, Y., Pritchard, H. D., Liu, Q., Hennig, T., Wang, W., Wang, X., Liu, S., Nepal, S., Samyn, D., Hewitt, K. & Chen, X. Glacial change and hydrological implications in the Himalaya and Karakoram. *Nature Reviews Earth & Environment* **2**. 91 (2021).

3. Lund, J., Forster, R. R., Rupper, S. B., Deeb, E. J., Marshall, H. P., Hashmi, M. Z. & Burgess, E. Mapping Snowmelt Progression in the Upper Indus Basin With Synthetic Aperture Radar. *Frontiers in Earth Science* **7** (2020).

4. Hasson, S., Lucarini, V., Khan, M. R., Petitta, M., Bolch, T. & Gioli, G. Early 21st century snow cover state over the western river basins of the Indus River system. *Hydrology and Earth System Sciences* **18**. 4077 (2014).

5. Xie, F., Liu, S., Gao, Y., Zhu, Y., Bolch, T., Kääb, A., Duan, S., Miao, W., Kang, J., Zhang, Y., Pan, X., Qin, C., Wu, K., Qi, M., Zhang, X., Yi, Y., Han, F., Yao, X., Liu, Q., Wang, X., Jiang, Z., Shangguan, D., Zhang, Y., Grünwald, R., Adnan, M., Karki, J. & Saifullah, M. Interdecadal glacier inventories in the Karakoram since the 1990s. *Earth System Science Data* **15**. 847 (2023).

6. Immerzeel, W. W., Droogers, P., de Jong, S. M. & Bierkens, M. F. P. Large-scale monitoring of snow cover and runoff simulation in Himalayan river basins using remote sensing. *Remote Sensing of Environment* **113**, 40 (2009).

7. Tahir, A. A., Chevallier, P., Arnaud, Y. & Ahmad, B. Snow cover dynamics and hydrological regime of the Hunza River basin, Karakoram Range, Northern Pakistan. *Hydrology and Earth System Sciences* **15**. 2275 (2011).

8. Tahir, A. A., Chevallier, P., Arnaud, Y., Ashraf, M. & Bhatti, M. T. Snow cover trend and hydrological characteristics of the Astore River basin (Western Himalayas) and its comparison to the Hunza basin (Karakoram region). *Science of The Total Environment* **505**, 748 (2015).

9. Khan, A., Naz, B. S. & Bowling, L. C. Separating snow, clean and debris covered ice in the Upper Indus Basin, Hindukush-Karakoram-Himalayas, using Landsat images between 1998 and 2002. *Journal of Hydrology* **521**, 46 (2015).

10. Wu, X., Naegeli, K., Premier, V., Marin, C., Ma, D., Wang, J. & Wunderle, S. Evaluation of snow extent time series derived from Advanced Very High Resolution Radiometer global area coverage data (1982–2018) in the Hindu Kush Himalayas. *The Cryosphere* **15**. 4261 (2021).

11. Baghdadi, N., Gauthier, Y. & Bernier, M. Capability of multitemporal ERS-1 SAR data for wet-snow mapping. *Remote Sensing of Environment* **60**, 174 (1997).

12. Millan, R., Dehecq, A., Trouvé, E., Gourmelen, N. & Berthier, E. *Elevation changes and X-band ice and snow penetration inferred from TanDEM-X data of the Mont-Blanc area* in *2015 8th International Workshop on the Analysis of Multitemporal Remote Sensing Images (Multi-Temp)* (2015), 1.

13. Nagler, T., Rott, H., Ripper, E., Bippus, G. & Hetzenecker, M. Advancements for Snowmelt Monitoring by Means of Sentinel-1 SAR. *Remote Sensing* **8**, 348 (2016).

14. Nagler, T. & Rott, H. Retrieval of wet snow by means of multitemporal SAR data. *IEEE Transactions on Geoscience and Remote Sensing* **38**. 754 (2000).

15. Malnes, E. & Guneriussen, T. *Mapping of snow covered area with Radarsat in Norway* in. **1** (2002), 683.

16. Longepe, N., Allain, S., Ferro-Famil, L., Pottier, E. & Durand, Y. Snowpack Characterization in Mountainous Regions Using C-Band SAR Data and a Meteorological Model. *IEEE Transactions on Geoscience and Remote Sensing* **47**. 406 (2009).

17. Rondeau-Genesse, G., Trudel, M. & Leconte, R. Monitoring snow wetness in an Alpine Basin using combined C-band SAR and MODIS data. *Remote Sensing of Environment* **183**, 304 (2016).

18. Koskinen, J., Pulliainen, J. & Hallikainen, M. The use of ers-1 sar data in snow melt monitoring. *IEEE Transactions on Geoscience and Remote Sensing* **35**, 601 (1997).

19. Luojus, K., Pulliainen, J., Metsamaki, S. & Hallikainen, M. Accuracy assessment of SAR data-based snow-covered area estimation method. *IEEE Transactions on Geoscience and Remote Sensing* **44**. 277 (2006).

20. Pettinato, S., Santi, E., Paloscia, S., Aiazzi, B., Baronti, S. & Garzelli, A. Snow cover area identification by using a change detection method applied to COSMO-SkyMed images. *Journal of Applied Remote Sensing* **8**. 084684 (2014).

21. Liu, C., Li, Z., Zhang, P. & Wu, Z. Seasonal snow cover classification based on SAR imagery and topographic data. *Remote Sensing Letters* **13**, 269 (2022).

22. Liu, C., Li, Z., Zhang, P., Huang, L., Li, Z. & Gao, S. Wet snow detection using dual-polarized Sentinel-1 SAR time series data considering different land categories. *Geocarto International* **0**. 1 (2022).

23. Tsai, Y.-L. S., Dietz, A., Oppelt, N. & Kuenzer, C. Wet and Dry Snow Detection Using Sentinel-1 SAR Data for Mountainous Areas with a Machine Learning Technique. *Remote Sensing* **11**. 895 (2019).

24. Huang, L., Li, Z., Tian, B.-S., Chen, Q., Liu, J.-L. & Zhang, R. Classification and snow line detection for glacial areas using the polarimetric SAR image. *Remote Sensing of Environment* **115**, 1721 (2011).

25. Liu, C., Li, Z., Wu, Z., Huang, L., Zhang, P. & Li, G. An Unsupervised Snow Segmentation Approach Based on Dual-Polarized Scattering Mechanism and Deep Neural Network. *IEEE Transactions on Geoscience and Remote Sensing* **61**. 1 (2023).

26. Snapir, B., Momblanch, A., Jain, S. K., Waine, T. W. & Holman, I. P. A method for monthly mapping of wet and dry snow using Sentinel-1 and MODIS: Application to a Himalayan river basin. *International Journal of Applied Earth Observation and Geoinformation* **74**, 222 (2019).

27. Karbou, F., Veyssière, G., Coleou, C., Dufour, A., Gouttevin, I., Durand, P., Gascoin, S. & Grizonnet, M. Monitoring Wet Snow Over an Alpine Region Using Sentinel-1 Observations. *Remote Sensing* **13**. 381 (2021).

28. Karbou, F., James, G., Durand, P. & Atto, A. Thresholds and distances to better detect wet snow over mountains with Sentinel-1 image time series. **1: Unsupervised Methods**. 1 (2021).

29. Archer, D. Contrasting hydrological regimes in the upper Indus Basin. *Journal of Hydrology* **274**, 198 (2003).

30. Forsythe, N., Kilsby, C. G., Fowler, H. J. & Archer, D. R. Assessment of Runoff Sensitivity in the Upper Indus Basin to Interannual Climate Variability and Potential Change Using MODIS Satellite Data Products. *Mountain Research and Development* **32**. 16 (2012).

31. Li, H., Zhao, J., Yan, B., Yue, L. & Wang, L. Global DEMs vary from one to another: an evaluation of newly released Copernicus, NASA and AW3D30 DEM on selected terrains of China using ICESat-2 altimetry data. *International Journal of Digital Earth* **15**. 1149 (2022).

32. Guth, P. L. & Geoffroy, T. M. LiDAR point cloud and ICESat-2 evaluation of 1 second global digital elevation models: Copernicus wins. *Transactions in GIS* **25**. 2245 (2021).

33. European Space Agency & Airbus. *Copernicus DEM* 2022.

34. Drusch, M., Del Bello, U., Carlier, S., Colin, O., Fernandez, V., Gascon, F., Hoersch, B., Isola, C., Laberinti, P., Martimort, P., Meygret, A., Spoto, F., Sy, O., Marchese, F. & Bargellini, P. Sentinel-2: ESA's Optical High-Resolution Mission for GMES Operational Services. *Remote Sensing of Environment. The Sentinel Missions - New Opportunities for Science* **120**, 25 (2012).

35. Main-Knorn, M., Pflug, B., Louis, J., Debaecker, V., Müller-Wilm, U. & Gascon, F. *Sen2Cor for Sentinel-2* in *Image and Signal Processing for Remote Sensing XXIII* (eds Bruzzone, L., Bovolo, F. & Benediktsson, J. A.) (SPIE, Warsaw, Poland, 2017), 3.

36. Gascoin, S., Grizonnet, M., Bouchet, M., Salgues, G. & Hagolle, O. Theia Snow collection: high-resolution operational snow cover maps from Sentinel-2 and Landsat-8 data. *Earth System Science Data* **11**, 493 (2019).

37. Frey, O., Santoro, M., Werner, C. L. & Wegmuller, U. DEM-Based SAR Pixel-Area Estimation for Enhanced Geocoding Refinement and Radiometric Normalization. *IEEE Geoscience and Remote Sensing Letters* **10**. 48 (2013).

38. Werner, C., Wegmüller, U., Strozzi, T. & Wiesmann, A. GAMMA SAR AND INTERFEROMETRIC PROCESSING SOFTWARE (2000).

39. Dempster, A. P., Laird, N. M. & Rubin, D. B. Maximum Likelihood from Incomplete Data Via the EM Algorithm. *Journal of the Royal Statistical Society: Series B (Methodological)* **39**. 1 (1977).

40. Paul, F., Winsvold, S. H., Kääb, A., Nagler, T. & Schwaizer, G. Glacier Remote Sensing Using Sentinel-2. Part II: Mapping Glacier Extents and Surface Facies, and Comparison to Landsat 8. *Remote Sensing* **8**. 575 (2016).

41. Scher, C., Steiner, N. C. & McDonald, K. C. Mapping seasonal glacier melt across the Hindu Kush Himalaya with time series synthetic aperture radar (SAR). *The Cryosphere* **15**. 4465 (2021).

42. Hersbach, H., Bell, B., Berrisford, P., Hirahara, S., Horányi, A., Muñoz-Sabater, J., Nicolas, J., Peubey, C., Radu, R., Schepers, D., Simmons, A., Soci, C., Abdalla, S., Abellan, X., Balsamo, G., Bechtold, P., Biavati, G., Bidlot, J., Bonavita, M., De Chiara, G., Dahlgren, P., Dee, D., Diamantakis, M., Dragani, R., Flemming, J., Forbes, R., Fuentes, M., Geer, A., Haimberger, L., Healy, S., Hogan, R. J., Hólm, E., Janisková, M.,

Keeley, S., Laloyaux, P., Lopez, P., Lupu, C., Radnoti, G., De Rosnay, P., Rozum, I., Vamborg, F., Villaume, S. & Thépaut, J.-N. The ERA5 global reanalysis. *Quarterly Journal of the Royal Meteorological Society* **146**, 1999 (2020).

43. Helmert, J., Şensoy Şorman, A., Alvarado Montero, R., De Michele, C., De Rosnay, P., Dumont, M., Finger, D. C., Lange, M., Picard, G., Potopová, V., Pullen, S., Vikhamar-Schuler, D. & Arslan, A. N. Review of Snow Data Assimilation Methods for Hydrological, Land Surface, Meteorological and Climate Models: Results from a COST HarmoSnow Survey. *Geosciences* **8**. 489 (2018).

44. Schmugge, T. J., Kustas, W. P., Ritchie, J. C., Jackson, T. J. & Rango, A. Remote sensing in hydrology. *Advances in Water Resources* **25**, 1367 (2002).

45. Andreadis, K. M. & Lettenmaier, D. P. Assimilating remotely sensed snow observations into a macroscale hydrology model. *Advances in Water Resources* **29**, 872 (2006).

46. Dressler, K. A., Leavesley, G. H., Bales, R. C. & Fassnacht, S. R. Evaluation of gridded snow water equivalent and satellite snow cover products for mountain basins in a hydrologic model. *Hydrological Processes* **20**. 673 (2006).

47. Griessinger, N., Schirmer, M., Helbig, N., Winstral, A., Michel, A. & Jonas, T. Implications of observation-enhanced energy-balance snowmelt simulations for runoff modeling of Alpine catchments. *Advances in Water Resources* **133**, 103410 (2019).

48. Cluzet, B., Magnusson, J., Quéno, L., Mazzotti, G., Mott, R. & Jonas, T. Using Sentinel-1 wet snow maps to inform fully-distributed physically-based snowpack models. *EGUsphere*. 1 (2024).

Supplementary Material

Maps of snow index in three basins

Classification Metrics under different topographic conditions

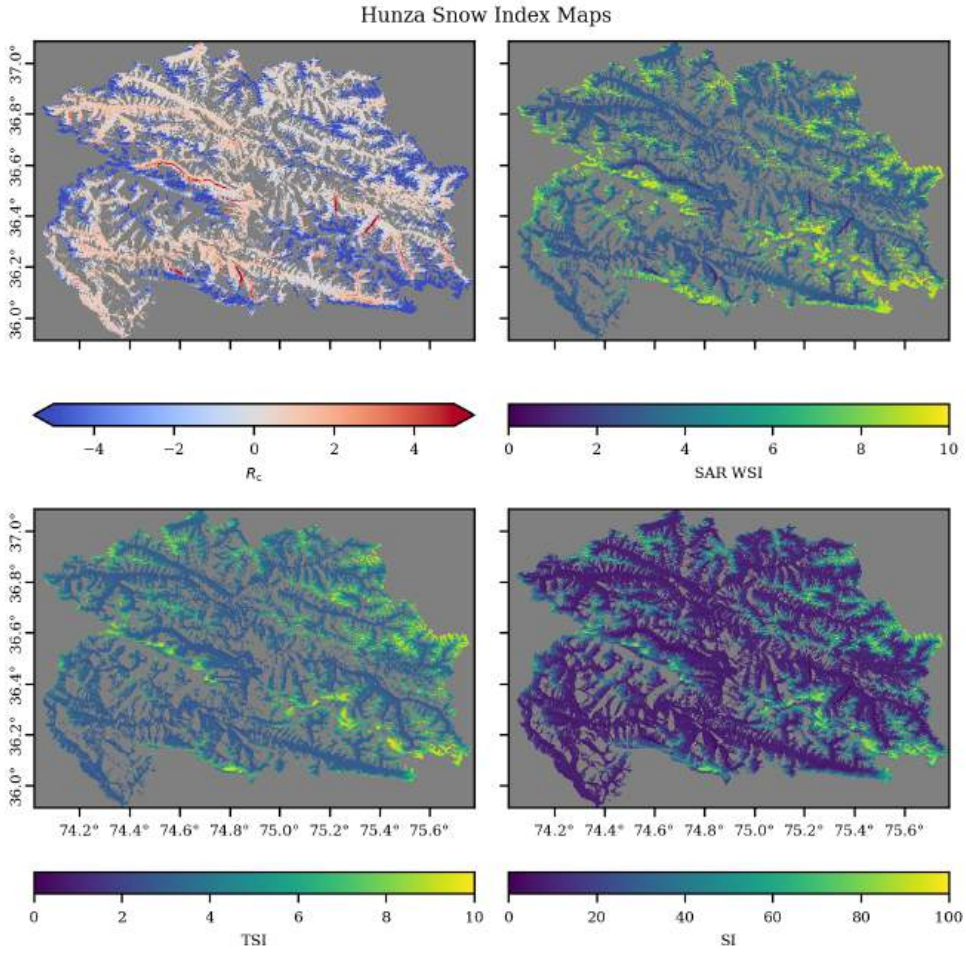

FIGURE S3.13: R_c, WSI, TSI and SI maps of Hunza.

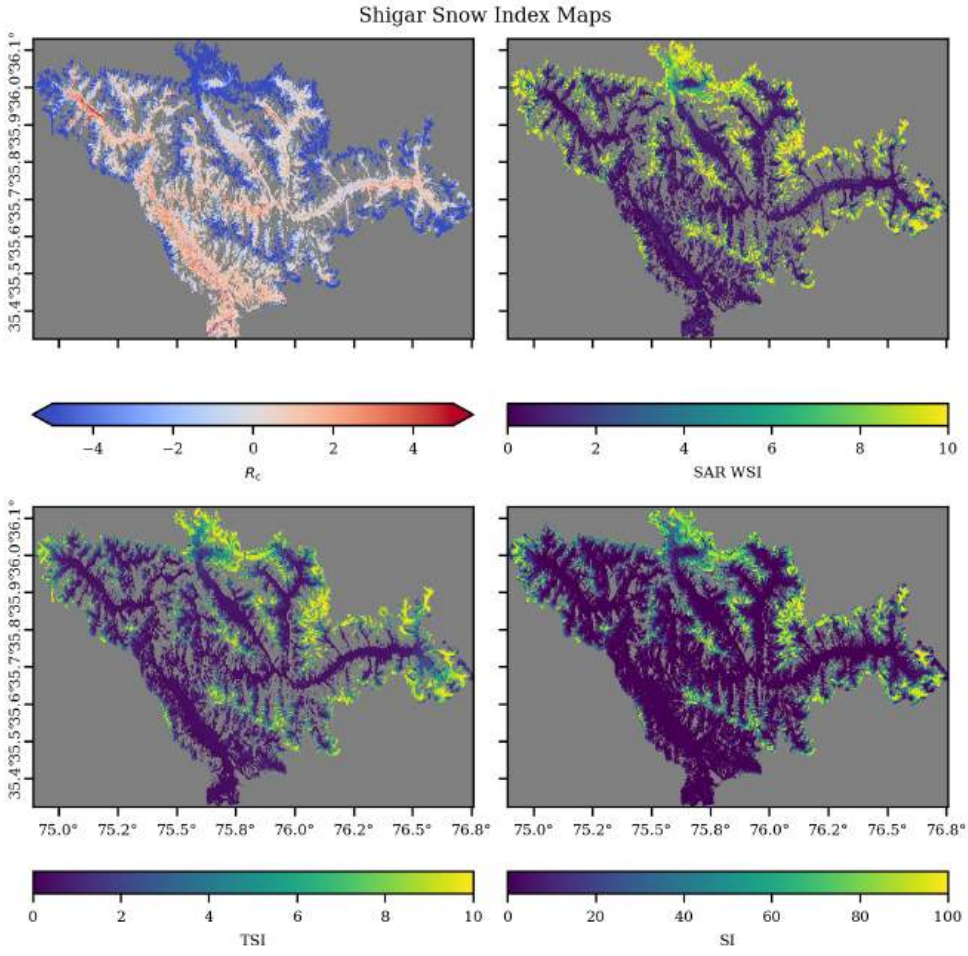

FIGURE S3.14: R_c, WSI, TSI and SI maps of Shigar.

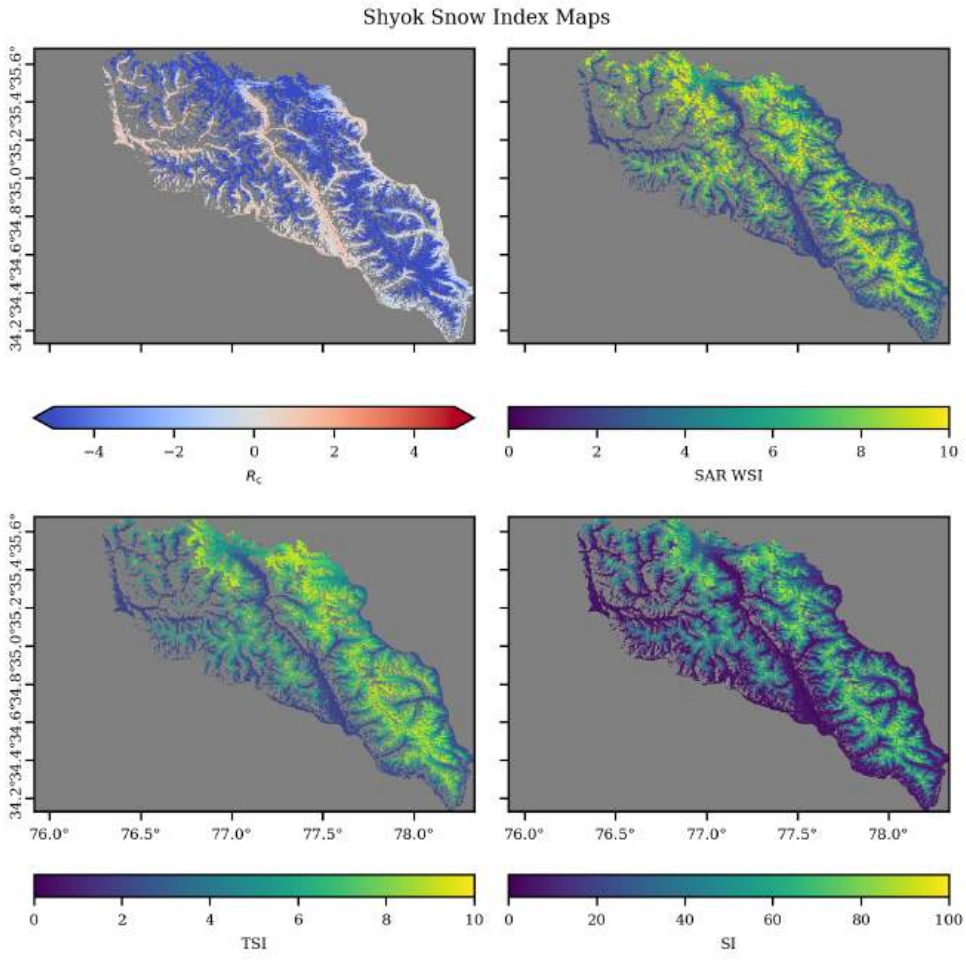

FIGURE S3.15: R_c, WSI, TSI and SI maps of Shyok.

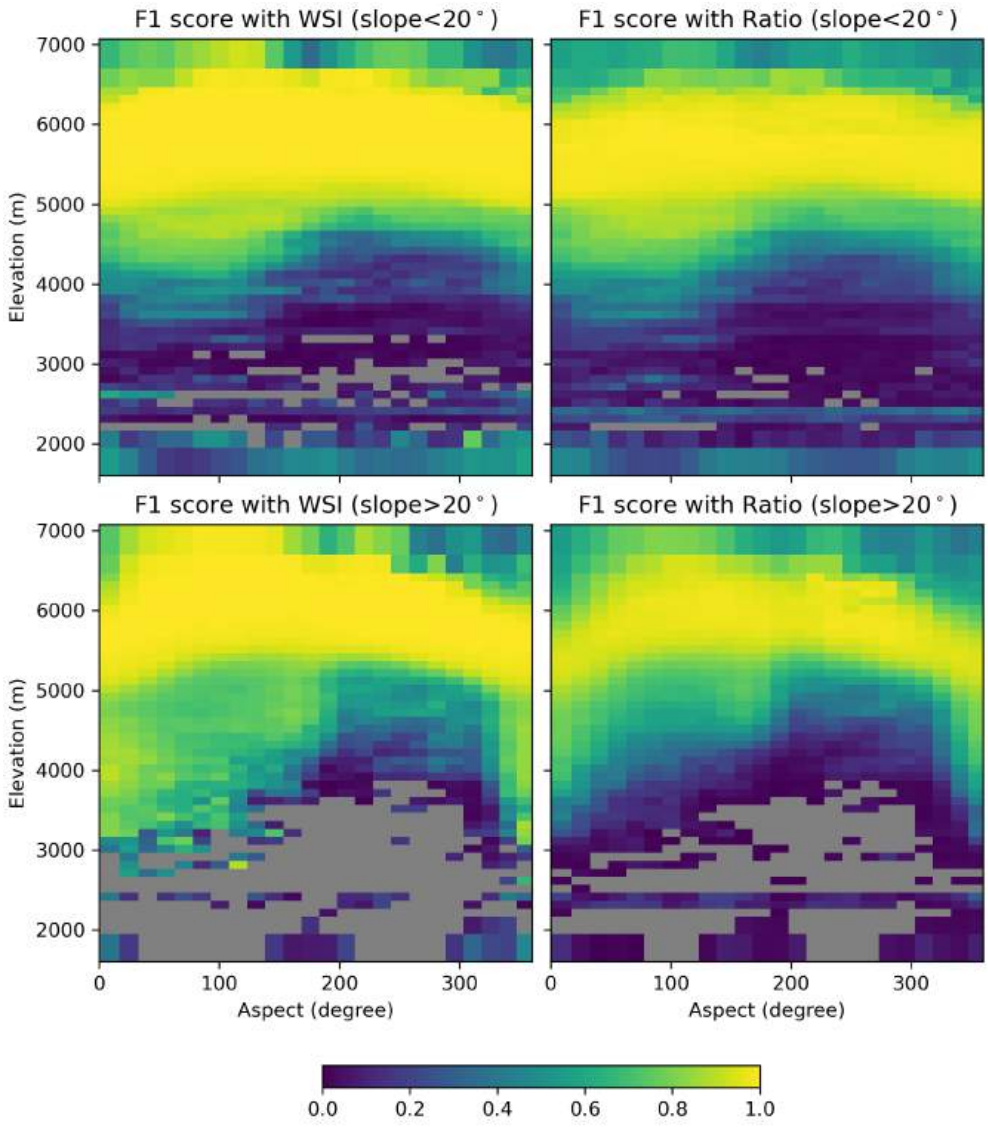

FIGURE S3.16: F1 score aggregated by topographic bins in Hunza. Top rows are with slope < 20 degrees, and bottom rows are with slope > 20 degrees. Missing values are indicated with gray.

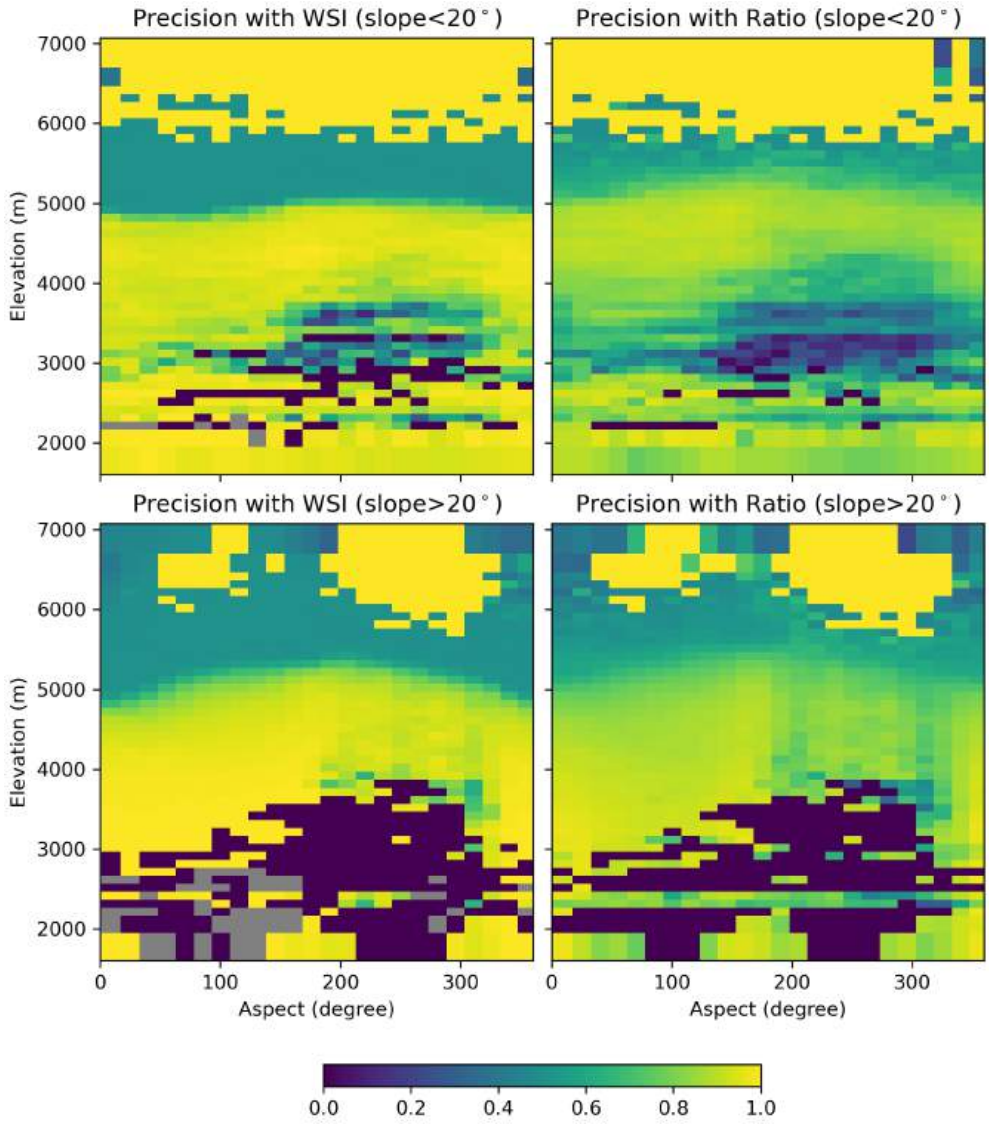

FIGURE S3.17: Precision metric aggregated by topographic bins in Hunza. Same arrangement as figure 3.16.

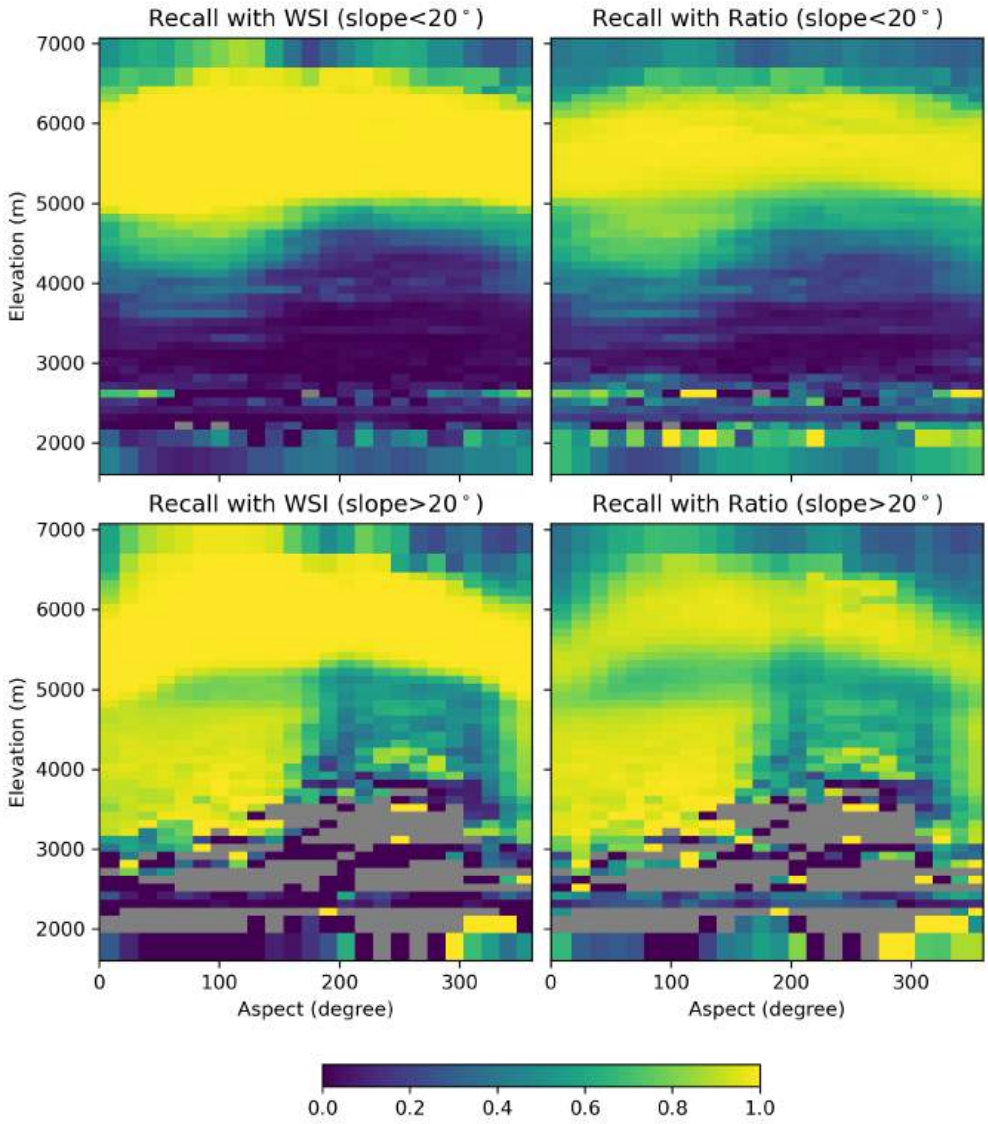

FIGURE S3.18: Recall metric aggregated by topographic bins in Hunza. Same arrangement as figure 3.16.

4

GEODETIC GLACIER MASS BALANCE IN THE KARAKORAM (2011–2019) FROM TANDEM-X: AN INSAR DEM DIFFERENCING FRAMEWORK

Shiyi Li[1], and Irena Hajnsek[1,2]

1 Institute of Environmental Engineering, ETH Zurich, Switzerland

4 Microwaves and Radar Institute, German Aerospace Center DLR, Germany

Article accepted by *Remote Sensing of Environment*

Key findings:

- Slightly thinning to near-balanced state was observed in Karakoram in 2011-2019.
- Strong heterogeneity and distinct dynamics were resolved for non- and surge glaciers.
- A comprehensive three-module framework enables scalable elevation change assessment.
- Significantly reduced the measurement uncertainty using highly accurate TanDEM-X DEM.

Author's contributions:

- Developed and implemented the presented methodology.
- Processed and analyzed the data over the study area.
- Interpreted the results and wrote the manuscript.

Co-author's contributions:

- I. Hajnsek contributed to the study design, result discussion, and revision of the manuscript.

This chapter is a pre-print of the above-listed manuscript, differing from the accepted version only in terms of layout, formatting, and citation style.

Abstract

Glaciers serve as sensitive indicators of climate change, influencing both regional water supplies and global sea-level rise. Contrasting to the global tendency towards retreat, glaciers in the Karakoram exhibits an unusual pattern of stability and modest thickening. However, the spatial variability and underlying causes of the mass balance anomalies remain insufficiently understood, primarily due to the limitations in previous measurement methods. To address this gap, we conducted a comprehensive geodetic analysis of glacier elevation changes in the central and eastern Karakoram, covering 681 glaciers of over 10,000 km^2 *between 2011 and 2019. The elevation was measured exclusively with TanDEM-X InSAR data to reduce penetration bias and temporal ambiguities. The geodetic analysis was conducted using a three-module DEM Differencing framework. In this framework, the first module generates high-quality InSAR DEM with an iterative approach to address the challenges of mountainous terrain for InSAR processing; the second module employed an innovative voids filling method using Gaussian Process Regression for robust elevation change mapping; and the third module incorporates a non-stationary uncertainty analysis for rigorous uncertainty quantification. The results reveal a regional mean elevation change rate of* 0.0038 ± 0.0042 $\mathrm{m/yr}$ *and a specific mass balance of* 0.0032 ± 0.0052 $\mathrm{m\ w.e.\ yr^{-1}}$*, indicating slight overall thickening during the study period. The spatial patterns of elevation change display pronounced heterogeneity and clear differences between surge-type and non-surge glaciers, reflecting the complex interplay of dynamic, climatic, and morphological factors in the region. This study demonstrates the capability of high-resolution TanDME-X InSAR DEM for accurate geodetic mass balance analysis in challenging mountain environments. The proposed framework provides a scalable methodology for future large-scale glacier studies.*

Keywords

Karakoram, Glacier Elevation Change, Mass Balance, TanDEM-X, InSAR

4.1 Introduction

Glaciers are vital components of the Earth's cryosphere, playing a key role in regional hydrology and serving as sensitive indicators of climate change [1]. The glacier mass balance reflects the difference between ice accumulation and ablation, offering crucial insights for understanding glacier dynamics and their response to climatic variability [2–5]. Studying the mass balance also plays an essential role for assessing a broader environmental processes

such as water resource availability, ecosystem functioning, and the impacts of climate change on vulnerable mountain communities [6–11].

Recent studies have documented a consistent trend of global glacier mass loss and ice thinning over the past few decades. For instance, Hugonnet *et al.* [9] reported a global glacier mass loss of 267±16 Gt/yr during 2000–2019, contributing to approximately 21±3 percent of observed sea-level rise. Similarly, Dussaillant *et al.* [12] estimated an annual loss of 172±27 Gt equivalent water since 1976, resulting in 22.7±2.3 mm of sea-level rise. More recently, Zemp *et al.* [11] reported an average annual glacier mass loss rate of -273±16 Gt/yr during 2000–2023. These findings underscore the critical role of glaciers in driving sea-level rise and highlighted the urgency of understanding regional variations in glacier behavior.

While most glaciers worldwide exhibit a general thinning trend, significant spatial variations and regional heterogeneity exist. One notable exception is the Karakoram region, part of the greater Himalaya-Karakoram-Hindukush (HKH) mountain system. The Karakoram region hosts one of the largest glaciated areas outside the polar regions, estimated from 36,845 km² to 50,750 km² [13]. This region is of particular importance due to its role in sustaining regional water resources and its unique climatic setting at the confluence of the westerlies and monsoon systems [14]. Since 1997–2001, a phenomenon known as the "Karakoram anomaly" has been observed, where many glaciers remain stable or even gain mass, contrary to the widespread retreat seen in other glacier regions [15]. This anomaly is believed to result from a combination of various factors, including regional climate variability, the influence of the westerlies, and the insulating effect of debris cover [16–18]. Understanding the Karakoram anomaly is crucial for deciphering the complex interplay between climate, glacier dynamics, and regional hydrology.

To enhance the understanding about Karakoram glaciers, large-scale digital elevation models (DEMs) have been widely used to quantify the unique mass balance dynamics in the region. Previous studies have employed DEM derived using either Synthetic Aperture Radar (SAR) or optical stereo images to measure the geodetic mass balance. For instance, Gardelle, Berthier & Arnaud [19] measured positive mass balance of $+0.11 \pm 0.22$ m yr^{-1} for 5,616 km² glaciated area in the central Karakoram during 1999-2008 using DEM obtained from the Shuttle Radar Topography Mission (SRTM) and stereoscopic SPOT-5 imagery. Seasonal difference in the elevation change trends were identified using ICESat time series from 2003 to 2008/09, including positive trends ($+0.41 \pm 0.04$ m yr^{-1}) in winter and slightly negative trends (-0.07 ± 0.04 m yr^{-1}) in autumn [20]. Similarly, Rankl & Braun [21] analyzed

71 glaciers in the central Karakoram (2000-2012) using high-quality DEMs from the TanDEM-X Mission, finding significant distinctions in mass changes for surge (-0.15 ± 0.10 m w.e.yr^{-1}) and non-surge (-0.07 ± 0.10 m w.e.yr^{-1}) glaciers. More recent studies using optical stereo DEMs (2000–2016) have measured GMB of -0.03 ± 0.07 m w.e.yr^{-1} for the region and confirmed that the Karakoram anomaly extends to the western Kunlun and eastern Pamir regions [22], with updated analysis showing positive ($+0.12 \pm 0.14$ m w.e.yr^{-1}) and negative (-0.24 ± 0.11 m w.e.yr^{-1}) mass balance for the central and Eastern Karakoram in 2008-2016, respectively [23].

Despite these valuable contributions, there remains limitations in current methodologies to obtain accurate and contemporary elevation change measurements in Karakoram. Comparing to optical stereo DEMs, generating DEM with the Interferometric SAR (InSAR) technique has the advantage of having higher spatial resolution and vertical accuracy. However, current InSAR based DEM often relies on SRTM data acquired in 2000 and TanDEM-X DEMs collected between 2011 and 2013. Such restricted temporal span has greatly limited the contemporary assessments of glacier dynamics with InSAR DEM. Integrating optical stereo DEM with InSAR DEM can alleviate such limitation, but the discrepancy in the penetration of the two types of sensors may introduce extra systematic bias and uncertainties [24, 25].

To address these limitations and produce high-resolution, contemporary measurements of glacier elevation changes using InSAR data, we exploited TanDEM-X InSAR dataset acquired during its two global missions, including the first mission in 2011-2013 and the second mission in 2017-2020 [26]. By exclusively using InSAR DEM of the same sensor, we can avoid the penetration bias that is often introduced when combining TanDEM-X with SRTM or optical DEMs [27, 28]. In our work, the InSAR DEM were generated by the raw acquisitions from TanDEM-X individually, which preserved the timestamp of each acquisition and reduced temporal ambiguities. However, using exclusive InSAR data for regional elevation change mapping introduces new challenges for spatial coverage, as the complex terrain of the Karakoram causes large voids in the InSAR DEM due to shadowing, layover, and low coherence. To address this challenge, we developed a Gaussian Process Regression (GPR) method for void filling, enabling robust preservation of the spatial patterns while reconstructing the missing data. We further implemented an uncertainty propagation framework to account for the non-stationarity and spatial correlations of uncertainties.

Through these efforts, we seek to present the recent patterns of elevation and mass change in the Karakoram region during the 2011-2019 period by

leveraging the advanced capabilities of the TanDEM-X mission. This can contribute to a better understanding of the Karakoram anomaly and its implications for regional hydrology and climate systems. Additionally, our methodological improvements in DEM generation and void filling can serve as a valuable reference for future studies of glacier mass balance in complex mountain environments.

4.2 Study Region and Dataset

4.2.1 Study region

The specific study region lies within 34.10°N to 36.53°N and 74.25°E to 78.95°E, covering the central and eastern Karakoram range (Fig. 4.1). The altitude of the region ranges from about 1000 to more than 8500 m above sea level (m a.s.l.), with a mean altitude of 4580 m a.s.l. The climatic regime is primarily influenced by the mid-latitude westerlies, with a secondary contribution from the South Asian monsoon [29]. The westerlies dominate during the winter and spring, delivering the majority of the annual snowfall, while the monsoon provides limited precipitation during the summer. Pronounced seasonal temperature variations drive surface melt during summer and snow accumulation during winter [30].

Glaciers in this region span a wide range of elevations, from approximately 3000 to over 7500 m a.s.l., with 60 to 80 % of the glaciated area located between 3800 and 5800 m a.s.l. [32]. The Karakoram is notable for its distinct glacier dynamics, including frequent surge events characterized by episodic, rapid advances of glacier fronts [32–34]. Debris-covered glaciers are also widespread in the region and exhibit lower mass loss rates compared to clean-ice glaciers due to the insulating effect of debris layers [35]. The interplay of debris cover, steep topographic gradients, and surge dynamics contributes to the spatial heterogeneity of glacier mass balance across the region.

4.2.2 TanDEM-X data

The TanDEM-X mission, launched by the German Aerospace Center (DLR) in June 2010, was designed to generate a consistent global DEM with unprecedented accuracy using an innovative bi-static satellite formation [36, 37]. The mission's SAR instrument operates in the X-band frequency (9.65 GHz), offering less ground penetration compared to C-band instruments such as SRTM. The initial global DEM acquisition was completed between 2011 and 2014. Building on the mission's stable performance, a new global mission — later referred to as the DEM 2020 mission — was conducted between 2017

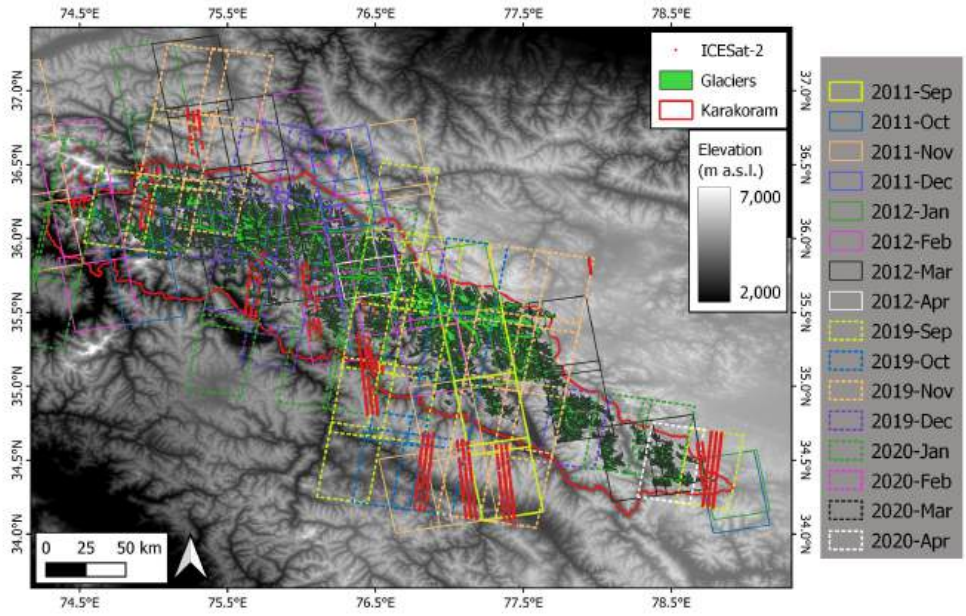

FIGURE 4.1: Overview of the study region and datasets. The Karakoram region is outlined in red, representing the study area. The footprints of individual TanDEM-X acquisitions are displayed as with color-coded rectangles. Glacier outlines (green) are sourced from the Randolph Glacier Inventory (RGI) v7.0 database [31]. ICESat-2 measurements are represented by red dots. The background grayscale shading indicates elevation measured by the Copernicus Global 1-arc-second (COP-30) DEM.

and 2020, facilitating the measurement of surface changes on Earth between the two global missions [26, 38].

In both mission phases, the TanDEM-X SAR satellites collected Co-registered Single-look Slant-range Complex (CoSSC) data products for DEM generation. Each CoSSC product consists of two focused and co-registered Single Look Complex (SLC) images acquired by the twin satellites operating in bi-static InSAR strip-map mode. With InSAR processing, high-resolution DEMs can be produced from the CoSSC datasets. Each SLC image has a spatial resolution of approximately 3×3 meters in both ground range and azimuth, allowing the generation of DEMs with a spatial resolution of approximately 8×8 meters.

In this study, we leveraged the raw CoSSC datasets and generated high-resolution DEMs using the proposed InSAR processing pipeline. This approach preserved the acquisition timestamp of each DEM, thereby reducing temporal ambiguity when performing DEM differencing. To minimize seasonal effects in the mass balance calculations, only acquisitions during the accumulation period of a hydrological year (September to April) were used. Specifically, a total of 117 CoSSC images were collected for the Karakoram region, comprising 62 images acquired in 2011–2012 and 55 images in 2019–2020. The 2011 acquisitions were captured exclusively in ascending orbits, while the 2019 acquisitions were captured in descending orbits. The Height-of-Ambiguity (HOA) values ranged from 50 to 100 meters for the 2011 images and were consistently around 50 meters for the 2019 images (Fig. 4.2). The nine-year temporal gap between the two datasets satisfies the minimum five-year duration required for applying the constant volume-to-mass conversion factor [39].

4.2.3 Reference DEM

In this study, the Copernicus Global 1-arc-second (COP-30) DEM was used as the reference in the DEM generation module. Released by the European Space Agency (ESA) in 2020, the COP-30 DEM was derived from the initial global acquisitions of the TanDEM-X mission and provides a vertical Root Mean Square Error (RMSE) of 1.68 meters over flat terrain.

Beyond its exceptional vertical accuracy, the COP-30 DEM offers significant advantages when generating DEMs from TanDEM-X CoSSC data. Since it was produced using the same X-band TanDEM-X data, the penetration bias between the reference DEM and the CoSSC measurements is negligible. This eliminates the need for complex corrections related to penetration

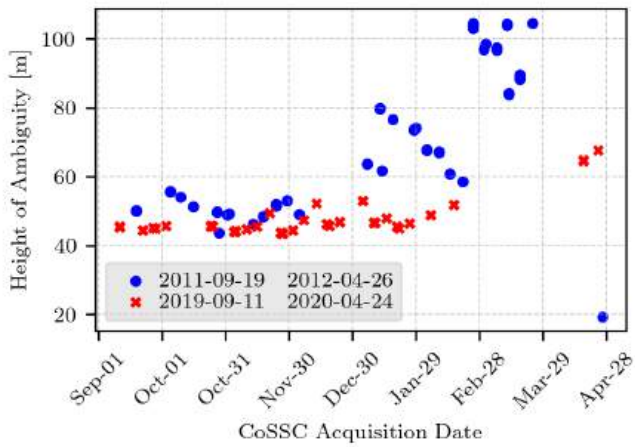

FIGURE 4.2: Height of ambiguity (HOA) of CoSSC products used in this study for 2011 winter (blue dots) and 2019 winter (red cross).

depth differences, allowing direct updates to the reference DEM through interferometric phase differences to produce the final DEM products.

The COP-30 DEM is referenced in geographic coordinates based on the World Geodetic System 1984 (WGS84), with vertical heights aligned to the EGM2008 geoid model. The dataset covering the study area was obtained through the Copernicus Space Component Data Access PANDA Catalog [40].

4.2.4 Glacier outlines

The glacier outlines used in this study were sourced from the Randolph Glacier Inventory (RGI) v7.0 [31]. Released in September 2023, the RGI v7.0 provides a comprehensive global dataset of glacier outlines, primarily representing conditions around the year 2000.

For the Karakoram region, the inventory includes 17,559 glaciers, covering a total area of 21,675 km^2. To improve the reliability of our analysis, we excluded smaller glaciers with an area less than 0.5km^2, as they are more prone to higher relative uncertainties in area measurements and contribute minimally to the overall glacier volume. Following this filtering, the final glacier inventory used for mass balance analysis consisted of 4,299 glaciers, encompassing a total area of approximately 20,000 km^2.

4.3 Methods

In this study, we developed a three-module framework to generate and analyze glacier elevation change rates (dh/dt) and mass balance in Karakoram (Fig. 4.3). Module 1 focuses on generating temporally accurate DEMs from individual TanDEM-X acquisitions, providing the basis for calculating elevation changes. Module 2 involves creating differential DEMs (dDEMs) by combining seasonal DEM mosaics, which are used to derive the dh/dt and mass balance. Module 3 estimates the uncertainties in dh/dt and mass balance using a non-stationary spatial framework following the method proposed by Hugonnet *et al.* [41]. The final output includes a regional dataset of glacier dh/dt and mass balance estimation. The following sections describe the details of each module.

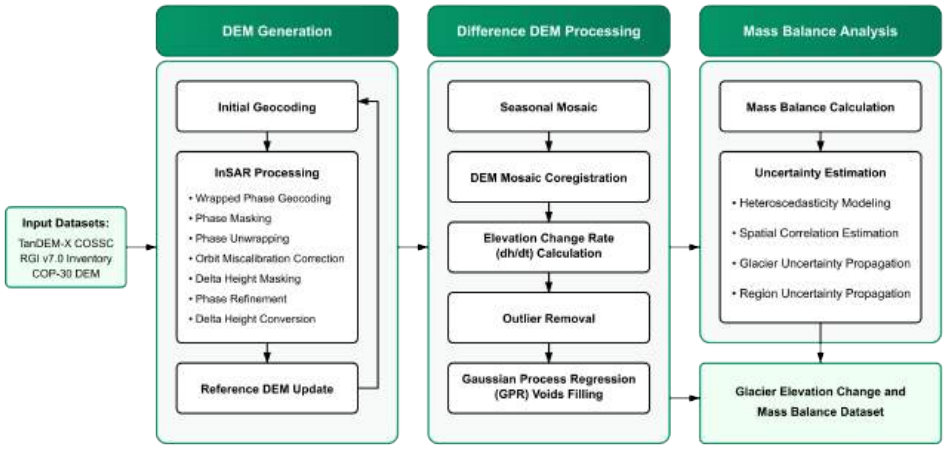

FIGURE 4.3: Flow chart of the proposed framework for this work. The framework comprises three core modules, including the DEM generation module, difference DEM processing module and the mass balance analysis module.

4.3.1 DEM generation

This section describes the detailed steps for DEM generation using a single TanDEM-X CoSSC product. The primary goal is to produce a temporally accurate DEM for each acquisition through an iterative refinement process, which ensures precise geocoding and reduces phase unwrapping errors using the residual phase derived from the CoSSC interferogram and a reference topography [42].

4.3.1.1 Residual phase decomposition

In DEM generation, the key component of the method is the residual phase between the CoSSC interferogram and the reference topography. Given an interferogram I_{CoSSC} calculated from a CoSSC product and I_{ref} simulated from the reference DEM, the residual phase can be expressed as:

$$\delta\varphi = I_{\text{CoSSC}} - I_{\text{ref}} \tag{4.1}$$

Ideally, after phase unwrapping, the residual phase $\delta\varphi$ would contain only the elevation difference between the CoSSC measurement and the reference topography. However, due to the presence of additional practical error sources, the residual phase $\delta\varphi$ should be further decomposed into the following components:

$$\delta\varphi = \delta\varphi_{\Delta h} + \delta\varphi_{\text{miscal}} + \delta\varphi_{\text{noise}} + \delta\varphi_{\text{error}} \tag{4.2}$$

where $\delta\varphi_{\Delta h}$ is the phase related to the topographic height difference, $\delta\varphi_{\text{miscal}}$ represents phase contributions from orbit mis-calibration, $\delta\varphi_{\text{noise}}$ corresponds to incoherent noise in the CoSSC data and noise in the reference DEM, and $\delta\varphi_{\text{error}}$ accounts for phase unwrapping errors.

Accurately estimating the elevation difference to refine the reference topography requires proper isolation of the phase term $\delta\varphi_{\Delta h}$ from the other error terms. To achieve this isolation, we developed a series of interferometric SAR (InSAR) processing steps, which are detailed in the following section.

4.3.1.2 InSAR processing

Before starting the InSAR processing steps, we geocoded the CoSSC images using the reference DEM to obtain an initial Look-Up Table (LUT) that converts SAR slant-range coordinates into DEM map coordinates. The geocoding process also generates the first simulated interferogram I_{ref} from the reference DEM, which is used to calculate the wrapped residual phase $\delta\varphi$.

To isolate the phase term $\delta\varphi_{\Delta h}$ from other error terms, we first used the LUT to inversely geocode the wrapped residual phase $\delta\varphi$ back into the map geometry. This step is crucial in mountainous regions to minimize unwrapping errors caused by extreme topographic features, such as steep slopes and sharp mountain peaks. Under the map geometry, we applied a coherence mask with a threshold value of 0.3 and masked out layover and shadow areas to eliminate unreliable phase data. The remaining phase data were then unwrapped using the Minimum-Cost-Flow (MCF) algorithm. To reduce phase jumps caused by large data voids, data gaps were filled with random noise prior to unwrapping. While this may introduce artifacts, it stabilizes the unwrapping process when data gaps are unavoidable.

After phase unwrapping, a quadratic polynomial phase model was fitted to the unwrapped phase map to estimate and remove phase trends caused by orbit mis-calibration. The fitted phase trend was subtracted from the unwrapped phase map, resulting in a preliminary phase map. However, extreme phase values caused by unwrapping errors may still be present and could propagate into the height difference maps. To address this, we converted the preliminary phase map into height differences Δh and created an extreme height mask to filter out unreliable phase pixels. The extreme height mask was generated by applying a threshold of $|\Delta h| > \min(10, 3\sigma_{\Delta h})$, where $\sigma_{\Delta h}$ is the standard deviation of Δh. After applying the extreme height mask, we refitted the quadratic phase model on the masked phase map and subtracted the newly fitted phase trend. This produced the corrected phase map, which successfully isolated the phase term $\delta\varphi_{\Delta h}$. Finally, the corrected phase map was converted into a height difference map Δh, which was used to update the reference DEM.

4.3.1.3 Iterative reference DEM update

In the previous step, we obtained a height difference map Δh representing the topographic height difference between the CoSSC measurement and the reference DEM. This difference arises not only from actual topographic change but also from geocoding errors introduced by the inaccurate LUT [27]. To separate the geocoding error from the actual topographic change, an iterative refinement process was applied.

In the first iteration, the initial reference DEM H_0 was updated using the height difference map Δh_1 derived from the InSAR processing steps, resulting in a corrected DEM $H_1 = H_0 + \Delta h_1$. The corrected DEM H_1 was then used to regenerate a new LUT with reduced geocoding errors. Following the same InSAR processing steps, a new height difference map Δh_2 was obtained from the corrected DEM.

In the second iteration, the DEM H_1 was updated using the new height difference map Δh_2, producing a second corrected DEM $H_2 = H_1 + \Delta h_2$. As the updated LUT from the previous iteration had already minimized geocoding errors, the geocoding step was no longer necessary. Instead, the corrected DEM H_2 was directly used to generate the simulated interferogram and calculate the residual phase. Following the InSAR processing steps, a new height difference map Δh_3 was obtained, representing the topographic difference between the CoSSC measurement and the second corrected DEM H_2.

After two iterations, geocoding errors were sufficiently reduced, and the final DEM H_3 was generated by updating the second corrected DEM H_2 with the new height difference map Δh_3:

$$H_3 = H_2 + \Delta h_3$$

This iterative process ensured that the final DEM was both accurate and free from significant geocoding errors.

4.3.2 Difference DEM processing

The individual DEMs generated from the CoSSC products were used as input in the second module for dDEM processing. This module involved a series of steps to create the regional dDEM map, including DEM mosaicking, coregistration, dh/dt calculation, outlier removal, and void filling.

4.3.2.1 Mapping the elevation change rate

To calculate the elevation change rate, the DEMs of the two study periods (2011-2012 and 2019-2020) were firstly merged to generate two seasonal DEM mosaics. Individual DEMs were re-projected onto a common grid aligned with the reference DEM to ensure proper pixel alignment. For overlapping pixels within the same grid cell, we applied a mean-merge strategy and calculated the average value of all overlapping pixels for the same grid cell. Each seasonal DEM mosaic was then co-registered to the reference DEM using the method proposed by Nuth & Kääb [43]. This step effectively reduced residual elevation errors caused by minor differences in geocoding transformations among the individual DEMs. As summarized in Table 4.1, co-registration have greatly improved the alignment between the seasonal mosaic and the reference DEM. For the 2011 winter DEM, the median elevation difference over stable regions decreased from -1.112 m to 0.016 m, with the Normalized Median Absolute Deviation (NMAD) decreased from 8.891 m to 2.456 m. Similarly, the median difference for the 2019 winter DEM was reduced from 0.486 m (NMAD: 7.058 m) to -0.044 m (NMAD: 2.183 m).

Using the two seasonal DEM mosaics, we generated the dDEM map by subtracting the 2011 winter DEM mosaic from the 2019 winter mosaic. The dh/dt map was then calculated by dividing the dDEM by the time difference between the two mosaics. Instead of using a fixed time interval, we calculated the interval for each pixel based on the timestamps of the individual DEMs used in the mosaics. This approach preserved the temporal accuracy of the dDEM and avoided ambiguities that might arise from using a fixed interval. Outliers in the dh/dt map were identified using an elevation binning method

		2011 Winter	2019 Winter
Before	Mean ± Std (m)	-1.460 ± 10.555	0.974 ± 8.554
	Median ± NMAD (m)	-1.112 ± 8.891	0.486 ± 7.058
After	Mean ± Std (m)	0.016 ± 6.893	-0.244 ± 5.759
	Median ± NMAD (m)	0.016 ± 2.456	-0.044 ± 2.183

TABLE 4.1: Comparison of seasonal DEM mosaics over stable ground before and after co-registration

[23]. For each 100-meter elevation bin, values deviating by more than ±3 NMAD from the median were masked as outliers. Pixels on slopes steeper than 40° were excluded from the calculation of median and NMAD values within each bin to reduce the impact of unreliable measurements.

4.3.2.2 Voids filling using Gaussian process regression

The generated dh/dt map exhibited substantial data gaps, primarily due to insufficient SAR acquisitions during the study period, low coherence in certain regions, and geometric effects such as layover and shadow. To ensure temporal consistency in the dh/dt map, we did not use DEMs from other years for void filling, as this could introduce temporal mismatches and ambiguity. Although hypsometric interpolation is a widely used alternative [9, 23, 44, 45], it often fails to accurately reconstruct large voids, particularly in complex glacier systems like those in the Karakoram.

To address these challenges, we adopted GPR for void filling, leveraging its ability to model spatially correlated data and to quantify prediction uncertainty [46]. Unlike deterministic interpolation methods, GPR provides both mean predictions and associated uncertainty estimates, thereby enhancing the interpretability and reliability of the reconstructed dh/dt values.

Given the strong influence of topography on glacier elevation changes, we modeled dh/dt as a function of several observable features, including the absolute elevation (h), terrain slope (α), aspect (θ), and spatial coordinates (x, y). The relationship is expressed as:

$$dh/dt = f(h, \alpha, \theta, x, y) + \epsilon \tag{4.3}$$

where $\epsilon \sim \mathcal{N}(0, \sigma^2)$ is the residual Gaussian noise. The function $f(\cdot)$ can be expressed as a Gaussian process defined by its mean function $m(\mathrm{X})$ and covariance function $k(\mathrm{X}, \mathrm{X}')$:

$$f(\mathrm{X}) \sim \mathcal{GP}(m(\mathrm{X}), k(\mathrm{X}, \mathrm{X}')) \tag{4.4}$$

where $X = [h, \alpha, \theta, x, y]$ is the input feature vector. These features were selected based on their established relevance to glacier surface processes; however, future work could explore additional predictors such as curvature or distance from glacier centerline.

For the mean function, we set $m(\mathbf{X}) = 0$. The covariance function was defined as a sum of a Radial Basis Function (RBF) kernel and a Matérn kernel with $\nu = 1.5$, allowing the model to capture both smooth, large-scale and moderate, local variations in dh/dt. This hybrid kernel configuration was chosen based on preliminary experiments and previous literature, which indicate improved flexibility for representing glacier surface variability.

To account for glacier-specific dynamics, we trained a separate GPR model for each glacier. For each glacier, a stack of gridded features $(h, \alpha, \theta, x, y)$ was extracted from the reference DEM, paired with corresponding observed dh/dt values. Only pixels with measured dh/dt were used for model training and validation, while pixels with missing values were reserved for inference. To minimize spatial autocorrelation between training and validation sets, we employed a spatially stratified split: 80% of available pixels were randomly selected for training and 20% for validation, ensuring spatial independence where possible. To ensure computational efficiency, the training and validation sets were capped at 30,000 and 3,000 pixels, respectively. All input features and target values were standardized to zero mean and unit variance prior to modeling.

The GPR models were trained by maximizing the exact marginal log likelihood (MLL), using the Adam optimizer with a learning rate of 0.01 and a maximum of 1,000 epochs. Early stopping was applied with a patience threshold of 100 epochs, based on validation root-mean-squared error (RMSE). We set a fixed random seed for reproducibility and used gpytorch for model implementation, leveraging GPU acceleration to reduce computation time [47]. Model performance was primarily evaluated using RMSE on the validation set. We also computed mean absolute error (MAE) and coefficient of determination (R^2) to provide a more comprehensive assessment.

After training, the GPR model was used to infer both the mean and standard deviation of dh/dt in void regions. This probabilistic approach ensured that the void-filled dh/dt map not only reconstructed missing values but also provided pixel-wise uncertainty estimates, thus improving the reliability and interpretability of the final product.

4.3.3 Glacier mass balance analysis

Using the measured dh/dt map, the glacier-wide specific mass balance ($\bar{b}$) was calculated for individual glaciers in the study region. To avoid unreliable calculations, we limited the mass balance analysis to glaciers with an area larger than 1 km² and a minimum measurement coverage ratio of 30%. This resulted in 681 glaciers included in the analysis, with a total area of 10963.29 km².

For each glacier, the specific mass balance of glacier i is calculated using the mean dh/dt ($\overline{\frac{dh}{dt}}$) over the glacier, as expressed in Eq. (4.5):

$$\bar{b}_i = \rho \cdot \frac{1}{N} \sum_{i=1}^{N} \frac{dh}{dt}_i \tag{4.5}$$

where $\rho = 850 \pm 60$ kg/m³ is the volume-to-mass conversion factor [39], N is the number of pixels within the glacier outline obtained from the RGI v7.0 dataset, and $\left(\frac{dh}{dt}\right)_i$ is the dh/dt value at pixel i.

The regional mass balance was calculated using the area-weighted mean dh/dt of all glaciers in the study region, as expressed in Eq. (4.6):

$$\bar{b}_{\text{region}} = \rho \cdot \frac{\sum_i^N A_i \cdot \overline{\frac{dh}{dt}}_i}{\sum_i^N A_i} \tag{4.6}$$

where A_i is the area of glacier i, $\overline{\frac{dh}{dt}}_i$ is the mean dh/dt of glacier i and N is the number of glaciers in the study region.

4.3.3.1 Glacier-wide uncertainty propagation

The uncertainty of the glacier-wide mass balance was calculated considering the uncertainty of the mean dh/dt per glacier and the uncertainty of the volume-to-mass conversion factor, as defined in Eq. (4.7):

$$\sigma_{\bar{b}}^2 = \left(\rho \cdot \sigma_{\overline{dh}}\right)^2 + \left(\overline{dh} \cdot \sigma_\rho\right)^2 \tag{4.7}$$

where $\sigma_{\overline{dh}}$ is the uncertainty of the mean dh/dt per glacier, and $\sigma_\rho = 60$ kg/m³ is the uncertainty of the volume-to-mass conversion factor [39].

In Eq. (4.7), the uncertainty of the glacier-wide mean dh/dt ($\sigma_{\overline{dh}}$) can be further divided into two components, including the uncertainty of the measured region $\mathcal{M}$ and the voids filled region $\mathcal{V}$, as expressed in Eq. (4.8), assuming the two uncertainties are independent:

$$\sigma_{\overline{dh},\mathcal{G}}^2 = \left(\frac{A_\mathcal{M}}{A_\mathcal{G}} \sigma_{\overline{dh},\mathcal{M}}\right)^2 + \left(\frac{A_\mathcal{V}}{A_\mathcal{G}} \sigma_{\overline{dh},\mathcal{V}}\right)^2 \tag{4.8}$$

where $A_{\mathcal{M}}$ and $A_{\mathcal{V}}$ are the areas of the measured and voids filled regions, respectively, and $A_{\mathcal{G}}$ is the total glacier area.

4.3.3.2 Uncertainty propagation in measured regions

To quantify the uncertainty of the mean dh/dt in the measured region $\mathcal{M}$, we employed a non-stationary spatial framework proposed by Hugonnet *et al.* [41]. This framework comprises three steps: standardizing errors, modeling spatial correlation, and propagating uncertainty.

Firstly, we used non-glaciated regions as proxies to quantify the systematic bias and random errors in dh/dt, with the assumption that elevation changes in these regions are negligible. By calculating the median and NMAD of dh/dt over the non-glaciated regions, we found that the median dh/dt value was -0.00024 m/yr, and the NMAD of dh/dt was 0.20 m/yr. These indicates negligible systematic bias and relatively low uncertainties in the dh/dt measurements. However, we must consider the heteroskedasticity of the dh/dt dispersion before modeling the spatial correlation of random errors [41]. Using the proxy errors, we modeled the dependence of elevation change errors on terrain slopes with an exponential curve, fitting the model using the average NMAD of dh/dt across 1-degree slope bins. Based on the heteroskedasticity model, we standardized dh/dt following Equation 4.9:

$$Z_{dh/dt} = \frac{dh/dt}{\sigma_{dh/dt}} \tag{4.9}$$

where $\sigma_{dh/dt}$ represents the modeled dispersion of dh/dt and $Z_{dh/dt}$ is the standardized dh/dt.

Secondly, the spatial correlations of dh/dt uncertainties was modeled using $Z_{dh/dt}$. To model the spatial correlation, we employed the Dowd estimator and derived the empirical variogram from the stable region. A variogram quantifies how data similarity decreases as the distance between data points increases. The Dowd estimator is expressed in Equation 4.10,

$$2\hat{\gamma}_{Z_{dh/dt}}(d) = 2.198 \cdot \text{median}\left(z(x,y) - z(x',y')\right)^2, \tag{4.10}$$

where $Z_{dh/dt}$ is the standardized dh/dt, and $z(x,y)$ and $z(x',y')$ are the standardized dh/dt of two sampled points with distance d [48]. Points in the estimator were sampled using a pairwise subsampling method proposed by Hugonnet *et al.* [41]. Compared to the classical Matern estimator, the Dowd estimator is less sensitive to outliers. Using the estimated variogram $\hat{\gamma}$, a spatially continuous variogram γ was fitted using a long-short range model,

in which a Gaussian model and a Spherical model were employed to account for the short and long range correlations, respectively.

Finally, with the continuous variogram model γ , the uncertainties for the mean dh/dt of a glacier can be propagated using an exact analytical solution as shown in Equation 4.11:

$$\sigma^2_{\overline{dh}} = \frac{1}{N^2} \sum_{i=1}^{N} \sum_{j=1}^{N} \sigma_i \sigma_j (1 - \gamma(d_{ij})) \tag{4.11}$$

where N is the number of pixels within the glacier outline, σ_i and σ_j are uncertainties of dh/dt at pixel i and j, respectively, and d_{ij} is the distance between pixel i and j. However, this analytical solution is computationally expensive for large glaciers. To address this, an approximate method proposed by [41] was adopted to reduce the computational cost while maintaining accuracy. This approximation uses a random subset of K pixels and is expressed as:

$$\sigma^2_{\overline{dh}} \approx \frac{1}{N^2 \cdot K} \sum_{i=1}^{N} \sigma^2_{dh,i} \cdot \sum_{k=1}^{K} \sum_{i=1}^{N} (1 - \gamma(x_k - x_i)) \tag{4.12}$$

where K is a random subset with k pixels, and x_k and x_i are the locations of pixel k and i, respectively.

4.3.3.3 Uncertainty propagation in void regions

For the voids filled region $\mathcal{V}$, we used the covariance matrix of the GRP model $k(X, X')$ to propagate the uncertainty for the mean dh/dt of the voids filled region following Eq. (4.13):

$$\sigma^2_{\overline{dh},\mathcal{V}} = \frac{1}{N^2_{\mathcal{V}}} \sum_{i=1}^{N_{\mathcal{V}}} \sum_{j=1}^{N_{\mathcal{V}}} k(x_i, x_j) \tag{4.13}$$

where $N_{\mathcal{V}}$ is the number of pixels within the voids filled region. In practice, $k(x_i, x_j)$ on large glaciers was not feasible to calculate due to the large number of pixels. To address this, we used a random subset of K pixels to approximate the covariance matrix, assuming the covariance structure is stationary.

4.3.3.4 Regional mass balance uncertainty propagation

To propagate the mass balance uncertainty from glacier-wide to regional scale, the uncertainty of glacier areas (σ_{A_i}) needed to be included additional to the uncertainty of the mean dh/dt ($\sigma_{\overline{dh}}$) and the volume-to-mass conversion factor

(σ_ρ). Assuming the three uncertainty sources are independent, the uncertainty of the regional mass balance can be expressed as:

$$\sigma^2_{\bar{b}_{\text{region}}} = \left(\rho \cdot \sigma_{\overline{dh}_\Sigma}\right)^2 + \left(\overline{dh}_\Sigma \cdot \sigma_\rho\right)^2 \tag{4.14}$$

where $\sigma_{\overline{dh}_\Sigma}$ is the uncertainty of the area-weighted mean dh/dt of all glaciers in the study region.

The uncertainty of the area-weighted mean dh/dt can be calculated using the following equation:

$$\sigma^2_{\overline{dh}_\Sigma} = \frac{1}{(\sum A_i)^2}\left[\sum_i^N \left(\overline{dh}_i - \overline{dh}_\Sigma\right)^2 \sigma^2_{A_i} + \sum_i^N \sum_j^N A_i A_j \text{Cov}(\overline{dh}_i, \overline{dh}_j)\right] \tag{4.15}$$

where $\overline{dh}_\Sigma$ is the area-weighted mean dh/dt of all glaciers in the study region, and $\text{Cov}(\overline{dh}_i, \overline{dh}_j)$ is the covariance between the mean dh/dt of glacier i and glacier j. Using again the variogram model γ, the covariance can be expressed as:

$$\text{Cov}(\overline{dh}_i, \overline{dh}_j) = \sigma_{\overline{dh}_i}\sigma_{\overline{dh}_j} - V \tag{4.16}$$

where $\sigma_{\overline{dh}_i}$ and $\sigma_{\overline{dh}_j}$ are the uncertainties of the glacier-wide mean dh/dt for glacier i and glacier j, respectively, and V is the variogram model. Detailed derivation of Eq. 4.16 can be found in 4.6.

4.4 Results

4.4.1 Glacier surface elevation change

The spatial distribution of glacier dh/dt across the Karakoram region revealed a wide range of behaviors, with both thinning and thickening observed across the 681 glaciers analyzed (Fig. 4.4). The average dh/dt across the region was 0.0038 ± 0.0042 m yr^{-1} (STD = 1.18), while the median dh/dt was 0.036 m yr^{-1} (NMAD = 0.47). The observed variability reflected the complex interplay of climatic and dynamic processes affecting glaciers in this region.

The regions of maximum thickening and thinning are highlighted in Fig. 4.4(a). The maximum dh/dt value, 21.44 m yr^{-1}, was observed on the Hispar Glacier (RGI2000-v7.0-G-14-21670), specifically along the glacier trunk near its Kunyang Tributary. This corresponded to a documented surge event

on the glacier's main trunk between 2013 and 2016, during which a maximum thickening of over 180 m was observed, aligning well with our dh/dt measurements [49]. Conversely, the minimum dh/dt value, -10.27 m yr^{-1}, was found on the Panmah Glacier (RGI2000-v7.0-G-14-12063), near its tributaries. The observed high rates of thinning (dh/dt) were likely a result of reduced ice flux and increased ablation during the quiescent phase of the surge cycle. Historical records indicate that several surge events occurred on these tributaries between 1995 and 2005, prior to the study period (Hewitt, 2007). Following these surges, the glacier likely entered a quiescent phase during the study period. Another notable thinning region was found on the Siachen Glacier (RGI2000-v7.0-G-14-20040, Fig. 4.4(d)), with around $-3 \sim -4$ m yr^{-1} of thinning. This anomalous elevation change was related to a rock avalanche event during 2001 and 2016 documented in Berthier & Brun [23].

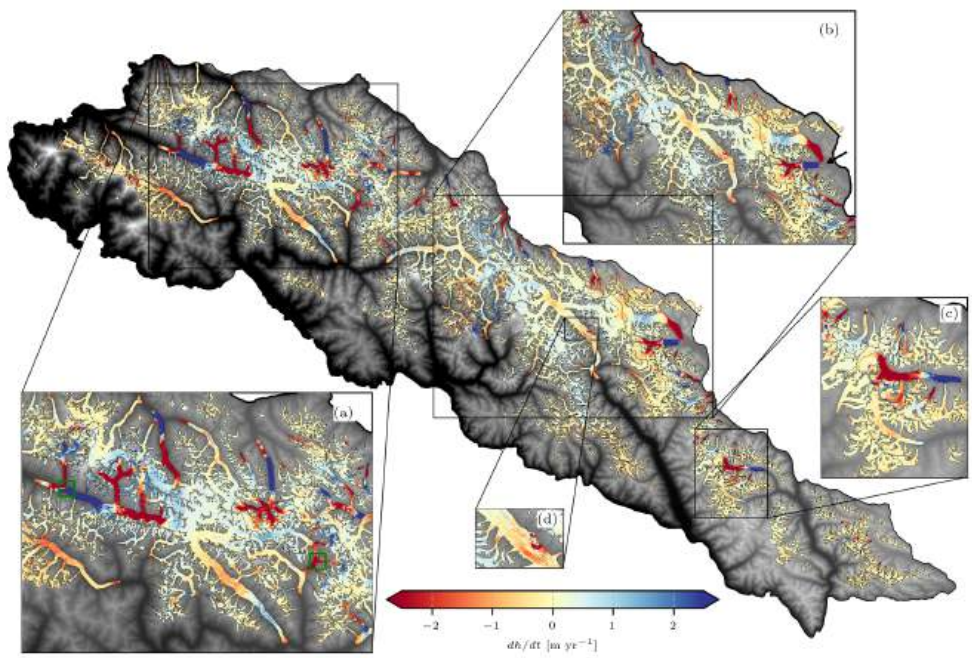

FIGURE 4.4: Spatial distribution of glacier elevation changes in the study region. The base map in the background is the COP-30 DEM used as reference. dh/dt of individual glaciers are color-coded using the color bar. Insets are zoom-in views of sub-regions to offer a closer look of local details. Green boxes in the inset (a) indicate the location of observed maximum thickening and thinning. The black arrow in the inset (b) indicates the location of the Rimo Glacier.

In the Karakoram region, surge-type glaciers are widely distributed. Their unique behaviors, which distinguish them from non-surge glaciers, making the analysis of surge-type glaciers critical for understanding regional glacier dynamics [33]. Surge glaciers are typically characterized by rapid mass redistribution events, such as advancing ice fronts and thickened lower glacier regions, followed by a quiescent phase during which ice flux is reduced and ablation dominates. In this study, surge-type glaciers were identified using the RGI v7.0 database, where glaciers are classified as observed surge, probable surge, possible surge, and no-evidence [31]. As summarized in Table 2, surge-type glaciers in the study region account for 19.23% of the total glacier population but cover 75.63% of the total glacier area. In contrast, non-surge glaciers make up 76.80% of the population but cover only 19.70% of the glaciated area. A comparison of surge-type and non-surge glaciers revealed distinct differences in their elevation change behaviors.

Category	**Population (%)**	**Area** (km^2, %)
0 - No Evidence	523 (76.80%)	2159.69 (19.70%)
1 - Possible Surge	3 (0.44%)	22.44 (0.20%)
2 - Probable Surge	24 (3.51%)	440.56 (3.02%)
3 - Observed Surge	131 (19.23%)	8340.61 (76.08%)

Table 4.2: Population size and area of glaciers in different surge categories.

During the studied period, surge-type glaciers exhibited diversified thickening and thinning in their ablation (areas of ice loss, typically at lower elevations) and accumulation zones (areas of ice gain, typically at higher elevations). Glaciers in the active surge phase generally experienced thickening in accumulation zones and thinning in ablation zones. One notable example was the South Rimo Glacier (Fig. 4.4(b), black arrow), which entered its surge phase in 2013 and experienced maximum thickening of approximately 28 m at the surge front by 2019 [50, 51]. Another example was the North Kunchhang Glacier I (Fig. 4.4(c)), which underwent a documented surge between June 2015 and June 2019 [52]. Such strong surge dynamics significantly impacted glacier mass distribution, leading to high variability in dh/dt values for surge-type glaciers. In contrary, glaciers in the post-surge recovery phase, such as the Panmah Glacier, were mostly characterized by thinning in the ablation zones but limited thickening in the accumulation zones.

Statistical analysis further highlighted the differences between surge-type and non-surge glaciers. The mean dh/dt for all surge-type glaciers (including possible and probable surge glaciers) is 0.019 ± 0.0052 m yr^{-1} (STD $= 1.32$), and the median dh/dt is 0.068 m yr^{-1} (NMAD $= 0.50$). This variability was largely driven by the dynamic processes of surging, which cause localized thickening and thinning. In contrast, non-surge glaciers were primarily influenced by climatic factors such as temperature and precipitation, which drive gradual thinning. Their mean dh/dt was -0.058 ± 0.0044 m yr^{-1} (STD $= 0.53$), and the median dh/dt was -0.054 m yr^{-1} (NMAD $= 0.35$). The narrower range of variability in non-surge glaciers reflected their more stable response to climate forcing, as opposed to the highly variable behavior of surge-type glaciers.

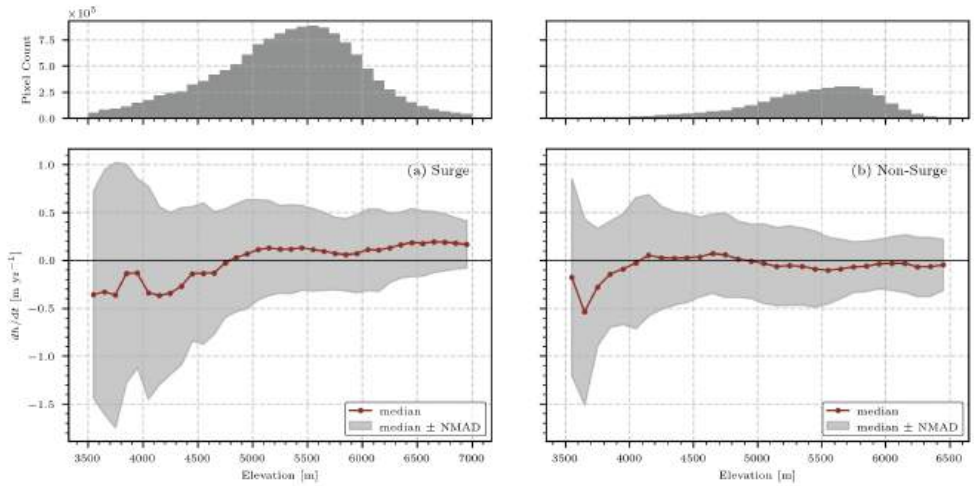

FIGURE 4.5: Dependency of glacier dh/dt on elevation for surge-type (a) and non-surge (b) glaciers. The number of pixels within each elevation bin are shown with the bar plots on top panels. The median and Normalized Median Absolute Deviation (NMAD) values of each elevation bin are shown with the red line and gray shaded area.

Distinctive patterns were also observed on the elevation dependence of dh/dt for surge and non-surge glaciers. As shown in Fig. 4.5, the median and NMAD of dh/dt were calculated for every 100 m elevation bins to capture the variability of dh/dt across different elevations. For surge glaciers, despite of the strong variability exhibiting in the data, a general transition altitude — where the median dh/dt approaches zero—was evident around 4700–4800 m a.s.l (above sea level). Below the transition altitude, the median dh/dt is

predominantly negative, reflecting thinning in the ablation zones for most surge glaciers in the region. The magnitude of thinning decreased with increasing elevation, indicating a transition toward accumulation zones. Above the transition altitude, the median dh/dt stabilized around $+0.1$ m yr^{-1}, reflecting the thickening trend within most surge glaciers. For non-surge glaciers, a similar increasing trend as surge glaciers was observed for dh/dt with elevation increasing, but the transition altitude is located at a lower regions of approximately 4200–4300 m a.s.l. Below this altitude, dh/dt values were consistently negative, indicating thinning in the ablation zones. Above the transition altitude, dh/dt values fluctuate around zero, suggesting a near-balance between mass gain and loss in these higher-elevation areas.

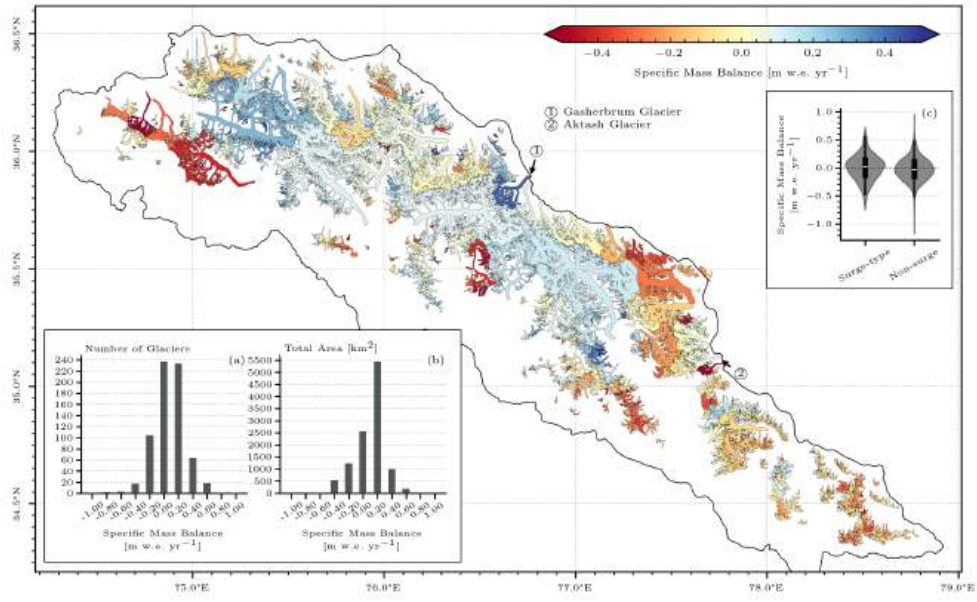

FIGURE 4.6: Spatial distribution of glacier mass balance in the Karakoram region (main panel). The population size (a) and area (b) of glaciated regions are calculated for mass balance bins between -1 to 1 m w.e. yr^{-1}. Distribution of glacier mass balance for surge-type and non-surge glaciers are shown with the violin plot (c).

4.4.2 Glacier mass balance

The area-weighted specific mass balance of the studied 681 glaciers was 0.0032 ± 0.0052 m w.e. yr^{-1}, showing a slightly positive mass balance for the

region. However, the strong spatial variability of glacier dh/dt resulted in a highly heterogeneous distribution of glacier-wide specific mass balance across the study region (Fig. 4.6). Glaciers in the eastern extent of the study area (i.e., from 77.10°E onward) generally exhibited negative mass balance. In contrast, glaciers in the central and north-western portions of the region are predominantly characterized by positive mass balance. However, a cluster of glaciers in the western extent of the region (around 75.0°E, 36.0°N) experienced significant mass loss, standing out as localized exceptions to the overall trend.

Among glaciers larger than 10 km², the Gasherbrum Glacier (RGI2000-v7.0-G-14-20459) showed the maximum mass gain, with a specific mass balance of 0.41 ± 0.044 m w.e. yr^{-1}. This glacier is a north-facing surge-type glacier with an area of 101.33 km². The most recent surge was observed between 2005 and 2007 and transited to its quiescent phase after 2008 [53]. While the exact reason for the substantial mass gain observed on the Gasherbrum Glacier remains unclear, it is likely resulted from the enhanced accumulation in the upper regions during the quiescent phase. In contrast, the glacier with the maximum mass loss is the Aktash Glacier (RGI2000-v7.0-G-14-18524), with a specific mass balance of -0.66 ± 0.070 m w.e. yr^{-1}. The Aktash Glacier is also a surge-type glacier, with an area of 24.43 km². Satellite imagery analysis reveals that this glacier has a relatively short surge cycle of approximately three years, with its most recent documented surge occurring between 2003/4 and 2009, advancing its terminus by more than 500 meters [54]. Approximate locations of the Gasherbrum and Aktash glaciers were marked on Fig. 4.6 with black arrows.

We analyzed the distribution of glacier population and area across different mass balance bins (Fig. 4.6(a) and (b)). The majority of glaciers have mass balance values within the range of -0.20 to 0.20 m w.e. yr^{-1}, with the peak population centered around 0.0 m w.e. yr^{-1}. However, the summed glacier area showed a clear bias toward positive mass balance. Specifically, more than 5000 km² of glacier area experienced slight mass gain of approximately 0.20 m w.e. yr^{-1}. This discrepancy between the distribution of glacier population and area was primarily attributed to the presence of large surge-type glaciers in the region. As illustrated in Fig. 4.6(c), surge-type glaciers exhibited a near balanced median mass change (0.0024 m w.e. yr^{-1}) and a density curve that skewed slightly towards positive. Their area-weighted specific mass balance is 0.0161 ± 0.0063 m w.e. yr^{-1}. This contrasted with non-surge glaciers, which had a negative median mass balance (-0.055 m w.e. yr^{-1}) and a slightly

negative skewed density curve. The area-weighted specific mass balance for non-surge glaciers is -0.049 ± 0.0067 m w.e. yr^{-1}.

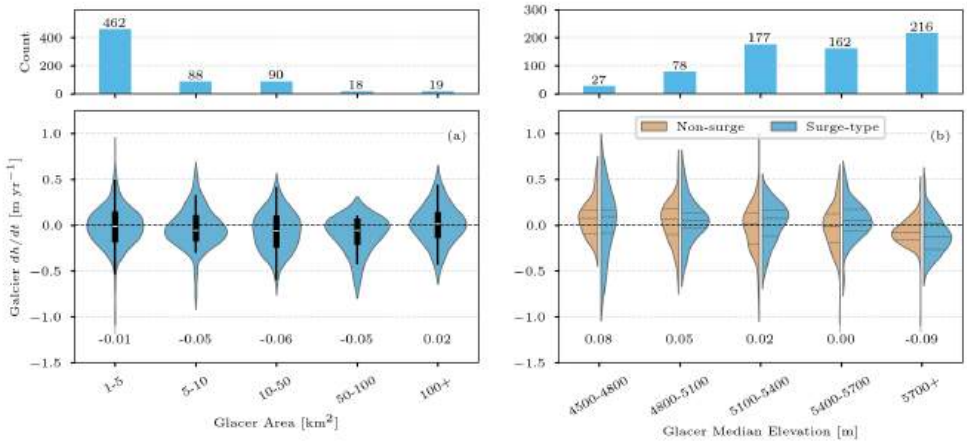

FIGURE 4.7: Mass balance distribution with respect to different (a) glacier size groups and (b) glacier median elevation groups. The top panels show the count of glaciers within the respective group. The distribution of mass balance are calculated for the entire group in panel (a), and separately for surge-type and non-surge glaciers in panel (b).

Two factors that may influence the individual glacier mass-balance variability were examined in Fig. 4.7, including glacier area and median elevation.

In the study region, the majority of glaciers fell within the smallest area category (1–5 km²), and the number of glaciers decreased exponentially with increasing glacier area. Only 19 glaciers were in the largest category (100+ km²). Smaller glaciers (1–5 km²) exhibited a median thinning rate of approximately -0.01 m w.e. yr^{-1}, while larger glaciers showed relatively stronger thinner rate at around -0.05 m w.e. yr^{-1}. The largest glaciers (100+ km²) displayed balanced mass change with the median value at approximately 0.02 m w.e. yr^{-1}). Despite the varying population of glaciers across area categories, the variance in individual glacier mass balance remained relatively consistent, with values generally ranging from -0.5 to 0.5 m w.e. yr^{-1}. While differences in skewness were observed among area categories, no clear trend toward positive or negative mass balance emerged.

For glacier median elevation, the majority of glaciers had median elevations above 5000 m a.s.l. A general stable near zero median mass balance were found for glaciers in groups of median elevations below 5400 m a.s.l., whereas strong median negative mass balance were found for glaciers in the group of

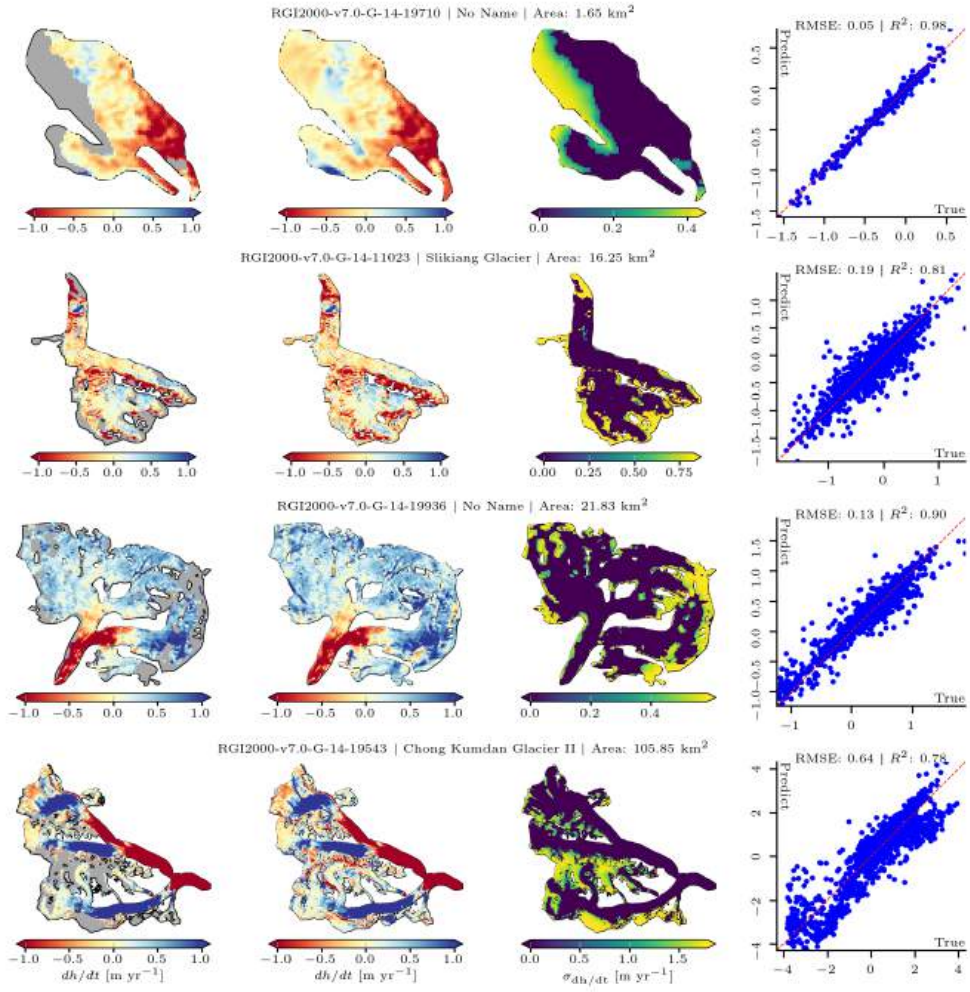

FIGURE 4.8: Example glaciers demonstrate the voids filling performance using Gaussian Process Regression (GPR). The leftmost column show original glacier dh/dt maps with voids (marked as gray shaded). The second column show dh/dt maps with voids filled using GPR models. The third column shows the distribution of voids filling uncertainties, with zero representing the measured area (i.e. no filling). The rightmost column shows the validation performance of GPR models for the respective glacier, with blue scatter dots showing the validation pixels and red line showing the 1-to-1 matching. The RGI-index, name and area of the glacier are reported on top of the respective row.

median elevations above 5700 m a.s.l. Comparing to surge-type glaciers, the median mass balance of non-surge glaciers were closer to near zero. Similar to area categories (Fig. 4.7(a)), differences in skewness were observed across elevation groups, but no clear trend toward positive or negative mass balance was apparent.

4.4.3 Voids filling evaluation

Voids filling is a crucial step in regional dh/dt mapping and geodetic mass balance measurement [44]. This step was particularly important in our study, as we avoided using DEMs from different times for voids filling to ensure no temporal ambiguity was introduced, thereby leaving relatively large voids in the dh/dt map.

Given the complex terrain and glacier dynamics in the region, we employed the GPR model to infer the missing data in voids region, taking into account the dependence of dh/dt over various terrain features. Fig. 4.8 illustrated examples of voids filling for glaciers of varying sizes. In these examples, voids were predominantly located in high-elevation regions, typically within glacier accumulation zones or near glacier edges. High-elevation regions are often characterized by steep slopes and are affected by SAR image artifacts such as shadow and layovers, leading to data gaps in these areas. To fill the missing values in such regions, it is crucial to account for the spatial distribution of missing values and ensure that the interpolation method considers the influence of topography on the distribution of glacier elevation change.

Comparing to the original dh/dt map with voids (leftmost column), the filled dh/dt maps (second column) showed that the spatial patterns of dh/dt distribution were effectively reconstructed by the GPR model. The uncertainty in the filled regions, as shown in the third column, varied across glaciers. This variability was raised because the GPR models were trained for each glacier specifically, and the inference confidence of the model depended on several factors, including the quality of training data, the density of measured samples near prediction points, and the noise level in the data. Validation results (rightmost column) indicated that the model performs well for small glaciers (area below 5 km²), achieving low RMSE and high R^2. For medium-sized glaciers, while the RMSE slightly increased, the R^2 remained high., indicating that the model continues to capture the dynamics effectively. For large glaciers, the validation RMSE showed only a moderate increase; however, the R^2 dropped below 0.8. This suggests that the model struggles to fully capture the more complex dynamics of large glaciers, which may be influenced by more diverse topographic conditions of large glaciers compared

to smaller ones. Note that the validation results presented here are obtained by dividing the measured data for each glacier into separate training and validation sets, as described in Section 3.2.2. The model is trained only on the training data, and its predictive accuracy is then evaluated on the validation data—these are real measurements that were not used during training. This approach allows us to measure how well the GPR model can predict missing values based on available data.

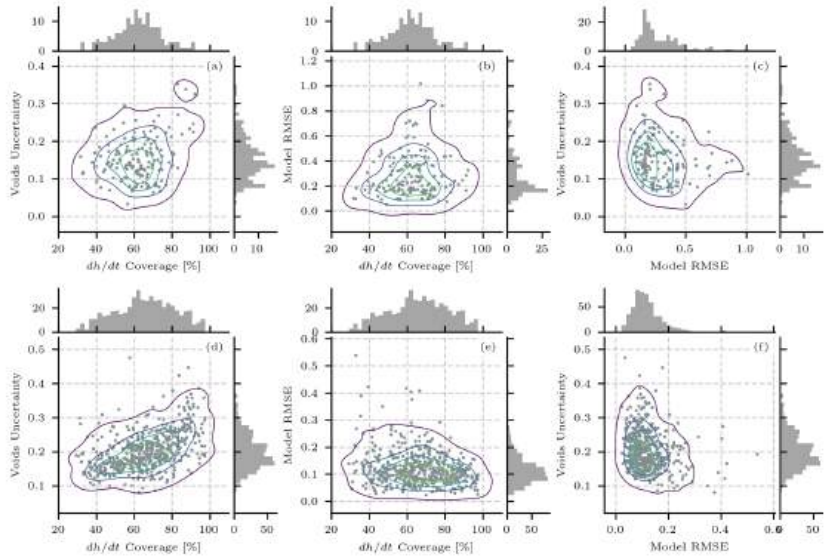

FIGURE 4.9: Distribution of (left column) voids uncertainty versus dh/dt measurement coverage, (middle column) validation Root-Mean-Squared-Error (RMSE) versus dh/dt measurement coverage, and (right column) voids uncertainty versus validation RMSE for surge-type (top row) and non-surge (bottom row) glaciers.

As shown in Fig. 4.9, we inspected the relationship between voids uncertainty, dh/dt measurement coverage, and the validation RMSE of GPR models for both surge-type (top row) and non-surge (bottom row) glaciers. For surge-type glaciers, the distribution of voids uncertainty exhibited a relatively isotropic pattern with respect to measurement coverage, suggesting that voids uncertainty was not strongly correlated with the measurement coverage. Similarly, the model validation RMSE showed a uniform pattern across different levels of measurement coverage. When examining the rela-

tionship between voids uncertainty and RMSE (Fig. 4.9c), a slight inverse correlation was observed for RMSE values between 0.0–0.5, where higher RMSE corresponded to lower voids uncertainty. For larger RMSE values (above 0.5), voids uncertainty became independent from RMSE and was concentrated between 0.1–0.2. For non-surge glaciers, voids uncertainty showed a weak and noisy positive correlation with measurement coverage. The model validation RMSE, on the other hand, does not exhibit a clear dependence on measurement coverage, with contours spread uniformly across different coverage levels. Finally, the relationship between voids uncertainty and RMSE revealed no strong dependence, as the contours were relatively uniform and do not indicate a clear trend.

This result shows that the uncertainty over the voided region does not depend on the size of the voids, nor on the overall validation accuracy of the model. This is due to the fundamental principle of how GPR model estimates uncertainty for a target variable. In GPR modeling, each predicted value is treated as a random variable described by a probability distribution, rather than a single fixed value. The shape of this distribution is determined by a kernel function, which captures the spatial correlation among all available data samples. As a result, the uncertainty provided by the GPR model is mainly influenced by the spatial distribution of the measured data points within the feature space. In the feature space, if a missing value is surrounded by many relevant and similar measurements, the model will be more confident in its prediction, resulting in lower uncertainty. Conversely, if the missing value is isolated or located in an area with unusual terrain features, the uncertainty will be higher. By incorporating various terrain features as inputs to the GPR model, we ensured that the distribution of available measurement samples in the feature space remains independent of voids size and the distribution of training samples. Consequently, the model achieves robust inference for missing values in the voids region.

4.4.4 DEM accuracy and uncertainty propagation

To validate the accuracy of the seasonal DEM mosaics, we compared the 2019 winter mosaic with ICESat-2 measurements over glacier-free surfaces. The ICESat-2 points were acquired between 2019-08-29 and 2020-04-26 and matched the time span of the second acquisition period of the CoSSC products. Points over slopes steeper than 40° were excluded due to the high uncertainty of TanDEM-X measurements in such areas. A total of 58,777 ICESat-2 points with surface slopes between 0° and 40° were used for validation. The spatial distribution of the validation points is shown in Fig. 4.1. The

comparison revealed that the ICESat-2 measurements were slightly higher than the generated DEM mosaic, with a mean difference of 0.29 m and a median difference of 0.28 m (Fig. 4.10). This discrepancy is likely due to the deeper penetration of SAR signals compared to ICESat-2 measurements [55]. The vertical accuracy of the DEM mosaic, estimated using the NMAD of elevation differences, was 3.53 m. This accuracy is lower than the typical accuracy of the COP-30 DEM, likely due to the complex terrain in the study area and the absence of post-editing steps.

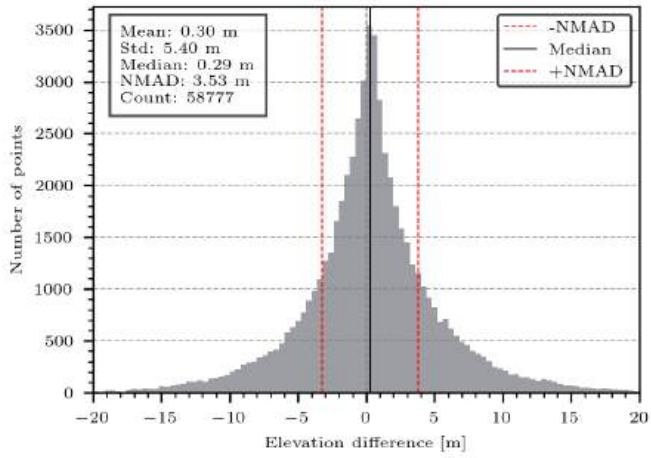

FIGURE 4.10: Distribution of elevation differences over stable ground between ICESat-2 measurements and the 2019 winter DEM mosaic. The median and ± 1 Normalized Median Absolute Deviation (NMAD) values are indicated by the black solid lines and red dashed lines, respectively.

Besides the highly accurate DEM, we also rigorously analyzed the uncertainty of the measured dh/dt using a non-stationary framework. This approach accounts for the heteroskedasticity of measurement errors in dh/dt and incorporates spatial error correlations over both short and long ranges.

As illustrated in Fig. 4.11, we investigated the relationship between dh/dt and terrain slope across non-glaciated regions. These areas revealed a clear dependence of dh/dt dispersion on slope, which is captured by the modeled exponential curve expressed in Equation 4.17:

$$\sigma_{dh/dt} = 0.018e^{(0.066\alpha)} + 0.074 \tag{4.17}$$

Here, $\sigma_{dh/dt}$ represents the dispersion of dh/dt and α denotes the terrain slope. This dependence can be attributed to the influence of local incidence

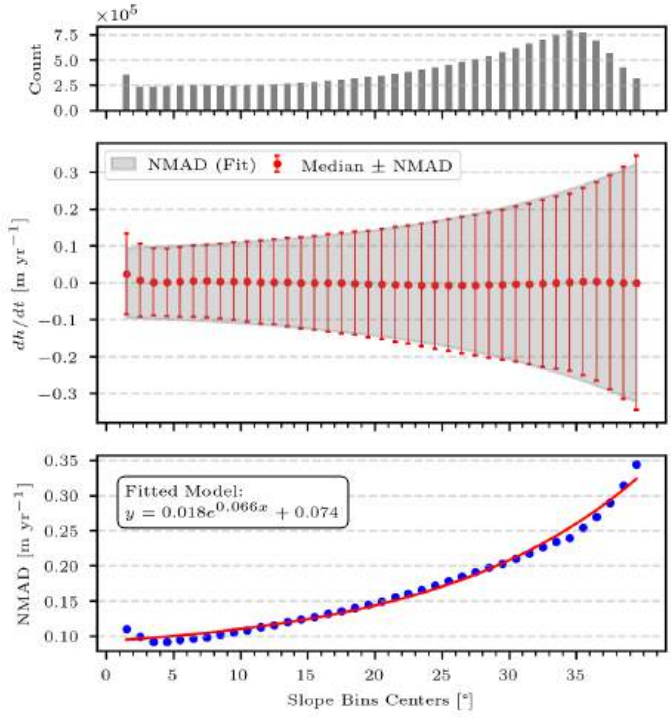

FIGURE 4.11: The dependence of dh/dt uncertainty (dispersion) on terrain slope, derived from stable regions. The dispersion is quantified using the Normalized Median Absolute Deviation (NMAD). Top: number of pixels in each slope bin. Middle: the median dh/dt in each slope bin and the NMAD shown as error bars; The fitted NMAD for each slope bin are shown with the shaded area. Bottom: the NMAD of dh/dt in each slope bin (blue dots) and the fitted exponential function for the dispersion dependence on slope (red line).

angles on the sensitivity of the interferometric phase to elevation within the InSAR system. On steeper terrain, the precision of InSAR digital elevation models (DEMs) decreases, resulting in higher dh/dt dispersion and greater uncertainty.

To further refine the analysis, we standardized dh/dt using the modeled heteroskedasticity and employed non-glaciated regions as proxies to infer spatial error correlations. The empirical variogram and its fitted continuous variogram are presented in Fig. 4.12. The spatial correlation model combines a short-range Gaussian component and a long-range Spherical component. Specifically, the Gaussian model has a range of 204.53 m and a partial sill of 0.76; the Spherical model has a range of 1590.40 m and a partial sill of 0.28. These results indicate that short-range correlations dominate the standardized dh/dt errors, but long-range correlations remain considerable. As noted by Hugonnet *et al.* [41], relying solely on short-range models may severely underestimate elevation uncertainties for areas larger than 0.1 km².

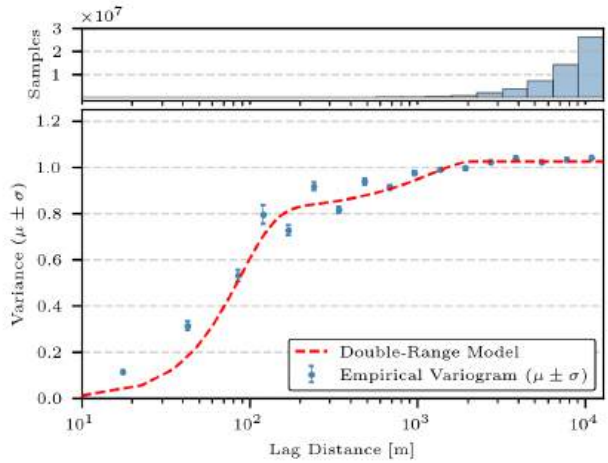

FIGURE 4.12: Spatial correlation of dh/dt uncertainty inferred from the non-glaciated regions. The bottom panel shows the spatial variogram of standardized elevation differences. The empirical variogram is based on Dowd's estimator. The fitted variogram is the sum of a short-range Gaussian model and a long-range spherical model. The top panel shows the count of samples in each distance bins.

4.5 Discussion

4.5.1 Regional mass balance in Karakoram

In Karakoram, the anomalous behavior of glacier mass balances has been identified since the 1970s, which was characterized by stable and weakly positive mass balance in the region in contrast to the mass loss observed in the Himalayas and other regions of the world [15, 16]. Benefiting from the increasingly available remote sensing data, geodetic mass balance measured by DEMs derived using LiDAR, optical stereo image pair and SAR data have provided valuable information on the mass balance of glaciers in Karakoram.

A recent review by Li *et al.* [56] summarized the changes of glacier mass balance in the Karakoram region since 1998 made by relevant studies (Fig. 4.13). Although these studies cover various temporal and spatial scales, the reported mean mass balance generally ranged between ± 0.1m w.e. yr^{-1}, indicating a near-equilibrium state for glaciers in the region. However, some recent global scale studies suggested that the anomaly of mass balance change in Karakoram was no longer as significant as before. For instance, the thickening of glaciers in central-western Asian was observed to be brought down to a generalized thinning in the late 2010s using large-scale ASTER DEMs [9], with the mean elevation change rate decreased from -0.1 ± 0.17 m/yr during 2000-2004 to -0.23 ± 0.14 m/yr in 2015-2019. The decade mean dh/dt during 2000-2019 for the region was reported to be -0.16 ± 0.06 m/yr, approximately equivalent to a specific mass balance of -0.135 ± 0.02m w.e. yr^{-1} with the assumption of a density of $\sim 850 \pm 60$ kg/m^3. A similar observation was made in the community that estimates the global glacier mass changes [11].

In our results, the regional mass balance over almost a decade (2011-2019) was estimated to be 0.0032 ± 0.0052 m w.e. yr^{-1}, demonstrating a near balance to positive trend comparing to previous studies (Fig. 4.13). Particularly, our area-weighted mass balance is strongly contrast to the negative value reported in the global scale studies. To further illustrate the difference between the results of our study and the previous work, we compared our glacier dh/dt measurements with the openly shared results from Hugonnet *et al.* [9]. The regional mass balance calculated using the Hugonnet dataset is -0.1138 m w.e. yr^{-1} for the same glaciers covered in our study. The uncertainty is not quantified as we do not have access to the spatial correlation model of the Hugonnet dataset. To understand the different mass balance for each glacier measured by our study and the Hugonnet dataset, detailed comparision is shown in Fig. 4.14. In the comparison, the histograms illustrate the overall distribution of glacier aggregated dh/dt for both studies.

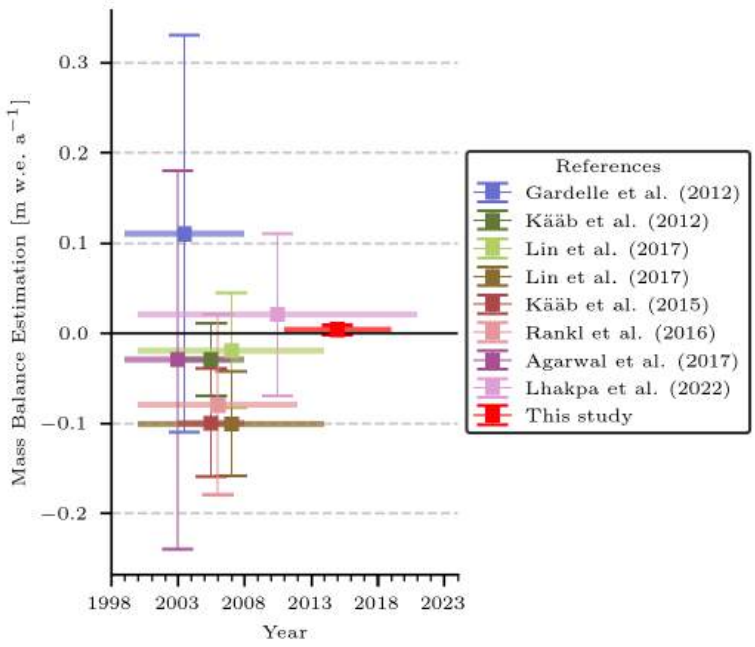

FIGURE 4.13: Comparison of the regional specific mass balance reported in relevant studies and this study. The horizontal bars represent the time periods covered by each study, and vertical bars indicate the uncertainty. References include Lhakpa, Fan & Cai [18], Gardelle, Berthier & Arnaud [19], Kääb *et al.* [20], Rankl & Braun [21], Kääb *et al.* [57], Agarwal *et al.* [58], and Lin *et al.* [59]. Result of this study is highlighted in red. The black solid line at 0 m w.e. yr^{-1} serves as a reference for no net mass change.

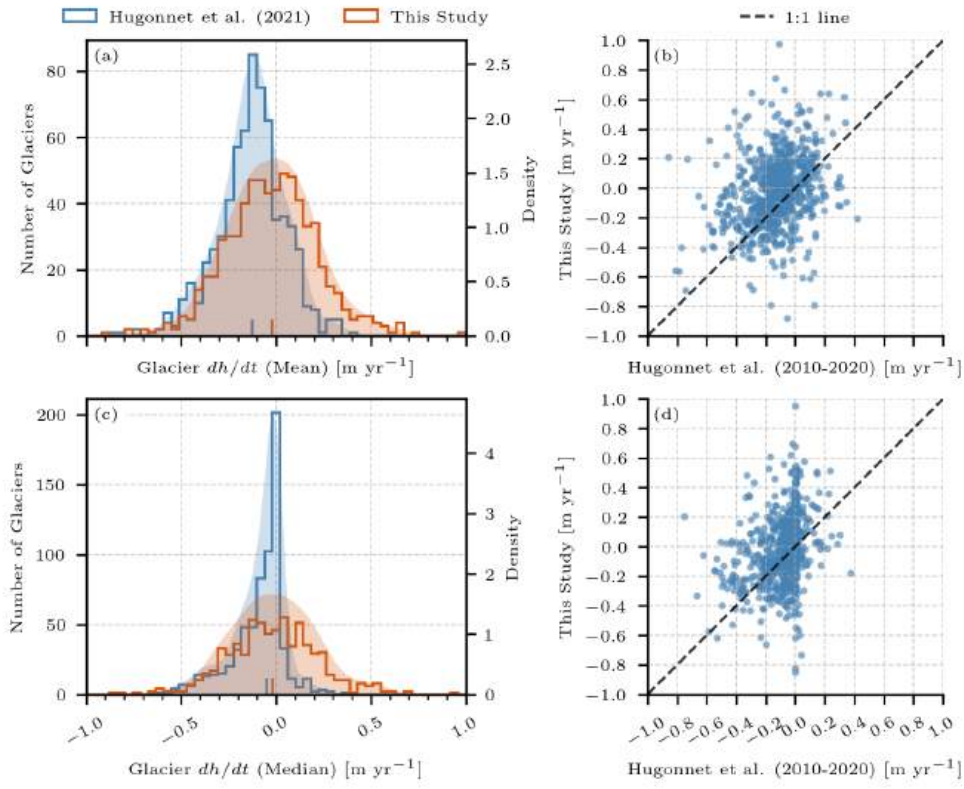

FIGURE 4.14: Comparison of glacier elevation change rates (dh/dt) between this study and the Hugonnet *et al.* [9] dataset. The top row and the bottom row shown the distribution of mean and median glacier dh/dt (a, c) and their scatterplot comparison (b, d), respectively. The histograms illustrate the number of glaciers and density for each dataset. The scatter plots include a 1:1 reference line for visual comparison.

While the distributions were largely overlapped, both the glacier-wide mean and median dh/dt of our results were slightly biased towards more positive values compared to the Hugonnet dataset. Additionally, our results exhibited slightly broader tails, indicating higher variability in glacier aggregated dh/dt. As median values were more robust to outliers, the distribution of median dh/dt values showed much less variability in both studies compared to the mean dh/dt distributions. The scatter plots provided a one-to-one comparison of glacier samples between our study and the Hugonnet dataset. For both the mean and median dh/dt, the data points were generally centered around the 1:1 line, indicating overall agreement between the two studies. However, noticeable scatterings were present, highlighting the different distribution of glacier-wide dh/dt distributions.

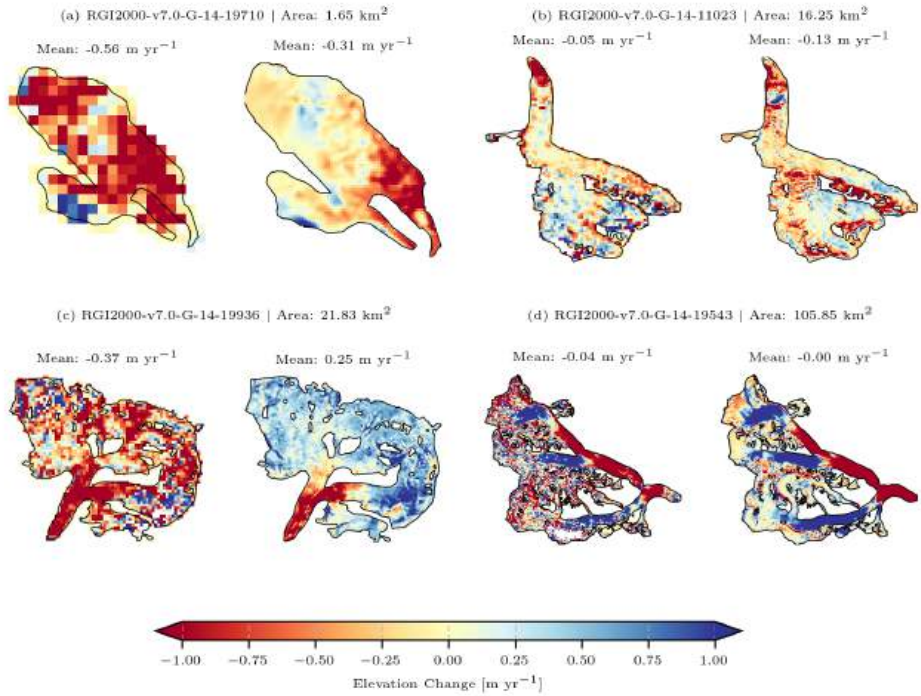

FIGURE 4.15: Elevation change rate (dh/dt) for example glaciers of varying sizes derived from this study and the dataset of Hugonnet *et al.* [9]. For each glacier in (a)-(d), the left map represents results from the dataset of Hugonnet *et al.* [9], and the right map corresponds to the results of this study. The mean dh/dt is indicated for each glacier. The color bar at the bottom illustrates the range of dh/dt.

A few example glaciers are presented in Fig. 4.15 to further illustrate the differences between the two datasets. For small and medium sized glaciers (Fig. 4.15 (a) and (b)), both dh/dt maps showed consistent and comparable spatial patterns. For instance, strong thinning was observed at similar locations in both datasets. However, our results resolved finer-scale variations, such as crevasses and isolated zones of thinning and thickening, which were smoothed out in the Hugonnet dataset due to the coarser resolution. For surge-type glaciers (Fig. 4.15 (c) and (d)), both studies captured the general thickening-thinning patterns along the main trunk of the glaciers. However, notable differences were observed in the accumulation zones. For the glacier in Fig. 4.15(c), our dh/dt map showed general positive elevation changes in the accumulation region, while the Hugonnet dataset exhibited substantial variability and large areas of negative elevation change. This discrepancy results in a positive glacier-wide mean dh/dt in our study, whereas the Hugonnet dataset yielded a negative mean dh/dt. A similar pattern was observed for the glacier in Fig. 4.15(d), where our results showed balanced or slightly positive elevation changes across the accumulation zone, and the Hugonnet dataset showed large variability with extensive areas of negative elevation changes.

The difference observed in the above comparison can be explained by the different data and methods used for the analysis. In the Hugonnet dataset, the elevation change was estimated using a multi-year time-series fitting approach with ASTER DEMs for the period 2000–2019. The dh/dt map for individual glaciers were provided with 100m resolution. In our study, we employed only the TanDEM-X data acquired in two operational phases (2011-2014 and 2015-2019) to avoid introducing artifacts caused by system bias and seasonal ambiguities. The former method is more robust in estimating the trend of mass changes, while our results preserved better temporal sensitivity and spatial variability. Besides, the Hugonnet dataset was produced using the ASTER DEM and relied on data interpolation to fill the spatial-temporal data gaps caused by cloud contamination. The interpolation process may introduce additional uncertainties and smooth out fine-scale spatial patterns, particularly in accumulation zones where elevation changes are generally smaller and more variable. In contrast, our use of TanDEM-X data, which offers stronger penetration capabilities through cloud, provides more reliable elevation measurements with less interference. Thus, the choice of data and processing methods may play a significant role in the reported mass balance differences. Considering the varying analysis performed in different studies, further investigation is needed to reconcile differences

across studies, integrate diverse datasets and methodologies, and derive consensus estimates [11].

4.5.2 Spatial variability of elevation and mass change

Benefiting from the high-resolution TanDEM-X CoSSC data, detailed maps of glacier dh/dt and mass balance were generated for over 10,000 km² of glacier covered area in Karakoram. The dh/dt map revealed the highly heterogeneous spatial distribution of glacier elevations changes in the region. From the dh/dt map, the spatial variability of elevations changes is observed to be predominantly contributed by the surge-type glaciers. Previous studies have reported that surging events in Karakoram were expanding and increasing, coincident with the positive glacier mass balance in the region [60]. A similar observation was made in our study, where the statistical analysis on dh/dt showed that surge-type glaciers in the region are generally in a near-equilibrium or positive mass balance state, while non-surge glaciers mostly experienced thinning and mass loss. Another notable observation from the dh/dt map is the varied surge-phase that the surge-type glaciers experienced. Glaciers experiencing (or just finished) the active surge phase mostly have large thickening close to the glacier front and strong thinning in their accumulation zones. In contrary, glaciers in the quiescent or post-surge recovery phase generally showed thinning in their middle and lower parts, with thickening observed in the upper reach. Example surge-type glaciers of such contradicting behaviors can be found in Fig. 4.4(b).

Besides the spatial heterogeneity, the distribution of elevation change along altitude also demonstrates distinctive behavior between surge-type and non-surge glaciers. Overall, both glacier types exhibit a similar trend of decreased thinning rates with increasing elevation. This altitude-dependent pattern has been widely documented in previous studies [22, 61, 62], and reflects the transition from ablation zones, where mass loss dominates, to accumulation zones, where mass gain increases. The thickening or near-balanced state observed at higher elevations may serve as an indicator of the overall mass balance condition. However, our results reveal a notable difference in between surge and non-surge glaciers. The transition altitude for surge glaciers is located at a higher altitude (4700–4800 m a.s.l.) compared to non-surge glaciers (4200–4300 m a.s.l.), suggesting distinct mass balance regimes influenced by glacier dynamics. Moreover, the altitude dependence of elevation change is known to be strongly influenced by localized glacier dynamics, morphological features, and climate regimes [22]. For instance, thick debris cover or delayed adjustment to balance velocities could alter thinning or

thickening trends at specific elevations, as observed in other regions such as Bhutan and Kunlun [22]. These localized factors highlight the complexity of interpreting elevation-dependent mass balance trends across large regions. Further investigation, particularly through coupling with glaciological models, could provide deeper insights into the elevation dependence of glacier mass balance [63].

It is important to note that the classification of surge-type glaciers in our analysis is based on the RGI 7.0 inventory, which may not fully capture the timing of individual surging events relative to our study period. Glacier surges are episodic and can occur outside the temporal window of our elevation change measurements, potentially leading to mismatches between the cataloged surge status and actual glacier dynamics during our observation timeframe. This limitation should be considered when interpreting the observed differences between surge and non-surge glaciers, as the surging activity may not be contemporaneous with our data. Future studies incorporating time-resolved surge inventories or direct monitoring of glacier dynamics would help to more accurately assess the impact of surging behavior on elevation change patterns.

Due to the strong variability of regional dh/dt, the mass balance of glaciers in Karakoram is also highly heterogeneous. From the mass balance map (Fig. 4.6), a general trend of mass balance change can be observed, with thinning in the eastern and thickening in the western part of the region. A similar finding was reported by Berthier & Brun [23], where the mass balance in the central and western part of the region showed stable to positive mass balance, with statistically significant difference to the eastern part. However, in our study, the longitude dividing the change of mass balance appeared to be around 77.1°E, which is slightly different from the 76.5°E reported by Berthier & Brun [23]. This difference is likely due to the different mass balance of the Siachen Glacier between the two studied period (2011-2019 vs 2000-2016).

Another factor contributing to the heterogeneous pattern of mass balance in the Karakoram is the extensive presence of debris-covered glaciers. Based on the survey of Herreid & Pellicciotti [64], the debris covered area accounts for approximately 17% of all glaciated area within the studied glaciers. One example of anomalous mass balance caused by debris-covered glaciers can be observed in the western part of the region (around 75°E, 36°N). As shown in Fig. 4.16, dh/dt on debris-covered regions show slightly right skewed distribution compared to non debris-covered areas, with the mean dh/dt of 0.01 m/yr (SD=2.47 m/yr) and median of -0.20 m/yr (NMAD=0.90 m/yr). In

contrast, the mean dh/dt on non debris-covered areas is 0.00 m/yr (SD=0.89 m/yr) and median of 0.05 m/yr (NMAD=0.43 m/yr). The difference in dh/dt distribution between debris-covered and clean-ice glaciers is statistically significant based on the two-sample Kolmogorov-Smirnov test ($p < 0.0001$). According to Herreid & Pellicciotti [64], the area of debris-covered glaciers in the entire South Asia West is approximately 3662 km², accounting for 13.7% of the total glaciated area in the region. On debris-covered glaciers, field surveys and modeling studies have shown that thick debris layers can reduce ice melt rates by insulating the glacier surface and limiting thermal energy transfer, whereas thin and moist debris layers can accelerate ablation by increasing the absorption of solar radiation [65–67]. The complex interactions between debris cover characteristics, glacier dynamics, and local climate conditions contribute to the observed heterogeneity in mass balance patterns across the Karakoram region.

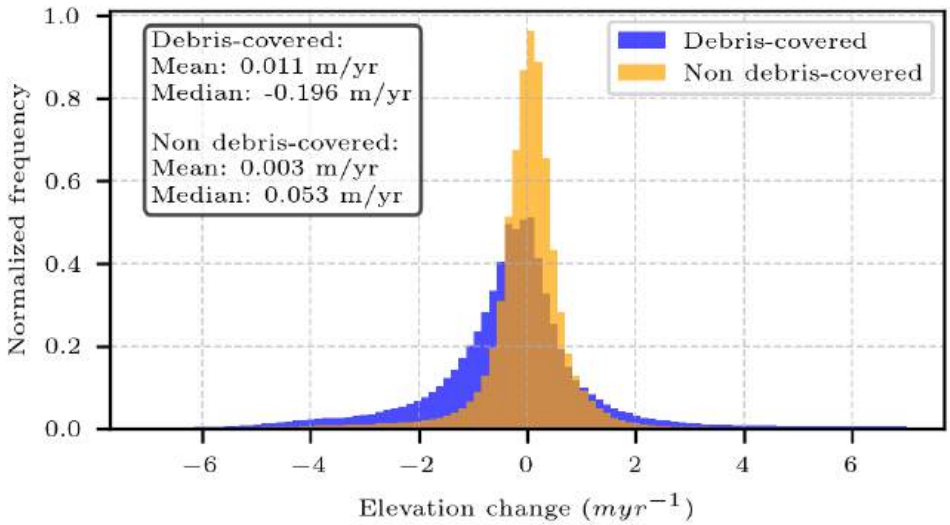

FIGURE 4.16: Distribution of glacier elevation change rates (dh/dt) for debris-covered and non debris-covered areas. The histogram illustrates the normalized frequency of dh/dt values.

4.5.3 Uncertainty of the mass balance estimation

In this study, we implemented a nonstationary heterogeneous framework to quantify uncertainties in glacier elevation change and mass balance estimations. By employing glacier-free terrain as proxies, we effectively modeled

both the heteroskedasticity of dh/dt measurement errors and their spatial correlation patterns. This approach ensured proper consideration of slope-dependent random errors and the correlation of errors in both short and long-range distances.

Our analysis revealed remarkably precise results, with the uncertainty of mean glacier dh/dt across the entire region measuring ± 0.0042 m/yr, and the uncertainty in regional specific mass balance at ± 0.0052 m w.e. yr^{-1}. These uncertainty values are approximately one order of magnitude lower than those reported in related studies (Fig. 4.13), primarily due to the high vertical accuracy of the TanDEM-X DEMs generated through our iterative refinement method.

To verify the quality of our DEMs generation approach, we conducted extensive validation of the 2019 DEM mosaic using ICESat-2 data, which demonstrated an overall vertical error of 3.53 m (Fig. 4.10). Assuming similar vertical accuracy for the 2011 DEM mosaic, the theoretical vertical accuracy of the differential DEM (dDEM) between these two mosaics would be approximately 2.49 m, or 0.31 m/yr when normalized by time. This theoretical estimate closely aligns with our empirical proxy uncertainty measurement of 0.20 m/yr observed on stable ground, confirming the reliability of our methodology.

When placed in the context of existing literature, the significance of our improved accuracy becomes apparent. Previous studies have typically reported much higher uncertainty values for dh/dt over stable ground, generally around 1-2 m/yr. For instance, Berthier & Brun [23] measured an uncertainty of 1.12 m/yr on stable ground using ASTER DEM, resulting in a mass balance uncertainty of ± 0.15 m w.e.yr^{-1}. Similarly, Rankl & Braun [21] reported an uncertainty of 1.90 m/yr for elevation differences between TanDEM-X and SRTM-X DEMs, yielding an uncertainty of ± 0.12 m/yr for mean glacier elevation change. Lv *et al.* [45] documented vertical uncertainties ranging from 5-10 m over stable ground for a time span of approximately 5 years, with an uncertainty of ± 0.04 m/yr for the mean mass balance of 55 glaciers in eastern Pamir. Compared to these studies, the vertical uncertainty of dh/dt in our work is significantly lower by an order of magnitude, resulting in substantially reduced uncertainty in both glacier mean elevation change and mass balance estimations.

The improvement in uncertainty quantification can be attributed primarily to our methodological choices. The exceptionally low uncertainty in our results underscored the value of TanDEM-X DEMs for glacier mass balance estimation. The TanDEM-X 2020 mission phase provided a unique opportunity

to generate high-resolution DEM pairs over extended time spans (exceeding 5 years), which is ideal for precise glacier mass balance calculations. Furthermore, by exclusively using DEMs generated from SAR data, the proposed method can substantially reduce the penetration bias typically caused by different sensors and acquisition modes [25, 68, 69].

Beyond DEM generation, the voids filling approach also contributed to uncertainty reduction. In this work, the challenge of dDEM void filling was addressed using the GPR method, which enabled both the reconstruction of spatial patterns in dDEM voids and the estimation of uncertainty across filled areas. Notably, the void uncertainty proved independent of measurement coverage and GPR model training performance, indicating robust and effective inference of missing values in the dDEM. By properly propagating void uncertainty into the total uncertainty calculation, this approach enabled reliable mass balance estimation considering both measurement and voids filling errors. Future work could involve a systematic comparison of the GPR approach with other gap-filling methods, such as linear and hypsometric interpolation [44], to further validate its effectiveness and identify optimal strategies for different glacier conditions.

4.6 Conclusion

In this study, we measured elevation changes and mass balances across 681 glaciers in the Karakoram region, covering over 10,000 km² of glaciated area. The results indicated a slightly negative or near-equilibrium status for the region, but with strong spatial heterogeneity in glacier dynamics and mass balances. The regional mean dh/dt was 0.0038 ± 0.0042 m/yr, and the regional specific mass balance was 0.0032 ± 0.0052 m w.e. yr^{-1}. These values are consistent with previous studies reporting near-stable conditions for the Karakoram glaciers. Within the region, surge-type glaciers exhibited distinct behaviors, with an average dh/dt of 0.019 ± 0.0052 m/yr and a specific mass balance of 0.0161 ± 0.0063 m w.e. yr^{-1}. In contrast, non-surge glaciers showed an average dh/dt of -0.0058 ± 0.0044 m/yr and a specific mass balance of -0.049 ± 0.0067 m w.e. yr^{-1}. Spatial patterns revealed increasing thickening from east to west, except for a cluster of debris-covered glaciers in the western part of the region. Overall, the findings suggest a slight thinning trend for Karakoram glaciers during the study period, highlighting the complex and heterogeneous glacier behavior in the region.

The detailed elevation and mass change measurement were enabled by the comprehensive framework proposed in this work, which integrated three

core modules to overcome the challenges of glacier mass balance assessments in complex mountainous terrains. The first module involves the generation of high-resolution, high-accuracy DEMs using individual TanDEM-X interferometric acquisitions, leveraging the TanDEM-X 2020 mission phase to enable long time-span measurements for the mass balance. The second module processed dDEM mosaics to produce time-sensitive, void-free dh/dt maps. The use of the GPR modeling approach for void filling ensured that uncertainties in data gaps are properly quantified. The third module incorporated rigorous uncertainty propagation methods, ensuring properly quantified uncertainties by modeling heteroskedasticity and spatial error correlations. By integrating these modules, the framework provided a robust and scalable solution for producing accurate elevation change and mass balance measurements, even in highly heterogeneous and data-sparse regions.

In summary, this study advanced the understanding of glacier dynamics in the Karakoram region and addressed the challenges of measuring mass balance in its complex mountainous terrain. Beyond the measurement results, the proposed framework provided a scalable and adaptable solution for future studies in other glaciated regions. By integrating high-resolution DEM generation, advanced dDEM processing, and robust uncertainty quantification, the proposed framework enhanced the accuracy and reliability of glacier mass balance assessments. These contributions not only improve our understanding of glacier responses to climate change but also establish a methodological foundation for studying regional glacier behavior globally.

Appendix: Proof of regional mass balance uncertainty propagation

The area-weighted average dh/dt for the entire region can be calculated as:

$$\overline{dh}_{\Sigma} = \frac{\sum_{i=1}^{N} A_i \cdot \overline{dh}_i}{\sum_{i=1}^{N} A_i}, \tag{4.18}$$

where A_i is the area of the i-th glacier, $\overline{dh}_i$ is the average dh/dt of the i-th glacier, and N is the total number of glaciers in the region. To estimate the uncertainty of $\overline{dh}_{\Sigma}$, we apply the first-order Taylor expansion for both A_i and

$\overline{dh}_i$, assuming independence between the two variables and independence for errors of A_i between glaciers, to obtain:

$$\sigma^2_{\overline{dh}_\Sigma} = \sum_i^N \left[\left(\frac{\partial \overline{dh}_\Sigma}{\partial A_i} \right)^2 \sigma^2_{A_i} + \left(\frac{\partial \overline{dh}_\Sigma}{\partial \overline{dh}_i} \right)^2 \sigma^2_{\overline{dh}_i} \right] + 2 \sum_{i<j} \frac{\partial \overline{dh}_\Sigma}{\partial \overline{dh}_i} \frac{\partial \overline{dh}_\Sigma}{\partial \overline{dh}_j} \mathrm{Cov}(\overline{dh}_i, \overline{dh}_j)$$

where σ_{A_i} and $\sigma_{\overline{dh}_i}$ are the uncertainties of A_i and $\overline{dh}_i$, respectively, and $\mathrm{Cov}(\overline{dh}_i, \overline{dh}_j)$ is the covariance between $\overline{dh}_i$ and $\overline{dh}_j$. The covariance term is zero if the errors of $\overline{dh}_i$ are independent between glaciers, however it must be considered in our case due to the spatial correlation of the errors.

Let $T = \sum A_i$, the partial derivatives of $\overline{dh}_\Sigma$ with respect to A_i and $\overline{dh}_i$ can be drived as:

$$\frac{\partial \overline{dh}_\Sigma}{\partial A_i} = \frac{\overline{dh}_i T - \sum A_i \overline{dh}_i}{T^2} = \frac{\overline{dh}_i - \overline{dh}_\Sigma}{T},$$
$$\frac{\partial \overline{dh}_\Sigma}{\partial \overline{dh}_i} = \frac{A_i}{T}$$

which can be substituted into the equation above to obtain the uncertainty of $\overline{dh}_\Sigma$ as:

$$\sigma^2_{\overline{dh}_\Sigma} = \frac{1}{T^2} \left[\sum_i^N \left(\overline{dh}_i - \overline{dh}_\Sigma \right)^2 \sigma^2_{A_i} + \sum_i^N A_i^2 \sigma^2_{\overline{dh}_i} + \sum_{i \neq j}^N A_i A_j \mathrm{Cov}(\overline{dh}_i, \overline{dh}_j) \right] \tag{4.19}$$

Coverting the summation to a double summation over all pairs of glaciers, we have:

$$\sigma^2_{\overline{dh}_\Sigma} = \frac{1}{T^2} \left[\sum_i^N \left(\overline{dh}_i - \overline{dh}_\Sigma \right)^2 \sigma^2_{A_i} + \sum_i^N \sum_j^N A_i A_j \mathrm{Cov}(\overline{dh}_i, \overline{dh}_j) \right] \tag{4.20}$$

Consider variogram

$$V = V(\sigma_{\overline{dh}_i}, \sigma_{\overline{dh}_j}, r, d)$$

where r is the correlation range and d is the distance between glacier i and j. Assuming second-order stationarity, the covariance term can be expressed as:

$$\mathrm{Cov}(\overline{dh}_i, \overline{dh}_j) = \sigma_{\overline{dh}_i}\sigma_{\overline{dh}_j} - V(\sigma_{\overline{dh}_i}, \sigma_{\overline{dh}_j}, r, d) \tag{4.21}$$

replacing the covariance term in Eq. (4.20), and re-write the summation as a double summation over all pairs of glaciers, we have:

$$\begin{aligned}\sigma^2_{\overline{dh}_\Sigma} = \frac{1}{T^2}\Bigg[\sum_i^N \left(\overline{dh}_i - \overline{dh}_\Sigma\right)^2 \sigma^2_{A_i} + \\ \sum_i^N \sum_j^N A_i A_j \left(\sigma_{\overline{dh}_i}\sigma_{\overline{dh}_j} - V\right)\Bigg]\end{aligned} \tag{4.22}$$

In Eq. (4.22), the first term shows that the uncertainty of glacier area is scaled by the deviation of the glacier's average $\overline{dh}$ from the regional weighted average $\overline{dh}_\Sigma$. The second term shows that the uncertainty of the regional weighted average, adjusted by the correlation between glaciers, is scaled by the product of the glacier areas. Note that the second term

$$\frac{1}{T^2}\sum_i^N \sum_j^N A_i A_j (\sigma_{\overline{dh}_i}\sigma_{\overline{dh}_j} - V)$$

is the same as the uncertainty propagation of spatial ensembles derived by Hugonnet *et al.* [41].

References

1. IPCC. *The Ocean and Cryosphere in a Changing Climate: Special Report of the Intergovernmental Panel on Climate Change* (Cambridge University Press, Cambridge, 2022).
2. Zemp, M., Thibert, E., Huss, M., Stumm, D., Rolstad Denby, C., Nuth, C., Nussbaumer, S. U., Moholdt, G., Mercer, A., Mayer, C., Joerg, P. C., Jansson, P., Hynek, B., Fischer, A., Escher-Vetter, H., Elvehøy, H. & Andreassen, L. M. Reanalysing glacier mass balance measurement series. *The Cryosphere* **7**, 1227 (2013).
3. Farinotti, D. On the effect of short-term climate variability on mountain glaciers: insights from a case study. *Journal of Glaciology* **59**, 992 (2013).
4. Liu, X., Xu, Z., Yang, H. & Vaghefi, S. A. Responses of the Glacier Mass Balance to Climate Change in the Tibetan Plateau During 1975–2013. *Journal of Geophysical Research: Atmospheres* **126**, e2019JD032132 (2021).

5. Bolibar, J., Rabatel, A., Gouttevin, I., Zekollari, H. & Galiez, C. Nonlinear sensitivity of glacier mass balance to future climate change unveiled by deep learning. *Nature Communications* **13**, 409 (2022).

6. Hirabayashi, Y., Döll, P. & Kanae, S. Global-scale modeling of glacier mass balances for water resources assessments: Glacier mass changes between 1948 and 2006. *Journal of Hydrology* **390**, 245 (2010).

7. Radić, V. & Hock, R. Glaciers in the Earth's Hydrological Cycle: Assessments of Glacier Mass and Runoff Changes on Global and Regional Scales. *Surveys in Geophysics* **35**, 813 (2014).

8. Huss, M. & Hock, R. Global-scale hydrological response to future glacier mass loss. *Nature Climate Change* **8**, 135 (2018).

9. Hugonnet, R., McNabb, R., Berthier, E., Menounos, B., Nuth, C., Girod, L., Farinotti, D., Huss, M., Dussaillant, I., Brun, F. & Kääb, A. Accelerated global glacier mass loss in the early twenty-first century. *Nature* **592**, 726 (2021).

10. Nie, Y., Pritchard, H. D., Liu, Q., Hennig, T., Wang, W., Wang, X., Liu, S., Nepal, S., Samyn, D., Hewitt, K. & Chen, X. Glacial change and hydrological implications in the Himalaya and Karakoram. *Nature Reviews Earth & Environment* **2**. 91 (2021).

11. Zemp, M., Jakob, L., Dussaillant, I., Nussbaumer, S. U., Gourmelen, N., Dubber, S., A, G., Abdullahi, S., Andreassen, L. M., Berthier, E., Bhattacharya, A., Blazquez, A., Boehm Vock, L. F., Bolch, T., Box, J., Braun, M. H., Brun, F., Cicero, E., Colgan, W., Eckert, N., Farinotti, D., Florentine, C., Floricioiu, D., Gardner, A., Harig, C., Hassan, J., Hugonnet, R., Huss, M., Jóhannesson, T., Liang, C.-C. A., Ke, C.-Q., Khan, S. A., King, O., Kneib, M., Krieger, L., Maussion, F., Mattea, E., McNabb, R., Menounos, B., Miles, E., Moholdt, G., Nilsson, J., Pálsson, F., Pfeffer, J., Piermattei, L., Plummer, S., Richter, A., Sasgen, I., Schuster, L., Seehaus, T., Shen, X., Sommer, C., Sutterley, T., Treichler, D., Velicogna, I., Wouters, B., Zekollari, H., Zheng, W. & The GlaMBIE Team. Community estimate of global glacier mass changes from 2000 to 2023. *Nature*, 1 (2025).

12. Dussaillant, I., Hugonnet, R., Huss, M., Berthier, E., Bannwart, J., Paul, F. & Zemp, M. Annual mass changes for each glacier in the world from 1976 to 2023. *Earth System Science Data Discussions*, 1 (2024).

13. Azam, M. F., Wagnon, P., Berthier, E., Vincent, C., Fujita, K. & Kargel, J. S. Review of the status and mass changes of Himalayan-Karakoram glaciers. *Journal of Glaciology* **64**, 61 (2018).

14. Mukhopadhyay, B. & Khan, A. Rising river flows and glacial mass balance in central Karakoram. *Journal of Hydrology* **513**, 192 (2014).

15. Hewitt, K. The Karakoram Anomaly? Glacier Expansion and the 'Elevation Effect,' Karakoram Himalaya. *Mountain Research and Development* **25**, 332 (2005).

16. Farinotti, D., Immerzeel, W. W., Kok, R. J. d., Quincey, D. J. & Dehecq, A. Manifestations and mechanisms of the Karakoram glacier Anomaly. *Nature Geoscience* **13**, 8 (2020).

17. Dimri, A. P. Decoding the Karakoram Anomaly. *Science of The Total Environment* **788**, 147864 (2021).

18. Lhakpa, D., Fan, Y. & Cai, Y. Continuous Karakoram Glacier Anomaly and Its Response to Climate Change during 2000–2021. *Remote Sensing* **14**, 6281 (2022).

19. Gardelle, J., Berthier, E. & Arnaud, Y. Slight mass gain of Karakoram glaciers in the early twenty-first century. *Nature Geoscience* **5**, 322 (2012).

20. Kääb, A., Berthier, E., Nuth, C., Gardelle, J. & Arnaud, Y. Contrasting patterns of early twenty-first-century glacier mass change in the Himalayas. *Nature* **488**, 495 (2012).

21. Rankl, M. & Braun, M. Glacier elevation and mass changes over the central Karakoram region estimated from TanDEM-X and SRTM/X-SAR digital elevation models. *Annals of Glaciology* **57**, 273 (2016).

22. Brun, F., Berthier, E., Wagnon, P., Kääb, A. & Treichler, D. A spatially resolved estimate of High Mountain Asia glacier mass balances from 2000 to 2016. *Nature Geoscience* **10**, 668 (2017).

23. Berthier, E. & Brun, F. Karakoram geodetic glacier mass balances between 2008 and 2016: persistence of the anomaly and influence of a large rock avalanche on Siachen Glacier. *Journal of Glaciology* **65**, 494 (2019).

24. Millan, R., Dehecq, A., Trouvé, E., Gourmelen, N. & Berthier, E. *Elevation changes and X-band ice and snow penetration inferred from TanDEM-X data of the Mont-Blanc area* in *2015 8th International Workshop on the Analysis of Multitemporal Remote Sensing Images (Multi-Temp)* (2015), 1.

25. Dehecq, A., Millan, R., Berthier, E., Gourmelen, N., Trouvé, E. & Vionnet, V. Elevation Changes Inferred From TanDEM-X Data Over the Mont-Blanc Area: Impact of the X-Band Interferometric Bias. *IEEE Journal of Selected Topics in Applied Earth Observations and Remote Sensing* **9**, 3870 (2016).

26. Hajnsek, I., Busche, T., Abdullahi, S., Bachmann, M., Baumgartner, S. V., Bojarski, A., Bueso-Bello, J.-L., Esch, T., Fritz, T., Alonso-Gonzalez, A., Gonzalez, C., Huang, L., Kraus, T., Lachaise, M., Li, S., Dekker, F. L., Maier, K., Martone, M., Milillo, P., Mittermayer, J., Nannini, M., Papathanassiou, K., Pardini, M., Pinheiro, M., Prats-Iraola, P., Rizzoli, P., Rodriguez-Cassola, M., Roth, A., Schandri, M., Scheiber, R., Steinbrecher, U., Schweisshelm, B., Villano, M., Warmedinger, L. J., Wessel, B., Krieger, G., Zink, M. & Moreira, A. TanDEM-X: The 4D Mission Phase for Earth Surface Dynamics: Science activities highlights and new data products after 15 years of bistatic operations. *IEEE Geoscience and Remote Sensing Magazine*, 2 (2025).

27. Leinss, S. & Bernhard, P. TanDEM-X:Deriving InSAR Height Changes and Velocity Dynamics of Great Aletsch Glacier. *IEEE Journal of Selected Topics in Applied Earth Observations and Remote Sensing* **14**, 4798 (2021).

28. Piermattei, L., Zemp, M., Sommer, C., Brun, F., Braun, M. H., Andreassen, L. M., Belart, J. M. C., Berthier, E., Bhattacharya, A., Boehm Vock, L., Bolch, T., Dehecq, A., Dussaillant, I., Falaschi, D., Florentine, C., Floricioiu, D., Ginzler, C., Guillet, G., Hugonnet, R., Huss, M., Kääb, A., King, O., Klug, C., Knuth, F., Krieger, L., La Frenierre, J., McNabb, R., McNeil, C., Prinz, R., Sass, L., Seehaus, T., Shean, D., Treichler, D., Wendt, A. & Yang, R. Observing glacier elevation changes from spaceborne optical and radar sensors – an inter-comparison experiment using ASTER and TanDEM-X data. *The Cryosphere* **18**, 3195 (2024).

29. Thapa, A. & Muhammad, S. Contemporary Snow Changes in the Karakoram Region Attributed to Improved MODIS Data between 2003 and 2018. *Water* **12**, 2681 (2020).

30. Kapnick, S. B., Delworth, T. L., Ashfaq, M., Malyshev, S. & Milly, P. C. D. Snowfall less sensitive to warming in Karakoram than in Himalayas due to a unique seasonal cycle. *Nature Geoscience* **7**, 834 (2014).

31. RGI Consortium. *Randolph Glacier Inventory - A Dataset of Global Glacier Outlines, Version 7* 2023.

32. Hewitt, K. *Glaciers of the Karakoram Himalaya: Glacial Environments, Processes, Hazards and Resources* (Springer Netherlands, Dordrecht, 2014).

33. Quincey, D. J., Braun, M., Glasser, N. F., Bishop, M. P., Hewitt, K. & Luckman, A. Karakoram glacier surge dynamics. *Geophysical Research Letters* **38** (2011).

34. Quincey, D. J., Glasser, N. F., Cook, S. J. & Luckman, A. Heterogeneity in Karakoram glacier surges: KARAKORAM GLACIER SURGE HETEROGENEITY. *Journal of Geophysical Research: Earth Surface* **120**, 1288 (2015).

35. Miles, K. E., Hubbard, B., Quincey, D. J., Miles, E. S., Sherpa, T. C., Rowan, A. V. & Doyle, S. H. Polythermal structure of a Himalayan debris-covered glacier revealed by borehole thermometry. *Scientific Reports* **8**, 16825 (2018).

36. Zink, M., Bachmann, M., Brautigam, B., Fritz, T., Hajnsek, I., Moreira, A., Wessel, B. & Krieger, G. TanDEM-X: The New Global DEM Takes Shape. *IEEE Geoscience and Remote Sensing Magazine* **2**, 8 (2014).

37. Krieger, G., Zink, M., Bachmann, M., Bräutigam, B., Schulze, D., Martone, M., Rizzoli, P., Steinbrecher, U., Walter Antony, J., De Zan, F., Hajnsek, I., Papathanassiou, K., Kugler, F., Rodriguez Cassola, M., Younis, M., Baumgartner, S., López-Dekker, P., Prats, P. & Moreira, A. TanDEM-X: A radar interferometer with two formation-flying satellites. *Acta Astronautica* **89**, 83 (2013).

38. Lachaise, M., Schweisshelm, B. & Fritz, T. *The New Tandem-X Change Dem: Specifications And Interferometric Processing* in *2020 IEEE Latin American GRSS & ISPRS Remote Sensing Conference (LAGIRS)* (IEEE, Santiago, Chile, 2020), 646.

39. Huss, M. Density assumptions for converting geodetic glacier volume change to mass change. *The Cryosphere* **7**, 877 (2013).

40. European Space Agency & Airbus. *Copernicus DEM* 2022.

41. Hugonnet, R., Brun, F., Berthier, E., Dehecq, A., Mannerfelt, E. S., Eckert, N. & Farinotti, D. Uncertainty Analysis of Digital Elevation Models by Spatial Inference From Stable Terrain. *IEEE Journal of Selected Topics in Applied Earth Observations and Remote Sensing* **15**, 6456 (2022).

42. Schweisshelm, B. & Lachaise, M. *Calibration of the Tandem-X Craw DEMs for the Tandem-X DEM Change Maps Generation* in *IGARSS 2022 - 2022 IEEE International Geoscience and Remote Sensing Symposium* (2022), 291.

43. Nuth, C. & Kääb, A. Co-registration and bias corrections of satellite elevation data sets for quantifying glacier thickness change. *The Cryosphere* **5**, 271 (2011).

44. McNabb, R., Nuth, C., Kääb, A. & Girod, L. Sensitivity of glacier volume change estimation to DEM void interpolation. *The Cryosphere* **13**, 895 (2019).

45. Lv, M., Quincey, D. J., Guo, H., King, O., Liu, G., Yan, S., Lu, X. & Ruan, Z. Examining geodetic glacier mass balance in the eastern Pamir transition zone. *Journal of Glaciology* **66**, 927 (2020).

46. Williams, C. & Rasmussen, C. *Gaussian Processes for Regression* in *Advances in Neural Information Processing Systems* **8** (MIT Press, 1995).

47. Gardner, J. R., Pleiss, G., Bindel, D., Weinberger, K. Q. & Wilson, A. G. *GPyTorch: Blackbox Matrix-Matrix Gaussian Process Inference with GPU Acceleration* 2021.

48. Dowd, P. A. in *Geostatistics for Natural Resources Characterization: Part 1* (eds Verly, G., David, M., Journel, A. G. & Marechal, A.) 91 (Springer Netherlands, Dordrecht, 1984).

49. Guo, L., Li, J., Li, Z.-w., Wu, L.-x., Li, X., Hu, J., Li, H.-l., Li, H.-y., Miao, Z.-l. & Li, Z.-q. The Surge of the Hispar Glacier, Central Karakoram: SAR 3-D Flow Velocity Time Series and Thickness Changes. *Journal of Geophysical Research: Solid Earth* **125**, e2019JB018945 (2020).

50. Li, S., Leinss, S., Bernhard, P. & Hajnsek, I. *Recent Surge of the South Rimo Glacier, Karakoram: Dynamics Characterization Using SAR Data* in *2021 IEEE International Geoscience and Remote Sensing Symposium IGARSS* (2021), 5520.

51. Jiang, Z., Wu, K., Liu, S., Wang, X., Zhang, Y., Tahir, A. A. & Long, S. Surging dynamics of South Rimo Glacier, Eastern Karakoram. *Environmental Research Letters* **16**, 114044 (2021).

52. Zhao, F., Long, D., Fang, C., Wang, Y. & Duan, X. Satellite-observed surging dynamics of North Kunchhang Glacier I in the Eastern Karakoram. *EGUsphere*, 1 (2025).

53. Usman, M. & Furuya, M. Interannual modulation of seasonal glacial velocity variations in the Eastern Karakoram detected by ALOS-1/2 data. *Journal of Glaciology* **64**, 465 (2018).

54. Bhambri, R., Bolch, T., Kawishwar, P., Dobhal, D. P., Srivastava, D. & Pratap, B. Heterogeneity in glacier response in the upper Shyok valley, northeast Karakoram. *The Cryosphere* **7**, 1385 (2013).

55. Abdullahi, S., Wessel, B., Huber, M., Wendleder, A., Roth, A. & Kuenzer, C. Estimating Penetration-Related X-Band InSAR Elevation Bias: A Study over the Greenland Ice Sheet. *Remote Sensing* **11**, 2903 (2019).

56. Li, J., Sun, M., Yao, X., Duan, H., Zhang, C., Wang, S., Niu, S. & Yan, X. A Review of Karakoram Glacier Anomalies in High Mountains Asia. *Water* **15**, 3215 (2023).

57. Kääb, A., Treichler, D., Nuth, C. & Berthier, E. Brief Communication: Contending estimates of 2003–2008 glacier mass balance over the Pamir–Karakoram–Himalaya. *The Cryosphere* **9**, 557 (2015).

58. Agarwal, V., Bolch, T., Syed, T. H., Pieczonka, T., Strozzi, T. & Nagaich, R. Area and mass changes of Siachen Glacier (East Karakoram). *Journal of Glaciology* **63**, 148 (2017).

59. Lin, H., Li, G., Cuo, L., Hooper, A. & Ye, Q. A decreasing glacier mass balance gradient from the edge of the Upper Tarim Basin to the Karakoram during 2000–2014. En. *Scientific Reports* **7**, 6712 (2017).

60. Copland, L., Sylvestre, T., Bishop, M. P., Shroder, J. F., Seong, Y. B., Owen, L. A., Bush, A. & Kamp, U. Expanded and Recently Increased Glacier Surging in the Karakoram. *Arctic, Antarctic, and Alpine Research* **43**, 503 (2011).

61. Gardelle, J., Berthier, E., Arnaud, Y. & Kääb, A. Region-Wide Glacier Mass Balances over the Pamir-Karakoram-Himalaya during 1999–2011. *The Cryosphere* **7**, 1263 (2013).

62. Ragettli, S., Bolch, T. & Pellicciotti, F. Heterogeneous Glacier Thinning Patterns over the Last 40 Years in Langtang Himal, Nepal. *The Cryosphere* **10**, 2075 (2016).

63. Cogley, J. G. Geodetic and Direct Mass-Balance Measurements: Comparison and Joint Analysis. *Annals of Glaciology* **50**, 96 (2009).

64. Herreid, S. & Pellicciotti, F. The State of Rock Debris Covering Earth's Glaciers. *Nature Geoscience* **13**, 621 (2020).

65. Scherler, D., Bookhagen, B. & Strecker, M. R. Spatially variable response of Himalayan glaciers to climate change affected by debris cover. *Nature Geoscience* **4**, 156 (2011).

66. Mayer, C. & Licciulli, C. The Concept of Steady State, Cyclicity and Debris Unloading of Debris-Covered Glaciers. *Frontiers in Earth Science* **9**, 710276 (2021).

67. Huo, D., Bishop, M. P. & Bush, A. B. G. Understanding Complex Debris-Covered Glaciers: Concepts, Issues, and Research Directions. *Frontiers in Earth Science* **9**, 652279 (2021).

68. Rignot, E., Echelmeyer, K. & Krabill, W. Penetration depth of interferometric synthetic-aperture radar signals in snow and ice. *Geophysical Research Letters* **28**, 3501 (2001).

69. Abdullah, T., Romshoo, S. A. & Rashid, I. The satellite observed glacier mass changes over the Upper Indus Basin during 2000–2012. *Scientific Reports* **10**, 14285 (2020).

5

CONCLUSIONS AND OUTLOOK

In this dissertation, SAR-based advancements were introduced to study cryosphere processes in complex alpine environments. Through three interconnected studies, novel methodologies and frameworks were developed to address key challenges in glacier dynamics monitoring, snowmelt mapping, and mass balance assessments. Collectively, the research demonstrated the potential of SAR data to enhance the accuracy, scalability, and applicability of remote sensing techniques, providing valuable insights into glacier flow dynamics, snow processes, glacier mass change, and their implications for water resources and climate resilience.

This chapter summarizes the main findings of the three studies conducted in this dissertation. For each study, the research questions presented in Section 1.5 are addressed. Following the summary of each study, potential directions for future work are discussed.

5.1 Cross-Correlation Stacking for Robust Offset Tracking using SAR Image Time-Series

This study introduced a novel cross-correlation stacking method to improve offset tracking for measuring ground surface displacements using remote sensing data. Traditional offset tracking methods relied on pair-wise NCC to determine displacement offsets, but these methods were often limited by noise interference, which affected the precision and coverage of the reliable results. The proposed method addressed this limitation by stacking multiple pair-wise NCCs from image time-series and averaging them before tracking the NCC peak. This approach leveraged redundant temporal information across multiple NCCs, effectively suppressing noise while preserving the NCC peak height.

In the study, the proposed method was tested on the Great Aletsch Glacier in Switzerland using SAR images from TanDEM-X and Sentinel-1A missions. Results demonstrated significant improvements in spatial resolution and coverage of velocity fields, particularly when using smaller image templates. The study also explored the generalization capability of the method to different

SAR sensors and acquisition characteristics, highlighting its potential for broad applications in offset tracking across diverse datasets.

5.1.1 Addressing the research questions

1. How does cross-correlation stacking improve the robustness of displacement estimation compared to single-pair NCC methods?

The study showed that cross-correlation stacking improves the robustness of displacement estimation by significantly enhancing the SNR of the NCC. Unlike single-pair NCC methods, which can be more susceptible to noise and unreliable peak tracking, stacking involves averaging multiple NCCs (e.g., from 7–8 images in this study for TanDEM-X and Sentinel-1A data). This averaging process effectively suppresses noise interference, thereby improving the SNR and ensuring that the NCC peak can be tracked more reliably and robustly. As a result, displacement estimation becomes more accurate, with extended spatial coverage even in challenging conditions, such as areas with subtle features or high noise levels.

2. Can smaller image templates achieve comparable spatial coverage to larger templates when combined with stacking? The study confirms that smaller image templates can achieve spatial coverage comparable to larger templates when combined with NCC stacking. The research demonstrated that stacking significantly enhances the performance of smaller templates, enabling them to deliver velocity fields nearly equivalent to those obtained using larger templates in single-pair NCC methods. For example, velocity estimates derived from small templates of 48×48 combined with a stack of seven pair-wise NCCs were comparable to those generated with larger templates of 96×96 pixels using single-pair NCC. This approach is particularly advantageous for studies focused on small glaciers or regions where the use of larger templates is impractical, making NCC stacking a more effective and versatile solution in such scenarios.

3. How does the method generalize across SAR sensors with different resolutions and acquisition characteristics?

The result of the study shows that the stacking method generalizes effectively across SAR sensors with varying resolutions and acquisition characteristics. The study demonstrated its applicability to different SAR datasets, such as TanDEM-X and Sentinel-1A, which differ in resolution, wavelength, and acquisition parameters. Consistent performance improvements were observed in spatial coverage and velocity estimation across both datasets. Moreover, it is argued that the method's adaptability extends beyond SAR sensors, showing potential for broader applications, including the integration of data

from other spectral channels, sensor types (e.g., SAR and optical), and image combinations from diverse temporal intervals. This flexibility underscores the method's capability for generalization and its suitability for leveraging the expanding archives of remote sensing data.

5.1.2 Outlook for future studies

The proposed cross-correlation stacking method presents promising opportunities for enhancing offset tracking in glacier velocity monitoring, with significant potential for future applications. To further develop this method, several refinements in methodology can be explored.

A key area for future exploration is the optimization of parameters used for stacking. While this study employed a moderate stacking size of seven to eight images, further research could focus on identifying the optimal number of pair-wise NCCs to be used for stacking under various scenarios, such as differing flow velocities or image acquisition intervals. Additionally, the influence of surface features on offset tracking performance under varying stacking sizes warrants investigation. For example, future studies could examine whether features of smaller sizes are better tracked with larger stacks. Moreover, although the findings suggest that significant performance improvements can be achieved without requiring large stacks, future studies are needed to refine the trade-offs between temporal resolution, computational efficiency and tracking accuracy. Adaptive stacking strategies, where the number of NCCs is dynamically adjusted based on factors like noise levels or temporal resolution, also offer exciting possibilities for enhancing scalability and performance, especially in large-scale applications.

Another promising direction involves integrating the method with multi-sensor and multi-modal datasets. This study highlights the stacking method's ability to accommodate data from different sensors, such as SAR and optical imagery, or across various spectral channels. Building on this foundation, future research could investigate how combining datasets from multiple sensors might enhance displacement tracking in regions where single-sensor data is insufficient. For instance, integrating SAR data with optical or thermal imagery could improve tracking performance in areas with diverse surface characteristics or significant seasonal variations. Additionally, the stacking method has the potential to complement other deformation measurement techniques, enabling a more comprehensive reconstruction of offset fields. For example, combining offset tracking with DInSAR could facilitate the tracking of three-dimensional displacement fields, providing a deeper understanding of surface deformation processes. This integration could be particularly bene-

ficial for applications requiring detailed insights into complex geophysical phenomena, such as glacier dynamics or tectonic activity.

Finally, future research could focus on automating the stacking process for handling extensive datasets to better leverage the expanding archives of remote sensing data. This would involve developing efficient algorithms and workflows that optimize computational performance while maintaining accuracy. Cloud-based or distributed computing solutions could play a key role in streamlining processing, enabling the method to handle large-scale applications effectively. Such advancements would not only enhance the accessibility of the stacking approach for global monitoring but also broaden its use in environmental research. By facilitating the analysis of vast datasets, the method could support efforts to monitor large-scale glacier.

5.2 Mapping Seasonal Snow Melting in Karakoram Using SAR and Topographic Data

This study focused on mapping seasonal snow melting in the challenging terrain of the Karakoram region, which was critical for understanding water resources, natural hazards, and climate impacts. To address the limitations of conventional remote sensing methods in such complex mountainous areas, a novel framework was developed to incorporate SAR data and topographic information. The framework integrated two key indices: the WSI and the TSI. The WSI was derived using the GMM to adaptively process SAR backscattering data, while the TSI was introduced to account for terrain influences on wet snow distribution. The proposed method was validated against Sentinel-2 snow cover maps, showing significant improvements in mapping accuracy. Applied across three major water basins in the Karakoram, large-scale wet snow maps were generated in this study, offering valuable insights into the spatial and temporal dynamics of snow melting. The findings contributed to hydrological modeling, water resource management, and climate resilience in vulnerable regions.

5.2.1 Addressing the research questions

1. How can SAR and topographic data be effectively integrated to mitigate terrain-induced errors in wet snow classification?

The study integrated SAR data and topographic information through two innovative indices: the Wet Snow Index (WSI) and Topographic Snow Index (TSI) . The WSI is calculated from SAR backscattering ratio using the Gaussian Mixture Model (GMM). It enables the adaptive processing

of SAR backscattering ratios to robustly represent the probability of wet snow presence given the SAR backscattering intensigy. The TSI, on the other hand, complemented this by incorporating topographic factors to capture terrain-induced variations in snow presence. Together, these indices effectively mitigated errors caused by complex terrain, enabling more accurate wet snow classification.

2. Does the proposed method outperform conventional SAR or optical-based approaches in mapping accuracy?

Validation against Sentinel-2 snow cover maps demonstrated that the proposed method greatly improved the accuracy of wet snow classification compared to the conventional single-threshold method. By combining adaptive backscatter ratio processing with terrain-based corrections, the framework addressed the limitations of traditional single-threshold methods, particularly in high-altitude regions with complex topography.

3. What temporal and spatial insights into snowmelt patterns can be derived from the application of the method across major basins in Karakoram?

The application of the method produced large-scale wet snow maps across three major water basins in the Karakoram, enabling detailed analyses of key snow variables such as the Wet Snow Extent and Snow Melting Duration. These analyses revealed dynamic patterns in the temporal and spatial distribution of wet snow, providing insights into snowmelt processes. The dataset generated by this study offered valuable information for hydrological model calibration and validation, enhancing water resource management and climate modeling efforts in the region.

5.2.2 Outlook for future studies

The advancements presented in this study pave the road for several promising methodology enhancement and application expansion.

While SAR has proven effective, extreme terrain complexity can introduce geometric distortions, and dense vegetation may interfere with backscatter signals, leading to challenges in interpretation. Additionally, the 12-day revisit interval of Sentinel-1 limits the temporal resolution of observations, which may miss rapid snowmelt events or short-term fluctuations.

To address these challenges, integrating data from other modalities, such as optical and thermal imagery, into the framework offers significant potential for improvement. The GMM used in this study provides a flexible mechanism to convert signals from any modality into a probability metric, such as the WSI. This capability enables seamless combination of data across modalities, improving the robustness of snow detection under diverse conditions.

Furthermore, leveraging observations from multiple sensors allows for the creation of dense time-series datasets, enhancing the temporal resolution and overcoming the limitations of single-sensor approaches.

Another opportunity for refinement lies in the use of topographic features for snow presence estimation. While the Topographic Snow Index TSI demonstrated effectiveness, there is room to better capture the complex interactions between snow and topography. Certain topographic conditions may lead to over- or under-estimation of snow probability, highlighting the need for more advanced methods. Employing cutting-edge machine learning techniques, such as deep neural networks, could provide a powerful solution to model these non-linear and highly dynamic interactions more accurately. These techniques are well-suited to handle the intricacies of mountainous terrain and snow patterns, enabling more reliable and adaptive snow mapping processes.

Beyond these enhancements, additional research directions offer exciting possibilities. For example, coupling wet snow maps from remote sensing and snowmelt dynamics from advanced hydrological models could enable more accurate simulations of water resource availability, enhance streamflow predictions, support flood risk assessments, and enable early detection of snow avalanches. By pursuing these opportunities for improvement and exploring innovative research directions, future studies can refine methodologies for wet snow mapping while expanding their applications in hydrological modeling, climate adaptation, and disaster mitigation. These advancements will be crucial for improving water resource management and ensuring resilience in high-altitude regions facing the impacts of a changing climate.

5.3 Geodetic Glacier Mass Balance in the Karakoram (2011–2019) from TanDEM-X: An InSAR DEM Differencing Framework

This study investigates glacier mass balance (GMB) and elevation changes (dh/dt) in Karakoram, a region where glaciers exhibit anomalous stable mass change compared to the global thinning trend. Using long-term TanDEM-X observations over nearly a decade (2011–2019), this work analyzed the elevation and mass changes across over 10,000 km² of glaciated area in Karakoram. The regional mean dh/dt is 0.0038 ± 0.0042 m/yr and the specific GMB is 0.032 ± 0.0052 m w.e. yr^{-1}, indicating a near balanced and slightly thickening tendency. Spatial patterns of the elevation change are strongly heterogeneous, with contrasting behaviors between surge-type and non-surge glaciers. These findings underscore the complexity of Karakoram glacier

dynamics, shaped by climatic forcing, topographic controls, and glacier-specific dynamics.

To address the challenges of measuring glacier mass balance in complex terrains, the study proposed and implemented a comprehensive framework. This framework integrated high-resolution DEM generation, advanced elevation change mapping, and rigorous uncertainty quantification methods. It proved effective in producing accurate and scalable glacier mass balance assessments, offering a methodological foundation for future studies in other glaciated regions.

5.3.1 Addressing the research questions

1. What are the spatial patterns and magnitude of elevation changes (dh/dt) and glacier mass balance in the Karakoram region during 2011-2019?

The study revealed that glaciers in the Karakoram region were in a slightly negative or near-equilibrium state during the study period, with a regional mean dh/dt of 0.0038 ± 0.0042 m/yr and a specific mass balance of 0.032 ± 0.0052 m w.e. yr^{-1}. Spatial analysis indicated an increasingly thickening trend from the east to the west, except for a cluster of debris-covered glaciers in the western region. These findings emphasize the spatial heterogeneity of glacier behavior in the Karakoram and are consistent with previous studies, further reinforcing the unique stability of glaciers in this region compared to other parts of the Himalayas.

2. How do surge-type and non-surge glaciers differ in their elevation change and mass balance behaviors?

Surge-type glaciers demonstrated relatively stable or thickening trends, with an average dh/dt of 0.019 ± 0.0052 m/yr and a specific mass balance of 0.0161 ± 0.0063 m w.e. yr^{-1}. In contrast, non-surge glaciers exhibited thinning trends, with an average dh/dt of -0.0058 ± 0.0044 m/yr and a specific mass balance of -0.049 ± 0.0067 m w.e. yr^{-1}. These findings highlight the importance of accounting for the diverse glacier dynamics in the region, particularly the distinct behaviors of surge-type and non-surge glaciers, to fully understand the spatial and temporal variations in glacier mass balance changes.

3. Can a comprehensive framework combining advanced DEM generation, elevation change mapping, and uncertainty analysis improve glacier mass balance assessments in complex terrains?

The study developed and validated a robust, comprehensive framework that integrates high-resolution DEM generation, advanced dDEM processing, and rigorous uncertainty quantification. This framework effectively addressed

challenges posed by the Karakoram's complex terrain, enabling accurate assessments of glacier elevation changes and mass balance. By utilizing TanDEM-X observations and innovative methods for void filling and error modeling, the framework significantly reduced measurement uncertainties and improved the reliability of results. Its scalability and adaptability make it a valuable tool for glacier mass balance studies in other complex and glaciated regions worldwide.

5.3.2 Outlook for future studies

This study has laid a strong foundation for understanding glacier dynamics in the Karakoram region by addressing the challenges of measuring glacier mass balance in complex mountainous terrains. While the methods and findings presented here provide valuable insights, there remain several opportunities to further enhance this field of study.

One key area for improvement is to further employ the full temporal observations collected by the TanDEM-X mission over nearly a decade. In this study, only the data collected at 2011 and 2019 were used to generate DEMs. Although this provides a time-sensitive measurement of elevation change, it represents only a static status of the elevation and mass changes during this period. Expanding the analysis to include the entire time series would enable a more detailed and robust assessment of temporal trends and inter-annual variability, offering a more dynamic perspective on glacier behavior and its evolution over time. From this perspective, the continuation of a single-pass SAR mission for DEM generation after the TanDEM-X would be highly beneficial to ensure long-term monitoring of elevation changes and glacier dynamics.

Another important direction is the refinement of radar signal penetration bias quantification. As this study exclusively used TanDEM-X data to calculate elevation differences, it was assumed that penetration biases were effectively canceled out. Nonetheless, variations in surface conditions can significantly influence radar penetration, potentially introducing additional uncertainties. Future research could focus on developing robust methods to quantify penetration biases under diverse surface conditions, further reducing measurement uncertainty and improving the reliability of glacier mass balance assessments.

Furthermore, scaling up this methodology to larger regions is another promising direction. Applying this framework on a global scale would require more efficient processing algorithms and enhanced computational capabilities. Advancing these technical tools would enable comparative analyses across

diverse glaciated regions, helping to identify global patterns and regional anomalies in glacier responses to climate change.

By addressing these opportunities, future research can build on the advancements of this study to unravel the complexities of glacier dynamics and their critical role in the Earth's climate system. These efforts will not only deepen scientific understanding but also support practical applications in sustainable water resource management and climate adaptation strategies in glacier-dependent regions worldwide.

5.4 Summary and outlook of the dissertation

In this dissertation, the application of SAR in alpine cryosphere studies has been advanced by developing innovative methodologies and applying them in diverse alpine regions, including the Alps and the Karakoram. The three studies presented in this dissertation have demonstrated the potential of SAR to enhance the accuracy, scalability, and applicability of remote sensing techniques for monitoring glacier dynamics, snowmelt and glacier mass balance. These advancements provide deeper insights into the interactions between glaciers, snowpack, and climate change, offering important implications for water resource management and climate adaptation strategies in vulnerable alpine environments.

The primary contributions of this research include the development of a novel cross-correlation stacking method for glacier velocity tracking, an integrated framework for seasonal snowmelt mapping, and a comprehensive methodology using InSAR derived DEMs for assessing glacier mass balance. Collectively, these innovations underscore the transformative potential of SAR data in cryosphere studies, offering crucial insights for climate resilience, sustainable water management, and environmental monitoring.

Looking into the future, the methodologies and frameworks developed in this dissertation establish a foundation for continued advancements in cryosphere research, particularly as new SAR technologies and satellite missions emerge.

In recent years, the SAOCOM (Satélite Argentino de Observación Con Microondas) constellation has delivered high-quality L-band SAR data with an 8-day revisit interval [1]. These data have shown promising results in retrieving soil moisture, demonstrating performance comparable to Sentinel-1 [2]. Given the similarities between detecting soil moisture and snow wetness, the proposed snowmelt mapping framework could be applied to SAOCOM data to produce comprehensive wet snow maps for alpine regions.

In a near future, the NISAR (NASA-ISRO Synthetic Aperture Radar) mission, scheduled for launch in 2025, will offer L-band SAR data with validated capabilities for glacier velocity monitoring [3]. The unique penetration characteristics of L-band SAR, compared to the X- and C-band SAR data used in this dissertation, can enhance the cross-correlation stacking method by providing complementary insights into deeper layers of snowpack and glacier ice. This integration could further improve the robustness of glacier dynamics tracking and expand the applicability of the developed methodologies.

In the longer term, although the TanDEM-X mission is still in operation, its data acquisition frequency has been significantly reduced, and the mission is preliminarily scheduled to conclude around 2028–2030[4]. Building upon the legacy of TanDEM-X, the European Space Agency's Harmony mission, expected to launch around 2029–2030, will form a bi-static constellation with two passive satellites and one Sentinel-1 satellite [5]. This mission will enable the generation of DEM time-series using InSAR, similar to TanDEM-X, to extend long-term DEM measurements into the next decade. By combining the DEMs generated by Harmony with the glacier mass balance assessment framework developed in this dissertation, long-term glacier dynamics can be monitored with high temporal resolution. This will provide a more comprehensive understanding of glacier mass change trends and their temporal variability, offering deeper insights into the impacts of climate change on glaciers.

Future research can build upon these approaches to explore broader spatial and temporal scales, integrate additional remote sensing techniques, and address pressing questions in cryosphere-climate interactions. Interdisciplinary collaborations—spanning hydrology, climatology, and geospatial data science—can unlock new opportunities for advancing cryosphere research and tackling the challenges posed by climate change. In conclusion, this dissertation contributes to the broader goal of understanding and mitigating the impacts of climate change on the alpine cryosphere. By advancing SAR applications in alpine cryosphere studies, this dissertation has provided local and global communities with valuable tools and insights for building a sustainable future.

References

1. Palomeque, M., Ferreyra, J. & Thibeault, M. Monitoring Results of the SAOCOM-1 Constellation: A Mission Overview and Summary of Results. *IEEE Geoscience and Remote Sensing Magazine*, 2 (2024).

2. Brunelli, B. & Mancini, F. Comparative Analysis of SAOCOM and Sentinel-1 Data for Surface Soil Moisture Retrieval Using a Change Detection Method in a Semiarid Region (Douro River's Basin, Spain). *International Journal of Applied Earth Observation and Geoinformation* **129**, 103874 (2024).

3. Chapman, B., Anconitano, G., Borsa, A., Christensen, A., Cushman, K. C., Das, A., Donnellan, A., Downs, B., Fielding, E., Holt, B., Joughin, I., Kellndorfer, J., Kim, S., McDonald, K., Meyer, F. J., Oliver-Cabrera, T., Parra, A., Patnai, C., Peacock, A. M., Pinto, N., Putrevu, D., Rosen, P., Saatchi, S., Simons, M., Siqueira, P., Taglialatela, C., Tymofyeyeva, E., Vaccaro, A., Zinke, R. & Zwieback, S. *The NASA ISRO SAR (NISAR) Mission - Validation of Science Measurement Requirements* in *IGARSS 2024 - 2024 IEEE International Geoscience and Remote Sensing Symposium* IGARSS 2024 - 2024 IEEE International Geoscience and Remote Sensing Symposium (2024), 6623.

4. Hajnsek, I., Busche, T., Abdullahi, S., Bachmann, M., Baumgartner, S. V., Bojarski, A., Bueso-Bello, J.-L., Esch, T., Fritz, T., Alonso-Gonzalez, A., Gonzalez, C., Huang, L., Kraus, T., Lachaise, M., Li, S., Dekker, F. L., Maier, K., Martone, M., Milillo, P., Mittermayer, J., Nannini, M., Papathanassiou, K., Pardini, M., Pinheiro, M., Prats-Iraola, P., Rizzoli, P., Rodriguez-Cassola, M., Roth, A., Schandri, M., Scheiber, R., Steinbrecher, U., Schweisshelm, B., Villano, M., Warmedinger, L. J., Wessel, B., Krieger, G., Zink, M. & Moreira, A. TanDEM-X: The 4D Mission Phase for Earth Surface Dynamics: Science activities highlights and new data products after 15 years of bistatic operations. *IEEE Geoscience and Remote Sensing Magazine*, 2 (2025).

5. Kääb, A., Mouginot, J., Prats-Iraola, P., Rignot, E., Rabus, B., Benedikter, A., Rott, H., Nagler, T., Rommen, B. & Lopez-Dekker, P. Potential of the Bi-Static SAR Satellite Companion Mission Harmony for Land-Ice Observations. *Remote Sensing* **16**, 2918 (2024).

- The End -

PUBLICATIONS

Articles in peer-reviewed journals:

1. Li, S., Leinss, S. & Hajnsek, I. Cross-Correlation Stacking for Robust Offset Tracking Using SAR Image Time-Series. *IEEE Journal of Selected Topics in Applied Earth Observations and Remote Sensing* **14**, 4765 (2021).
2. Li, S., Huang, L., Bernhard, P. & Hajnsek, I. Mapping seasonal snow melting in Karakoram using SAR and topographic data. *The Cryosphere* **19**, 1621 (2025).

Conference contributions:

1. Li, S., Leinss, S., Bernhard, P. & Hajnsek, I. *Recent Surge of the South Rimo Glacier, Karakoram: Dynamics Characterization Using SAR Data* in *2021 IEEE International Geoscience and Remote Sensing Symposium IGARSS* (2021), 5520.
2. Li, S., Huang, L., Bernhard, P. & Hajnsek, I. *Wet Snow Mapping In Karakoram Using Sar And Topographic Data* in *IGARSS 2023-2023 IEEE International Geoscience and Remote Sensing Symposium* (2023), 2177.
3. Li, S., Huang, L., Bernhard, P. & Hajnsek, I. *Karakoram Glacier Elevation Change During the Recent Decade Revealed by Tandem-X Dem Series* in *IGARSS 2024-2024 IEEE International Geoscience and Remote Sensing Symposium* (2024), 10867.

Contributions as the co-author:

1. Hajnsek, I., Busche, T., Abdullahi, S., Bachmann, M., Baumgartner, S. V., Bojarski, A., Bueso-Bello, J.-L., Esch, T., Fritz, T., Alonso-Gonzalez, A., *et al.* TanDEM-X: The 4D Mission Phase for Earth Surface Dynamics: Science activities highlights and new data products after 15 years of bistatic operations. *IEEE Geoscience and Remote Sensing Magazine* (2025).
2. Jiang, D., Li, S., Hajnsek, I., Siddique, M. A., Hong, W. & Wu, Y. Glacial lake mapping using remote sensing Geo-Foundation Model. *International Journal of Applied Earth Observation and Geoinformation*, 104371 (2025).

3. Maier, K., Bernhard, P., Ly, S., Volpi, M., Nitze, I., Li, S. & Hajnsek, I. Detecting mass wasting of Retrogressive Thaw Slumps in spaceborne elevation models using deep learning. *International Journal of Applied Earth Observation and Geoinformation* **137**, 104419 (2025).
4. Leinss, S., Li, S. & Frey, O. *Measuring glacier velocity by autofocusing temporally multilooked SAR time series* in *2021 IEEE International Geoscience and Remote Sensing Symposium IGARSS* (2021), 5493.
5. Stefko, M., Li, S., Luck, M. & Hajnsek, I. *Real-Time Simulation of Synthetic Aperture Radar for Educational Augmented-Reality Applications* in *IGARSS 2023-2023 IEEE International Geoscience and Remote Sensing Symposium* (2023), 2301.
6. Jiang, D., Li, S. & Hajnsek, I. *Detection of Supraglacial Lakes using Gaofen-3 data and Advanced Attention U-Net* in *EGU General Assembly Conference Abstracts* (2024), 6243.
7. Leinss, S., Li, S., Yan, Y. & Altena, B. in *Surface Displacement Measurement from Remote Sensing Images* 59 (John Wiley & Sons, Ltd, 2022).